UNIVERSITY OF SOUTHAMPTON

FACULTY OF ENGINEERING, SCIENCE AND MATHEMATICS

School of Chemistry

DIRECTOR DISORDER IN LIQUID CRYSTALS: ESR INVESTIGATIONS

by

Che Rozid Mamat

Thesis for the degree of Doctor of Philosophy

September 2007

UNIVERSITY OF SOUTHAMPTON

ABSTRACT

FACULTY OF ENGINEERING, SCIENCE AND MATHEMATICS
SCHOOL OF CHEMISTRY

Doctor of Philosophy

DIRECTOR DISORDER IN LIQUID CRYSTALS: ESR INVESTIGATIONS

by Che Rozid Mamat

This Thesis reports a range of liquid crystal research which has as its common theme the mis-alignment of the director in liquid crystals when an aligning field is present. The random director distribution for the liquid crystal host is made possible by doping it with guest materials having molecular and macroscopic dimensions. The core investigative technique employed for determining the director distribution is Electron Spin Resonance (ESR) spectroscopy.

The first guest material employed to destroy the uniform director alignment is a clay. On the application of a weak magnetic field inherent in the spectrometer, ESR found partial director alignment for clay concentrations less than 3.0wt%, but not for higher amounts. We believe that the competition between the magnetic and the surface fields, with the elastic effect, accounts for these results. Our results also suggest, indirectly, that the clay particles are also aligned as a consequence of surface coupling to the director alignment.

Gelation produces a network bound with physical bonds in the liquid crystal host, which results to a random director alignment. At a sufficiently high concentration of gelator, the magnetic field of the spectrometer is unable to align the director. The resultant three-dimensional director distribution and powder pattern could be used to determine the principal components of the partially averaged hyperfine tensor. The symmetry of this tensor can then be used to determine that of the nematic phase and so identify the elusive biaxial nematic phase.

The investigation of the behaviour of liquid crystals in porous materials, namely controlled porous glasses, has produced some surprising results. ESR has revealed a range of dynamic behaviour not observed in the bulk. For example, the molecular reorientation is found to be partly in the slow motion regime and partly in the fast. As the pore size increases so the fast motion fraction increases.

In a chiral nematic phase, the spectrometer magnetic field aligns the helix axis perpendicular to the field. This produces a 2D director distribution which can be further perturbed by the field. However, as the pitch of the helix decreases so the director distribution is observed, by ESR, to pass from 2D to 3D. This offers another method of destroying the director alignment and hence determining the phase symmetry.

CONTENTS

Acknowledgements

Page

CHAPTER I Introduction to Liquid Crystals

1.1 Introduction 1
1.2 The Nematic Phase 3
1.3 The Other Liquid Crystal Phases 6
1.4 The Elastic Continuum Theory 9
1.5 The Freedericksz Transition 11
1.6 Director Alignment in Liquid Crystals 13
1.6.1 Surface Field 14
1.6.2 Magnetic Field 15
1.6.3 Electric Field 17
1.7 Liquid Crystal Display Devices 18
1.7.1 Display Modes 19
1.7.1.1 Twisted Nematic (TN) Display 20
1.7.1.2 In-plane Switching (IPS) Display 21
1.7.2 Threshold Voltages 22
1.7.3 Switching Times 23
1.8 Mixtures 24
1.9 Overview of the Thesis 26
1.10 References 27

CHAPTER II Electron Spin Resonance

2.1 Introduction 29
2.2 Basic Theory of Electron Spin Resonance 30
2.2.1 ESR Spectroscopy 31
2.2.2 ESR Spectrometer 38
2.2.3 ESR Spin Probes 40

2.2.4 ESR Spectral and Simulations 42
2.3 Analysis of ESR Powder Pattern and Simulations 46
2.4 Director Distribution Function 50
2.5 References 55

CHAPTER III Experimental

3.1 Introduction 56
3.2 Liquid Crystal Compounds 56
3.3 Sample Preparation 58
3.4 ESR Optimum Parameters 59
3.5 Liquid Crystal Systems 62
3.5.1 Colloidal Particles in a Liquid Crystal 62
3.5.2 Liquid Crystal Gels 62
3.5.3 Liquid Crystal in Confined Materials 63
3.5.4 Chiral Dopants in a Liquid Crystal 64
3.7 References 64

CHAPTER IV Colloidal Nematics

4.1 Introduction 66
4.2 The Chemistry and Physics of Colloids 68
4.3 Colloidal Particles in Nematic Liquid Crystals 70
4.4 Colloidal Nematics: SAXS Studies 74
4.5 Alignment of Colloidal Particles in a Magnetic Field 83
4.6 ESR Spectroscopy and Spectral Simulations 89
4.6.1 The Effect of adding Colloidal Particles to Nematics 90
4.6.2 Dynamic Experiments for Colloidal Nematic Sample 105
4.6.3 Nematic-Isotropic Transition Temperature 113
4.6.4 High-Field Alignment Experiment 118
4.6.5 Isotropic at High-Field 125
4.6.6 Memory Effect: Discussion 126

4.6.7 Flow Alignment 129
4.7 Colloidal Nematics: NMR Studies 134
4.8 Conclusion 139
4.9 References 142

CHAPTER V Nematic Gels and Phase Biaxiality

5.1 Introduction 144
5.2 The Science of Gels 145
5.3 Nematic Gels 149
5.4 Biaxiality and Phase Symmetry 152
5.5 ESR Spectroscopy and Spectral Simulations 165
5.5.1 Gelation of Nematic ZLI-4792 165
5.5.2 Gelation of Nematic 2,3,4-trihexyloxycinnamic acid 173
5.6 Conclusion 178
5.7 References 179

CHAPTER VI Nematics in Confined Geometries

6.1 Introduction 181
6.2 Polymer Dispersed Liquid Crystals 183
6.3 Liquid Crystals in Porous Materials 186
6.4 ESR Spectroscopy of Confined Mesogens 192
6.5 ESR Spectroscopy and Spectral Simulations 196
6.5.1 Tempone Spin Probe 197
6.5.1.1 Temperature Dependent Study: Pore Size 500Å 198
6.5.1.2 Temperature Dependent Study: Pore Size 700Å 200
6.5.1.3 Temperature Dependent Study: Pore Size 1000Å 202
6.5.1.4 Temperature Dependent Study: Pore Size 1400Å 202
6.5.1.5 Temperature Dependent Study: Pore Size 3000Å 205
6.5.2 Cholestane Spin Probe 207
6.5.2.1 Temperature Dependent Study: Pore Size 500Å 207

6.5.2.2 Temperature Dependent Study: Pore Size 700Å 209
6.5.2.3 Temperature Dependent Study: Pore Size 1000Å 209
6.5.2.4 Temperature Dependent Study: Pore Size 1400Å 212
6.5.2.5 Temperature Dependent Study: Pore Size 3000Å 212
6.5.3 Discussion of the Measurement of the ESR Spectra 215
6.5.4 Spin Probes in Viscous Materials 219
6.5.5 Isotropic Solution in Porous Media 221
6.5.6 Simulation for Fast and Slow Motion ESR Spectra 222
6.6 Deuterium NMR of d_2-8CB in a CPG 224
6.7 Conclusion 227
6.8 References 229

CHAPTER VII Magnetic Field Alignment of Chiral Nematics

7.1 Introduction 232
7.2 Chiral Nematics 234
7.3 Perturbation of the Helix by a Magnetic Field 239
7.4 ESR Spectroscopy and Spectral Simulations 246
7.4.1 Concentration of Chiral Dopants in Chiral Nematics: 0.5wt% 251
7.4.2 Concentration of Chiral Dopants in Chiral Nematics: 1.0wt% 255
7.4.3 Concentration of Chiral Dopants in Chiral Nematics: 1.5wt% 261
7.4.4 Concentration of Chiral Dopants in Chiral Nematics: 2.0wt% 267
7.4.5 Concentration of Chiral Dopants in Chiral Nematics: 5.0wt% 270
7.5 Quantitative Calculations for ESR Spectra 273
7.5.1 Temperature Dependence: ($\parallel$ / $\perp$) VS ($\perp$ / $\parallel$) 274
7.5.2 Concentration Dependence: ($\parallel$ / $\perp$) VS ($\perp$ / $\parallel$) 276
7.6 Isotropic to Chiral Nematic Cooling Experiment 277
7.7 Conclusion 279
7.8 References 279

ACKNOWLEDGEMENTS

Alhamdulillah

Through His blessings, I am given this opportunity, strength, motivation and will to go through this journey and complete my PhD.

First and foremost, I would like to thank Professor Geoffrey Luckhurst, my wonderful supervisor for his unfailing guidance, his warmth and unwavering support, his expertise and intelligence, his time and encouragement, and most importantly, his belief in me. Indeed, I am so proud to be one of his students from the first day of my PhD.

I would like to extent my gratitude to Professor George Attard for being my co-supervisor, and to Professor Jim Emsley for the discussion I had with him on the subject matter and for lending me his book which really help me to understand my studies.

My deepest appreciation to Dr. Bakhir Timimi for his kindness and hard work on the porous material experiments, Dr. Azizah Mainal for her friendship and work on the colloidal nematic system, and Mr. Richard Parker for his work on the gelled nematic studies, which contributed to the work in this Thesis.

Along this tremendous journey, I am indebted to the following colleagues for their advice, support or assistance. I must thank all my good friends, especially Ghoyye, Tini and Adi.

Massive appreciation goes to the Universiti Teknologi Malaysia for the sponsorships of my PhD and for entrusting me with this fantastic opportunity.

Last, I don't know how to thank my father, my oldest friend and the inspiration for all that is noble in 'ayah'; my 'mak' who prayed for me and did nazr at every stage of this Thesis's writing. For your patience and understanding, thank you very much.

"no gain without pain"

bismillahirrahmanirrahim

Chapter I

Introduction to Liquid Crystals

1.1 Introduction

Liquid crystal materials are unique in their properties and uses. As research into this field continues and as new applications are developed, liquid crystals will play an important role in modern technology. They are clearly making a major contribution in revolutionising electro-optic display devices, which now range from simple alphanumeric displays to the extremely sophisticated flat panel screens used as electronic monitors and TV screens; and more recently for the latest rear-view mirror for a car radar system; see the picture:

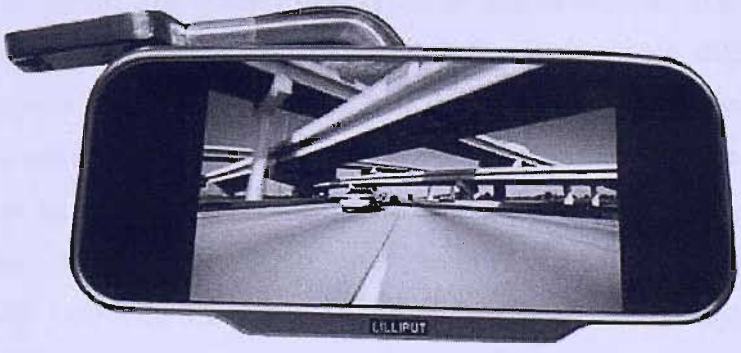

(Courtesy of Lilliput UK), not to mention, that liquid crystals also have applications for non-display technologies which include temperature sensors and optical switches. It is well known that the field of liquid crystals is very broad, and it is studied by scientists from many different disciplines; chemists, physicists, engineers, biologists as well as mathematicians. Thus, the technologies invented were an essential combination from various disciplines and backgrounds.

Lehmann first used the term 'liquid crystal' in 1890 to label a state of matter intermediate between solid crystals and ordinary liquids [1]. Physically, liquid crystals flow like ordinary liquids, e.g. they adopt the shape of their container. On the other hand, they also exhibit anisotropic properties, as for solid crystals. It is then a condensed fluid phase with a spontaneous anisotropy. Liquid crystals are also called mesophases or mesomorphic phases because of their intermediate nature between that of a solid and of a liquid. This fourth state of matter can often be identified visually by its characteristic turbidity or by its optical birefringence with polarising microscopy.

A phase transition occurs when the turbid liquid becomes clear, or the optical textures seen between crossed polarisers appears dark, as the birefringence vanishes, which is called the liquid crystal-isotropic transition temperature. Generally, in a broad sense, there are two classes of liquid crystals. One of these depends for its existence on temperature is called a *thermotropic* liquid crystal. The other is known as a *lyotropic* liquid crystal, made upon dissolution in an appropriate solvent (usually water). Organic compounds form liquid crystals when the solid crystal is heated above its melting point. Some of them exhibit more than one liquid crystal phase between the solid and isotropic phases and they are said to be 'polymorphous'. There are three main types of liquid crystal; *Nematic*, *Smectic* and *Chiral nematic*. These three varieties of liquid crystals differ from each other in their molecular organisation, but they all show one common feature in which the molecules tend to have their near symmetry axes parallel over distances large in comparison with molecular dimensions, that is the long axis for rod-like molecules and the short axis for discotic molecules. In this Thesis, we will concentrate only on thermotropic liquid crystals, mainly nematic and chiral nematic phases.

1.2 The Nematic Phase

To describe a liquid crystal, there are two concepts that are relevant; the director, $\hat{n}$, and a complete set of molecular order parameters [2]. The director is a unit vector defined at every point of the mesophase and giving the local preferred molecular orientation which coincides with the optic axis of the mesophase. In an unperturbed mesophase, the director can adopt all orientations with equal probability, as shown in Figure 1. Moreover the director mainly varies slowly and continuously from one point in the system to the other, except at singularities called disclinations where the preferred orientation changes abruptly.

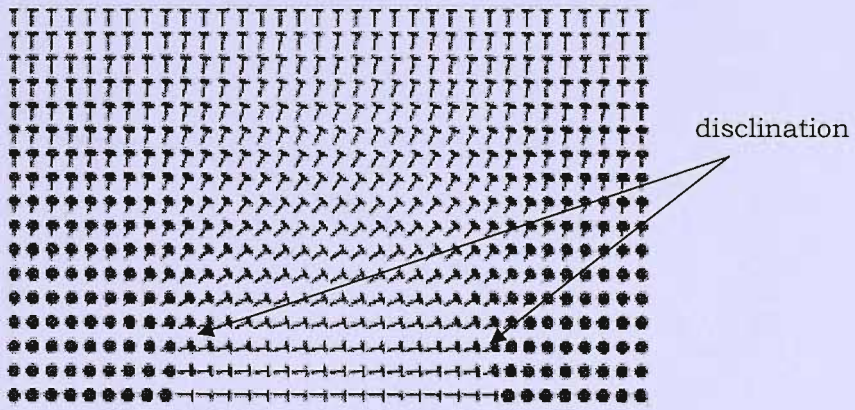

Figure 1: The adoption of director orientation with equal probability (each nail represents director).

In general, the extent of molecular alignment with respect to the director is described by a set of orientational order parameters. However, in practice, only the second rank order parameter, $\overline{P_2}$ is used to describe the degree of such alignment in uniaxial liquid crystals. A phase is said to be uniaxial when there is only one principal axis that governs the properties of the phase. For molecules with D_{nh} symmetry or higher with $n \geq 3$, the second rank orientational order parameter is defined as

$$\overline{P_2} = \frac{\overline{3\cos^2\theta - 1}}{2}, \qquad (1.1)$$

where θ is the angle between the director and the symmetry axis of the molecule (assumed to be cylindrically symmetry). Obviously, $\overline{P}_2$ reduces to zero in the case of zero order (an isotropic system), and unity for perfect alignment. The orientational order for a nematic is typically around 0.4, just below the nematic-to-isotropic transition and extends to as high as 0.8 when the temperature is lowered [4]. It changes abruptly to zero at the nematic-isotropic transition. Experimentally, $\overline{P}_2$ is usually found to decrease with increasing temperature and vanishes suddenly at the nematic-isotropic transition temperature, T_{NI}. Figure 2 shows the changes of $\overline{P}_2$ with changing temperature.

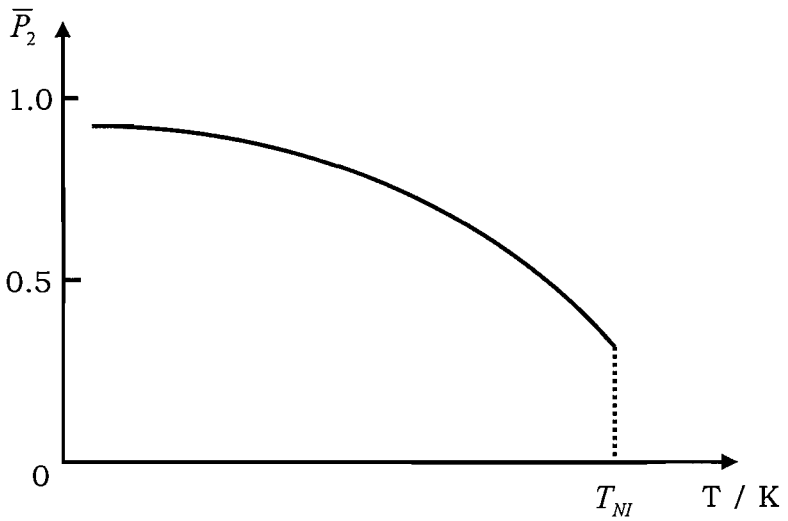

Figure 2: A plot of $\overline{P}_2$ versus temperature for a nematic liquid crystal.

The nematic liquid crystal has the simplest molecular arrangement within the mesophase and is the most disordered phase out of the three types. It has long-range orientational order, that is the molecules align approximately parallel to each other, but has no long-range positional order (see Figure 3) which allows them to move freely. One of the characteristics of the nematic mesophase is that the axis of symmetry has no polarity, even if the molecules themselves are polar. Consequently, the sign of the unit vector is of no physical importance that is $\hat{n}$ and $-\hat{n}$ are equivalent.

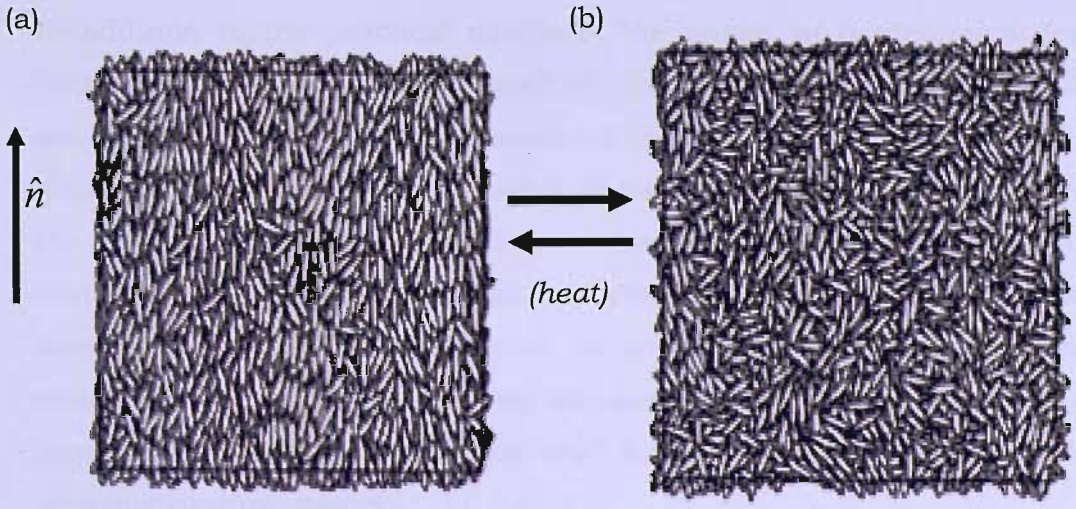

Figure 3: *Schematic representation at a molecular level for (a) nematic phase and (b) isotropic phase.*

Observation of a nematic under a polarising microscope shows many dark lines which originate from differences in the director pattern caused by the defects in the director field; these are also known as disclinations. The dark lines result from the optical extinction caused by the crossed polarisers and for this to happen, the director must be aligned in the direction of either one of the other polariser. These disclinations could occur at points, which result in defects known as brush defects. The texture observed for a nematic with homogenous alignment is known as a *Schlieren* texture. The homogeneous alignment often induced close to the clearing point where the phase could appear to be most colourful as could be seen in Figure 4. The changes of birefringence throughout the sample produce a colour change across the texture.

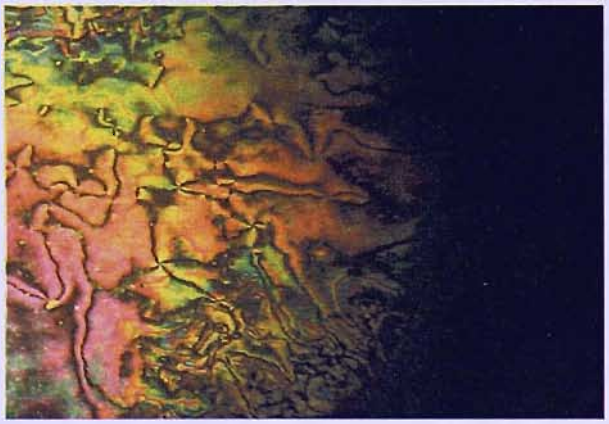

Figure 4: *Schlieren texture for liquid crystal 5CB under microscope. The black region represents the isotropic phase. The defects indicate that the director is not uniformly aligned.*

In addition to the practical details of the phase, at a theoretical level the occurrence of the liquid crystalline phase is caused by the molecular anisotropy. This includes the molecular polarisability, as well as by the shape anisotropy. The molecular statistical theory by *Maier* and *Saupe* [3] accorded the molecular anisotropy to that of the polarisability although it is now realised that the shape plays an important if not dominant role. Therefore, mesomorphic behaviour is found in compounds composed of elongated molecules, which in most but not all cases consist of a conjugated aromatic system. Most of the compounds that form nematic liquid crystals have a simple structure, namely

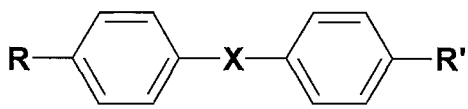

where the important groups X linking the two substituted phenyl rings are listed in Table 1.

Table 1: *The name for the X linking group of compounds forming nematic liquid crystals.*

-X-	**Name**
-N=N-	*azobenzenes*
-N=NO-	*azoxybenzenes*
-CH=CH-	*stilbenes (trans)*
-C≡C-	*tolanes*
-CH=N(O)-	*nitrones*
-CH=N-	*Schiff bases*
-O-CO-	*phenyls benzoates*
-	*biphenyls*

1.3 The Other Liquid Crystal Phases

Chiral nematic liquid crystals have much in common with the nematic phase, but the director is spontaneously twisted into a helix. This phase used to be called *cholesteric* which stems from the observation that the majority of chiral nematic phases are formed by esters and other derivatives of cholesterol [5]. The helical structure is characterised by a pitch, P, that is equal to the length over which a rotation of 360° of the preferred molecular

direction, or director, occurs. Likewise, the nematic mesophase can be considered as a chiral nematic phase but with infinite pitch. Figure 5 shows a schematic representation for chiral nematic phase.

In chiral nematic phase, the helical arrangement of the director can be exploiting to rotate the plane polarised light. The helix also reflects light selectively which is analogous to that encountered in X-ray crystallography. The pitch of the helix for most chiral nematic mesophases is usually in the range 0.2 to 20μm. It is known that chiral nematic materials are only found in substances which are optically active, while the racemates of such substances give only a nematic phase. Alternatively, if two chiral nematic phases with left and right handed helices are mixed then a nematic phase results at a particular temperature and composition.

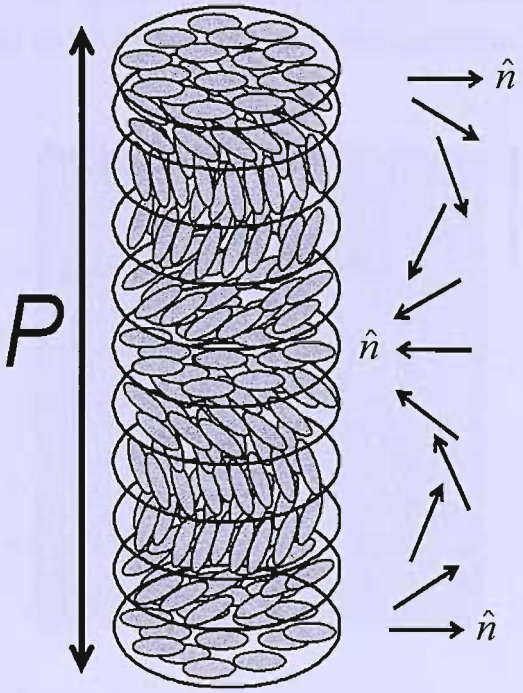

Figure 5: *Schematic representation of the chiral nematic mesophase showing the helical structure.*

The other type of liquid crystals is the smectic mesophases. The name smectic was selected from the Greek word *smectos* meaning soap-like, because of the slippery nature of soaps [6]. The phase has long-range orientational order but unlike a nematic, this smectic phase also has a long-range positional order, that is there is a tendency for the molecules to be

arranged with their ends forming well-defined layers as shown in Figure 6. The layer structure is the defining characteristic for the smectic phase. Because of the formation of the lamellar structure, molecular motion within this mesophase is much restricted, the main restriction being the longitudinal translation between the layers. This also gives rise to its considerably higher viscosity. Within the layers, rotation and lateral motions are possible.

There are varieties of smectic mesophases, and they can be recognised clearly by the molecular arrangements in the layers of the mesophase. For example, in the smectic A phase the molecules are generally pictured as aligned parallel to the layer normal, and the centres of mass are uncorrelated within a layer as in a liquid; here more accurately the director is normal to the layers. Like the nematic mesophase, the smectic A phase has D_{3h} or higher symmetry and is optically uniaxial. The orientational order in the smectic phase is found to be higher than for the nematic phase [7].

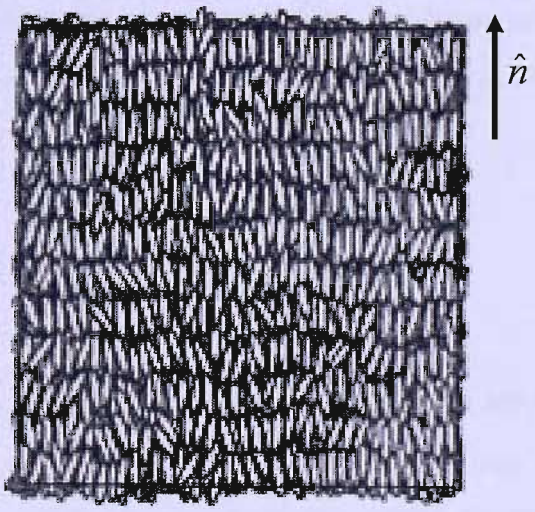

Figure 6: The molecular organisation within a smectic A mesophase.

1.4 The Elastic Continuum Theory

In a macroscopic volume of liquid crystal, the director is generally not uniform. However, on a microscopic level, the local distribution of the molecules does not vary throughout the sample that is the orientational and positional order parameters do not vary within the sample. The continuum theory, therefore, concerns itself with the elastic properties of the sample, assuming all order parameters remain constant, hence the liquid crystal phase remains locally uniaxial. This assumption is not effective if there are defects in the director field. Nevertheless, these defects are ignored in this discussion.

When the director undergoes a change from one orientation to another, a curvature is introduced. The curvature or distortion of the undisturbed state requires a certain amount of energy since elastic torques attempt to maintain the original uniform configuration. From a theoretical point of view, the curvature is described by the continuum theory that gives the elastic energy as a function of the director curvature. The fundamental equation of the continuum theory for a nematic liquid crystal is for F_{dist}, the distortion free energy per unit volume [8]:

$$F_{dist} = \frac{1}{2}K_1\left[\nabla\cdot\hat{n}\right]^2 + \frac{1}{2}K_2\left[\hat{n}\cdot\left(\nabla\times\hat{n}\right)\right]^2 + \frac{1}{2}K_3\left|\hat{n}\times\left(\nabla\cdot\hat{n}\right)\right|^2, \tag{1.2}$$

where K_1, K_2 and K_3 are the elastic constants, also known as the *Oseen-Zocher-Frank* constants, since the continuum theory was actually proposed independently by these three [9-10]. The three elastic constants represent the stiffness of liquid crystal phase to distortions of the director. For the director along z-axis as its origin, the evaluation of the derivatives in each term at a point in a liquid crystal gives three examples that highlight the meaning of this expression for the free energy per unit volume. Accordingly the first derivative of n_z with respect to x, y, or z is zero at this point.

The three principal or fundamental distortions of the director, namely splay, twist and bend distortion, are shown in Figure 7 and the formal definitions of the deformations are:

Splay: $$\left[\nabla \cdot \hat{n}\right] = \left(\frac{\partial n_x}{\partial x}\right)_{y,z} + \left(\frac{\partial n_y}{\partial y}\right)_{x,z}, \tag{1.3}$$

Twist: $$\left[\hat{n} \cdot (\nabla \times \hat{n})\right] = \left(\frac{\partial n_y}{\partial x}\right)_{y,z} - \left(\frac{\partial n_x}{\partial y}\right)_{x,z}, \tag{1.4}$$

Bend: $$\left|\hat{n} \times (\nabla \times \hat{n})\right|^2 = \left(\frac{\partial n_x}{\partial z}\right)^2_{x,y} + \left(\frac{\partial n_y}{\partial z}\right)^2_{x,y}. \tag{1.5}$$

Thus K_1, K_2 and K_3 are called the splay, twist and bend elastic constants, respectively; typical values for these constants are about 10^{-12}N. The total elastic energy associated with the distortion must, of course, be a minimum to obtain the condition for equilibrium in the bulk of a nematic. In the presence of a magnetic field or an electric field, the total free energy is the sum of the magnetic free energy density (see equation 1.10) [11] or the electric free energy density (see equation 1.14) and the elastic free energy density (see equation 1.2).

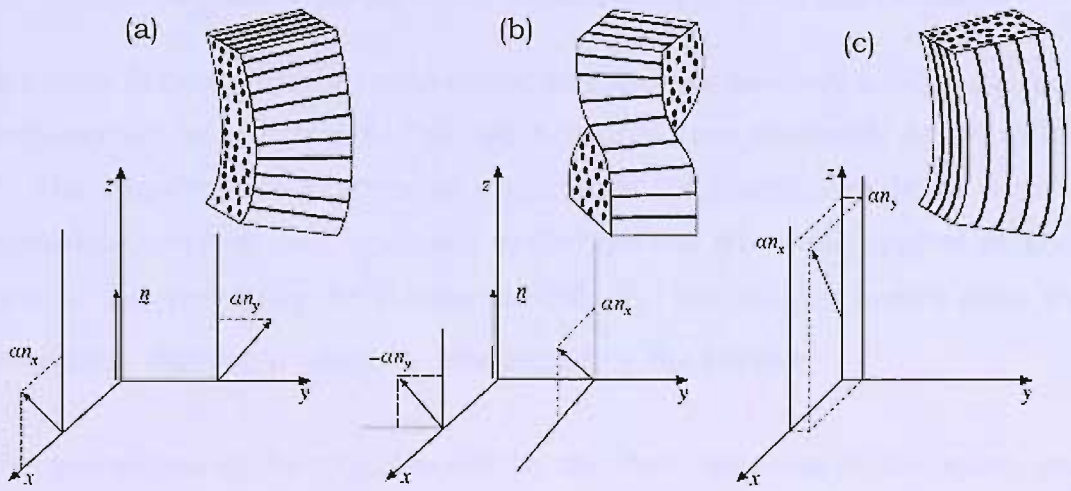

Figure 7: The three fundamental deformations for the nematic director, (a) splay, (b) twist and (c) bend distortion [13].

1.5 The Freedericksz Transition

The Freedericksz transition occurs when the alignment at a substrate boundary opposes the alignment by an applied field. It is a threshold phenomenon that results from the competition between an external field with the surface and elastic effect for the director alignment. Three simple experiments devised by Freedericksz actually provide a way to determine the three elastic constants, K_1, K_2 and K_3 [12]. Figure 8 shows the separate geometries of the cells' configurations with the preferred director alignment, at the interfaces and the direction of an external field.

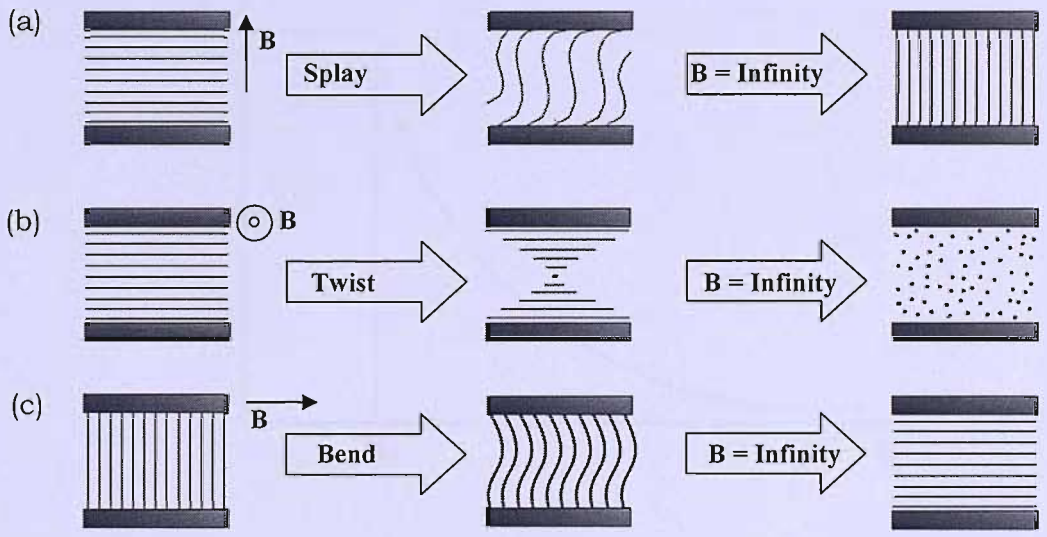

Figure 8: *The configuration of the cells before and after the Freedericksz transition for (a) splay, (b) twist and (c) bend deformations.*

The lines between the two substrates indicate the director, which is strongly anchored at the substrates. The two substrates are separated by a distance, d. The Freedericksz experiment determines the elastic constants when an increasing external field is applied to the system. When the applied magnetic field, B is larger than the threshold field, B_{th}, the director moves away from its original alignment which is determined by the surface.

The geometries of the experiments for the determination of the splay, twist and bend deformations are similar, they differ only in the initial director orientation with respect to the surface and the direction of the applied field. For a liquid crystal with a positive diamagnetic susceptibility, the magnetic

field will align the director parallel to the field, so that the deformations shown in Figure 8 are produced. Formerly, the angle, θ, between the director and the applied field is consistent with the increasing field and so the elastic forces are dominant. However, as the threshold field, B_{th}, is approached, θ begins to decrease until the magnetic energy is dominant and so the elastic forces are overcome. At this stage, the director is aligned parallel (since $\Delta\tilde{\chi} > 0$) to the magnetic field, to its new equilibrium position with a limiting value of $\theta = 0°$. The plot in Figure 9 illustrates the change of the angle θ with the increasing magnetic field.

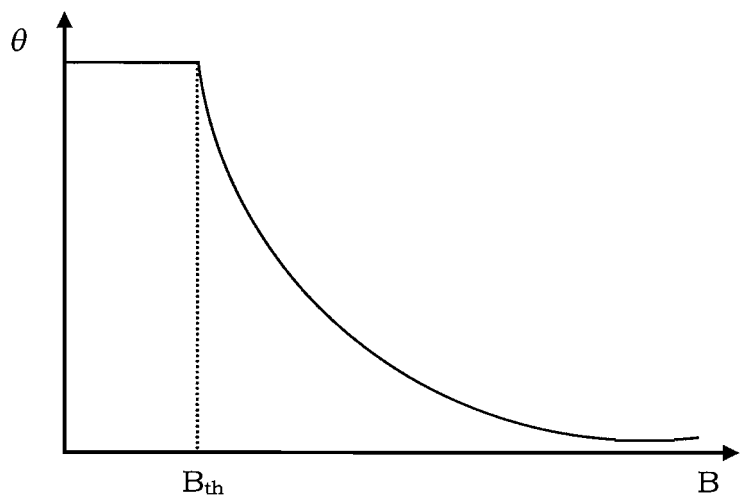

Figure 9: *Plot of angle, θ versus magnetic field, B showing the threshold field of a cell.*

At the threshold field, the elastic and magnetic energies balance; that is

$$U_{magnetic} \approx U_{elastic}, \tag{1.6}$$

therefore, for the twist deformation

$$\Delta\tilde{\chi}B_2 / 2\mu_0 \approx K_2 / d^2, \tag{1.7}$$

giving

$$K_2 = \Delta\tilde{\chi}B_{th}^2 d^2 / 2\mu_0. \tag{1.8}$$

This approximate result is close to the exact result which is [14]

$$K_i = \Delta\tilde{\chi} B_{th}^2 d^2 / \pi^2 \mu_0. \tag{1.9}$$

As shown in Figure 10, the elastic constant for the twist deformation seems to have the smallest value, which means this is the easiest deformation to produce. While the bend deformation is the hardest to create as the bend elastic constant takes the highest values; it requires a higher magnetic field to align the director than any other director deformations. The elastic constants are not in fact constant but vary with the temperature [13]. They decrease with increasing temperature in keeping with the decreasing order as the transition to the isotropic phase is approached.

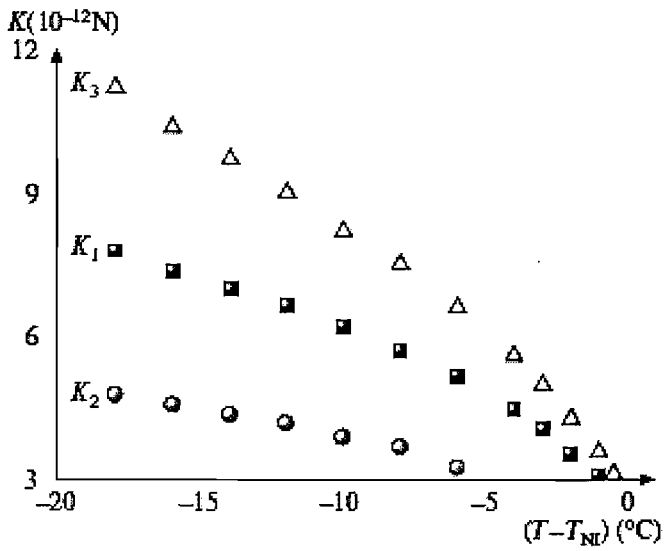

Figure 10: The temperature dependence of the three elastic constant, K_1, K_2, and K_3 for nematic 5CB.

1.6 Director Alignment in Liquid Crystals

In the absence of any external perturbations, the macroscopic order in a bulk liquid crystal is zero since the director is free to adopt all orientations with equal probability. However, it is possible to obtain a macroscopically well-aligned sample in several ways, such as proper surface treatment of the substrate and the application of a magnetic or an electric field. Even a large

sample of the mesophase can be aligned by both magnetic and electric fields [15]. This is in contrast to the very weak field effects in ordinary liquids where the field-induced alignment is very weak. The enhanced field-induced ordering is due to the anisotropic intermolecular forces responsible for the mesomorphic state which leads to a cooperative behaviour of the molecules.

There are two possible extreme types of director alignment at a substrate; uniform planar (also known as homogenous) and homeotropic. Figure 11 shows the both types of director alignment between glass substrates.

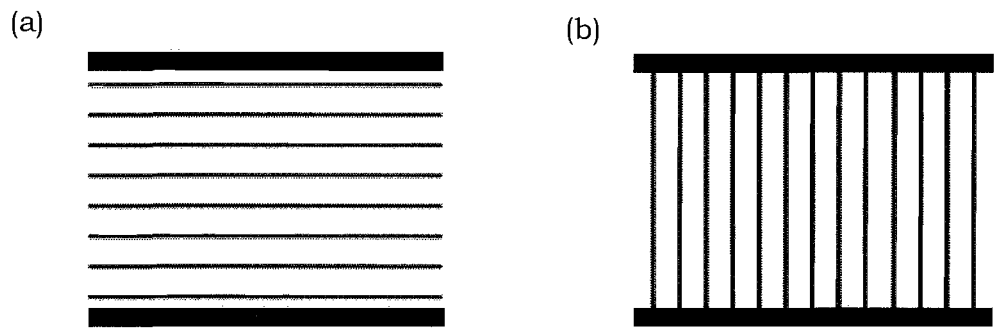

Figure 11: Extreme types of director alignment between the glass substrates; (a) uniform planar and (b) homeotropic director alignment.

The director of the liquid crystal phase is orientated parallel to the substrate and to a given direction in a uniform planar alignment. It exhibits a strong birefringence between crossed polarisers and defects or disclinations are observed if the director is not perfectly aligned. While for homeotropic alignment, the director tends to align orthogonal to the substrates, so under a polarising microscope, complete blackness is observed since the polarisation of the light is not changed on passing through the nematic film.

1.6.1 Surface Field

Use of the surface field alone, can produce director alignment, both uniform planar and homeotropic. We can obtain a uniform planar alignment when the two supporting substrates are suitably treated prior to insertion of the liquid crystal, and rubbed many times along one direction [16-18]. This gives a parallel orientation to the direction of rubbing and to the surface of the

substrates. Liquid crystal cells with uniform planar alignment require the glass substrates to be coated with multifunctional groups such *polyimides*, then followed by rubbing in order to induce a preferred alignment direction in the surface.

While for homeotropic alignment, the glass substrates need to be treated with base and then acid to produce a surface covered with silanol groups that will interact with polar liquid crystals. This happens when the alignment layer of mesogenic molecules at the surface that interact with the mesogenic molecules from the bulk, which then induces alignment perpendicular to the surface of the glass substrates. However, this procedure will not work for non-polar liquid crystals, so to overcome this problem, an alkylated surface needs to be produced by coating the glass with a long chain alcohol at high temperatures. The long alkyl chains, which are normal to the glass, then interact with the alkyl chains of the mesogenic molecules to induce a normal alignment.

Both uniform planar and homeotropic director alignments can also be obtained by coating certain organic chemicals onto the surface of the substrates. Materials such as *lecithin* [19], *polyamide resin Versamid* [20], *alkoxysilane* monomers of the general type $RSiX_3$ where R is an organofunctional group and X is a *hydrolysable* group [21], *hexadecyl-trimethylammonium bromide* (HTAB) [22] and many others have been successfully used to prepare the desired alignment.

1.6.2 Magnetic Field

In the presence of a magnetic field, the magnetic free energy density takes the form [23,24]

$$F_{mag} = -\frac{1}{2}\mu_0^{-1}\Delta\tilde{\chi}(\boldsymbol{B}.\hat{\boldsymbol{n}})^2, \tag{1.10}$$

where μ_0 is the permeability of a vacuum, $\Delta\tilde{\chi}$ is the anisotropy in the magnetic susceptibility and B is the magnetic field strength. Paramagnetic

molecules have one or more unpaired electrons which force the sample to move to regions of high field, whereas diamagnetic molecules have no unpaired electrons and are forced to regions of low magnetic field. Most liquid crystal molecules are generally diamagnetic. When a diamagnetic material is subject to a uniform magnetic field its energy is changed and this change is

$$U = -\chi B^2 / 2\mu_0, \tag{1.11}$$

The negative value for the magnetic susceptibility means they become more stable as it moves to regions of low field.

The behaviour is even more interesting for a liquid crystal phase since the magnetic susceptibility can take two extreme values, $\tilde{\chi}_{\parallel}$ for along the director and $\tilde{\chi}_{\perp}$ for the component perpendicular to the director, depends on the anisotropy of the liquid crystal phase. The anisotropy in the diamagnetic susceptibility, $\Delta\tilde{\chi}$, is

$$\Delta\tilde{\chi} = \tilde{\chi}_{\parallel} - \tilde{\chi}_{\perp}. \tag{1.12}$$

Then, the difference in energy between the director being parallel and perpendicular to the magnetic field is

$$\Delta U = -\Delta\tilde{\chi} B^2 / 2\mu_0. \tag{1.13}$$

This means that the energy difference, ΔU, is negative when $\Delta\tilde{\chi}$ is positive, which causes the director to align parallel to the magnetic field and vice versa. As we have noted the enhancement of $\Delta\tilde{\chi}$ is caused by the long-range orientational correlation in nematic liquid crystals. The large value of $\Delta\tilde{\chi}$ accounts for the relative ease with which quite modest fields of about one or two kilogauss are able to align a nematic liquid crystal. Since most nematogens have positive $\Delta\tilde{\chi}$ the director is aligned parallel to the applied field.

However, it is more difficult to align a steroidal chiral nematic mesophase. This is because most chiral nematics contain saturated rings which lead to a small $\Delta\tilde{\chi}$ for an individual molecule. The helical structure of the chiral nematic mesophase further reduces the total $\Delta\tilde{\chi}$ for the system. Also, the helical structure causes a complication when the applied field is perpendicular to the helix axis, the magnetic contribution to the orientational free energy will force the director to lie parallel to the field (assuming $\Delta\tilde{\chi}$ is negative). In this geometry the mesophase preserves its helical structure and the pitch of the helix remains independent of the field strength. As we shall see the situation is more interesting when the diamagnetic susceptibility is positive.

1.6.3 Electric Field

Since most applications of liquid crystals in display devices need an electric field for their operation, then the understanding of the response of nematogens to an electric field is of particular importance. The effect of applying a high frequency electric field (~20kHz) is analogous to that of a magnetic field. It is increased by the enhanced anisotropy in the dielectric constant, $\Delta\tilde{\varepsilon}$. In the presence of an electric field, the total free energy of a nematic is the sum of the electric free energy density,

$$F_{diel} = -\frac{1}{2}\varepsilon_0 \Delta\tilde{\varepsilon}_2 (\boldsymbol{E}.\hat{\boldsymbol{n}})^2, \tag{1.14}$$

where ε_0 is the permittivity of a vacuum, $\Delta\tilde{\varepsilon}$ is the relative anisotropy in the permittivity and E is the electric field strength. When a uniaxial mesophase is subject to a uniform electric field, E, its energy is changed, depending on whether the field is parallel or perpendicular to the director. The resultant energy difference is

$$\Delta U = -\varepsilon_0 \Delta\tilde{\varepsilon} E^2. \tag{1.15}$$

$\Delta\tilde{\varepsilon}$ is also known as the dielectric anisotropy of the nematic and is given by

$$\Delta\tilde{\varepsilon} = \tilde{\varepsilon}_{\parallel} - \tilde{\varepsilon}_{\perp}. \tag{1.16}$$

The director aligns either parallel or perpendicular to the field depending on whether $\Delta\tilde{\varepsilon}$ is positive or negative, respectively. The sign of $\Delta\tilde{\varepsilon}$ takes positive and negative with approximately equal frequency [25]. However, compounds exhibiting negative $\Delta\tilde{\varepsilon}$ such as 4,4'-dimethoxyazoxybenzene have been found to align parallel to a direct current or low frequency electric field [26] which probably results for ionic conduction. It is apparent that electric field effects are more complicated that magnetic field effects.

The transition from a chiral nematic to a nematic phase can also be induced by a strong electric field. This transition only occurs for a chiral nematic material with a positive dielectric anisotropy. The untwisting of the chiral nematic structure happens in much the same way as that induced by a large magnetic field.

1.7 Liquid Crystal Display Devices

Even in the early days of liquid crystal research, the use of liquid crystals as an important material for electro-optic device was discussed. It started in 1918 when a Swedish physicist, *Björnståhl*, demonstrated that an electric field could vary the intensity of light transmitted through liquid crystals [27]. In addition, in 1936, the *Marconi Company* patented the use of high birefringence nematic liquid crystals as an electro-optic shutter [28]. This electro-optic property of liquid crystals was not exploited until 35 years later when it was gradually used to an increasing extent in commercial devices. However, one of the problems was the lack of suitable materials that could be used in such displays.

1.7.1 Display Modes

Today, conventional cathode ray tube (CRT) is less apparent in the market since the thin, light and low power consumption of liquid crystal display (LCD) has replaced as an important display device. There are many LCD modes that have been created to fulfil the needs for the display market from the dynamic scattering (DS) mode, the twisted nematic (TN) mode [29], the super twisted nematic (STN) mode [30] to the latest display technology, thin film transistor (TFT) mode [31]. In all of these display devices, the birefringence of liquid crystals is exploited, as is director alignment by an electric field. Therefore, electrical properties such as the dielectric anisotropy also play a fundamental role.

The device behaviour depends on the nature and configuration of the cell used. The basic cell configuration in displays contains the liquid crystal between two glass substrates coated with a transparent alloy of *indium* and *tin oxides*. These electrodes are covered with plastic to prevent the electrochemical degradation of the liquid crystal. Between the two substrates, there are thin plastic spacers, typically several microns thick, and sealed with a thermoplastic resin. In order to produce the preferred alignment of the director, the surfaces of the electrodes are also treated, according to the type of device. Figure 12 illustrates the configuration of a typical liquid crystal cell. Every mode for the various display devices are controlled by an electric field. Therefore, electrical properties such as the dielectric anisotropy play a fundamental role in this area.

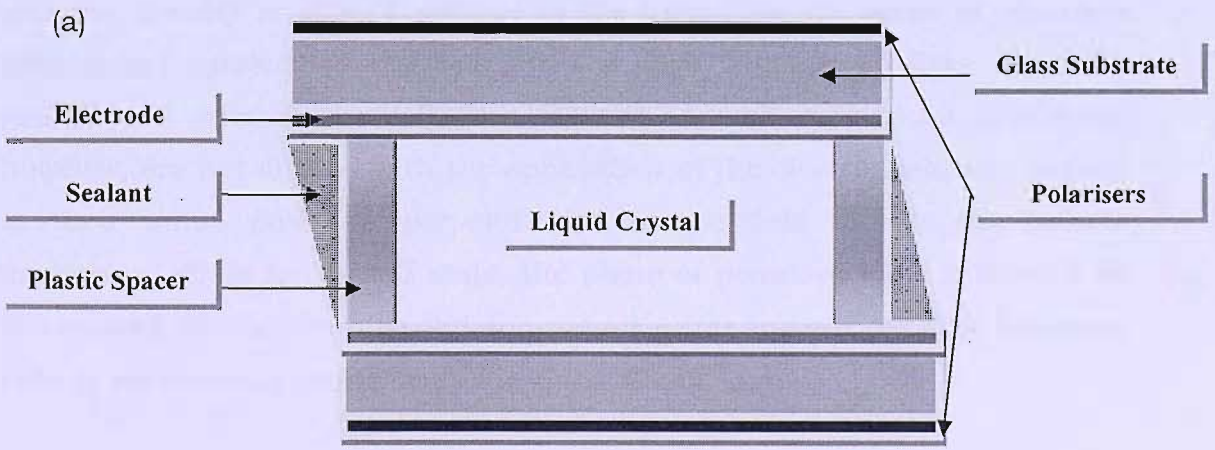

(b)

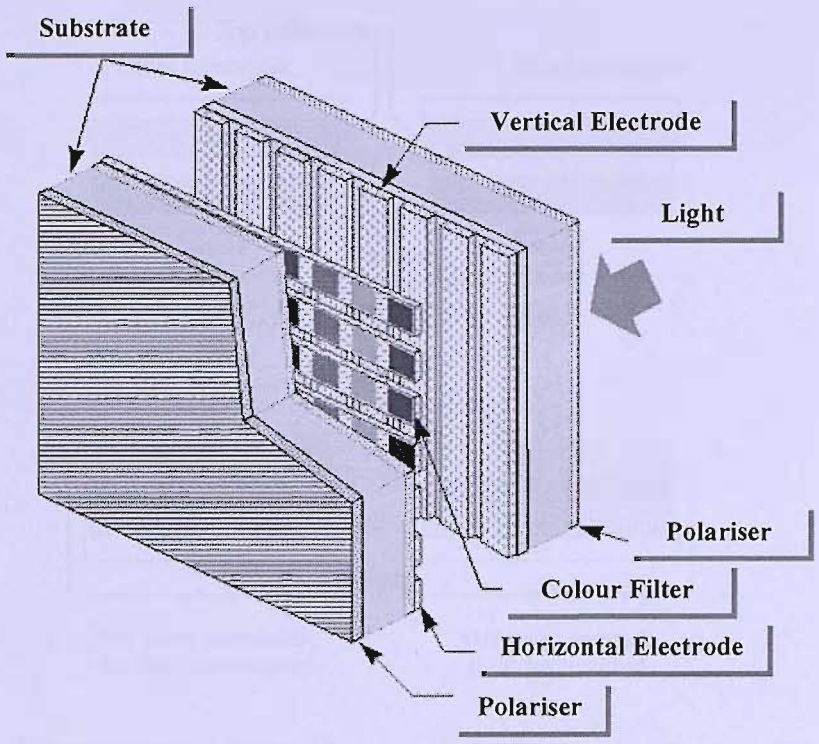

Figure 12: Construction of display devices; (a) typical cell diagram and (b) side-view of simple matrix LCDs.

1.7.1.1 Twisted Nematic (TN) Display

The most common LCD mode is the twisted nematic display, in which the director forms a one-quarter helix across the cell, as shown in Figure 13. There are two modes describing the operation of a TN cell; an on state and an off state. On the application of an electric field (on state), provided the dielectric anisotropy is positive, the quarter helix of the director is unwound and the director is aligned parallel to the field. Now the plane of polarised light is not rotated, so the cell appears dark because no light has been transmitted through the cell. The director at each surface for this state, however, are not aligned with the application of the electric field and remain at their initial positions perpendicular to the field due to the infinite anchoring. While for the off state, the plane of polarised light is rotated by the twisted director through 90° to produce a transparent cell. The polarised light is successfully transmitted through the cell.

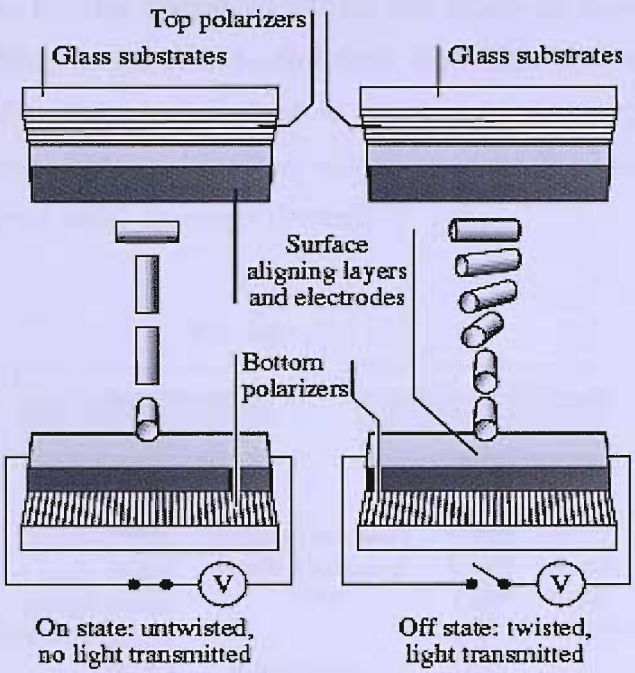

Figure 13: Schematic of a twisted nematic (TN) display, for on state and off state [37].

The introduction of thin film transistor (TFT) technology has had a very good impact to the development of LCDs area [31]. This technology has been combined with the TN mode to produce TN-TFT-LCD which has the best quality and occupies the main LCD market. Nevertheless, there are several disadvantages of TN-TFT-LCD, mainly their slow response time and relatively narrow viewing angle. Slow response time gives difficulty to any display device especially when the pictures are required to move. The narrow viewing angle has limited the use of the display. New switching modes have been developed to solve these problems, such as the in-plane switching (IPS) mode.

1.7.1.2 In-plane Switching (IPS) Display

The in-plane switching mode especially with combination of the TFT mode gives an extremely wide viewing angle [35, 36]. The IPS mode takes place for a director orientation in a plane parallel to the glass substrates. The applied field should be in the same direction and this is achieved by placing interdigital electrodes on one side of the substrate. These electrodes also limit the aperture ratio to achieve high brightness and good contrast [32]. The

schematic diagram for the operation of the IPS mode is shown in Figure 14. The director, at first, is parallel to the field direction and also to the glass substrates, but after the electric field is applied to the in-plane electrodes, the director at the bottom surface aligns perpendicularly to its initial direction, to induce a twist through the cell.

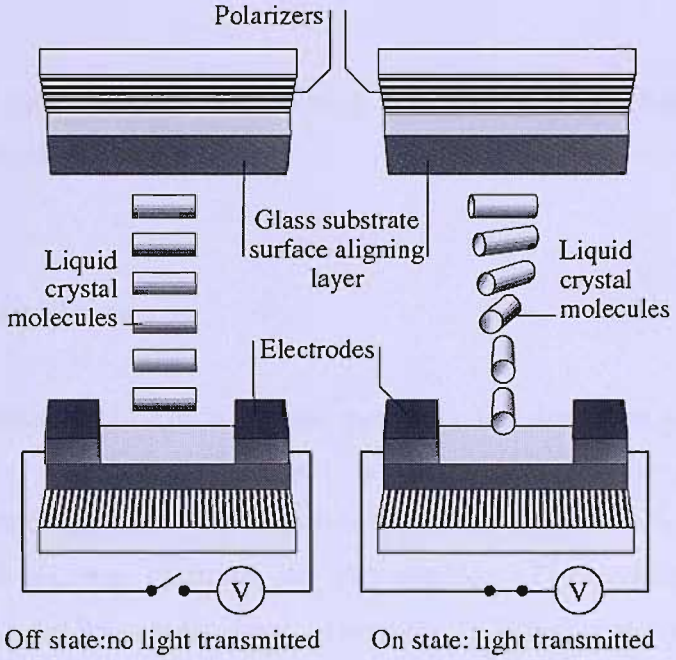

Figure 14: Schematic diagram of an IPS switching mode display; the state is stabilised by the electric field which depends on the dielectric anisotropy of liquid crystal material [37].

1.7.2 Threshold Voltages

The threshold voltage for a LCD determines the range of applied electric fields required to operate the LCD and also determines the cost of the driving devices. The threshold voltage in the TN mode is given by [29, 33, 34]

$$V_{th} = \pi \left[\frac{(K_1 + (K_3 - 2K_2)/4)}{\varepsilon_0 \Delta\tilde{\varepsilon}} \right]^{1/2} . \qquad (1.17)$$

This expression is obtained from the Freedericksz transition experiment for the twisted planar layer, which can be derived by the rotating the upper

substrate of a uniform planar layer through an angle 90°. For the IPS mode, the expression is slightly different, since V_{th} depends exclusively on the twist elastic constant, K_2. The threshold voltage in the IPS mode is given by [35]

$$V_{th} = \frac{\pi l}{d}\sqrt{\frac{K_2}{\varepsilon_0 \Delta\tilde{\varepsilon}}}, \tag{1.18}$$

where d is the gap of the LCD cell and l is the distance between a pair of interdigital electrodes.

1.7.3 Switching Times

The switching time for LCDs is a vital property for displays as it determines how rapidly the director orientation can be changed on application or removal of an external field. This time is of prime importance for the quality of the image of moving pictures on the display. The switching times are largely governed by the rotational viscosity, γ_1. For the twisted nematic mode, the switching time when the electric field is applied, τ_{ON} and when the electric field is removed τ_{OFF}, are given by [29,33,34]

$$\tau_{ON} = \frac{\gamma_1 d^2}{\varepsilon_0 \Delta\tilde{\varepsilon} V^2 - \pi^2\{K_1 + (K_3 - 2K_2)/4\}}, \tag{1.19}$$

$$\tau_{OFF} = \frac{\gamma_1 d^2}{\pi^2\{K_1 + (K_3 - 2K_2)/4\}}, \tag{1.20}$$

where γ_1 is the rotational viscosity coefficient and V is the applied voltage. For the TN mode, all three elastic constants are involved. While for the IPS mode, the switching times are given by [36]

$$\tau_{ON} = \frac{\gamma_1 d^2}{\varepsilon_0 \Delta\tilde{\varepsilon} V^2 - \pi^2 K_2}, \tag{1.21}$$

$$\tau_{OFF} = \frac{\gamma_1 d^2}{\pi^2 K_2}. \tag{1.22}$$

As for V_{th}, the main difference from the TN mode is that the response times depend only on the single twist elastic constant, K_2. In order to improve the switching times, a smaller γ_1 and a larger $\Delta\varepsilon$ are needed.

1.8 Mixtures

The liquid crystal material is the most important thing in the LCD since its performance governs the development of the display devices. To find a single liquid crystal, which possesses all of the desired properties for a display, is quite impossible. So that, all display devices use liquid crystal mixtures made up of many liquid crystal components to obtain a system with ideal physical properties necessary for a particular application.

Since the mixtures contain several nematogens with different properties the relationship between them should be considering especially their physical properties. The nematic-isotropic transition temperature for a two-component mixture has been predicted by the *Humphries-James-Luckhurst* theory [38], which gives

$$T_{NI}^{mixture} = xT_{NI}^{A} + (1-x)T_{NI}^{B}, \tag{1.23}$$

where T_{NI}^{A}, T_{NI}^{B} and $T_{NI}^{mixture}$ are the nematic-isotropic transition temperatures for component A, component B and the resulting mixture, respectively while x is the mole fraction of component A.

The diamagnetic anisotropy, $\Delta\tilde{\chi}$ for a binary mixture is predicted to be

$$\Delta\tilde{\chi}_{mixture} = x\Delta\chi_A \overline{P}_2^{A} + (1-x)\Delta\chi_B \overline{P}_2^{B}, \tag{1.24}$$

where $\Delta\chi_A$ and $\Delta\chi_B$ are the diamagnetic anisotropies of component A and component B in the limit of complete order, respectively, $\overline{P}_2^A$ and $\overline{P}_2^B$ are the order parameters of component A and B, respectively in the mixture.

The same expression is applicable for the dielectric anisotropy, $\Delta\tilde{\varepsilon}$, that is

$$\Delta\tilde{\varepsilon}_{mixture} = x\Delta\varepsilon_A\overline{P}_2^A + (1-x)\Delta\varepsilon_B\overline{P}_2^B, \tag{1.25}$$

where $\Delta\varepsilon_A$ and $\Delta\varepsilon_B$ are the dielectric anisotropies of component A and component B in the limit that the order parameters $\overline{P}_2^A$ and $\overline{P}_2^B$ are unity, respectively.

For the elastic constants, $K_i (i = 1,2,3)$ it is expected that they are approximately proportional to the square of the order parameter, $\overline{P}_2$ [39]. So the values for a binary mixture are predicted to be

$$K_i^{mixture} = \left(x\sqrt{K_i^A}\overline{P}_2^A + (1-x)\sqrt{K_i^B}\overline{P}_2^B\right)^2, \tag{1.26}$$

where K_i^A and K_i^B are the elastic constants of component A and component B in the limit of complete order, respectively.

As well as using mixtures of liquid crystal compounds to produce an ideal system to be used in displays, there is a wide range of research to include organic-inorganic nanometre-size composites in mixtures of liquid crystals. These hybrid systems have attracted many researchers in the display area since they frequently exhibit unexpected properties derived from both components; liquid crystal and nanocomposites. For example, they show various superior physical properties such as high strength and a high heat distortion temperature, compared to the single component system [40]. However, there are different mechanisms and problems for each system (different nanocomposites in liquid crystal) that will not be discussed in detail here. In this Thesis, we have actually studied some systems with

nanocomposites dispersed in liquid crystals and have made some interesting discoveries that will be discussed in the following chapters.

1.9 Overview of the Thesis

The creation of the aligned state of a liquid crystal is usually of primary concern, nevertheless, there are circumstances when the destruction of the director alignment can also be of value. Indeed, this principle is employed in one of the earliest display devices, in which information was written onto the display by destroying the uniform alignment produced by the cell surfaces on application of an electric field [41].

The research described in this Thesis is concerned with liquid crystal systems, to which the director is designed to be randomly disordered, in the presence of an aligning field. These random alignments were obtained by suspending clay particles in the liquid crystal host, creating a gel network throughout the liquid crystal structure, dispersing liquid crystals in the porous materials and doping a liquid crystal phase with a chiral dopant. A relatively weak magnetic field of 0.3T is used to align the liquid crystal director, which could be exploited to determine the extent of director disorder with the utilization of analytic form for the director distribution function and to match the experimental and simulated spectra by varying the parameters in this distribution. In addition, the new liquid crystal physics that may involve in the process of director disordering could also be observed.

The aim of this Thesis is to investigate the induced director mis-alignment in the liquid crystals. The electron spin resonance (ESR) technique is employed to study the director distribution for these liquid crystal systems.

The next Chapter will discuss the theories and background of ESR spectroscopy and the director distribution function. In Chapter III, we explain the experimental methods used to prepare the samples and measure the ESR spectra. Then, Chapter IV describes the results and discussion for clay liquid-crystalline systems. Chapter V, is mainly concerned with liquid crystal gels related to the study of phase symmetry. Liquid crystal dispersed in

confined geometries is the topic of Chapter VI, and finally Chapter VII ends this Thesis with the studies on the mis-alignment of the director in chiral nematics in the presence of a magnetic field.

1.10 References

[1] G. Meier, E. Sackmann, J. G. Grabmaier; *Applications of Liquid Crystals,* Springer-Verlag, Berlin, (1975).

[2] P. G. de Gennes; *Mol. Cryst. Liq. Cryst.*, **7**, 325 (1969).

[3] W. Maier, A. Saupe; *Z. Naturforsch*, **13a**, 564 (1958).

[4] A. Saupe; *Angew. Chem. Int.*, Ed. 7, 97 (1969).

[5] G. W. Gray; *Molecular Structure and the Properties of Liquid Crystals*, Academic, New York (1962).

[6] P. J. Collings, M. Hird; *Introduction to Liquid Crystals: Chemistry and Physics*, Taylor and Francis, London (1997).

[7] G. R. Luckhurst, A. Sanson; *Mol. Cryst. Liq. Cryst.*, **16**, 179 (1972).

[8] F. C. Frank; *Disc. Faraday Soc.;* **59**, 958 (1958).

[9] H. Zocher; *Physik,* **28**, 790 (1927).

[10] C. W. Oseen; *Arkiv Matematik Astron. Fysik*, **A19**, 1 (1925); *Fortschr. Chem. Physik u. Physik Chem.* **20**, 1 (1929); *Trans. Faraday Soc.*, **29**, 883 (1933).

[11] W. Haase in *Physical Properties of Liquid Crystals: Nematics,* eds. D. A. Dunmur, A. Fukuda and G. R. Luckhurst, (INSPEC London 2001), Chapter 6.3, 288.

[12] V. Freedericksz, V. Zolina; *Trans. Faraday. Soc.*, **29**, 919 (1933).

[13] D. A. Dunmur, G. R. Luckhurst; *Liquid Crystals in Springer Handbook of Condensed Matter and Materials Data*, Springer, Berlin (2006).

[14] M. Schadt, W. Helfrich; *Appl. Phys. Lett.*, **18**, 127 (1971).

[15] E. F. Carr; *Adv. Chem.*, **63**, 76 (1967).

[16] T. R. Taylor, J. L. Fergason, S. L. Arora; *Phys. Rev. Lett.*, **24**, 359 (1970).

[17] P. Chatelain; *Acta Cryst.*, **1**, 315 (1948).

[18] H. Zocher, K. Coper; *Z. Phys. Chem.*, **132**, 195 (1928).

[19] J. F. Dryer; *Liquid Crystals,* Vol. 3, Ed. By G. H. Brown and M. M. Labes, Gordon and Breach, London, 1113 (1973).

[20] W. Haas, J. Adams, J. Flannery; *Phys. Rev. Lett.*, **25**, 1326 (1970).

[21] F. J. Kahn; *Appl. Phys. Lett.*, **22**, 386 (1973).

[22] J. E. Proust, T. Sarage, E. Guyon; *Solid State Comm.*, **11**, 1227 (1972).

[23] G. R. Luckhurst; *Phys. Bulletin*, **23**, 279 (1972).

[24] W. Maier, A. Saupe; *Z. Phys. Chem.*, **6**, 327 (1959).

[25] W. Maier, G. Maier; *Z. Naturforsch*, **16a**, 262, 470, 1200 (1961).

[26] L. S. Ornstein, W. Kast; *Trans. Faraday Soc.*, **29**, 881 (1933).

[27] Y. Björnståhl; *Ann. Der Phys*, **56**, 161 (1918).

[28] B. Levin, N. Levin; *British Patent* 441,274 (1936).

[29] M. Schadt, W. Helfrich; *Appl. Phys. Lett.*, **18**, 127 (1971).

[30] M. Schadt; *Mol. Cryst. Liq. Cryst.*, **165**, 405 (1988).

[31] T. F. Brody, F. C. Luo, D. H. Davies, E. W. Greeneich; SID Digest, New York, 132 (1981).

[32] D. Pauluth, K. Tarumi; *J. Mater. Chem.*, **14**, 1219 (2004).

[33] H. Koelmans, A. M. van Boxlel; *Mol. Cryst. Liq. Cryst.*, **12**, 185 (1971).

[34] E. Jakeman, E. P. Raynes; *Phys. Lett.*, **39A**, 69 (1972).

[35] M. Oh-e, K. Kondo; *Appl. Phys. Lett.*, **67**, 3895 (1995).

[36] M. Oh-e, K. Kondo; *Appl. Phys. Lett.*, **69**, 623 (1996).

[37] S. Kasap, P. Capper; *Springer Handbook of Electronic and Photonic Materials,* Part D, Springer Science and Business Media, Inc, New York (2006).

[38] R. L. Humpries, P. G. James, G. R. Luckhurst; *Symposia of the Faraday Society,* **5**, 107 (1971).

[39] W. H. de Jeu; *Physical Properties of Liquid Crystalline Materials,* Ch. 6, Gordon and Breach, London (1980).

[40] M. Kawasumi, N. Hasegawa, A. Usuki, A. Okada; *Appl. Clay Sci.*, **15**, 93 (1999).

[41] S. Chandrasekhar; *Liquid Crystals* 2nd Ed., Cambridge Univ. Press, Cambridge (1992).

Chapter II

Electron Spin Resonance Spectroscopy

2.1 Introduction

This Chapter reviews the basic principles of magnetic resonance spectroscopy with particular reference to their applications in the study of liquid-crystalline phases. The very first magnetic resonance studies were reported in 1953 [1]; since then this technique has become increasingly important in studying the nature of intermolecular interactions and the state of macroscopic alignment in liquid crystals.

There are two representative methods for magnetic resonance; ESR (electron spin resonance) spectroscopy and the other is NMR (nuclear magnetic resonance) spectroscopy. Both methods share some of the basic principles of magnetic resonance, but they also have major differences between them. The obvious one is that the magnitude of the magnetic field used in ESR is much less than for NMR. However, this actually is an advantage for ESR when used for measurement of field-induced relaxation time for the director, where the errors in its measurements are likely to be smaller in ESR than NMR. Another advantage is that it is easier to mis-align the director in ESR than in NMR.

Other than that, the magnetic properties of the samples required in order to obtain a spectrum are also differ for these methods. In ESR, the samples must be paramagnetic to obtain a spectrum. Therefore, in the case of liquid crystals, which are usually diamagnetic, a paramagnetic solute must be

added to the sample; this probe is then orientationally ordered by its anisotropic interaction with molecules of the liquid crystal host. The details for this method are described in Section 2.2.3. Meanwhile for NMR, there is no need for a paramagnetic sample in order to obtain a spectrum, however a simple and strong signal is produced when deuterium NMR is used. Therefore, some of the hydrogen atoms of the liquid crystal sample should be replaced by deuterium atoms or a deuteriated solute should be added to a normal (protonated) liquid crystal sample. In general, the preparation of sample is easier for the ESR experiment rather than NMR experiment.

ESR is experimentally easier and is more sensitive than NMR spectroscopy, owing to the fact that electrons have a greater magnetic moment than those of nuclei [2]. The timescale, which means the rate of rotational motion needed to average the anisotropic magnetic interactions, is nanoseconds ESR and not milliseconds as in NMR experiment, which provides ESR for a scope of studying faster dynamics. From these points of views, this Chapter will continue with a detailed consideration of ESR spectroscopy since it is the main method used to investigate the director disorder in liquid crystals, as suggested by the title of this Thesis.

2.2 Basic Theory of Electron Spin Resonance

The Wikipedia encyclopedia defines Electron Spin Resonance (ESR) spectroscopy as a spectroscopic technique which detects species that have unpaired electrons, generally meaning that the molecule in question is a free radical if it is an organic molecule, or that it has transition metal ions if it is an inorganic complex. It was first discovered in 1944 by the Soviet physicist, *Yevgeniy Konstantinovich Zavoyskiy* at the Kazan State University. Since then it has matured into a powerful, versatile, non-destructive and non-intrusive analytical method for any paramagnetic system; these include:

1. Free radicals in the solid, liquid, or gaseous state, and some point defects (localized crystal imperfections) in solids.
2. Molecules containing two unpaired electrons sufficiently remote from one another that the spin interactions between them are very weak.

3. Systems in the triplet state (two unpaired electrons closely coupled).
4. Systems with three or more unpaired electrons and most transition metal ion and rare earth ions [3, 4].

Yevgeniy Zavoyskiy

2.2.1 ESR Spectroscopy

When scientists began to apply the principles of quantum mechanics to describe atoms or molecules, they found that a molecule or atom has discrete (or separate) states, each with a corresponding, quantized energy. Spectroscopy is the measurement and interpretation of the energy differences, ΔE, between the atomic or molecular states. In addition, with the knowledge of these energy differences, we gain an insight into the identity, structure and the dynamics of the sample under study. There is an important relationship between the energy differences and the absorption of electromagnetic radiation. This energy difference can be measured and according to Planck's law, electromagnetic radiation of frequency, ν, will be absorbed by the system if

$$\Delta E = h\nu , \tag{2.1}$$

where h is the Planck constant. The absorption of energy causes a transition from the lower energy state to the higher energy state. In conventional spectroscopy, ν is varied or swept and the frequencies at which absorption occurs correspond to the energy differences of the states. This record is

called a spectrum. Radiation in the gigahertz range is normally used for ESR experiments. Figure 1 shows the transition from lower energy state to the excited state.

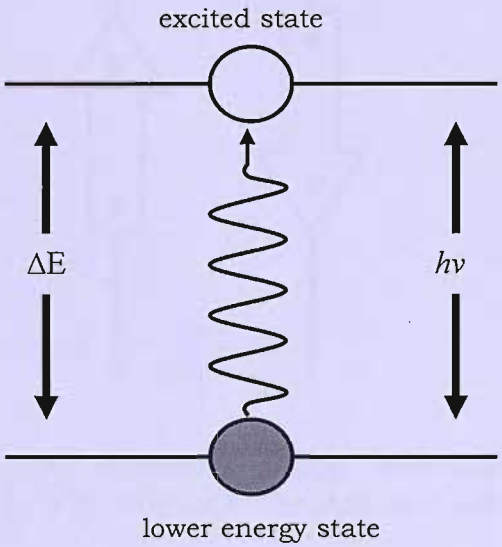

Figure 1: Transition associated with the absorption of electromagnetic energy.

In Electron Spin Resonance (ESR) spectroscopy, the energy differences are predominantly due to the interaction of the unpaired electron in the sample with the magnetic field produced by a magnet in the laboratory; this is the Zeeman interaction. The electron has a magnetic moment, which acts like a compass or bar magnet when it is in a magnetic field, $\boldsymbol{B}$. It will have a state of lowest energy when the moment of the electron, μ, is aligned along the magnetic field and a state of highest energy when μ is aligned against the magnetic field (see Figure 2). The two spin states are labelled by the projection of the electron spin, m_s, on the direction of the magnetic field. As the electron is a spin ½ particle, the parallel state is designated as m_s = -½ and the antiparallel state is m_s = + ½ .

Most basic equations needed in ESR spectroscopy can be derived from quantum mechanics, thus for the spin energies

$$E = g\mu_B B_0 m_s = \pm\frac{1}{2} g\mu_B B_0 \qquad (2.2)$$

$$\Delta E = h\nu = g\mu_B B_0 \qquad (2.3)$$

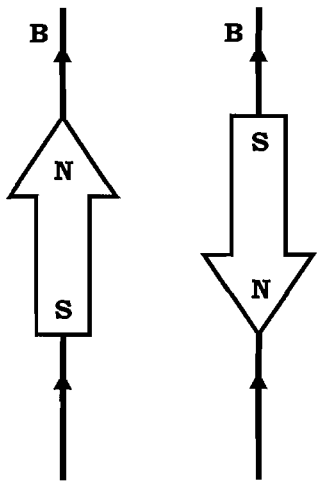

Figure 2: *Minimum and maximum energy orientations of the magnetic moment, μ, with respect to the magnetic field, $\boldsymbol{B}$.*

where $\boldsymbol{g}$ is the $\boldsymbol{g}$-factor, which is the proportionality constant and is approximately equal to the value of 2.0 for most samples, but varies depending on the electronic configuration of the radical or ion containing the electron. μ_B is the *Bohr magneton*, which is the natural unit of electronic magnetic moment. The two spin states have the same energy in the absence of a magnetic field. The energies of the spin states increase linearly as the magnetic field increases, as can be seen from equation (2.2) and as shown in Figure 3.

The energy difference between the two spin states can be changed by varying the magnetic field strength. This suggests for an alternative means to obtain spectra, other than varying the frequency. The electromagnetic radiation frequency could be kept constant and magnetic field could be scanned. A peak in the absorption spectrum will occur when the magnetic field tunes the two spin states so that their energy difference matches the energy of the radiation. This phenomenon is called resonance and the tuned field is called the resonance field. There is a pragmatic reason for fixing the frequency and varying the magnetic field, which is that it is difficult to vary the frequency of the klystron. The resonance field is not a unique fingerprint for the

identification of a compound because the ESR spectra can be acquired at several different frequencies.

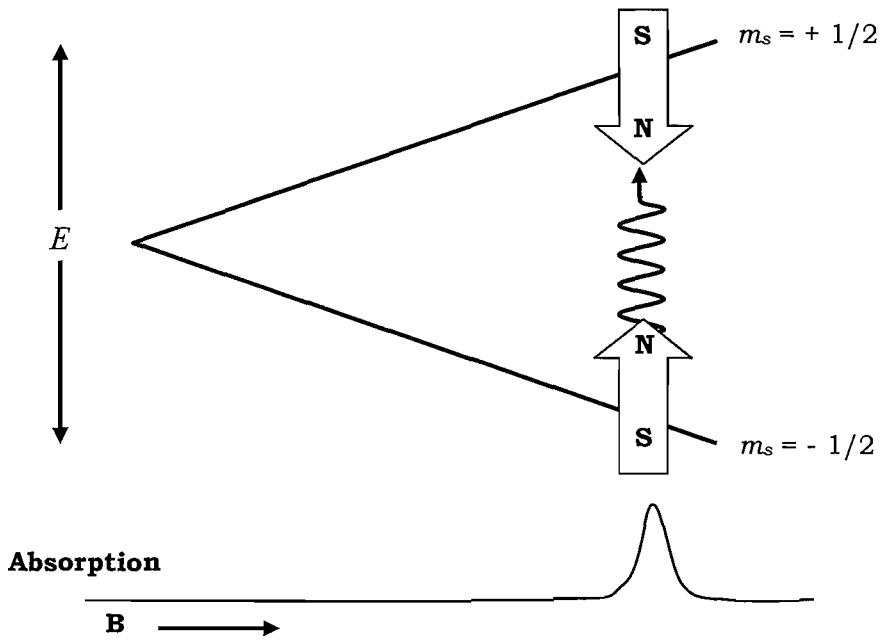

Figure 3: *Variation of the spin state energies as a function of the applied magnetic field.*

Therefore, the g-factor which is independent of the microwave frequency has an important role. The lines with high values of g occur at low magnetic fields and vice versa. The measurement of the g-factors alone does not tell us much about the molecular structure of a radical. The unpaired electron, which gives the ESR spectrum, is very sensitive to its local surroundings. The nuclei of the atoms in a molecule or complex often have a magnetic moment, which produces a local magnetic field at the electron (see Figure 4). This interaction between the electron and the nuclei is called the hyperfine interaction. It gives a wealth of information about a sample, for example the identity and number of atoms, which make up a molecule as well as their distances from the unpaired electron.

The magnetic moment of the nucleus acts like a bar magnet and produces a magnetic field at the electron, B_I. This magnetic field opposes or adds to the magnetic field from the laboratory magnet, depending on the direction of the moment of the nucleus. For example, when B_I adds to the magnetic field, a

smaller magnetic fields is needed from laboratory magnet and so B_I lowers the field needed for resonance.

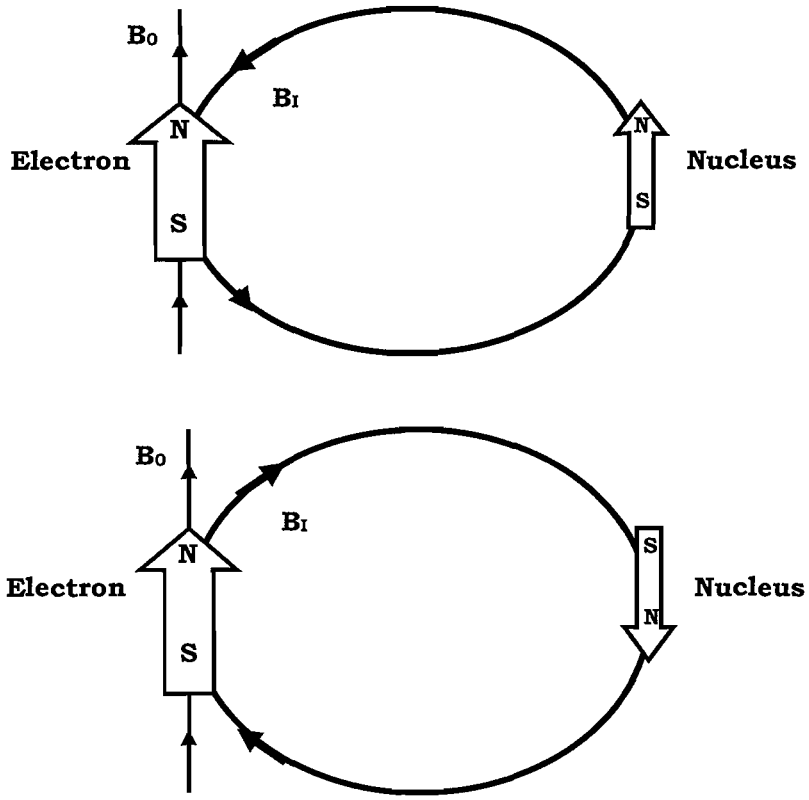

Figure 4: *Local magnetic field at the electron, B_I due to a nearby magnetic nucleus.*

For a nucleus of spin ½, a single ESR absorption signal for just the electron is split into two peaks which are equidistant from the original signal (see Figure 5). The number of lines is due to a $(2I+1)$ principle where I is the spin of the nucleus, for example in the case the nitrogen atom I is one, and so the absorption signal will split into three peaks. If there is a second nucleus of spin ½, each of the original signals is further split into a pair, resulting in four peaks. For N spin ½ nuclei, generally there will be 2^N ESR peaks. As the number of number of nuclei grows, so the number of spectral lines increases exponentially. However, there is a chance of so many peaks that they overlap and the ESR spectrum contains only one broad signal.

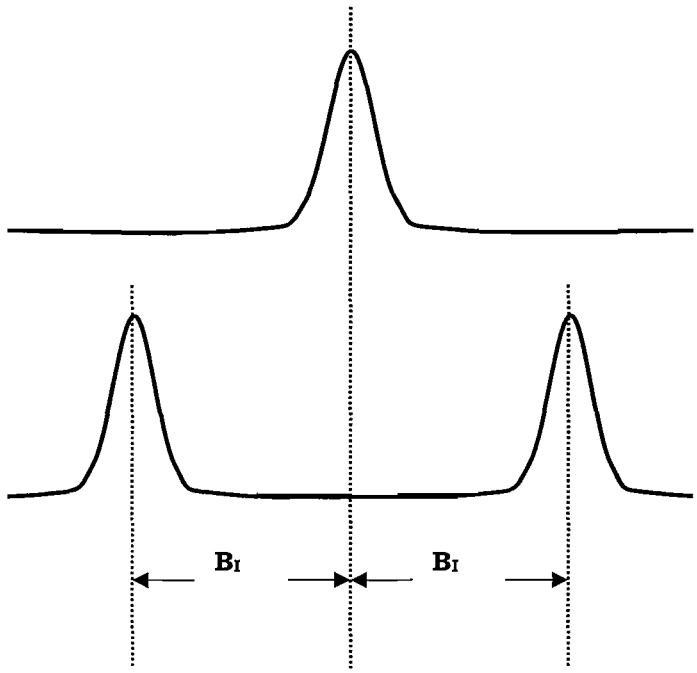

Figure 5: *Splitting in an ESR signal due to the local magnetic field of a nearby nucleus.*

In spectroscopy, the intensity or magnitude of a spectral line is defined as the integrated intensity, which is the area beneath the absorption curve. The integrated intensity of an ESR signal is proportional to the concentration of the paramagnetic solute, characterized by the ESR spectrum, in the sample. However, signal intensities do not depend solely on the spin concentration. They also depend on the microwave power.

In ESR, the klystron frequency is fixed at a value equal to the mechanical frequency of the microwave cavity; typically this is of the order of 9GHz. At lower microwave power the signal intensity grows as the square root of the power. While at higher power levels, the signal diminishes as well as broadens with increasing microwave power. This effect is called saturation when the populations of the spin levels involved in the transition tend to be equal. Saturation can be avoiding by using low microwave power. Figure 6 shows two absorption signals for a similar integrated intensity but with different linewidths.

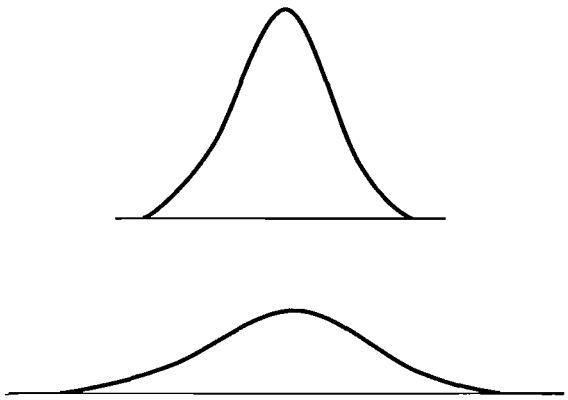

Figure 6: *Two absorption signals for the same integrated intensity but different linewidths.*

To enhance the signal-to-noise ratio the ESR spectrum is measured as the first derivative of the normal absorption curve, which corresponds to a measurement of the gradient of the original peak. These two types of lineshapes are shown in Figure 7. We see that the position of the line in the derivative mode corresponds to the cross-over point.

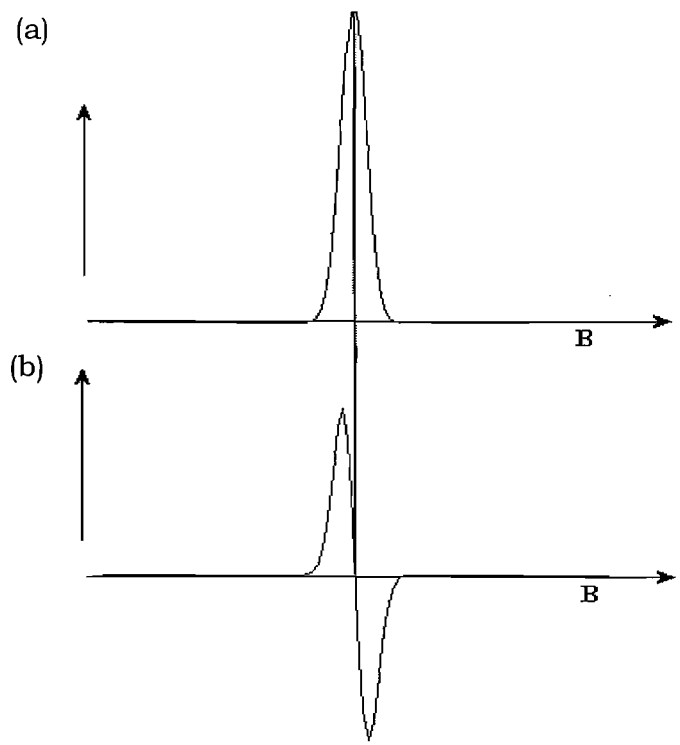

Figure 7: *(a) an absorption peak and (b) its first derivative.*

2.2.2 ESR Spectrometer

A simple generic spectrometer has four essential components: a source of microwave radiation, a magnet, a sample container and a detector. The layout of the ESR spectrometer is shown in Figure 8. In the ESR spectrometer, the microwave radiation source and the detector are in a box called the microwave bridge. The sample is contained in a microwave cavity, which is a metal box in which a standing wave pattern is established that helps to amplify the weak signals from the sample. There is also a magnet to 'tune' the spin energy levels and to match the microwave frequency. The magnetic field values and the timing of the magnetic field sweep are controlled by a microprocessor in the field control unit. In addition, the console contains the signal processing, control electronics and a computer. The computer is used for analyzing data as well as coordinating the entire unit for acquiring a spectrum.

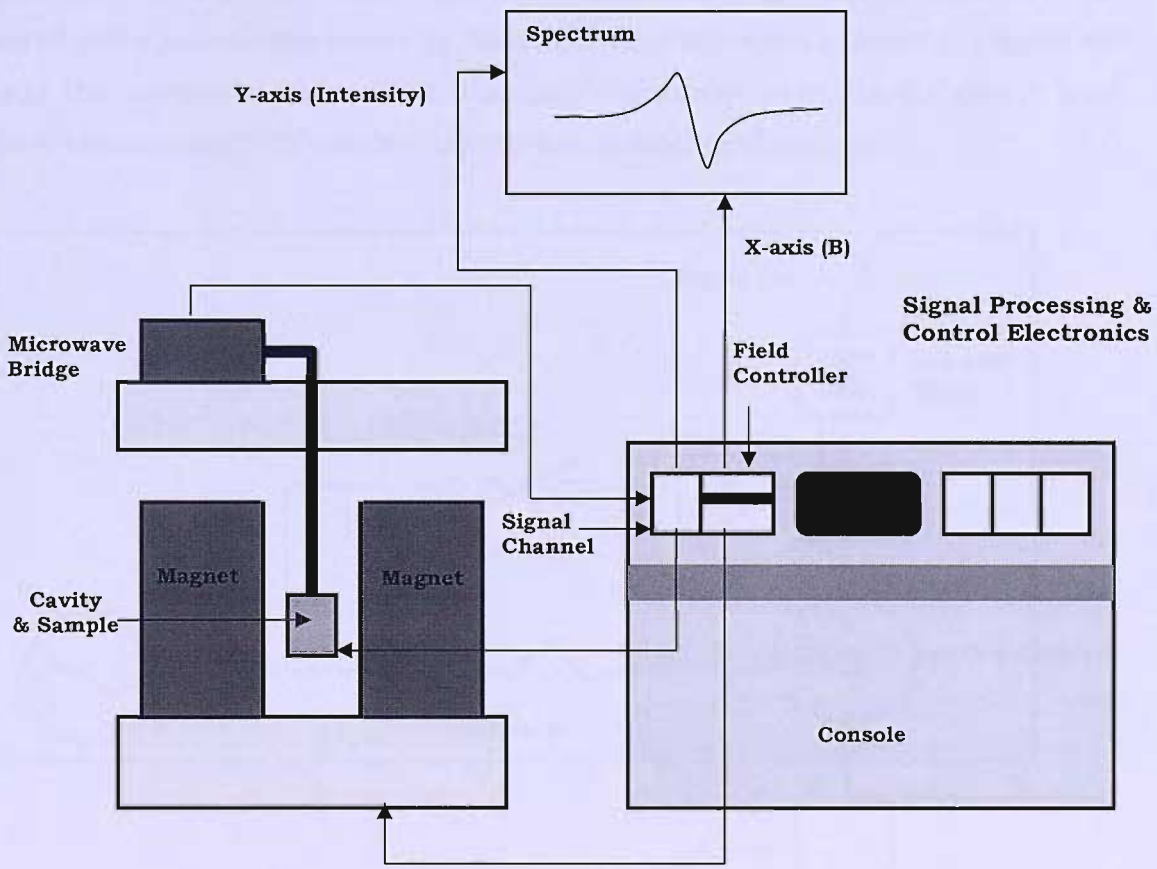

Figure 8: *The general outlay of an ESR spectrometer.*

The microwave bridge is one of the most important parts of the ESR spectrometer. Figure 9 shows the block diagram for the microwave bridge. Microwave source for ESR spectrometer is an electronic valve oscillator called a klystron. It is the most stable high power microwave source available and, therefore, gives the highest sensitivity. The next component is a variable attenuator, a device that blocks the flow of microwave radiation to the cavity. It controls the microwave power that arrives at the sample precisely and accurately. Then, the circulator allows microwaves coming from port 1 only go to the sample cavity through port 2 and not directly to the detector through port 3. Reflected microwaves are directed only to the detector and not back to the microwave source. A Schottky barrier diode is used to detect the reflected microwaves. It converts the microwave power to an electrical current. The best results for quantitative signal intensity as well as optimal sensitivity, the diode should be operating with the detector current of approximately 200μA. In order to insure the detector operates at this level, a reference arm is necessary. The reference arm supplies the detector with some extra microwave power or 'bias'. Some of the source power is tapped-off into the reference arm, where a second attenuator controls the power level (and consequently the diode current) for optimal performance.

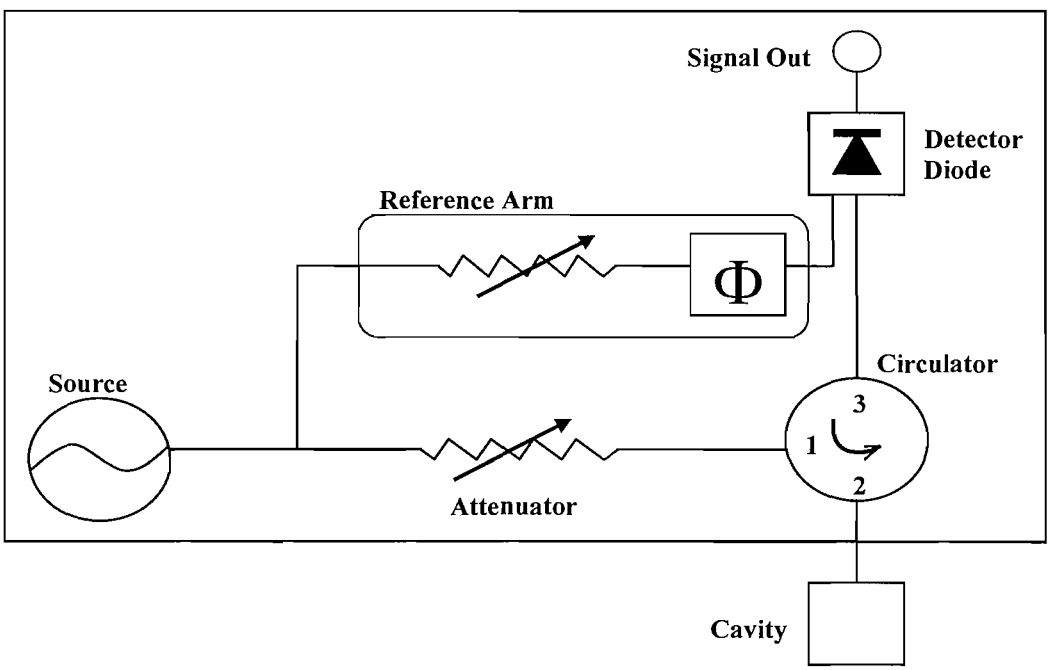

Figure 9: Block diagram of the microwave bridge for ESR spectrometer.

2.2.3 ESR Spin Probes

In our studies, all of the experiments with ESR spectroscopy are to investigate liquid crystals as the primary sample. The majority of liquid crystals are diamagnetic and so cannot be studied by electron resonance spectroscopy directly. To solve this problem, a trace amount of a paramagnetic substance (solute/guest), also called a 'spin probe', is dissolved in the liquid crystals (solvent/host); it is possible to study very small concentrations of spin probe due to the high sensitivity of modern ESR spectrometers. The concentration of the spin probe can be as low as 10^{-4}M, so that the perturbation of the mesophase by the solute is very small. With the strong influence by the anisotropic solute-solvent interactions, the analysis of the solute spectrum provides information which reflects the properties of the pure mesophase [1, 5]. Unlike NMR spectroscopy which can measure the orientational ordering matrix of a liquid crystal, ESR can only give the ordering matrix of the spin probe. This doping technique can also be applied to probe the dynamic behaviour of the mesophase [6], where the ESR spectrum of the spin probe often exhibits a variation in linewidth which provides information relating to the static state as well as the dynamic behaviour of the mesophase at a molecular level [7].

Not all spin probes can be used to study the liquid crystal phase; there are some factors which need to be considered and these depend on the nature of the liquid crystal systems. Three prime features of importance for the spin probe properties are the following. First, the spin probe must be stable over the temperature range of the mesophase studied to prevent the decomposition of the radical which would lead to the loss of the ESR signal. Secondly, the molecules of the spin probe must deviate from spherical symmetry so that they will be highly ordered orientationally by their anisotropic environment. Finally, there must be a considerable anisotropy in the magnetic interactions in order for the extent of the partial alignment can be readily discerned from the electron resonance spectrum.

The use of a paramagnetic solute in liquid crystals, is perhaps more useful than the approach of studying the pure mesophase directly as in NMR. As an example, for a macroscopic director alignment experiment by a magnetic

field, a suitable spin probe will give a simple ESR spectrum, where the director orientation can be inferred from the solute spectrum; the probe molecules must deviate markedly from spherical symmetry. However, for a direct measurement on the pure mesogen, the large number of protons in the mesogenic molecules makes the spectrum very complex and in many cases, it is virtually impossible to analyse the complex proton NMR spectrum. In order to solve this problem, deuterium NMR is the best alternative because, as we shall see, the spectra are dominated by the quadrupolar interaction and so are readily analysed.

In the past, a large variety of spin probes has been used in ESR studies and these have been well reviewed especially by *Jost* and *Griffith* [8]. In general, the spin probe is an organic molecule containing the nitroxide moiety

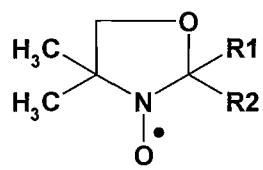

which contains an unpaired electron effectively localized on the N—O group. In our ESR experiments, two types of organic nitroxides were used, Cholestane (see Figure 10) and Tempone (see Figure 11). These spin probes differ by their structure and shape, but are similar in that they have an unpaired electron whose spin interacts predominantly with the spin of the nitrogen nucleus because of their close proximity [9]. These two probes have been chosen in our studies because of their stability in the mesophases. In addition the long backbone of the Cholestane spin probe actually increases the well-ordered and anisotropic interactions with the liquid crystal host [7].

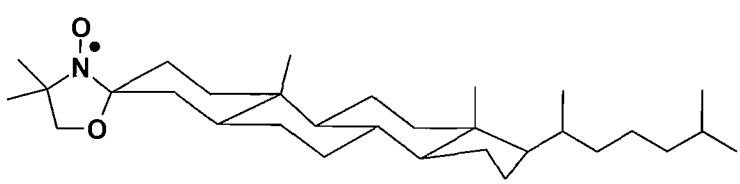

Figure 10: 4,4'-dimethylspiro(5-α-cholestane-3,2'-oxazolidin)-3'-yloxy (Cholestane).

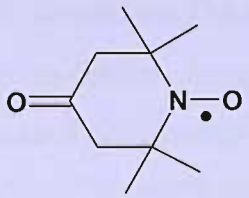

Figure 11: 2,2,6,6-tetramethyl-4-piperidone-N-oxide (Tempone).

2.2.4 ESR Spectral and Simulations

For a nitroxide spin probe in which the spin of the unpaired electron interacts predominantly with the spin of the nitrogen nucleus, three hyperfine lines are observed. The allowed transitions and the corresponding ESR spectrum are shown in Figure 12, for the Cholestane spin probe in a nematic liquid crystal mixture, ZLI-4792. $\Delta\tilde{\chi}$ for ZLI-4792 is positive and therefore, the director is aligned parallel to the magnetic field of the spectrometer.

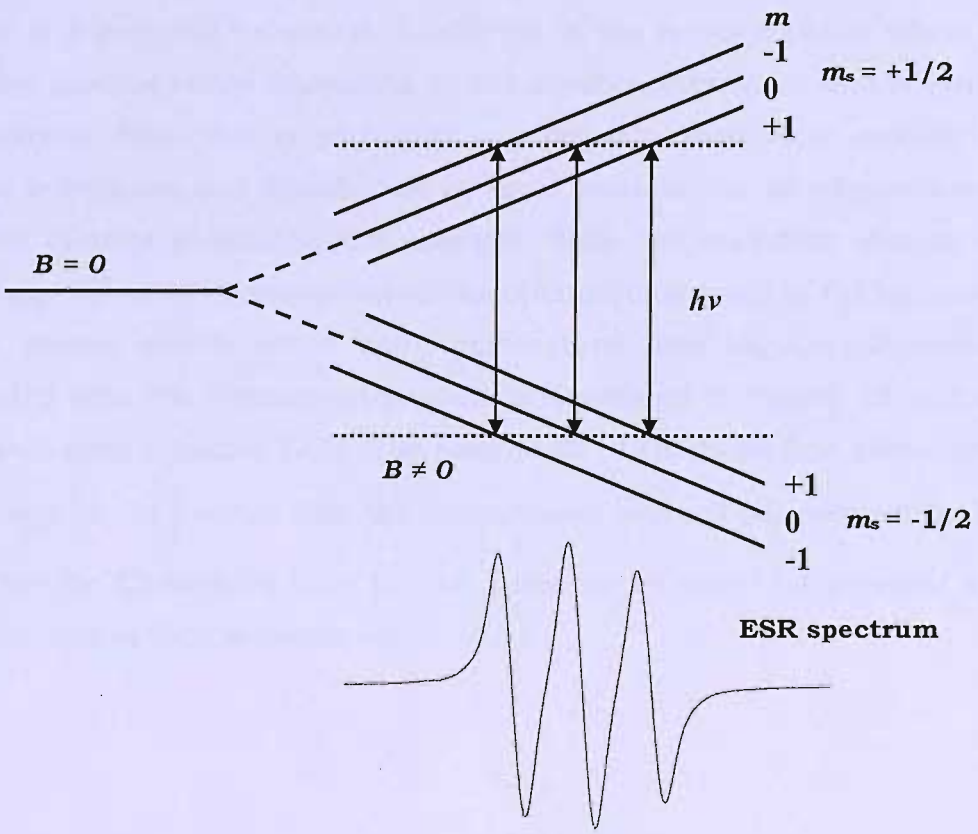

Figure 12: *Allowed transitions and the corresponding ESR spectrum.*

There are two tensors which determine the positions of the spectral lines; the $\tilde{g}$-tensor and the nitrogen hyperfine tensor, $\tilde{A}$. In the fast motion limit, these partially averaged tensors necessarily have the cylindrical symmetry of the nematic phase. The principal components parallel to the director are denoted by $\tilde{g}_{\parallel}$ and $\tilde{A}_{\parallel}$ while those perpendicular to the director are denoted by $\tilde{g}_{\perp}$ and $\tilde{A}_{\perp}$; as with other properties the tilde indicates that the value is for the liquid crystal phase.

The three hyperfine lines found for the nematic phase are also observed for the isotropic phase, but with a distinct difference in hyperfine spacings. In the isotropic phase, it takes an average value of the hyperfine tensor that is resulting from the three principal components of the nitrogen hyperfine tensor for the crystal as well as for the liquid crystal phase. When a magnetic field is applied along the three axes in a crystal sample, the two axes in the plane of oxazolidine ring yield a value for the hyperfine spacing of 5G and along the axis perpendicular to this plane gives a value of 35G. The hyperfine lines are separated by a spacing of ~15G in the isotropic phase which is the average of the crystal values. It is different in the nematic phase where the hyperfine spacing varies depending on the director orientation with respect to the magnetic field; this is why ESR is a powerful method to monitor the director orientation and distribution in liquid crystals. For an aligned sample with the director parallel to the magnetic field, the hyperfine spacing can range from 7G to 10G, depending on the orientational order of the spin probe in the system which varies with temperature. The angular dependence associated with the director orientation is illustrated in Figure 13 and was calculated from equation (2.7). The magnitude of the hyperfine difference or anisotropy $\left|\tilde{A}_{\parallel} - \tilde{A}_{\perp}\right|$ varies with the orientational order of the spin probe. It is larger for the Cholestane than for the Tempone as might be expected from the difference in their anisotropies.

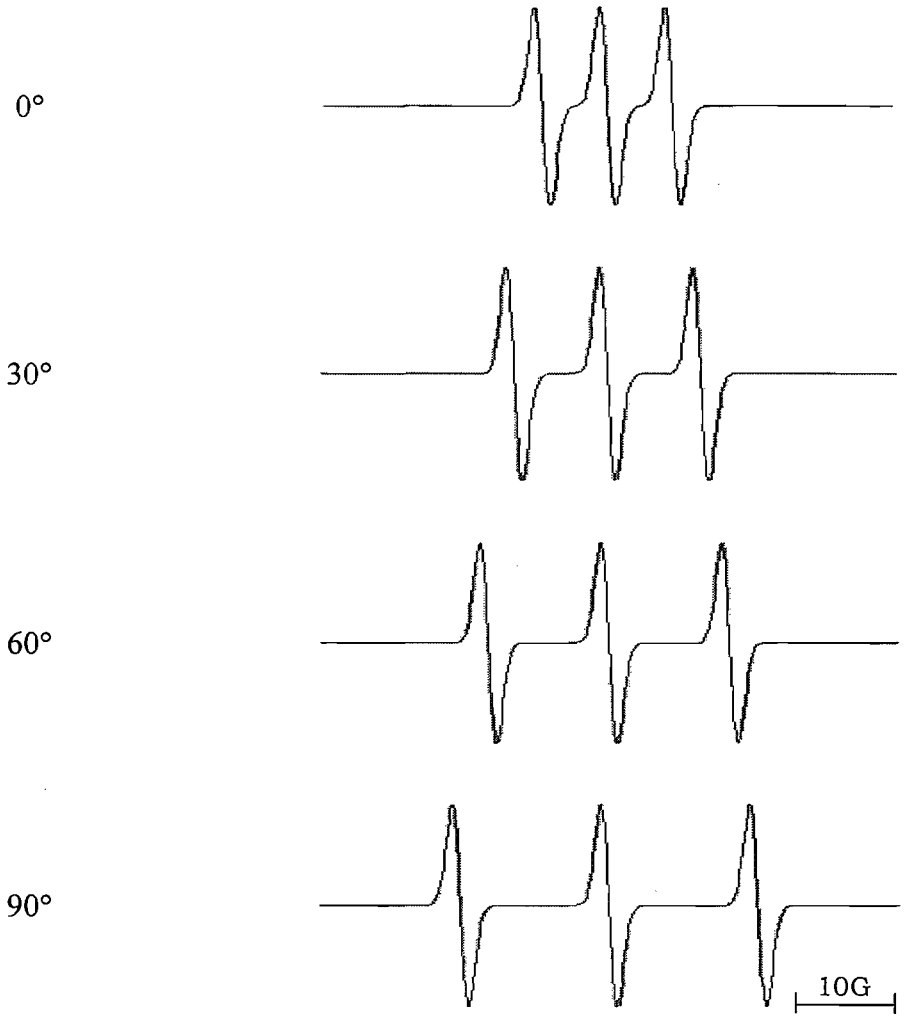

Figure 13: The angular dependence of the ESR spectrum of the Cholestane spin probe dissolved in a nematic liquid crystal simulated with $\widetilde{A}_{\parallel} = 8.2G$ *and* $\widetilde{A}_{\perp} = 18.1G$ *using equation (2.7).*

In some cases, the director is aligned at an intermediate angle, θ to the magnetic field and the resonance field for ESR spectrum varies according to [10]

$$\widetilde{B}_m(\theta) = h\nu / \widetilde{g}\mu_B B - h\widetilde{K}m / \widetilde{g}\mu B - (h^2\widetilde{A}_{\perp} / 4\widetilde{g}^2\mu_B B^2)$$
$$\times[(\widetilde{A}_{\parallel}^2 + \widetilde{K}^2)/\widetilde{K}^2][I(I+1) - m^2]$$
$$-(h^2m^2 / 2\widetilde{g}^2\mu^2{}_B B^2)[A_{\parallel}^2 - A_{\perp}^2)/K]^2$$
$$\times(\widetilde{g}_{\parallel}^2\widetilde{g}_{\perp}^2 / \widetilde{g}^4)\cos^2\theta\sin^2\theta. \qquad (2.4)$$

In this expression, h is the Planck constant, I is the nuclear spin quantum number and m is the magnetic quantum number. The quantities $\tilde{K}$ and $\tilde{g}$ also depend on the director orientation according to

$$\tilde{g}(\theta) = \{\tilde{g}^2{}_{\perp} + (\tilde{g}^2{}_{\parallel} - \tilde{g}^2{}_{\perp})\cos^2\theta\}^{1/2}, \tag{2.5}$$

and

$$\tilde{K} = [\tilde{A}_{\perp}{}^2\tilde{g}_{\perp}{}^2 + (\tilde{A}_{\parallel}{}^2\tilde{g}_{\perp}{}^2 - \tilde{A}_{\perp}{}^2\tilde{g}_{\perp}{}^2)\cos^2\theta]^{1/2}/\tilde{g}. \tag{2.6}$$

In order to simplify this calculation, for the nitroxide spin probes used in the experiments, it is valid to ignore the second order correction terms shown by the last two terms on the right hand side of equation (2.4). This makes the hyperfine spacing between the first and second spectral lines equal to the spacing between the second and third spectral line. The other simplification is to ignore the anisotropy in the g-tensor; that is when $\tilde{g}_{\parallel} = \tilde{g}_{\perp}$ which means that the central line in the spectrum for which $m = 0$ is independent of the director orientation. The resonance field in equation (2.4) then becomes

$$\tilde{B}_m(\theta) = B_0 - (h/\tilde{g}\mu_B)[\tilde{A}_{\perp}{}^2 + (\tilde{A}_{\parallel}{}^2 - \tilde{A}_{\perp}{}^2)\cos^2\theta]^{1/2}m, \tag{2.7}$$

where the factor $h/\tilde{g}\mu_B$ converts the hyperfine tensor components, which are in frequency units to field units.

This expression is also used for the spectral simulations when the director orientation is non-uniform to calculate the positions of the three hyperfine lines. To do that, the values for all the parameters should be known and in the appropriate units. For a nematic liquid crystal (provided $n \| B$ which means $\Delta\tilde{\chi} > 0$), the parallel hyperfine component, $\tilde{A}_{\parallel}$ can be measured from the static ESR spectrum while the perpendicular hyperfine component can be calculated from

$$\widetilde{A}_{\perp} = \frac{3a_{iso} - \widetilde{A}_{\parallel}}{2}, \tag{2.8}$$

where a_{iso} is the isotropic hyperfine spacing, ~15G for most nematogens. Although we ignore the anisotropy of the g-tensor (approximation $\widetilde{g}_{\parallel} = \widetilde{g}_{\perp}$), but for the record, the value of scalar g-factor for our experiment is 2.0056 and the position of the central spectral line was arbitrarily set equal to zero (that is the position of central peak does not change with temperature and director orientational order).

In our ESR investigations, the concentration of spin probe used for each experiment was about 1×10^{-2}wt% of the host. It is important to make sure that the concentration is sufficiently low to prevent the creation of a chiral nematic with its helical director distribution which would lead to a powder-like pattern in ESR spectrum. It is also to prevent line broadening or narrowing which results from the spin exchange. Since ESR allows the determination of director distribution which is usually the sum of spectra from all director orientations, the powder-like pattern contains six hyperfine lines from the director with extreme orientations, that is parallel and perpendicular to the magnetic field. Powder-like pattern ESR spectra are discussed further in the following Section.

2.3 Analysis of ESR Powder Pattern and Simulations

In a monodomain sample, the director is uniformly aligned. However, there are some cases where the director is disordered with respect to the magnetic field, the observed spectrum is then a weighted sum of the spectra from all orientations [11]; these are of major interest to us. Figure 14 shows the simulated powder pattern ESR spectra where the director is randomized.

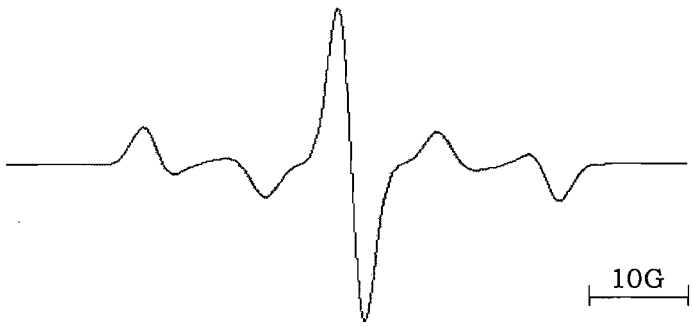

Figure 14: Simulated powder pattern ESR spectrum for the Cholestane spin probe in a liquid crystal. It contains five peaks resulting from the director both parallel and perpendicular to the magnetic field.

As has been said earlier, this pattern is called a powder-pattern spectrum; this occurs because the time taken for the spin probe to diffuse between different director orientations is large in comparison with the timescale of ESR experiment which is about 10^{-8}s. Thus, when no single director orientation is preferred, the spectrum, $I(B)$, is the convolution of the orientational distribution function for the director, $f(\theta)$, and the spectral lineshape, $L(B,B_m(\theta),T_2^{-1})$

$$I(B)=\sum_m \int f(\theta)L(B,B_m(\theta),T_2^{-1})\sin\theta d\theta. \tag{2.9}$$

Here θ is the angle between the symmetry axis of the magnetic tensors or the director and the magnetic field, B_m is the resonance field for the line with nuclear spin quantum number, m and the linewidth is denoted by T_2^{-1} which is the width of the absorption line at half of its height. The shape of the curve might take a Lorentzian form for a pure transition, or a Gaussian if the line is inhomogenously broadened by unresolved proton hyperfine structure, which is often for the case of nitroxide spin probes. The main difference between these two types of lineshape is that the outer wings of the Lorentzian line are much longer and drop more slowly than those of the Gaussian [12]. Figure 15 shown the first derivative for both Lorentzian and Gaussian lineshapes.

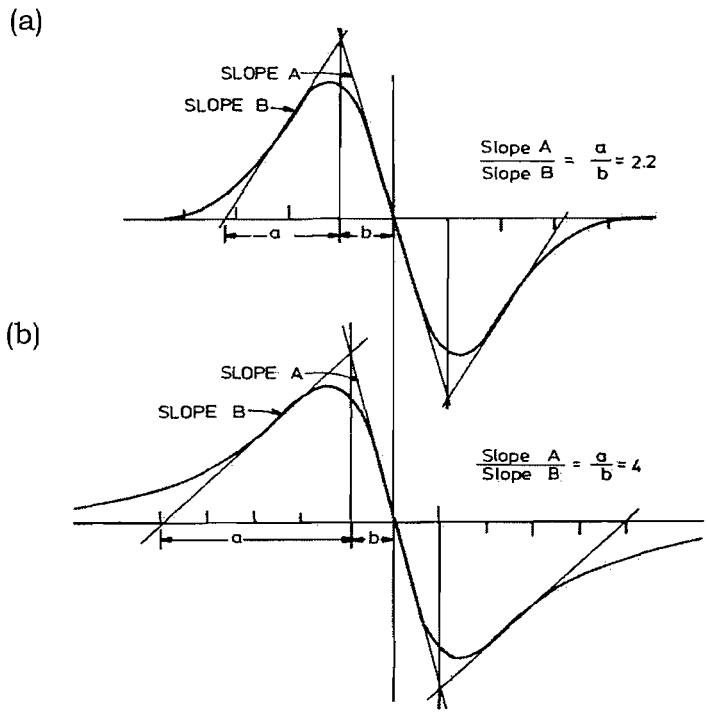

Figure 15: The slope method for the identification of (a) Lorentzian and (b) Gaussian derivative curves.

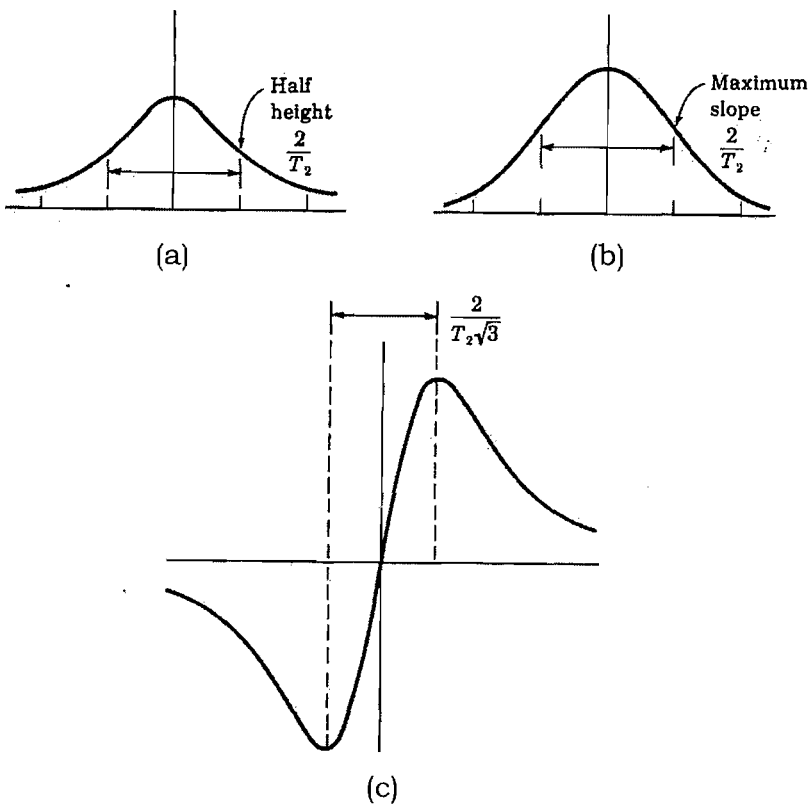

Figure 16: The linewidths of (a) Lorentzian, (b) Gaussian and (c) derivative of Lorentzian lineshape [13].

The ESR spectrum for a radical tumbling in solution with a Lorentzian lineshape has the characteristic form shown in Figure 16. The two peaks of the derivative curve correspond to points of maximum slope in the absorption; the separation between them is $\frac{2}{T_2\sqrt{3}}$ for a Lorentzian or $\frac{2}{T_2}$ for a Gaussian lineshape.

The normalised first derivative Lorentzian lineshape is

$$L(B,B_m(\theta),T_2^{-1}) = \frac{2T_2^3}{\pi}\frac{(B_m(\theta)-B)}{(1+T_2^2(B_m(\theta)-B)^2)^2}, \tag{2.10}$$

while the normalised first derivative Gaussian lineshape is

$$L(B,B_m(\theta),T_2^{-1}) = \frac{T_2^3}{\sqrt{2\pi}}(B_m(\theta)-B)\exp\left\{-\frac{T_2^2}{2}(B_m(\theta)-B)^2\right\}. \tag{2.11}$$

It has been assumed in the simulations that T_2^{-1} is independent of both m and θ although there are systems where this is not such a good approximation. However, the width of a spectral line will depend on the magnetic quantum number, m according to

$$T_2^{-1}(m) = A + Bm + Cm^2. \tag{2.12}$$

The three coefficients depend upon the rate of molecular motion. The A coefficient depends on the anisotropic $\tilde{g}$-tensor, B on the on the anisotropic $\tilde{g}$ and $\tilde{A}$ tensors, while C depends on the anisotropic $\tilde{A}$ tensor. If the relaxation process responsible for the linewidth is caused by molecular reorientation, then the linewidth coefficients for a radical dissolved in a liquid crystal are predicted to depend on the orientation of the director, and are of the form

$$A(\theta) = A_0 + A_2P_2(\cos\theta) + A_4P_4(\cos\theta). \tag{2.13}$$

In this expression, $P_L(\cos\theta)$ is the Lth Legendre polynomial. P_2 is

$$P_2 = \frac{(3\cos^2\theta - 1)}{2}, \tag{2.14}$$

while P_4 is given by

$$P_4 = \frac{1}{8}(35\cos^4\theta - 30\cos^2\theta + 3). \tag{2.15}$$

The linewidths themselves are readily measured from the spectrum. For a first derivative display T_2^{-1} is simply $\frac{2}{\sqrt{3}}$ times the peak-to-peak separation for a Lorentzian line, or twice this separation if the line is Gaussian.

2.4 Director Distribution Function

In order to match the experimental and simulated ESR spectra, the parameters in the line position, line shape and distribution function have to be varied. The model distribution function has been obtained from the solution of the torque-balance equation for a system in which the director is initially randomly distributed and then aligned by a magnetic field. The form of the distribution function is given by [14]

$$f(x) = \frac{a^2}{\{a^2 - (a^2 - 1)x^2\}^{3/2}}, \tag{2.16}$$

where $x = \cos\theta$ and θ is the angle between the director and the field. Here, x is defined in the half range from 0 to 1 and $f(x)$ is normalised over this range. The parameter a controls the orientational order of the director; it is infinite for a perfectly aligned system and unity for a director randomly distributed in three dimensions.

The value of a can take any value bigger than 1. As the number increases to infinity, so the director order becomes larger and it goes to perfectly ordered system with the order parameter of 1. In contrast, a = 1, means the director is randomly distributed and it gives the order parameter of 0. Figure 17 shows the director distribution function calculated for different a values. Here, it is shown that for the biggest a value of 30 the distribution is mainly focussed at x = 1, which means the director has become aligned. While for a between 1 and 30, the distribution curve varies with the values of a and this represents the orientational order of the director of liquid crystal. We could conclude that, the order parameter is sensitive to a (for smaller value of a) but when a becomes larger, the director order parameter tends to its limiting value of unity, but rather slowly. Figure 18 shows the plot of the relationship between a and director order parameter.

The second rank orientational order parameter for the director is defined by

$$\overline{P}_2^d = \int_0^1 \frac{(3x^2-1)}{2} f(x)dx, \tag{2.17}$$

which can be evaluated analytically for $f(x)$ given in equation (2.16) as

$$\overline{P}_2^d = \frac{a^2}{2}\left\{\frac{2a^2+1}{a^2(a^2-1)} - \frac{3\arctan(a^2-1)^{1/2}}{(a^2-1)^{3/2}}\right\}. \tag{2.18}$$

Evaluation of this expression gives an analytic route to the director order parameter, $\overline{P}_2^d$, from the value of a which, as we shall see, can be determined by fitting the ESR powder patterns. It is also possible to see that the expression is valid at the two limits namely $a \to 1$ and $a \to \infty$. The second limit is the easiest to impose since

$$\lim_{a\to\infty} \overline{P}_2^d \approx \frac{a^2}{2}\left\{\frac{2a^2}{a^4} - \frac{3\pi}{2a^3}\right\} \tag{2.19}$$

$$= 1 - \frac{3\pi}{4a} \tag{2.20}$$

and here the latter term vanishes as a goes to infinity. For the other limit, we need an expansion of arctan θ for small θ; this is

$$\arctan\theta \approx \theta - \frac{\theta^3}{3}. \tag{2.21}$$

This gives the second term in the expression for $\overline{P}_2^d$ as

$$\frac{3\arctan(a^2-1)^{1/2}}{(a^2-1)^{3/2}} \approx \frac{3}{(a^2-1)} - 1. \tag{2.22}$$

The director order parameter is then

$$\lim_{a\to 1} \overline{P}_2^d = \frac{a^2}{2}\left(\frac{2a^2+1}{a^2(a^2-1)} - \frac{3}{(a^2-1)} + 1\right) \tag{2.23}$$

$$= \frac{a^2}{2}\left(\frac{1-a^2}{a^2(a^2-1)} + 1\right) \tag{2.24}$$

$$= \frac{a^2}{2}\left(1 - \frac{1}{a^2}\right) \tag{2.25}$$

$$= 0.$$

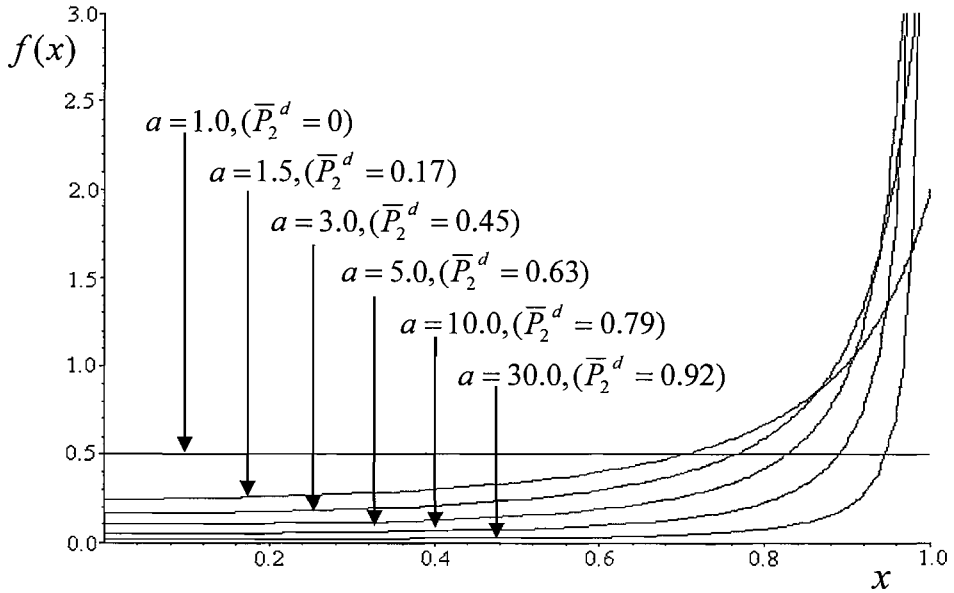

Figure 17: *The director orientational distribution function calculated from equation (2.16) for various values of a; the associated values of the director orientational order parameter, $\overline{P}_2^d$, are also given.*

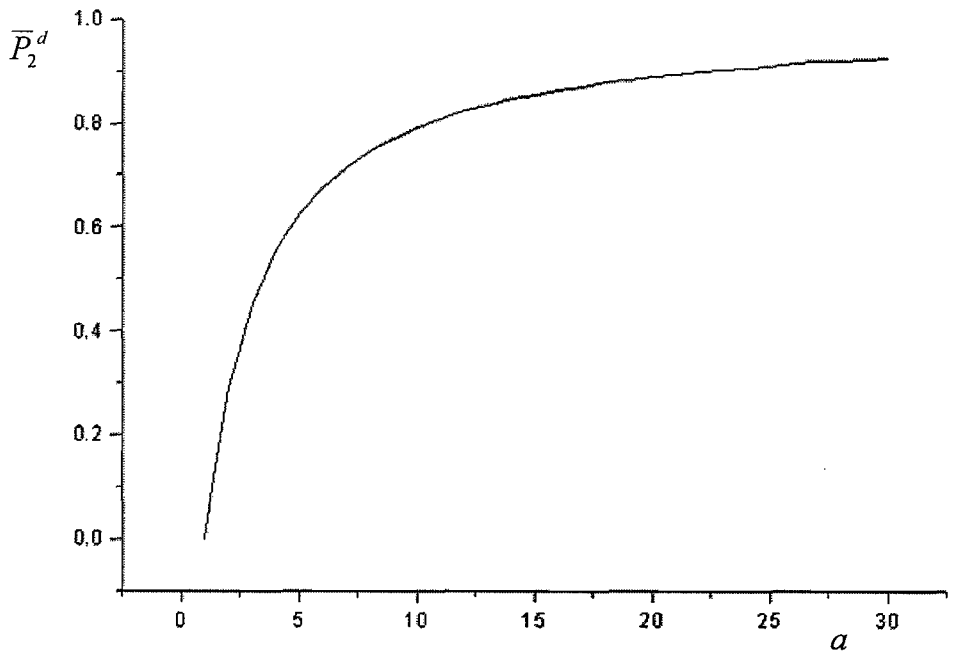

Figure 18: *The relationship between a values and director order parameter, $\overline{P}_2^d$.*

The ESR spectra changes as the orientational order of the director is gradually destroyed. Figure 19 shows the simulated ESR spectra for the Cholestane spin probe in a liquid crystal for a selection of a values. The spectrum contains three lines with equal hyperfine spacing corresponding to the value of $\tilde{A}_{\parallel}$, for a highly aligned director ($\overline{P}_2^d = 0.92$). A decrease in the orientational order parameter, ($\overline{P}_2^d = 0.63$) results in the appearance of two more lines in the spectrum, and their hyperfine spacing is approximately equal to $\tilde{A}_{\perp}$. The peak intensities of these new peaks are less than those for the parallel peaks, which means that the director parallel to the field is still dominant.

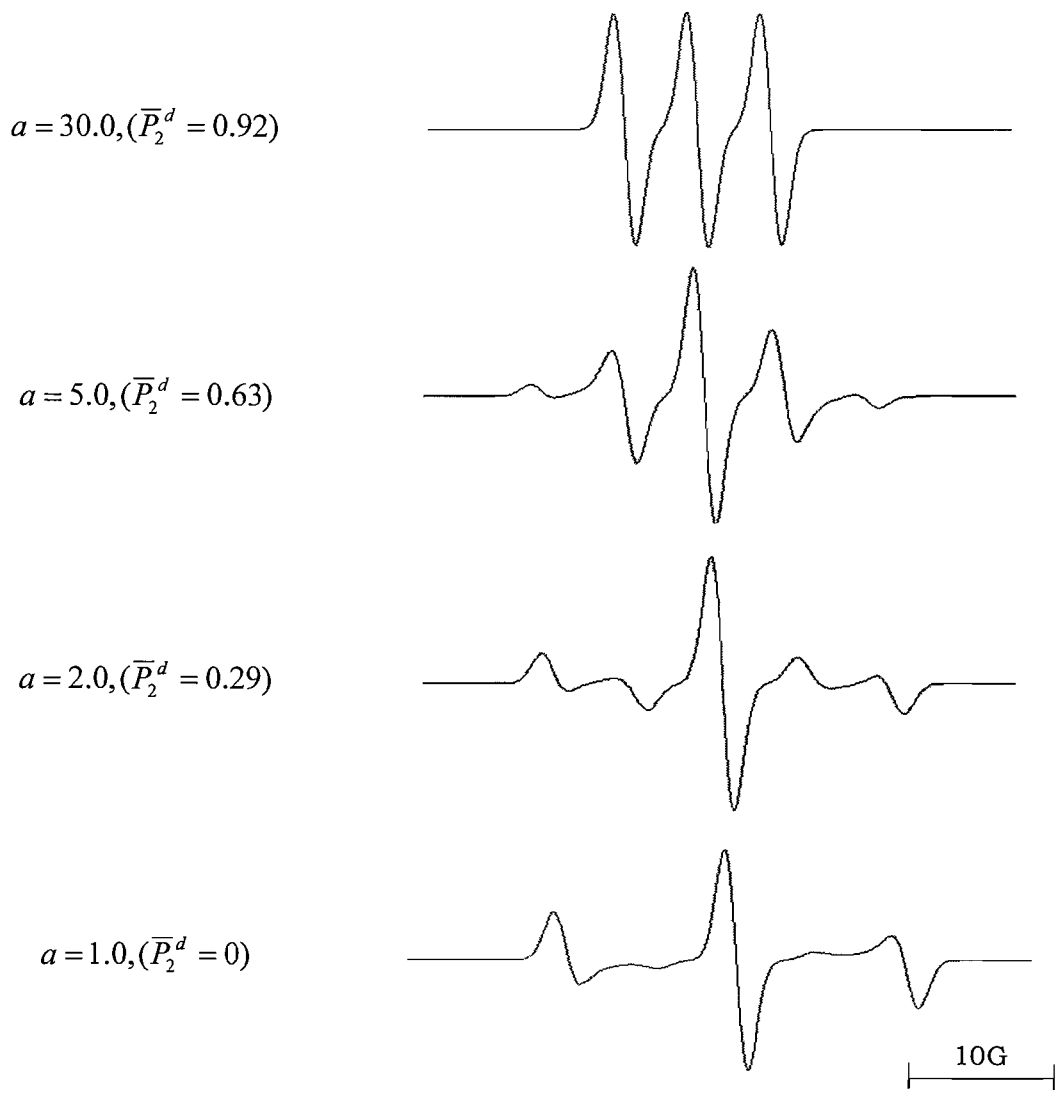

Figure 19: *Simulated ESR spectra for the Cholestane spin probe for different degrees of director orientational order as indicated by the parameter, a, for distribution function and by the director order parameter, $\overline{P}_2^d$.*

For ($\overline{P}_2^d = 0.29$), the spectrum still contains five lines but now perpendicular peaks are more intense than parallel peaks. The director ordering in the liquid crystal is almost random but with small parallel alignment since the parallel peaks still exist even though they are less intense. A totally random director orientation is produced when ($\overline{P}_2^d = 0$) as the ESR spectrum shows a powder pattern spectrum, corresponding to a weighted sum of spectra from all director orientations.

2.5 References

[1] A. Carrington, G. R. Luckhurst; *Mol. Phys.*, **8**, 401 (1964).

[2] N. S. Dhanjal, I. J. Cox, S.D. Taylor-Robinson; *GUT online*, doi:10.1136 / gut.52.9.1236, 1236 (2003).

[3] W. Gerlach, O. Stern; *Z.Phys.*, **8**, 110 (1922).

[4] E. J. Zavoiskii; *J. of Phys. USSR*, **9**, 211 (1945).

[5] D. H. Chen, G. R. Luckhurst; *Trans. Faraday Soc.*, **65**, 656 (1969).

[6] G. R. Luckhurst; *Electron Spin Relaxation*, Eds. L. T. Muus and P. W. Atkins, Pleum Press, (1972).

[7] G. R. Luckhurst, M. Setaka, C. Zannoni; *Mol. Phys.*, **28**, 49 (1974).

[8] P. Jost, O. H. Griffith; *Methods in Pharmacology*, Ed. Colin Chignell, **2**, Ch. 7 (1972).

[9] G. R. Luckhurst; *Thin Solid Films*. **506**, 36 (2006).

[10] G. R. Luckhurst; in *Liquid Crystals and Plastic Crystals*, Eds. G. W. Gray and P. A Winsor, Ellis Hordwood Ltd, Chichester, Vol. 2, Ch. 7 (1974).

[11] C. J. Dunn, D. Ionescu, N. Kunimatsu, G. R. Luckhurst, L. Orian, A. Polimeno; *J. Phys. Chem. B*, **104**, 10989 (2000).

[12] B. Rånby, J. F. Rabek; *ESR Spectroscopy in Polymer Research*, Ch. 1, Springer-Verlag, Berlin (1977).

[13] A. Carrington, A. D. McLachlan; *Introduction to Magnetic Resonance*, Ch. 1, Harper & Row Ltd, New York (1967).

[14] S. M. Fan, G. R. Luckhurst, S. J. Picken; *J. Chem. Phys.*, **101**, 3255 (1994).

Chapter III

Experimental

3.1 Introduction

The aim of this Chapter is to give an insight on the methods used and details of all the experiments in the investigation of director disorder in liquid crystals. This Chapter starts with a Section describing the information of the liquid crystal compounds used for our studies, this is followed by Section 3.3 which reports on the sample preparation, where we explain the procedures used to dissolve the spin probe in the liquid crystal. Then Section 3.4 presents the experimental setup for the ESR spectrometer, showing the optimum parameters to be used in the ESR measurements. Finally, the sample preparation for each liquid crystal system studied in this Thesis is given in Section 3.5, including liquid crystal mixtures of clay particles, gelator, porous materials and chiral dopant.

3.2 Liquid Crystal Compounds

The main mesogens used in the investigations were 4-pentyl-4'-cyanobiphenyl (5CB) and a commercial mixture of fluorinated compounds, ZLI-4792 from Merck. Both mesogens have actually been well studied with ESR spectroscopy [1]. They share the same properties in having a nematic phase at room temperature, and both compounds have a positive diamagnetic anisotropy, $\Delta\tilde{\chi}$, which allows the director to align parallel to the applied magnetic field.

5CB, was invented by *Gray* and co-workers at the University of Hull in 1972, and its structure is shown in Figure 1. Principally, *alkylcyanobiphenyls* were the first viable mesogens for use in commercial display devices [2]. This compound has a terminal cyano group, which gives a strong dipole moment to the structure [3]. Two benzene rings in the core structure give a conjugated system with its high polarisability anisotropy that contributes to the large value of the positive dielectric anisotropy, $\Delta\tilde{\varepsilon}$ [4] although the major contribution to this originates from the dipole moment. The conjugation with terminal cyano group also confers a reasonably high optical anisotropy (birefringence). Besides its low viscosity, 5CB is chemically and photochemically stable [5]. In addition, this compound has a low melting point, with a reasonably high T_{NI} ($T_{CrN} = 24°\,C$, $T_{NI} = 35°\,C$ [6]).

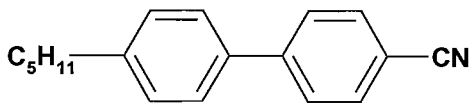

Figure 1: *Chemical structure of the nematogen 5CB.*

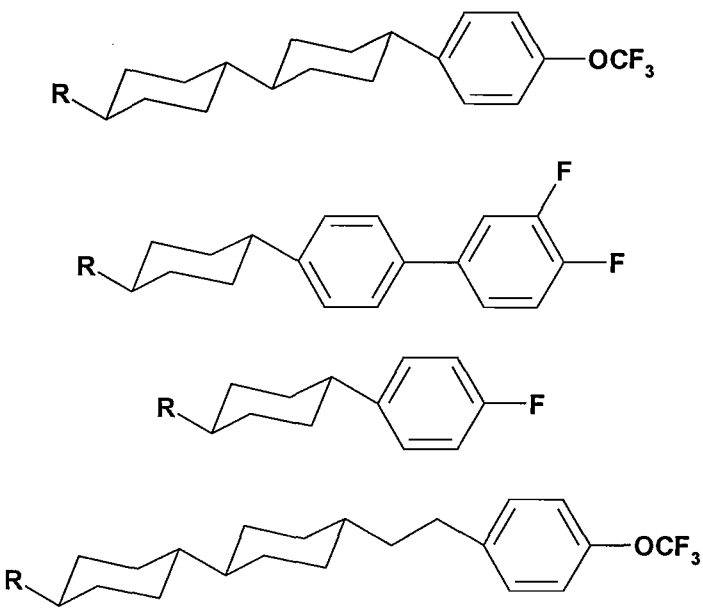

Figure 2: *Chemical structures of some of the components in the nematogenic mixture ZLI-4792 [7].*

The other liquid crystal compound used in our experiments is the commercial liquid crystal mixture of fluorinated compounds, ZLI-4792, which

actually is a standard liquid crystal in TFT-LCD. This mixture has a wide nematic range (−40° C to 92° C) and is thermally and chemically stable. Since this liquid crystal is commercial, the chemical structures of its components are undisclosed. However, some of its components are believed to be like the compounds shown in Figure 2 [7]; these are mesogenic molecules with phenyl or cyclohexane ring containing fluorine atoms at the end of one of its terminal phenyl groups.

3.3 Sample Preparation

In our experiments, the sample studied is a mixture of liquid crystal (in some cases with the further addition of dopants) and a spin probe which is essential for the ESR studies. This mixture is contained in a sample tube 20cm in length with an internal diameter of 4mm. We used two types of sample tubes; one made from quartz and the other composed of borosilicate glass (*Pyrex*). They both have the same capability to contain the sample but the borosilicate glass produces additional signals in the ESR spectrum, which are believed to originate from transition metals in the glass. A quartz tube is preferable, but in some cases in our experiment which needs the tube to be cut short, we experienced some difficulties due to the hardness of the quartz.

The procedure for sample preparation is as follows: a small volume (~0.5ml) of the spin probe dissolved in *dichloromethane* (concentration 10^{-2}wt%) was placed into the sample tube using a glass pipette. It is important to control the amount of spin probe to be small to prevent the conversion of the nematic mesophase to a weakly chiral nematic phase when the spin probe itself is chiral. In addition, the amount of spin probe needs to be sufficient to give a low signal-to-noise ratio for the spectrum, and to avoid the spin exchange broadening of the spectral lines. The solvent was then removed from the tube using a vacuum pump for 10min. Then, the liquid crystal host was placed into the same sample tube. The amount of liquid crystal required was about 5mm in length of the sample tube. A hot air gun was sometimes used to ensure the spin probe was well dissolved in this nematogenic host. However, the air gun has to be used carefully since it may result in the

decomposition of the spin probe if the sample is over heated. The sample was then degassed by a repeated freeze-thaw cycle in order to avoid line broadening in the ESR spectrum caused by dissolved oxygen in the sample. In an oxygenated sample, the free radicals interact with the molecular oxygen [8, 9]. Oxygen is a paramagnetic molecule, and interactions with the unpaired electron of the nitroxide spin probe could increase the spin lattice relaxation time which causes the line broadening. The removal of oxygen generally takes about 30min. Finally, the sample tube is sealed to prevent the oxygen re-entering the sample.

3.4 ESR Optimum Parameters

After the sample was prepared, the tube was placed in the ESR spectrometer (Bruker ECS106), specifically inside the microwave cavity (rectangular TE_{102}). While running the experiment, the axis of the sample tube was perpendicular to the static magnetic field. The magnetic field used has a strength in the region of 3kG (0.3T) produced by the electromagnet of the spectrometer. The water cooling system was turned on to ensure the electromagnet and the klystron were not over heated.

We have performed several ESR measurements for different liquid crystal systems before we decide our preferred ESR parameters; later we assumed as the optimum parameters. For each ESR measurements, the time resolution was set by the use of 1024 data points. The conversion time of 40.96ms per single data point is chosen for most of our experiments since this gives a low signal-to-noise ratio which is clearly desirable for a spectrum. The typical spectrometer settings are shown in Table 1. Most of the parameters are fixed except the modulation amplitude, receiver gain, time constant and conversion time. The modulation amplitude depends on the natural linewidth for the sample and should always be smaller than this. Indeed, too great amplitude makes the spectral line broader. The magnetic field scan range was normally set to 70G; since the whole spectrum could fit within this range.

Table 1: Typical experimental parameters used in the ESR time-sweep acquisition.

Parameters	**Magnitude**
Modulation amplitude /G	1.033
Modulation frequency / kHz	100
Sweep width /G	70
Point interval /G	0.2
Receiver gain	8×10^3
Time constant /ms	1.28
Conversion time /ms	40.96
Number of data points acquired	1024
Sweep time /s	5.24
Microwave power / mW	12.7

Figure 3 shows four different ESR spectra for the sample of the Tempone spin probe in the chiral nematic formed by adding 0.5wt% *cholesteryl propionate* to nematic ZLI-4792. ESR spectrum shown in Figure 3 (a) was obtained using the optimum ESR parameters, listed in Table 1. While Figure 3 (b) gives the ESR spectrum obtained using the same parameters as those in Table 1, except the conversion time was smaller than the optimum value; at 5.12ms. The spectrum here has a lower signal-to-noise ratio due to the faster scan rate. Figure 3 (c) was obtained by keeping the other optimum parameters fixed but increasing the modulation amplitude to 5.178G. The ESR signal now has much larger linewidths and the resolution of the parallel and perpendicular hyperfine lines is lost. It is clearly best to keep the modulation amplitude small at a value of about 1G. Figure 3 (d) shows the lowest signal-to-noise ratio as the microwave power when the spectrum is acquired is lower than the optimum value at 0.89mW. The other parameters used are the same as those in Table 1. However, if the microwave power is increased above the optimum value, the signal-to-noise ratio is improved but the spectral lines are broadened.

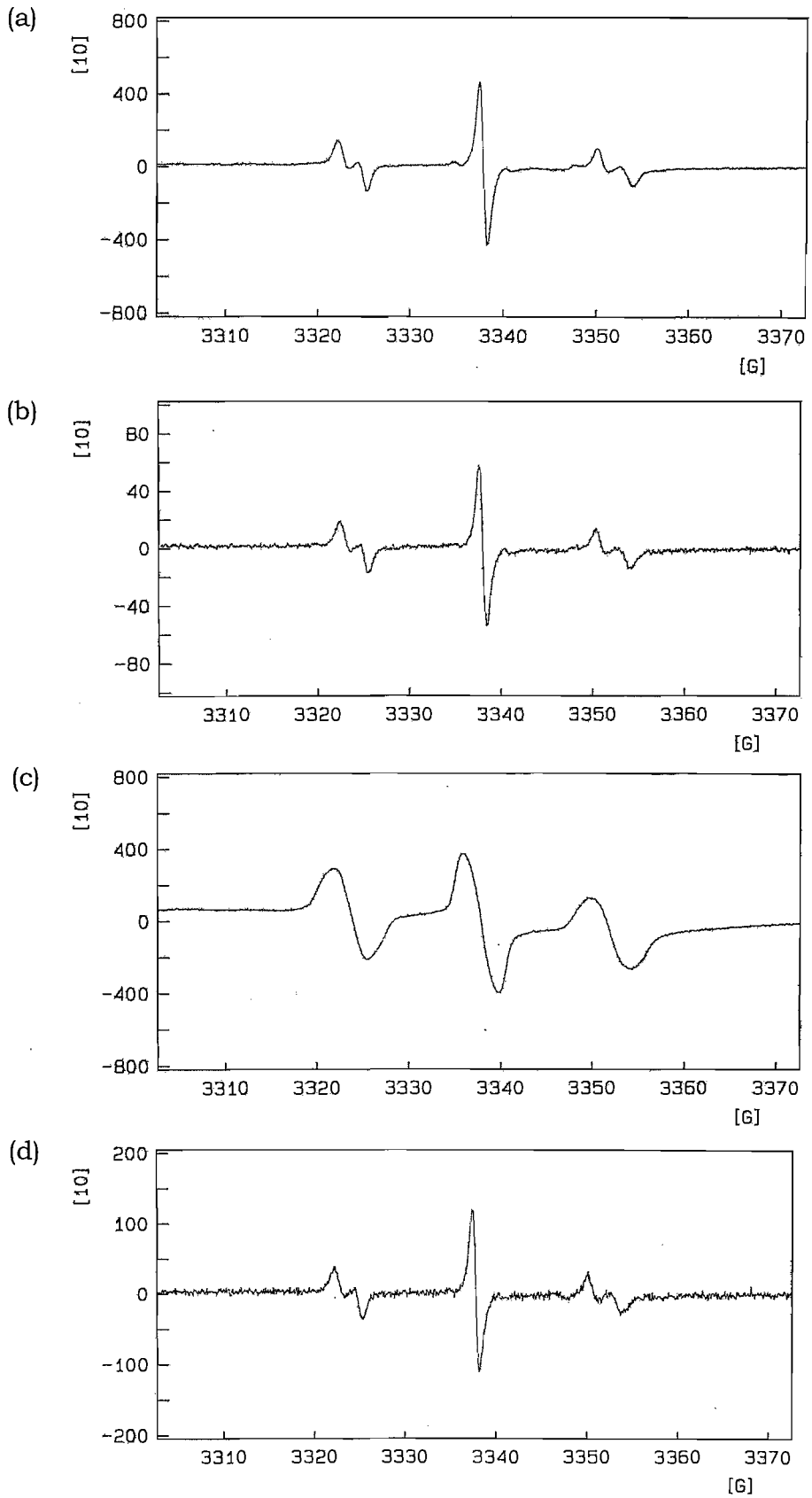

Figure 3: *The variation of ESR spectra acquired with, (a) using the optimum parameters, (b) optimum parameters but different conversion time, (c) optimum parameters but different modulation amplitude, and (d) optimum parameters but different microwave power.*

3.5 Liquid Crystal Systems

We have investigated several systems to explore the director disorder behaviour in liquid crystals. Each system has its own preparation methods. The systems studied are liquid crystal with colloidal particles, liquid crystals with a gelator, liquid crystals in confined geometries and the last is a liquid crystal with a chiral dopant. The preparation, methods and measurement details are explained in the following Sub-sections.

3.5.1 Colloidal Particles in a Liquid Crystal

Colloidal particles were dispersed in the liquid crystal, in this study we used nematic 5CB, and the suspensions were prepared by our collaborators at the *University of Bristol* and *Hewlett-Packard.* There were several types of colloidal particles with different sizes and quantities that were immersed into the nematic host. The preparation procedure for the colloidal nematic is explained in more detail in Chapter IV. To place the colloidal nematic into the ESR tube, first colloidal nematic which contained in a sample vial is heated to 38° C and stirred with a magnetic stirrer for 15min using a hot plate/stirrer until the nematic changes to isotropic. Then, a glass pipette was used to transfer the mixture into the sample tube (5mm in height of the tube) to which the probe had already been added. It was easier to transfer the colloidal nematic while it was in the isotropic phase since it is less viscous than in the nematic phase, especially for high-concentrations of colloids in the nematic. The oxygen removal procedure was performed for 30min, and then the sample tube was sealed and then the sample was ready for the ESR measurement.

3.5.2 Liquid Crystal Gels

In Chapter V, we report our studies of gelled nematic liquid crystals with a gelator made from amino acid derivatives which are able to form the hydrogen bonds necessary to create the network of fibres which trap the liquid crystal host. The process of gelling the liquid crystal ZLI-4792 was

performed by mixing and heating both the nematic and gelator. The preparation of the nematic gel was achieved as follows: the gelator (1.0mg) was placed into a sample vial with a small magnetic stirrer inside it. The amount of gelator used was determined by the desired concentration of the nematic gel sample, for example, 2.0wt%, so the amount of liquid crystal was 0.2g. Using a pipette, nematic ZLI-4792 was added into the same sample vial and mixed with the gelator. The mixture was heated and stirred for 2½ hrs at 100° C. While the mixture still in the isotropic phase, it was transferred into the ESR sample tube that already contains the Tempone spin probe. The oxygen removal procedure was performed for 30min, and then the sample tube was sealed before the sample was ready for ESR measurement. The gel was formed on cooling and this was shown when the mixture turns to a milky white and its viscosity increases so that it does not flow.

3.5.3 Liquid Crystal in Confined Materials

The confining materials used in this experiment were Controlled Porous Glasses (CPG) obtained from Millipore. It is a borosilicate glass which has a narrow pore size distribution and a very large internal surface area. The idea of this experiment was to insert the liquid crystal materials inside the narrow and random pores of the CPG, and then ESR could be used to study the director alignment of liquid crystal by the magnetic field. This system will be explained further in Chapter VI. The sample of the liquid crystal in the CPGs was prepared as follows. Sample tubes containing the spin probes (we used both Cholestane and Tempone for a comparison study) were prepared. The liquid crystal ZLI-4792 (20mg) was then added into the sample tube, just after that, the oxygen was removed from the solvent and the tube. Then with a spatula, CPG (20mg) was added to the liquid crystal in the tube. A homogeneous mixture had been produced if the CPG could flow in the tube; the liquid crystal is absorbed by the CPG. The oxygen removal procedure was performed for 30min, and then the sample tube was sealed; the sample was then ready for the ESR measurement.

3.5.4 Chiral Dopants in a Liquid Crystal

The addition of chiral compounds to a liquid crystal would produce a chiral liquid crystal phase, in which the liquid crystal director is well organized into a helical structure. In Chapter VII, we explain the details of this system. *Cholesteryl propionate* was chosen as the chiral dopant for the liquid crystal, ZLI-4792. The Tempone spin probe was employed for this experiment, which employed several samples with different concentrations of the chiral dopants. The preparation of the chiral nematic sample was performed as follows: A mixture with a known weight of liquid crystal and a known weight of cholesteryl propionate was placed in a sample vial. The mixture was heated and stirred with a magnetic stirrer on a hot plate/stirrer for 30min until it was isotropic. Then, a glass pipette was used to transfer the mixture into a sample tube (5mm in height of the tube) with the probe already in it. The oxygen removal procedure was performed for 30min, and then the sample tube is sealed before performing the ESR measurement.

For all of the liquid crystal systems described in this Chapter, the sample can be heated or cooled, depending on the requirements of the experiments. The dewar of the temperature control unit (*Eurotherm B VT-2000*) was inserted in the ESR cavity, where the sample is placed, with continuous flow of the pressured air was provided at 0.6bar.

3.6 References

[1] C. J. Dunn, D. Ionescu, N. Kunimatsu, G. R. Luckhurst, L. Orian, A. Polimeno; *J. Phys. Chem. B*, **104**, 10989 (2000).

[2] P. J. Collings, M. Hird; *Introduction to Liquid Crystals: Chemistry and Physics*, Taylor and Francis, London (1997).

[3] A. J. Leadbetter, R. M. Richardson, C. N. Colling; *J. Phys. (France)*, **36**, C1 (1975).

[4] W. H. de Jeu; *Physical Properties of Liquid Crystalline Materials,* Chapt. 5, Gordon and breach, London (1980).

[5] L. Pohl, U. Finkenzeller; *Physical Properties of Liquid Crystals, Liquid Crystals Application and Uses.*, **1**, Chapt. 4, World Scientific (1990).

[6] K. Hori; *Physical Properties of Liquid Crystals,* Ed. by D. A. Dunmur, A. Fukuda, G. R. Luckhurst, Chapt. 4, An Inspec Publication, London (2001).

[7] N. Kunimatsu; *PhD Thesis.*, University of Southampton (2000).

[8] A. Moscatelli, M. F. Ottavioni, W. Adam, A. Buchachenko, S. Jockusch, N. J. Turro; *Helvetica Chim. Act.,* **89**, 2441 (2006).

[9] A. J. Hoff, R. Deen; *Int. J. Radiat. Biol.,* **19**, 499 (1971).

Chapter IV

Colloidal Nematics

4.1 Introduction

We might not even realize that milk, is an example of a colloidal system. Milk is an emulsion of butterfat globules within a water-based fluid. Each fat globule is surrounded by a membrane consisting of phospholipids and proteins; these emulsifiers keep the individual globules from coalescing into noticeable grains of butterfat and also protect the globules from the fat-digesting activity of enzymes found in the aqueous portion of the milk. In an unhomogenized cow's milk, the fat globules average size is about four micrometers across. The largest structures in the aqueous portion of the milk are casein protein micelles, which are the aggregates of several thousand protein molecules bonded with the help of nanometre-scale particles of calcium phosphate. Both the fat globule colloids and the smaller casein micelles, which are just large enough to deflect light, contribute to the opaque white appearance of milk.

The definition of a colloid or of a colloidal dispersion is a heterogeneous mixture that behaves and visually appears to be like a homogenous mixture.

It is a mixture of two phases in which the dispersed phase is made of tiny particles or droplets that are distributed evenly throughout the continuous phase [1-4]. There are many colloidal systems in our environment but what we are most interested in here is the dispersion of solid particles in a host fluid which has become a widespread and important state of matter. They are of considerable technological importance with applications in everything from paints and coatings to food and drugs. In recent years, the field of colloidal nanocomposites has attracted great interest from researchers since they frequently exhibit unexpected hybrid properties, basically derived from the two components of the composites [5-8]. For example, a 10Å thick silicate layer of clay minerals are dispersed homogeneously in the nylon 6 matrix to produce nylon 6-clay hybrids (NCH); these exhibit various superior properties such as high strength, high modulus and a high heat distortion temperature. Surprisingly, the drastic change in these properties could be obtained with the addition of just a few percent of the clay. The same concept has been applied for various polymer systems such as epoxy resins [9, 10] and polystyrene [11, 12]. With the aim of high performance properties, this hybrid technique should be able to be applied not only for such polymer systems, but also for various types of materials including low mass compounds. This has been done by *Kawasumi* who prepared a novel composite materials based on a low molar mass liquid crystal and organized clay mineral which exhibited an unusual electro-optical effect not observed in the original system [5]. In addition to strong light scattering effects the hybrid system also exhibited a memory effect which suggests a good prospective in display device technology.

In this Chapter, we report a study of suspensions of anisometric clay particles in the nematic phase of a liquid crystalline solvent. Clay particles such as Claytone AF and Laponite AF, both are treated *montmorillonite* clays with different aspect ratios have been dispersed in nematic 5CB. The suspensions were characterized by ESR spectroscopy with some other results from NMR and small angle X-ray scattering (SAXS) studies. This Chapter will conclude with the findings on the alignment of the liquid crystal host and the clay particles as well as the interactions between them. In the next two Sections, we describe the physical and chemical properties of our subject matter namely colloidal nematics, following the SAXS characterization for the

same samples that have been performed by our collaborators in Section 4.4. Afterwards, in Section 4.5, we explain some related theories and background to the magnetic field alignment for a colloidal particle. ESR results are presented in the Section 4.6 with several types of experiment including the high-field experiment on the colloidal nematic system. The ESR results are followed by the NMR results at the end of this Chapter.

4.2 The Chemistry and Physics of Colloids

Colloids are present as dispersed systems, characterized by slow diffusion and slow sedimentation under normal gravity, which set the size of the colloidal particles in the range of about 1nm to 1μm. Within this size range, the heterogeneous mixtures may be called colloidal aerosols, colloidal emulsions, colloidal foams, colloidal suspensions or colloidal dispersions. There is a wide variety of colloids from many familiar substances in various types of matters as shown in Table 1.

Table 1: The classification of colloids.

		Dispersed medium		
		Gas	Liquid	Solid
Continuous medium	Gas	**None** (All gases are soluble)	**Liquid aerosol** (e.g. Fog, mist)	**Solid aerosol** (e.g. Smoke, air particles)
	Liquid	**Foam** (e.g. Whipped cream)	**Emulsion** (e.g. Milk, mayonnaise, hand cream)	**Sol** (e.g. Paint, pigmented ink, blood)
	Solid	**Solid foam** (e.g. Aerogel, Styrofoam, pumice)	**Gel** (e.g. Gelatin, jelly, cheese, opal)	**Solid sol** (e.g. Cranberry glass, ruby glass)

Colloidal dispersions of insoluble substances are called lyophobic (hydrophobic) colloids. This type of colloid is not in thermodynamic equilibrium and is prepared either by dispersion methods or by condensation methods. The colloidal particles in lyophobic colloids always attract one another by dispersion forces, even across a condensed medium. These forces play an important role in the interaction of colloidal particles; (i) electrostatic

interaction: colloidal particles actually carry an electrical charge and therefore attract or repel each other. The charge of both the continuous and the dispersed phase, as well as the mobility of the phases are factors affecting this interaction, (ii) *van der Waals* forces: is short range and attractive, due to interaction between two dipoles which are either permanent or induced, (iii) excluded volume repulsion: refers to the impossibility of any overlap between hard particles, (iv) entropic forces: results in effective forces even between hard spheres as a system progresses to a state in which entropy is maximized, according to the second law of thermodynamics, and (v) steric force: interparticle forces between polymer-covered surfaces or in solutions containing non-adsorbing polymer which producing an additional repulsive steric force.

A colloidal system can only be thermodynamically stable if the particles repel one another with a force of sufficient strength and sufficiently long range. In order to prevent the colloids from coagulating or flocculating, stabilization or repulsion mechanisms have to be present. Two main mechanisms for stabilization of the colloid are electrostatic and steric [2]. Electrostatic repulsion is based on the mutual repulsion of like electrical charges, obtained by surface dissociation or by preferential adsorption of ions of one type. Different phases generally have different charge affinities, so that an electric double layer forms at any surface. When an electric field is applied to a sol with charged particles, all particles with the same charge migrate to the same electrode with a velocity proportional to the applied field strength. While the other type of repulsion, steric repulsion is obtained when the particle surface is covered with bulky molecules, usually long chain molecules. These molecules caused the colloidal particles to repel one another in the system. This type of repulsion is particularly important for stabilization in non-aqueous and non-polar medium. Figure 1 shows an illustration of steric repulsion for colloidal particles in system at equilibrium.

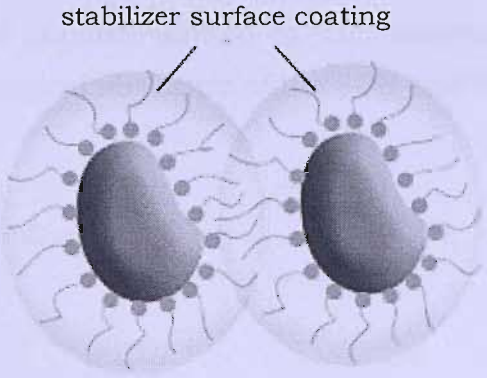

Figure 1: *Schematic representation of steric repulsion; colloidal particles with stabilizer molecules on their surfaces.*

4.3 Colloidal Particles in Nematic Liquid Crystals

Small water droplets dispersed in a nematic liquid crystal have been found to exhibit a novel class of colloidal interactions [6]. These interactions lead to the formation of anisotropic chain-like structures by the colloidal particles, including short range-range repulsion and a long-range dipolar attraction. The orientational elastic energy of the liquid crystal host produces this repulsive interaction which can lead to a novel mechanism for colloid stabilization. It has been mentioned earlier that nematic liquid crystals deposited with colloidal particles, i.e. clays, could produce high performance properties for the combination of both materials, even for the lowest percentage of the colloidal particles. Recently, the area of Liquid Crystal Clay Composite (LCC) has been given an intense focus by some researchers, especially in the display devices area. The growing interest in these composite materials has been to understand how the colloidal particles behave when suspended in nematic liquid crystals and how the properties of the nematic host are influenced by them [13].

A colloidal nematic is, by definition, a suspension of colloidal particles in a nematic liquid crystal. In our study, the nematic liquid crystals used were 5CB and MBBA, both with positive magnetic anisotropy, $\Delta\tilde{\chi} > 0$. However, much interest has been given to 5CB due to its high purity and room temperature nematic phase; this was purchased from Merck and was used as received. Moreover, it is a well-known compound and its nematic-isotropic

transition temperature is easily shifted by the presence of trace impurities. Figure 2 shows the chemical structure of the 5CB and MBBA molecules.

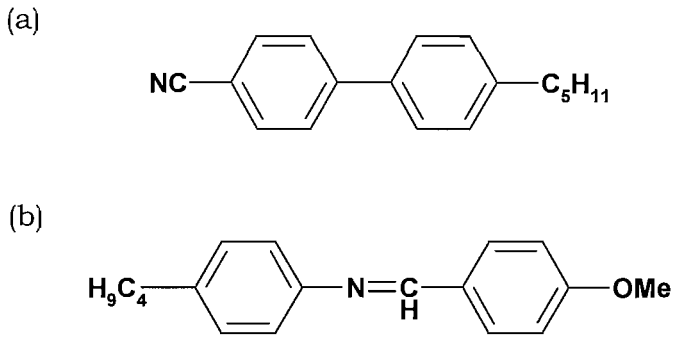

Figure 2: *The chemical structures of (a) 4-pentyl-4'-cyanobiphenyl or 5CB (T_{CrN} =24° C, T_{NI} = 35° C) and (b) N-4'-methoxy-benzylidene butylaniline or MBBA (T_{CrN} =22° C, T_{NI} = 48° C)*

Over the past few years, colloidal nematics have mostly involved spherical particles suspended in a nematic host [14]. However, spherical particles, such as colloidal silica and polymer lattices, actually cause the formation of topological defects and disruption of the nematic phase. *Filled nematics*, a defect stabilized network structure are produced when the phase acts to expel the spheres in order to minimize the energy in the system. To avoid this happening, a non-spherical colloidal particle should be selected to be dispersed in the nematic phase. Plate-like particles are the most appropriate for this reason and are used in our studies. Apparently this type of particle is not expelled and causes fewer topological defects than the spheres, therefore a good dispersion with minimum defect structures could be prepared [5,15].

Since most of the early studies in the colloidal nematic area used clays as the dispersing colloids, we wish to build on this experience. These systems could exhibit interesting ordering and phase behaviour as compared to the pure host nematic. The clays used in our experiments were Claytone AF®, Laponite AF®, and Sepiolite AF®. Claytone and Laponite particles have plate-like structures but Sepiolite exhibits a long needle-like structure. Originally, all of them gave unstable suspensions in a nematic host but in order to limit the defect formation, a low molecular weight surfactant, rather than a polymeric surface treatment, was introduced to stabilize the particles in the

suspension against their mutual attractive forces and subsequent aggregations.

These three types of clays share a similar chemical structure but differ greatly in their aspect ratios. Claytone AF is surface treated natural *montmorillonite* clay from Southern Clay Products with a thickness of approximately 1nm and a range of diameters from 500nm to 2000nm [16]. With such a high maximum aspect ratio (1:2000), these plates are not rigid in structure but have some major flexibility as can be seen from the SEM micrograph in Figure 3. Claytone is pre-treated with dehydrogenated tallow, a surfactant mixture with is *dimethyldioctadecylammonium bromide* (DODAB) as the main component to give stable suspensions in non-aqueous solvents. The treated clay is cleaned repeatedly with a 40/60 mixture of propanol and water (ultra pure, Millipore) to remove excess surfactant, dried under vacuum and finely ground and sieved prior to use.

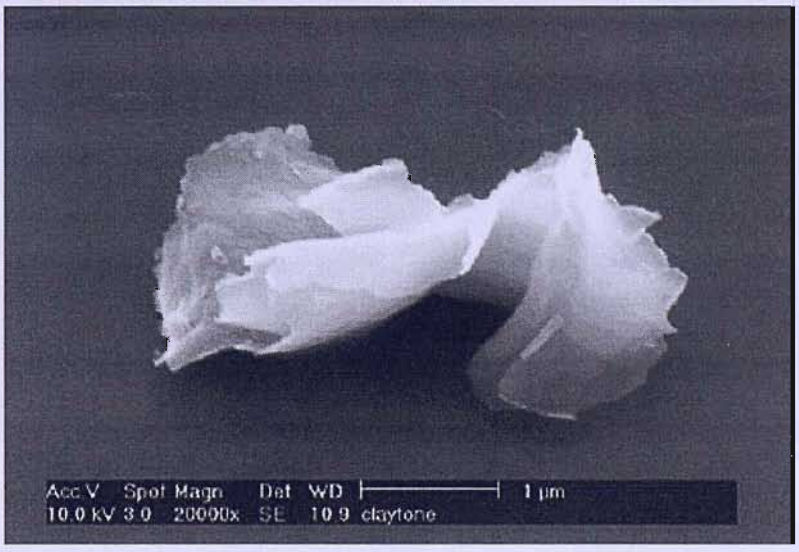

Figure 3: *Electron micrograph of Claytone AF. The image shows a flexible plate structure for this type of clay [21].*

Laponite RD from Rockwood Additives is a synthetic hectorite type clay with a thickness of approximately 1nm and a relatively small diameter of 25nm, aspect ratio of 1:8 as dispersed particles [17]. Laponite is totally dispersed in water (1.0wt%) by stirring for 24h prior to treatment with surfactant. As for Claytone, the surfactant DODAB from Acros Chemicals (used as received) is added in a dilute solution in 80:20 water : propanol to give 100% coverage

[18]. The particles are finely grounded and dried prior to suspension in the isotropic phase of the liquid crystal.

Inspection using Scanning Electron Microscopy (SEM) shows that Laponite when delaminated consists of plates with diameters smaller than 100nm. Laponite has a strong tendency to form films if it is mixed with water and then dried on a clean piece of glass. To obtain an SEM image of single plates (see Figure 4), a very dilute suspension (1 part of Laponite in 1000 parts of water) is used and sprayed onto a heated glass slide (180° C) to avoid droplet formation and hence agglomeration of the Laponite particles. Even after this treatment, single particles could only be seen in between agglomerates. These single particles have a diameter, *d*, of less than 100nm confirming the literature values of 10nm < d < 40nm [19] and 20nm < d < 95nm [20].

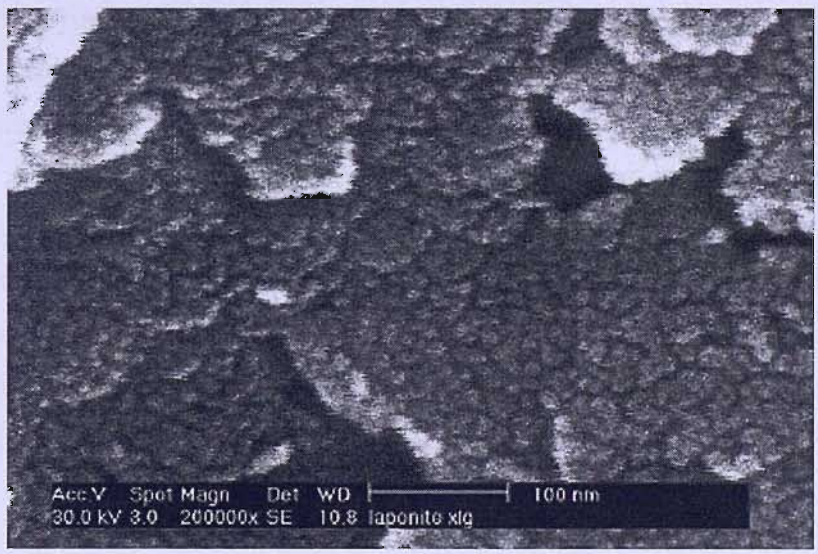

Figure 4: Electron micrograph of Laponite. The image shows the aggregates and smaller structures for this type of clay [21].

In contrast, Sepiolite clay particles are examples of *Attapulgite* or *Palygorskite* minerals which have an entirely different superposition of tetrahedral and octahedral elements of the unit cell [16]. The unit cell has very narrow channels in which water molecules and exchangeable cations are located. These channels are brought about by the inversion of alternate pairs of silica tetrahedral. Sepiolite crystallizes in the form of long needles as can be seen in Figure 5, which is the main difference with the other two clays.

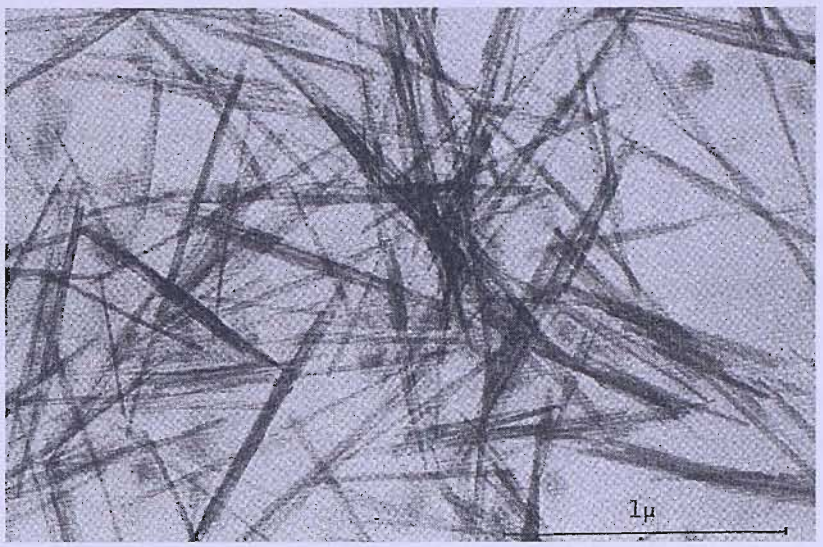

Figure 5: *Electron micrograph of Sepiolite. The image shows the needle-like structure of this type of clay [16].*

The suspensions of these three clay samples are prepared as follows: the dry powder is added to the isotropic phase of the liquid crystal and stirred for 15min. This is then followed by 6-7h of sonication, degassing under vacuum and then cooling to the nematic phase. The particles should not then sediment and the suspension is then stable for up to 24h, after which time flocculation is observed. The sample then develops into two discrete layers after phase separation; one particle poor and the other particle rich with an open floc structure. The co-existing layers of the aggregates are easily broken upon stirring at approximately 40° C for 15min.

4.4 Colloidal Nematics: SAXS Studies

Small angle X-ray scattering (SAXS) studies on colloidal nematics have been performed by our collaborators from the University of Bristol and Hewlett-Packard®, United Kingdom [21].

SAXS is a fundamental method for structure analysis of condensed matter. This technique is used for the determination of the microscale and nanoscale structure of particle systems, can be applied in various fields, from metal alloys to synthetic polymers in solution and in the bulk, biological macromolecules in solution, emulsions, porous materials, nanoparticles, etc.

In this technique, X-ray radiation is elastically scattered by a sample and the resulting scattering pattern, resulting from interference effects is analysed to provide information about the size, shape and orientation of some components of the sample. The scattering is caused by the differences in electron density within the periodic or local structure of a matter. For example, matter, like crystals, scatter X-rays in distinct patterns, however the scattering from an ordered crystal is quite different to that from the low order systems, such as liquid crystals. These patterns were quickly recognized to give a direct insight into the structure of the materials that caused the scattering. In accord with its name "small-angle", the SAXS patterns are collected at very small scattering angles (typically 0.1° to 10°), but the scattering patterns are capable of giving structural information of repeat distances, *d*, in partially ordered systems of up to 150nm.

In SAXS experiment, radiation is directed at a sample; some of the incident radiation is transmitted by the sample, some is absorbed and some is scattered. Here, the scattering vector, $\boldsymbol{Q}$, is introduced, which is defined as the modulus of the difference between two vectors, $\boldsymbol{k}_i$ and $\boldsymbol{k}_s$, ($\boldsymbol{Q}=\boldsymbol{k}_s-\boldsymbol{k}_i$) both represent the incident X-ray and the scattered X-ray, respectively. These vectors have the same magnitude, $2\pi/\lambda$, where λ is the wavelength of the radiation. The scattering vector is determined by the structural distance, *d*, which can be derived from Bragg's law equation,

$$n\lambda = 2d\sin\theta, \tag{4.1}$$

where θ is the angle made by the incident radiation to the scattering planes of the sample. The magnitude of $\boldsymbol{Q}$ is

$$|Q| = 2k_i \sin\theta, \tag{4.2}$$

therefore,

$$|Q| = 4\pi\sin\theta/\lambda, \tag{4.3}$$

and Bragg's law becomes

$$Q_n = n(2\pi / d), \tag{4.4}$$

where n is the order of the scattering. The diffraction pattern from equally spaced planes has intensity, $I(Q)$, which is everywhere zero except when $Q = n(2\pi / d)$ along a direction normal to the planes. From equation (4.4), the nature of the periodicities in the scattering object is revealed by the reciprocal of the pattern observed in the diffraction. The relative intensity of the peaks in the diffraction patterns or intensity distributions, $I(Q)$, gives information on the orientational and spatial order of the phase.

Figure 6 (a) shows a schematic diagram for the experimental setup of a typical SAXS study. The SAXS experiment generally is performed when a sample is irradiated with a well-collimated beam of X-ray radiation, and the resulting scattered intensity is measured as a function of the angle between the incoming beam and scattered beam. The diffraction pattern from the scattered X-ray beam from a nematic is shown in Figure 6 (b). There are two typical patterns, one corresponds to an unoriented and the other corresponds to an oriented specimen made by a magnetic field. An unoriented specimen produces a scattering pattern with one or more circles or ring-like patterns which are also called a powder pattern. This data is actually very useful for obtaining intermolecular spacings for the specimen. However, in general, the oriented specimens are more interesting to be studied quantitatively. Scattering data from an unoriented and an oriented specimen both contain contents relating to anisotropy and correlations; the positions of the peaks are the same for the two cases. The data collected for oriented specimens represents the repeat distance between particles or molecules in the specimens. To do this, we need the detector image from the scattered X-ray beams.

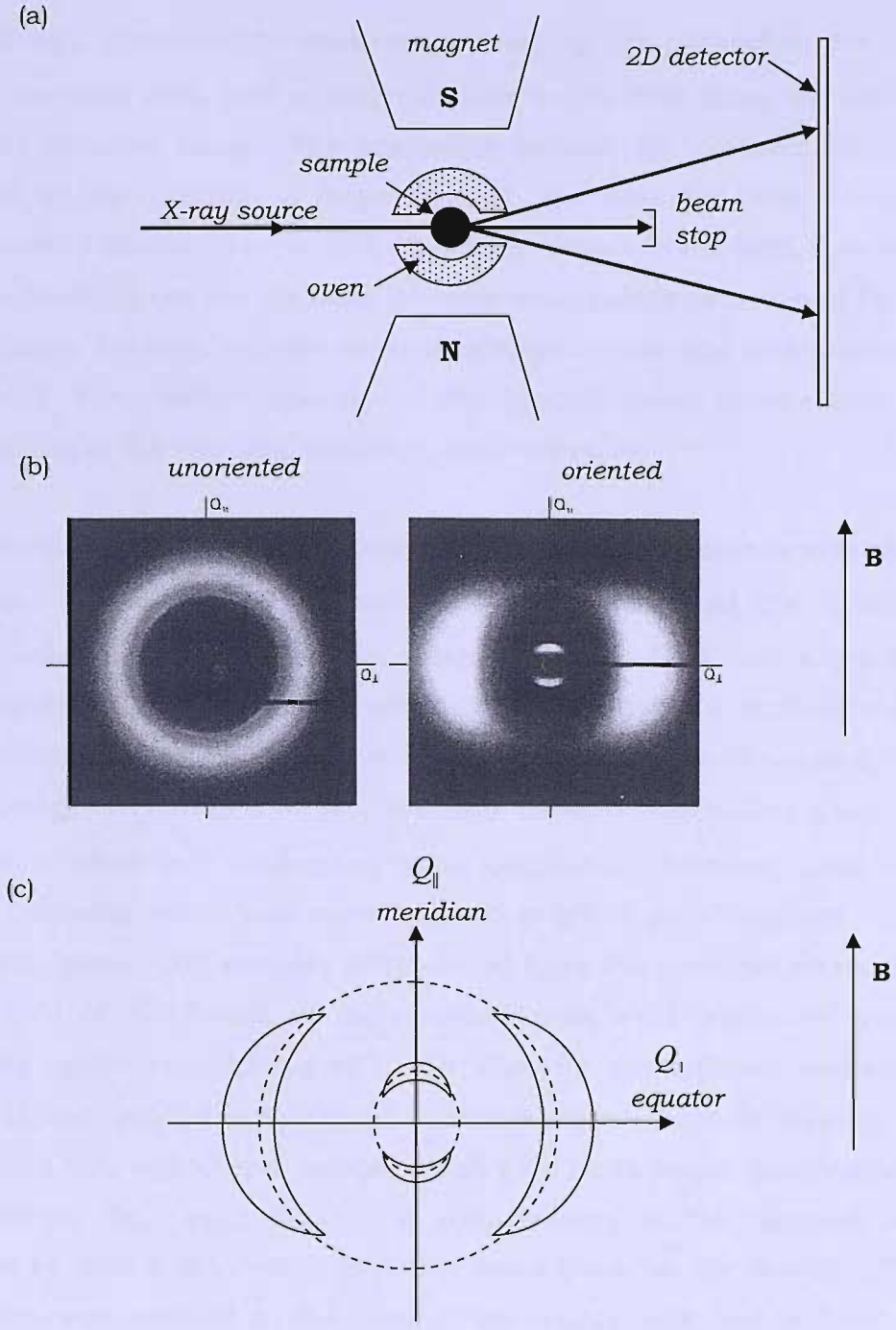

Figure 6: *The schematic of (a) a simple SAXS apparatus with the sample located in the magnetic field, (b) typical diffraction patterns of an oriented and unoriented nematic sample, and (c) schematic of detector image (diffraction pattern) for an oriented nematic sample.*

The schematic scattering pattern for the oriented nematic specimen is shown in Figure 6 (c). In this image, there are meridian, ($Q_{\parallel}$), and equator, ($Q_{\perp}$) axes, which both dependent on the magnetic field direction. Magnetic field direction, which is shown in Figure 6 (a), is parallel to the vertical axis of the

detector image, therefore the scattering vector, $\boldsymbol{Q}$, is parallel to the field along the meridian axis, and is perpendicular to the field along the equator axis of the detector image. The scattering pattern for nematic which is determined by the direction of magnetic field, also provides information on the alignment of the liquid crystal director with respect to the field. Two pairs of arcs are seen, where the distance between each pair is determined by the repeat distance between rod-like molecules (side-to-side and end-to-end) in the specimen. The smallest spacing on the detector image results from the biggest spacing in the nematic specimen, and vice versa.

In the experiment used by our collaborators, SAXS measurements were made using copper *Kα* X-rays (average wavelength, λ, is 0.154nm) from a sealed tube with other wavelengths removed using a nickel filter and a graphite monochromator. The diffraction pattern was detected using a multi-wire area detector which was placed 840mm from the sample with an evacuated path so that a range of Q from 0.03 to 0.6Å^{-1} was covered. The colloidal nematic samples were filled into *Lindemann* glass capillaries (diameter 2mm, wall thickness 0.01mm), which had been flattened to give a path length of ~1mm for the X-ray beam. The samples were cooled from the isotropic phase in a magnetic field of ~0.5T and all the measurements were performed over a temperature range from 25° to 40°C. To allow for the differing measuring efficiency of each pixel, the measured counts were corrected by dividing the counts from a ^{55}Fe radioactive source, which gave an isotropic distribution of X-rays. During data acquisition, the transmission of the samples was determined by taking the counts from the main beam on the detector. This transmission was resolved as the ratio of the counts with and without the sample in the beam. In this measurement, the scattering from the liquid or liquid crystal host was deduced from the scattering of the dispersions using the formula

$$I_{correct} = \frac{I_{L+P}}{T_{L+P}R_{L+P}} - \frac{I_L}{T_L R_L}. \qquad (4.5)$$

Here I_{L+P} is the scattering intensity from the colloidal dispersion (liquid and particles) in a sample tube, T_{L+P} is the transmission of the dispersion in a

sample tube, and R_{L+P} is the length of the run. While I_L, T_L and R_L are the corresponding quantities for a sample of the dispersion medium (liquid only). The second term in equation (4.5) is indeed used to remove the contribution to the scattering intensity from the host and so to leave just the intensity caused by the scattering from the suspended clay particles. This formula gives a reasonable correction for the scattering from the liquid host and container since the dispersion only contains a few percent of clay and the sample tubes were nominally of the same thickness. After the background correction, the data were radially averaged in order to improve the statistics and make the scattering from the isotropic and nematic phases comparable. This radial averaging also could improve the signal-to-noise ratio of the scattering intensity and so allow the peaks to be seen more clearly and their positions to be determined more accurately. These data were collected from the detector image, they cover the range from the centre of the image to the outside which is related to the scattering vector, $\boldsymbol{Q}$, and they are added together to give a log-log plot. Figure 7 shows the scattering pattern and the radially averaged plot for a sample of 1.0 wt% Claytone in 5CB at 25° C.

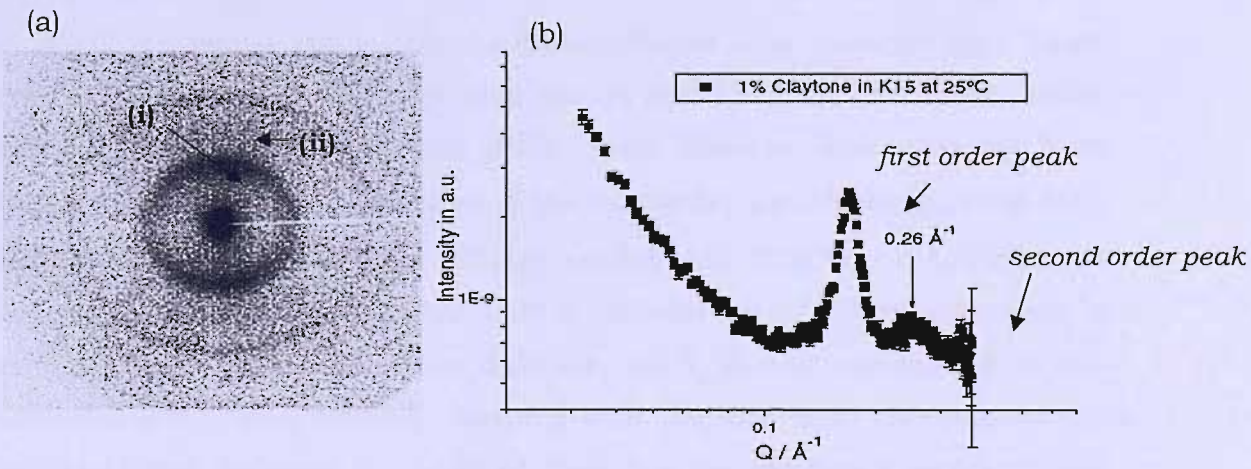

Figure 7: *SAXS measurement for 1.0wt% Claytone in 5CB at 25° C with the director aligned vertically in the form of (a) the detector image (i) Claytone scattering peak, (ii) 5CB scattering peak, and (b) the radially averaged scattering as a function of the scattering vector, Q. The peak corresponding to 0.26Å^{-1} is due to 5CB and the two other peaks are respectively first and second order pseudo Bragg peaks from the suspended particles. For this measurement, no detector or background correction has been applied, so a weak peak from the host in keeping with its low intensity in the scattering pattern is seen.*

From Figure 7 (a), we see a centre point (big dot) in the scattering pattern, which corresponds to the beam stop where most of the radiation is stopped from passing through and reaching the detector. Then, we see two (inner and outer) circles or rings which are produced by the scattered X-rays. Both circles indicate the presences of suspended Claytone particles in 5CB; the scattering from clay particles is most intense since they have a higher electron density difference compared to the nematic host. These peaks are assigned to the first and second order pseudo-Bragg peaks. The term *pseudo* is used, basically in a case when the translational order is not long range as in crystals (with long range order which consists of a series of sharp spots and these are called Bragg peaks). For example, in a nematic liquid crystal, the X-ray scattering produces diffuse peaks, so these are known as pseudo-Bragg peaks because they do not result from the long range order in the system. Between these two circles, there are two faint parts which are diffuse but noticeable in the detector image. This part is believed to originate from the scattering made by 5CB. The log-log plot in Figure 7 (b) shows three dominant peaks; two of them are from the suspended Claytone particles, and the weak peak at Q = 0.26Å^{-1} is due to 5CB. From this radial averaged plot, we could determine the repeat distance between clay particles and liquid crystals. The first pseudo-Bragg peak occurs at 0.18Å^{-1} and the second order peak occurs at 0.36Å^{-1}. The value of the repeat distance, d, is estimated from $d = 2\pi/Q$ where Q is the position of the first order pseudo-Bragg peak [21]. Therefore, the repeat distance of clay particles in 5CB is ~35Å, while the distance between 5CB molecules is 24Å. Certainly, for 5CB, this distance is too large to be the side-to-side distance, so it should correspond to the molecular end-to-end distance, keeping with the alignment direction of the director. Other information obtained from the pseudo-Bragg peaks of this radially averaged plot is the indication of the formation of layers or stacks for the clay particles by the widths of the peaks. Narrower peaks represent more discs in a stack.

The scattering from the suspended clay is found to be the most intense. In fact, with its high particle concentration, the pseudo-Bragg peaks for the dry clay powder have a larger difference (peaks position) to when the clays are suspended in some host materials, and this is shown in Figure 8. The comparison of radially averaged scattering data from the Claytone powder

with that from its suspension in 5CB and toluene indicates that the pseudo-Bragg peaks are not caused by the non-dispersed powder.

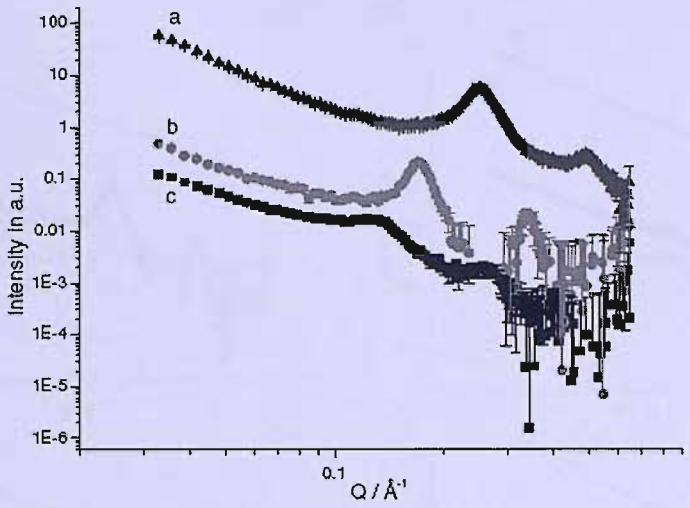

Figure 8: *Log I versus log Q plot for X-ray scattering data from (a) Claytone dry powder, (b) 1.0wt% suspension of Claytone in 5CB, and (c) 1.0wt% suspension in toluene. The scattering data have been corrected according to equation (4.5), therefore there is no peak in these plots coming from the host.*

The pseudo-Bragg peaks from the dry Claytone powder occurs at 0.25Å^{-1} (first order) and 0.48Å^{-1} (second order). The first order peak gives a repeat distance of 25Å between the plates in the stacks, which is consistent with 10Å thick discs [18] having surfactant layers about 15Å thick. Claytone as a suspension shows a clear increase in the repeat distance of the plates, from 25Å in the powder to 37Å in 5CB and 48Å in toluene. If the thickness of the plate is 10Å, it shows the spacing between the plate surfaces has increased from 15Å to 27Å in 5CB and to 38Å in toluene. All of these results suggest that the solvents delaminate (this happens when the solvent prevents the association of the clay into stacks or acts to break up the stack) the aggregates in the powder to produce small self-assembled stacks within the dispersion. Our collaborators have also shown in the logI-log$Q$ plot for the scattering data from the SAXS experiments, the line with I proportional to Q^{-2} [21]. Here, all the parameters considered in the experiments have been adjusted to fit the shape of the scattering data. This line has a slope of -2, which indicates that the particles studied are disc-like rather than rod-like.

The plot of log (I) versus log (Q) in Figure 9 shows the relation between the I-Q^{-2} plot with the scattering plot.

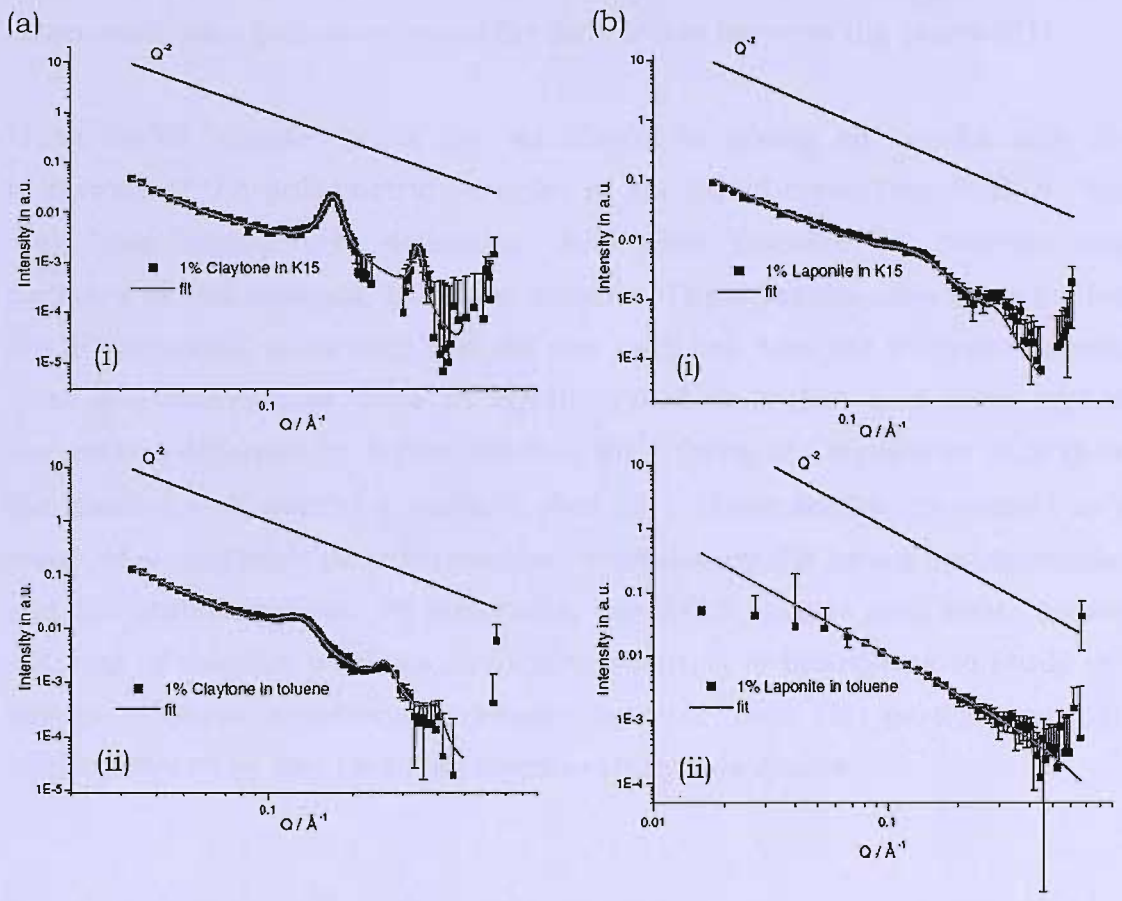

Figure 9: *(a) Scattering data and fit for 1.0wt% Claytone in (i) 5CB and (ii) toluene, (b) scattering data and fit for 1.0wt% Laponite in (i) 5CB and (ii) toluene. K15 is a commercial name for the liquid crystal 5CB. A line of slope -2 is included for comparison.*

The Q-dependent scattering intensity shown in Figure 9 indicates that the ordered stacks are more prominent in 5CB than in the toluene. The narrower peaks for Claytone in 5CB indicate that the nematic matrix promotes larger stacks than in the isotropic liquid. This may result from the interaction of the mesogenic molecules with the surfactant on adjacent plates which tend to fix and hold the plates together. On the other hand, the scattering data for clays in toluene (broader and less prominent peaks) suggests that the clay is well delaminated and the stacks forming within the dispersion contain fewer particles. Plates of Claytone with a greater aspect ratio have shown a strong tendency to self-organize into stacks. Laponite, although chemically similar to Claytone but with a smaller aspect ratio, tends not to form stacks. The greater aspect ratio of Claytone allows for a greater interaction with the

mesogenic molecules which helps the plates to be placed together. Between 5CB and toluene as dispersants for the clays, 5CB has a strong tendency to form stacks compared to smaller molecules like toluene. Apparently the larger molecules help to enhance the interaction between the plates [21].

These SAXS measurements are successful in giving an insight into the behaviour of the anisometric particles in the liquid-crystalline host. So far, they have managed to determine the repeat distance, *d*, between clay particles in the solvents; 5CB and toluene. These results also confirm that the liquid crystal is a better host for clay particles than the isotropic solvent, since the ordering of clays in liquid crystal is higher and more stable. Parameters obtained by fitting the data for 1.0wt% of Claytone in 5CB show the number of sheets in a stack is ~5±1 [21]. These stacks are formed as a result of strong inter-plate interaction, mediated by the mesogenic molecules and the stabilizer layer. To this point, the SAXS studies only focus on the ordering of the clay particles in its dispersant. It is interesting to study the alignment of the liquid crystal director between these clay particles as well. ESR spectroscopy has been employed to study this system.

4.5 Alignment of Colloidal Particles in a Magnetic Field

There are two ways by which materials interact with a magnetic field; these come from their paramagnetic and diamagnetic properties. In Chapter I, we had discussed how liquid crystals, as diamagnetic materials, behave in a magnetic field. The same concept applied here for colloidal particles in the presence of a magnetic field. Paramagnetic molecules with one or more unpaired electrons will force the sample to move to regions of high field while diamagnetic compounds with no unpaired electrons will be forced to the low magnetic field regions.

When a paramagnetic material such as a platelet is subject to a uniform magnetic field, its energy is changed and this change is given by

$$U = -V_0 \chi B^2 / 2\mu_0, \tag{4.2}$$

where V_0 is the volume of the platelet, χ is the magnetic susceptibility, B is the magnetic flux density and μ_0 is the permeability of the vacuum. Colloidal particles from *montmorillonite* are reported to be paramagnetic [22]. Most materials have an anisotropic magnetic susceptibility, for clay it can be expressed as the difference between components parallel and perpendicular to the clay layers

$$\Delta\chi = \chi_{\parallel} - \chi_{\perp}, \tag{4.3}$$

because of the cylindrical symmetry of the system. This results in a difference in energy for the clay platelet when they are either parallel or perpendicular to the magnetic field

$$\Delta U = -V_0 \Delta\chi B^2 / 2\mu_0. \tag{4.4}$$

For most clay minerals, $\Delta\chi$ is positive, therefore the energy difference, ΔU, is negative [23]. Consequently the normal of the platelets tends to align parallel to the magnetic field. In the case of *montmorillonite* clays, $\Delta\chi$ is positive, $(1.5\pm0.5)\times10^{-4}$ m^3kg^{-1} [24] and this is supported by the SAXS observations of the alignment along the field for *montmorillonite.*

The determination of the threshold field, B_{th}, for alignment can be performed by

$$B_{th} = \sqrt{\frac{2\mu_0 k_B T}{V_0 \Delta\chi}}. \tag{4.5}$$

Here k_B is the Boltzmann constant and T is the temperature for the sample. At the threshold field strength, the alignment should becoming observable, whilst with the information on the diameter, d and thickness, l of the platelets, V_0 could be calculated,

$$V_0 = \frac{\pi d^2 l}{4}, \tag{4.6}$$

in order to verify the typical critical field for alignment. Taking d=500nm and l=1nm, for *montmorillonite* particles, we have B_{th}=0.6T; this is the theoretical value of the magnetic field strength, needed to align the particles at room temperature. In ESR spectroscopy, the threshold field of 0.6T might not be reached since the magnetic field strength that is used to measure the ESR spectrum is around 0.3T.

For the alignment behaviour of the director, we have developed a model, which we have used to estimate the distance between two clay plates, d_c, as a function of the clay concentration in the liquid crystal. This idea originates from the *Freedericksz* experiments with homeotropic alignment; in this experiment, the angle made by the director with the surface is measured as a function of the magnetic field strength. The magnetic and elastic energy both compete for this alignment. Thus the surface and elastic effects want the director to be parallel to the surface normal, in contrast, the magnetic field is trying to align the director parallel to its direction and hence orthogonal to the normal of the surface. There is a transition point where the magnetic energy is greater than the elastic energy, and then the director alignment, changes from an angle of 90° to the surface to 0°. The transition point is called the *Freedericksz* transition and the two states either side of it are shown in Figure 10. In this case, the distance between two plates in a homeotropic alignment is constant and the magnetic field is varied.

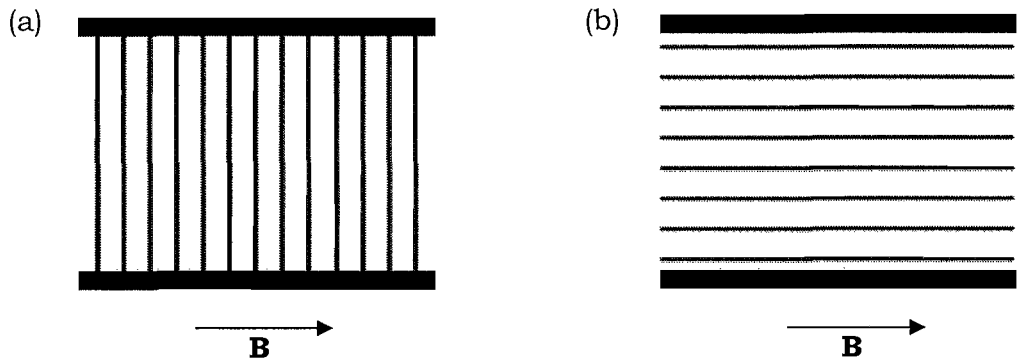

Figure 10: The director alignment between the glass substrates; (a) at initial transition when $B < B_{th}$ and (b) when $B > B_{th}$.

We modified the idea and we now take the field constant and vary the distance between two plates, d. We then work out the *Freedericksz* transition point at which the homeotropic alignment produced by the surface will change if the distant between the plates is larger than d_c, where

$$d_c = \frac{\pi}{B}\sqrt{\frac{\mu_0 K_{av}}{\Delta\chi}}. \tag{4.7}$$

(see equation 1.9, Chapter I), where μ_0 is the vacuum permeability constant, $\Delta\tilde{\chi}$ is the diamagnetic anisotropy, and K_{av} is the average elastic constant since for our colloidal system a range of elastic deformations are involved. For 5CB at 25° C, the parameters needed to estimate this threshold thickness are

$B = 0.33T,$

$\Delta\chi = 1.43\times10^{-6},$

$\mu_0 = 4\pi\times10^{-7}\,Hm^{-1},$

$K_1 = 6.2\times10^{-12}N, K_2 = 3.9\times10^{-12}N, K_3 = 8.2\times10^{-12}N,$

which gives the average elastic constant, K_{av} as $6.1\times10^{-12}N.$

The calculation gives d_c of 22μm, for an X-band ESR field, and for the high field of 7.05T of 300MHz NMR spectrometer, d_c is 1.03μm. This is the maximum spacing needed to achieve surface alignment of the director; it decreases with increasing field strength.

Moreover, to relate the critical thickness to the concentration of the clay particles, we propose a simple model for the colloidal nematic system. This model assumes a lattice structure with the clay particles being cubic with a length, l (see Figure 11). The model describes the weight percentage of clay relative to the weight for the whole system as used in the experiment. We used the relationship between the density, volume, and the weight of the clay particles. The distance between two neighbouring clay particles is d and our model will allow us to work out its value in terms of the weight fraction of the clay. The volume, V, of the liquid crystal surrounding a clay particle is given in terms of the volumes of several boxes with different sizes (see Figure 12).

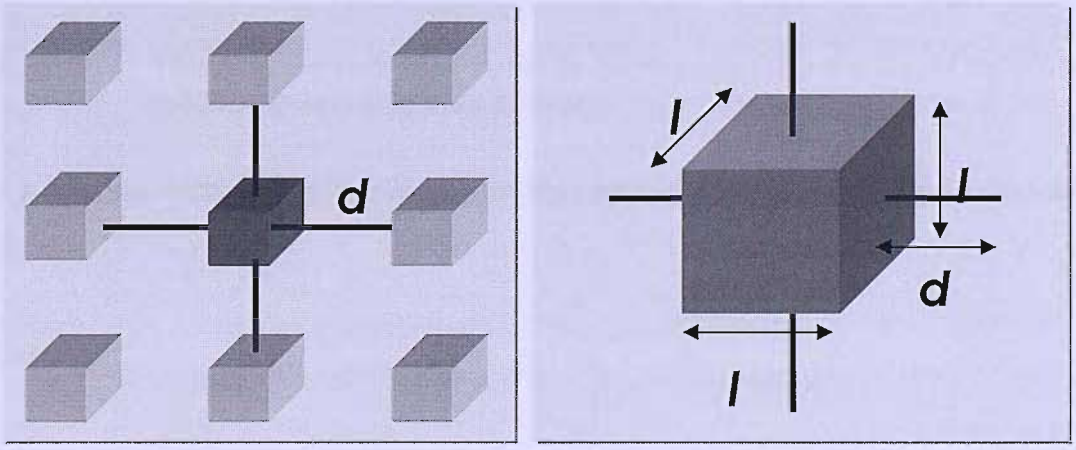

Figure 11 : The geometrical model for a colloidal nematic, in which d is the distance between cubic clay particles of length, l.

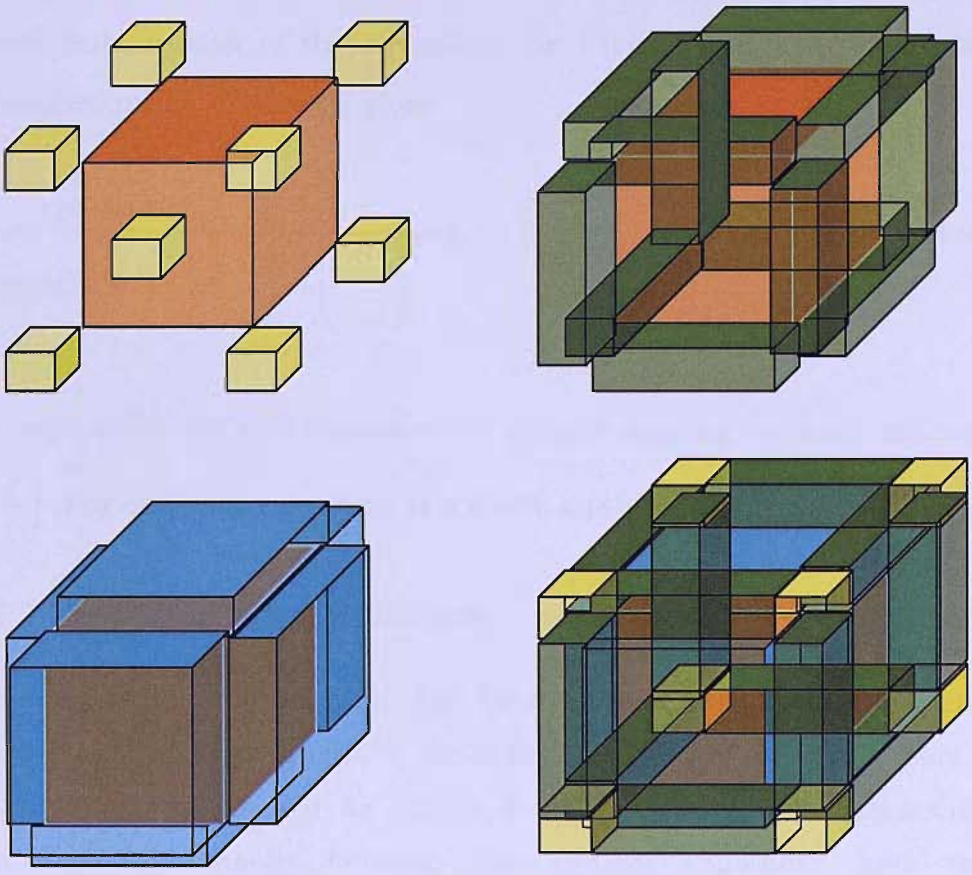

Figure 12: The clay particle (red cube) is surrounded by the liquid crystals (yellow, green and blue boxes)

For a system with n clay particles the volumes of the clay and liquid crystal are,

$$V(clay) = nl^3,$$

$$V(LC) = n(3l^2 d + 3d^2 l + d^3),$$

The weight % of clay is given by

$$\frac{\rho(clay)V(clay)}{\left[\rho(clay)V(clay) + \rho(LC)V(LC)\right]} \times 100 = \%wt, \qquad (4.8)$$

where $\rho(clay)$ and $\rho(LC)$ are the densities of the clay and liquid crystal respectively. Substitution of the equations for $V(clay)$ and $V(LC)$ for clay particles concentration of 4.0wt% gives

$$\frac{\rho(clay)\times 100}{\rho(clay)+\rho(LC)\left(3\left(\frac{d}{l}\right)+3\left(\frac{d}{l}\right)^2+\left(\frac{d}{l}\right)^3\right)}=4, \tag{4.9}$$

from this expression, we can calculate the relative spacing between the clay stacks, $\left(\frac{d}{l}\right)$. For clay concentration of 4.0wt% and using a density for liquid crystal of 1.01gcm^{-3} and clay of 2.35gcm^{-3}, we estimate $\left(\frac{d}{l}\right)$ to be 12.61. Strictly the clay stacks are not cubic but by relating their volume to the size of a cube gives the effective length, l, as 251nm for sides of the stack, 4nm × 2000nm × 2000nm, so gives d as 1.2μm. For this model to be successfully determine the relationship between the critical thickness and the concentration of clay particles, this might takes a long shot. Nevertheless, although the results obtained from this model is just an approximation, it is in the right order of magnitude; smaller than 22μm.

4.6 ESR Spectroscopy and Spectral Simulations

It was mentioned in Section 4.4 when colloidal nematic samples were examined with SAXS, the alignment was found for clay particles that formed into stacks. From the observed results, we could assume that the liquid crystals are also aligned, considering the fact that liquid crystal molecules are homeotropically or homogenously sandwiched between any two clay particles. However, obviously we need some additional characterization techniques that could help to discover the alignment behaviour of liquid crystal colloids in a magnetic field especially the liquid crystal itself. In order to achieve this, we have used both ESR and NMR spectroscopy which have been found to successfully study the director alignment in the liquid crystal as well as the orientational order of the nematic.

In this Section, we discuss the results from a series of experiments made on these colloidal nematic samples. The methods, apparatus and the way to perform the ESR experiments have been mentioned in Chapter III. In this Chapter, we discuss the ESR spectra recorded for each sample with different clay concentrations as well as different types of clays. In the next sub-sections, we will discuss several more ESR experiments that have been done to support and perhaps confirm the results that we already examined. The NMR studies on colloidal nematics are discussed in Section 4.7.

4.6.1 The Effect of adding Colloidal Particles to Nematics

To start the discussion on these studies, we first look at the ESR spectra for a static experiment, in which the sample was characterized while it stayed unmoved in the ESR cavity. As an introduction, all of these static and dynamic experiments have been carried out at room temperature (~20°C). The liquid crystal samples that we used are nematic 5CB and MBBA with different concentration of clay particles; these are as follows:

Liquid Crystal		Clay Type	Weight Percentage
5CB		Claytone AF	1.0wt%
5CB		Claytone AF	2.0wt%
5CB		Claytone AF	3.0wt%
5CB		Claytone AF	4.0wt%
5CB	+	Claytone AF	5.0wt%
5CB		Claytone AF	10.0wt%
5CB		Laponite RD	2.0wt%
5CB		Laponite RD	4.0wt%
5CB		Sepiolite	1.0wt%
MBBA		Claytone AF	1.0wt%

There were 10 samples altogether and all of these were actually prepared by our collaborator from the University of Bristol. However, in order to perform the ESR measurements, the sample was not used as it arrived in our laboratory. It has to be homogenous, so we heated (~40°C) and stirred the liquid crystal colloid sample for about 30min before placing it in the ESR sample tube.

We begin by presenting the ESR spectrum of Cholestane spin probe in the pure nematic 5CB; this is shown in Figure 13; it contains three symmetric hyperfine lines coming from the interaction of the unpaired electron and the nitrogen nucleus in the nitroxide group. The hyperfine spacing of 8.20G, measured from the linepositions at half height of the peaks labeled (1) and (2), or from the peaks labeled (2) and (3), shows that the spectrum comes from the spin probe in the 5CB, in its nematic phase, with the director parallel to the magnetic field. Since the hyperfine spacing for the spin probe in the isotropic phase is 15.04G. No other peaks appeared, indicating that there are no impurities in the sample and that the director was uniformly aligned by the field.

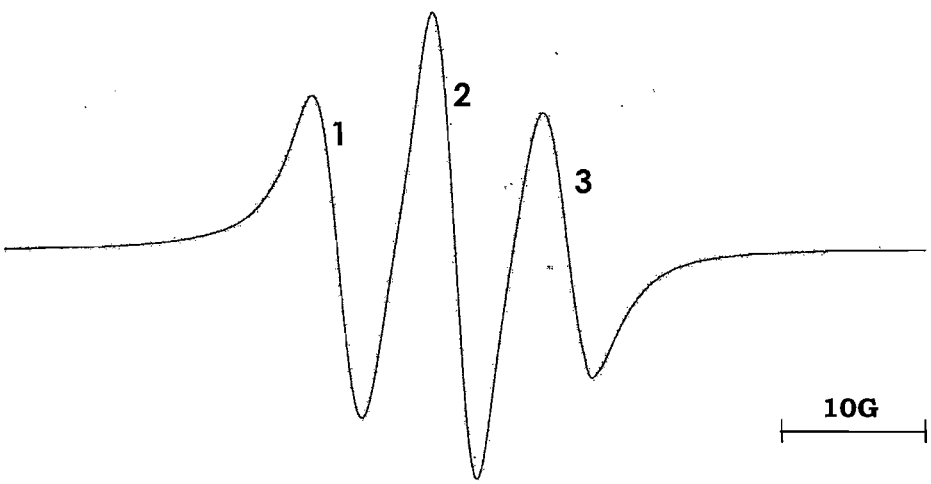

Figure 13: ESR spectrum for the Cholestane spin probe in pure 5CB at room temperature.

In contrast for 5CB with 1.0wt% of Claytone, new peaks appear (see Figure 14) which suggest that the addition of clay particles to the nematic host has changed the director distribution in the nematic. One new and relatively weak peak, labeled as (1) in Figure 14, appears at 3315G, which is associated with the director perpendicular to the field. It should be five lines as the signal for perpendicular director orientation had two lines one more at ~3350 G. However, this line (5) was not visible, possibly because the peak was broader than that at low field. Though, it should be present since the other peak (1) appeared. Thus from this spectrum, we have argued that the new peak comes from the director perpendicular to the field in the sample. The mixture of 5CB and Claytone behaves as we had expected and the

spectrum shows that the director is not completely aligned by the magnetic field. However, we see the three parallel peaks still remain and this shows that the director is largely aligned by the magnetic field presumably because the clay concentration is small.

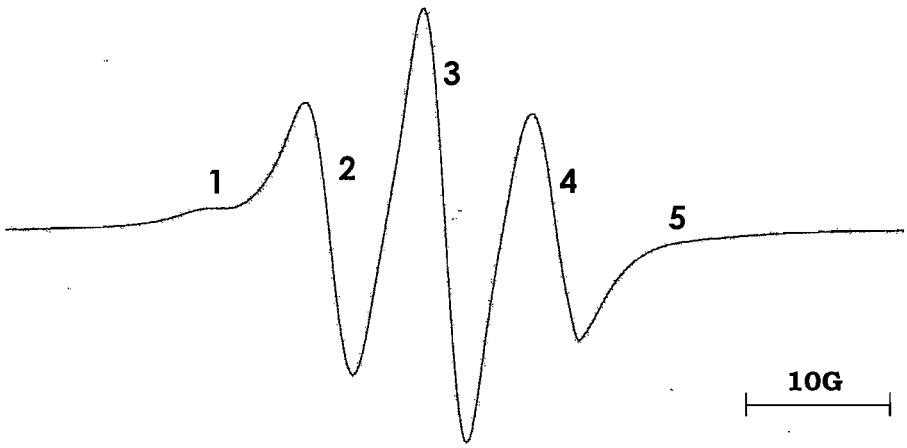

Figure 14: ESR spectrum of the Cholestane spin probe in 5CB with 1.0wt% Claytone at room temperature.

The addition of more Claytone to the nematic results in the increase in random distribution of the liquid crystal director. The smaller separation between the surfaces of the platelets inhibits the alignment of the director by the field and so generates a more random distribution of the director. Figure 15 shows four significant hyperfine peaks (1), (2), (3) and (4) and another one (5) with apparently a weaker height caused by its larger width. Peaks (1) and (5) actually come from the director perpendicular to the field while (2) and (4) clearly originate from the director parallel to the field. The spectral intensity between these peaks comes from all intermediate director orientations. We found that peaks (1) and (2) had similar intensities which provide information, as we shall see, on the director distribution. More importantly, the peaks associated with the perpendicular director orientation have become more intense compared to the ESR spectrum for the lower concentration of Claytone.

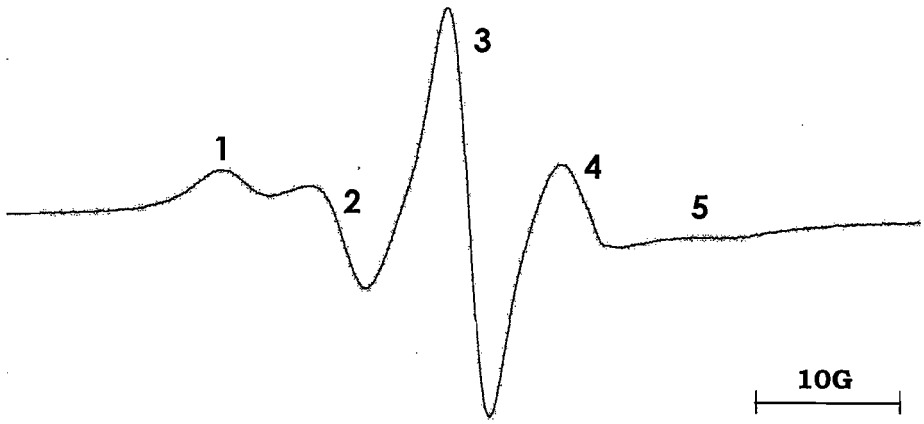

Figure 15: ESR spectrum of the Cholestane spin probe in 5CB with 2.0wt% Claytone at room temperature.

5CB with 3.0wt% Claytone at room temperature showed the ESR spectrum of Cholestane spin probe given in Figure 16. This spectrum has become more complex as the director has become more randomly distributed. We can see the intensity for the perpendicular peak (1) has become more intense compared to that in Figure 13 and in this ESR spectrum, peaks (4) and (5) are also far more obvious. We also found a new sharp line occurring between lines (4) and (5) of the spectrum for the Cholestane spin probe. We believe this might be caused by a paramagnetic impurity in the glass Dewar of the temperature control unit. This was confirmed by recording the spectrum of the empty Dewar which gave a single peak at the same reference field as can be seen in Figure 17. The poor signal-to-noise ratio in this spectrum is because the intensity for this spectrum is 10 times smaller than spectrum in Figure 16.

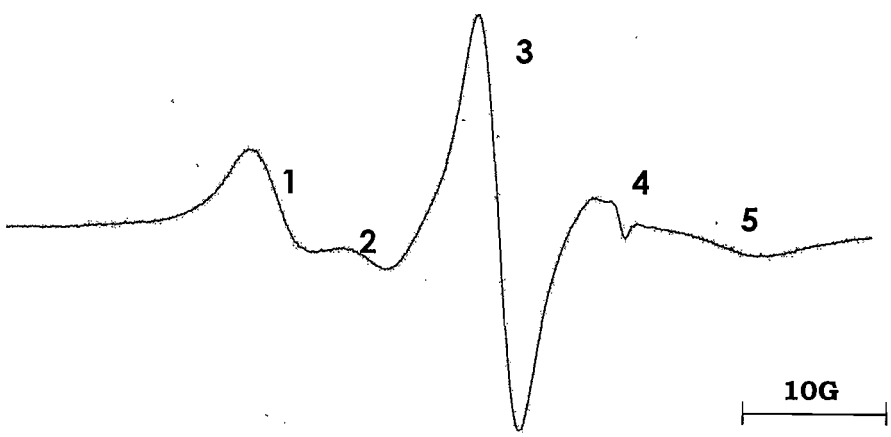

Figure 16: ESR spectrum of the Cholestane spin probe in 5CB with 3.0wt% Claytone at room temperature.

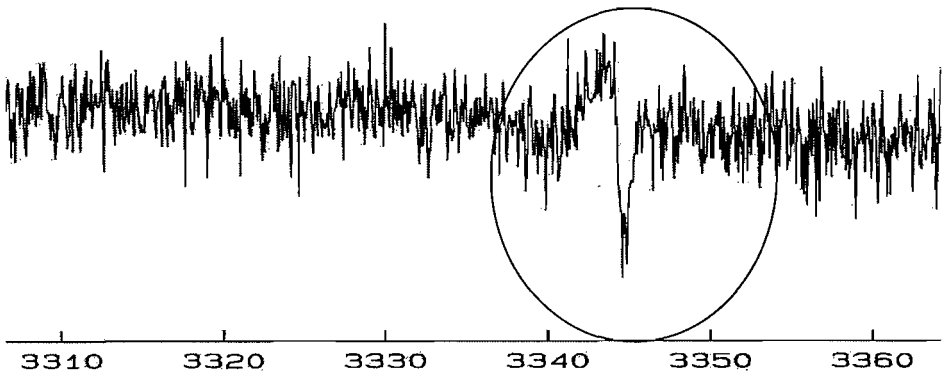

Figure 17: Single line in ESR spectrum coming from the glass Dewar at temperature control unit.

As with the previous spectrum (see Figure 16), the ESR spectrum for the spin probe in 5CB with 4.0wt% Claytone (see Figure 18) consists of five hyperfine peaks, and their relative intensities indicate an essentially random distribution of the director in the liquid crystal. The main difference of this spectrum was that lines (1) and (5) have become more intense, as the Claytone concentration was increased indicating an increase in the fraction of the director perpendicular to the magnetic field.

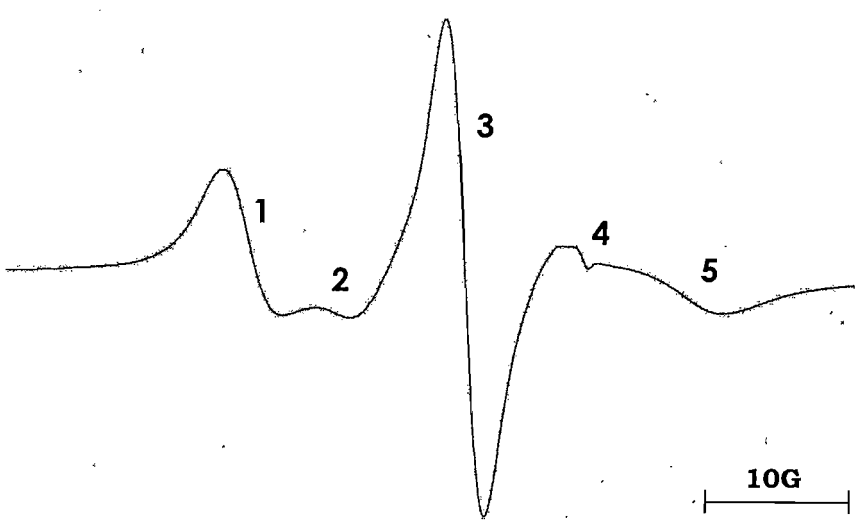

Figure 18: ESR spectrum of the Cholestane spin probe in 5CB with 4.0wt% Claytone at room temperature.

With more clay particles added to the nematic matrix, say 5.0wt% of Claytone, we observed the ESR spectrum shown in Figure 19 where the ESR signals looked the same with the one for 5CB with 4.0wt% Claytone. From a physical view the sample looked so viscous presumably because it has a higher concentration of clay particles. We could say that, at this stage the behaviour of colloidal nematics has saturated as far as the director distribution is concerned. The intensity for peak (1) has become higher than in the previous spectrum while peak (2) has become lower than ESR spectrum in Figure 15. Bear in mind, that peaks (1) and (5) which correspond to the director perpendicular to the field are related to each other as are lines (2) and (4) which correspond to the director parallel to the field. We could conclude that, as the colloidal concentration increases, so the signal from the director perpendicular to the field becomes stronger but weaker for director parallel to the field. This is caused, as we had expected from the beginning of this investigation, by the random alignment of the colloidal particles and the associated elastic energy, which increases with the concentration of the colloidal particles, exceeding the magnetic energy. The precise nature of this random director distribution function for colloidal nematics could be confirmed by ESR spectral simulations.

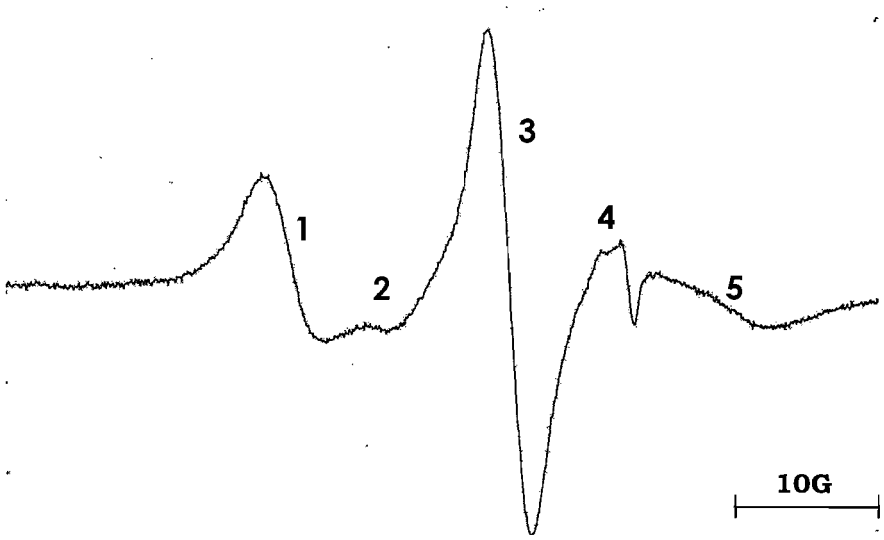

Figure 19: ESR spectrum of the Cholestane spin probe in 5CB with 5.0wt% Claytone at room temperature.

All of these ESR experiments were carried out at room temperature of approximately 20°C. The summary so far, we see that the addition of Claytone, even for a relatively small amount would disturb the director alignment of the nematic. We also found a large difference in the alignment behaviour of the director with smallest and the largest concentration of clay particles. For instance, 1.0wt% of Claytone seems to have very weak signals associated with the director perpendicular to the field; however if we subject the sample to a slightly higher magnetic field, the director will align parallel to the field. But for 4.0wt% sample, it is different. The random director alignment seems more stable. This is a state when the director is totally random and only a much stronger field could change this distribution.

The ESR results for Claytone particles dispersed in nematic 5CB are quite similar to those observed for samples with Laponite and Sepiolite particles. These results imply that the ESR spectra really depend on the concentrations of clay particles in the nematic. They all produce a random director distribution pattern as Claytone, especially for Laponite, since the physical properties and sheet-like structure of Laponite is quite similar to that Claytone but with a lower aspect ratio.

The magnetic field of 0.3T seems too small to align nematic director in the presence of a few wt% of the clay but this is not a disadvantage for ESR spectroscopy. Indeed from our studies we could investigate the competition between the field and surface alignment which produces the ESR spectra that we have seen. Obviously the alignment caused by the magnetic field was defeated, eventually, by surface and elastic forces so that we see the distribution in director alignment for nematic samples with clay particles and how this changes with the concentration of the clay.

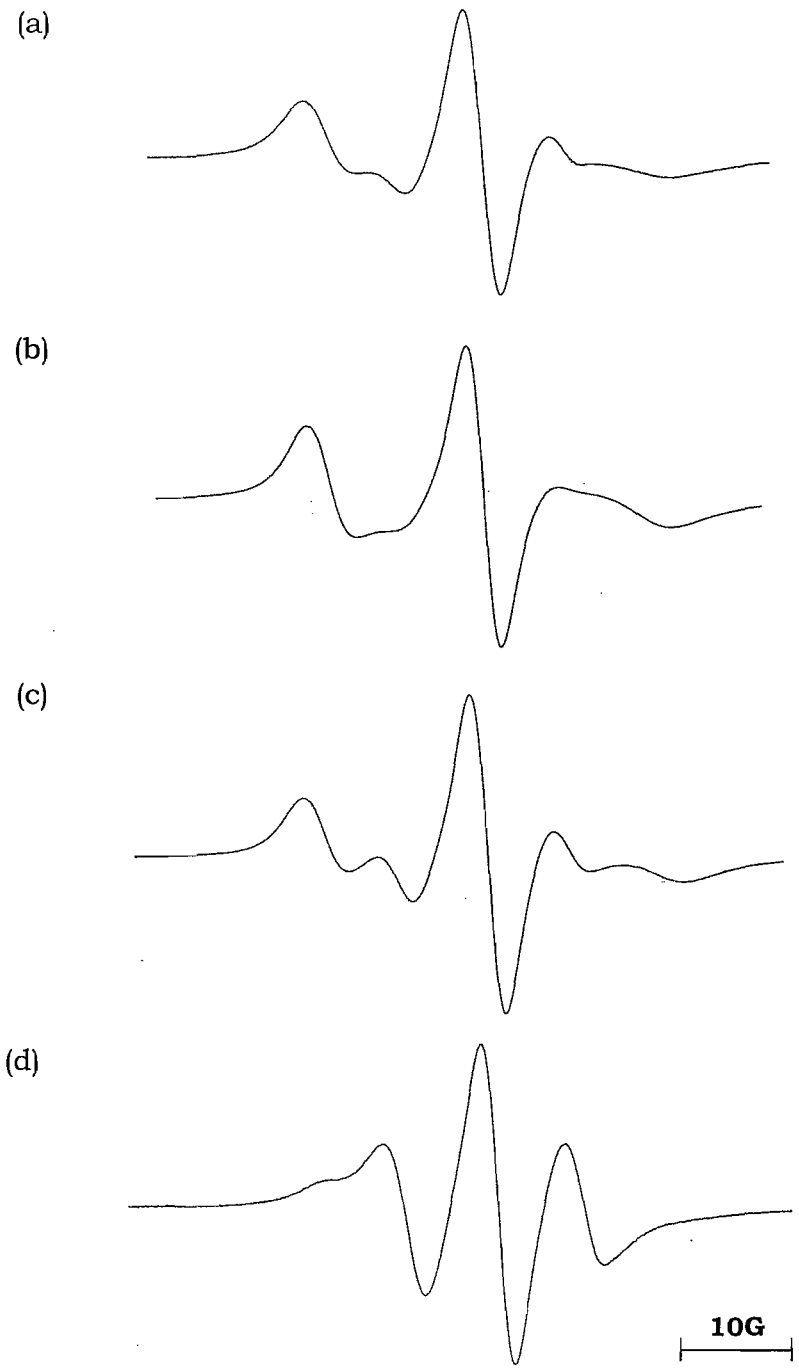

Figure 20: *The ESR spectra of the Cholestane spin probe in various nematics and clays (a) 5CB + 2.0wt% Laponite, (b) 5CB + 4.0wt% Laponite, (c) 5CB + 1.0wt% Sepiolite, and (d) MBBA + 1.0wt% Claytone.*

In order to interpret and understand more of this complex behaviour, the ESR spectra should be simulated so that we can determine quantitatively the director distribution function which we have discussed in Chapter II. To do this, some information such as the value of $\widetilde{A}_{\parallel}$, $\widetilde{A}_{\perp}$ and the linewidths for the

three peaks, $T_2^{-1}(-1)$, $T_2^{-1}(0)$ and $T_2^{-1}(1)$ is needed. All of these values were extracted directly from the ESR spectra and were subject to change to find the best fit of the real ESR powder-like spectra. Moreover, it is our aim to use these to determine from the ESR spectra, the director distribution function, so that there is another parameter value, '*a*' which is the parameter controlling the director orientational order. The form of the spectrum proves to be very sensitive to the value of *a* and a small change made to it would effect greatly the ESR spectrum. The ESR spectral simulations dependence on the value of *a* are shown in Figure 21. However, since our main interest is in the value of *a* and since the other parameters are not expected to vary significantly with the clay concentration we have concentrated on optimising *a* and not the other parameters.

5CB

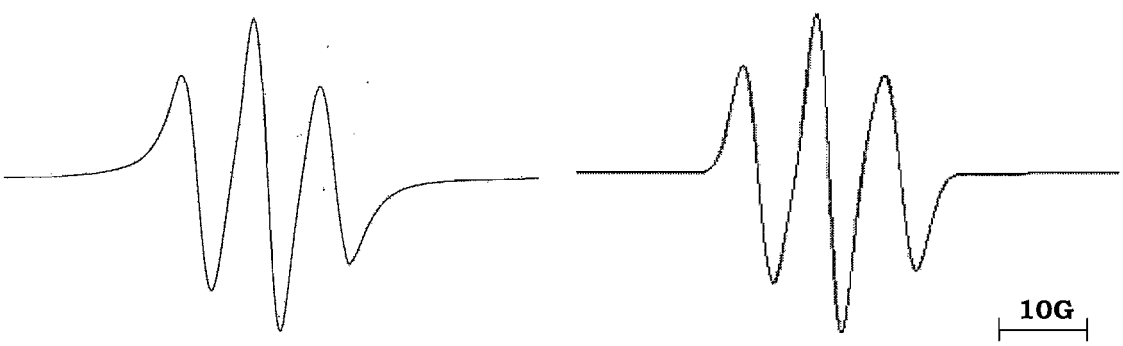

experiment *simulation*

$\tilde{A}_{\parallel} = 8.36G, \tilde{A}_{\perp} = 18.38G, T_2^{-1}(-1) = 1.80G, T_2^{-1}(0) = 1.50G, T_2^{-1}(1) = 1.90G, a = 26.0$

5CB + 1.0wt% Claytone

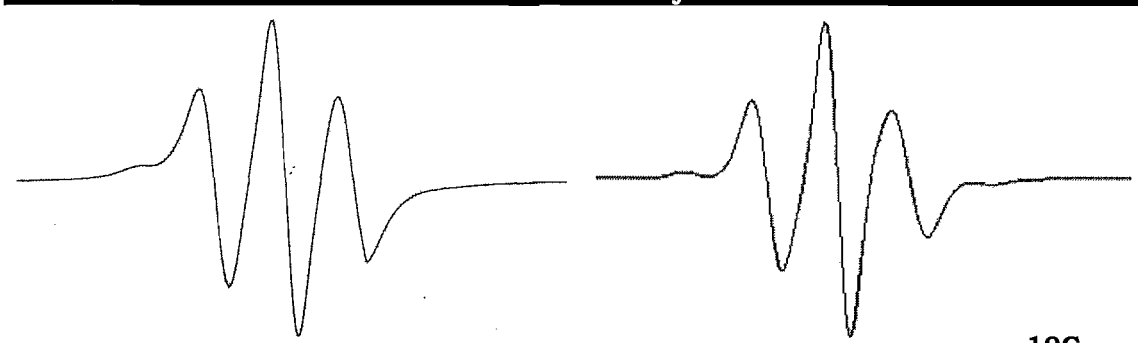

experiment *simulation*

$\tilde{A}_{\parallel} = 8.44G, \tilde{A}_{\perp} = 18.34G, T_2^{-1}(-1) = 1.78G, T_2^{-1}(0) = 1.55G, T_2^{-1}(1) = 1.80G, a = 8.0$

5CB + 2.0wt% Claytone

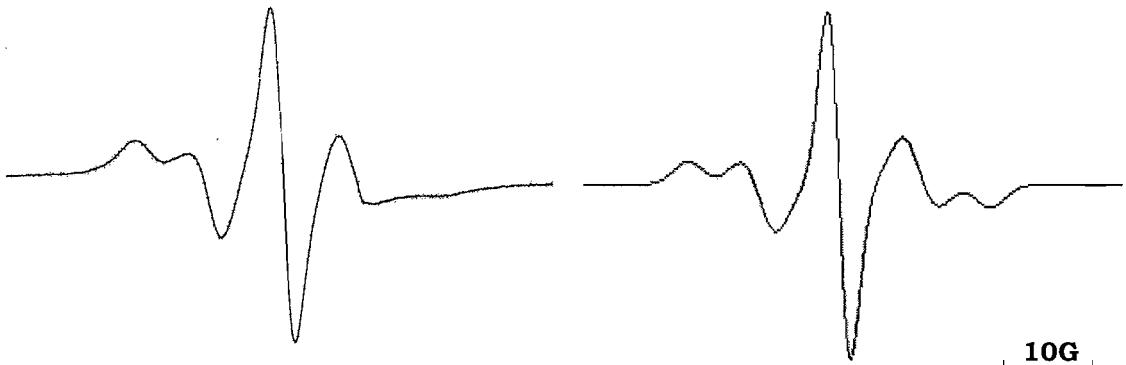

experiment *simulation*

$\widetilde{A}_{\parallel} = 8.90G, \widetilde{A}_{\perp} = 18.11G, T_2^{-1}(-1) = 1.80G, T_2^{-1}(0) = 1.60G, T_2^{-1}(1) = 2.50G, a = 3.0$

5CB + 3.0wt% Claytone

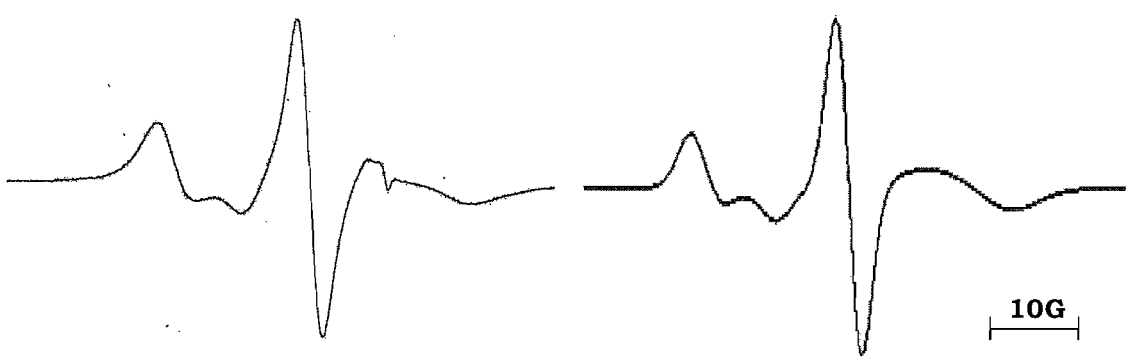

experiment *simulation*

$\widetilde{A}_{\parallel} = 8.90G, \widetilde{A}_{\perp} = 18.11G, T_2^{-1}(-1) = 1.60G, T_2^{-1}(0) = 1.55G, T_2^{-1}(1) = 3.50G, a = 1.5$

5CB + 4.0wt% Claytone

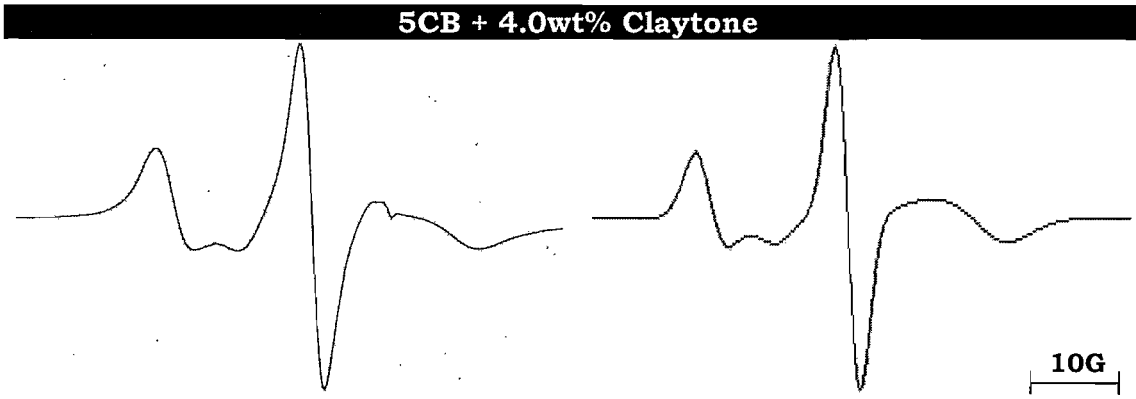

experiment *simulation*

$\widetilde{A}_{\parallel} = 8.90G, \widetilde{A}_{\perp} = 18.11G, T_2^{-1}(-1) = 1.80G, T_2^{-1}(0) = 1.60G, T_2^{-1}(1) = 3.50G, a = 1.2$

5CB + 5.0wt% Claytone

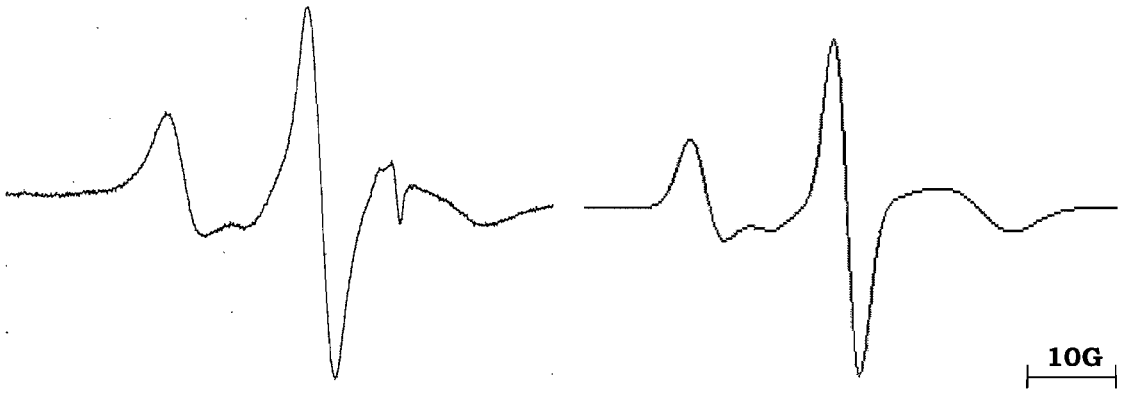

experiment *simulation*

$\widetilde{A}_{\parallel} = 8.90G, \widetilde{A}_{\perp} = 18.11G, T_2^{-1}(-1) = 1.80G, T_2^{-1}(0) = 1.60G, T_2^{-1}(1) = 3.50G, a = 1.1$

5CB + 2.0wt% Laponite

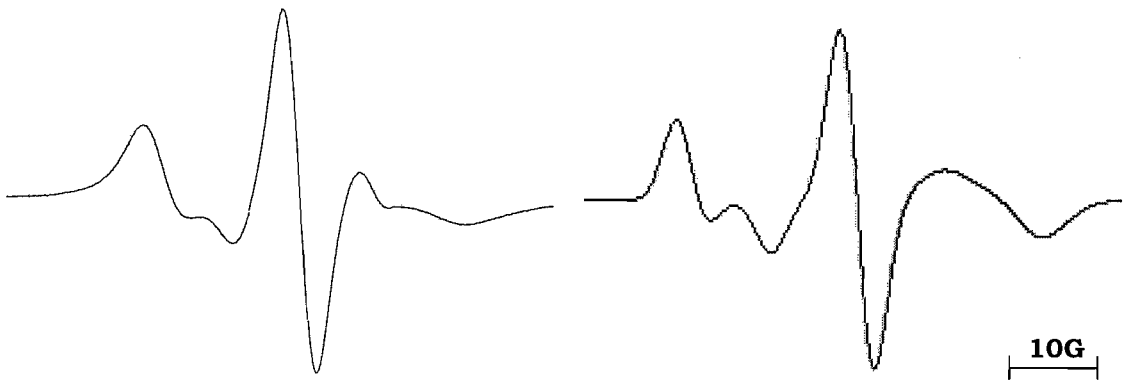

experiment *simulation*

$\widetilde{A}_{\parallel} = 8.20G, \widetilde{A}_{\perp} = 16.10G, T_2^{-1}(-1) = 1.40G, T_2^{-1}(0) = 1.60G, T_2^{-1}(1) = 2.50G, a = 1.6$

5CB + 4.0wt% Laponite

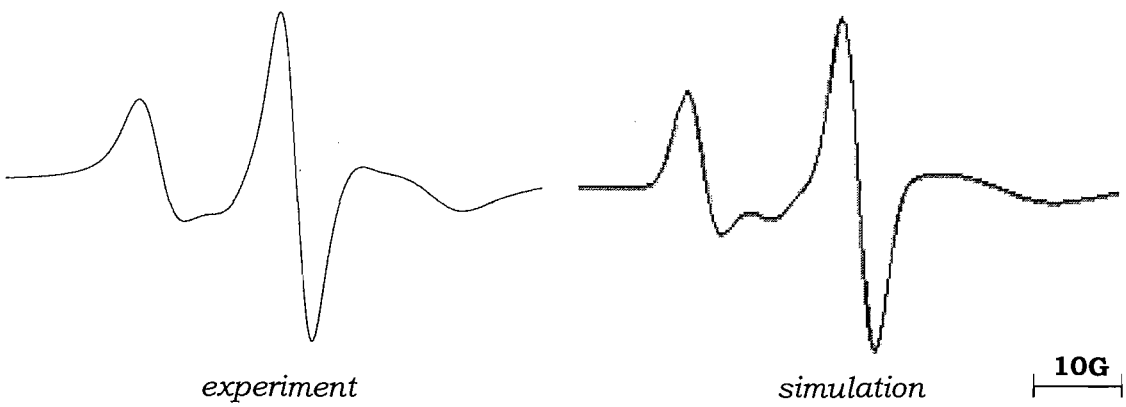

experiment *simulation*

$\widetilde{A}_{\parallel} = 8.20G, \widetilde{A}_{\perp} = 16.10G, T_2^{-1}(-1) = 1.50G, T_2^{-1}(0) = 1.60G, T_2^{-1}(0) = 5.0G, a = 1.1$

5CB + 1.0wt% Sepiolite

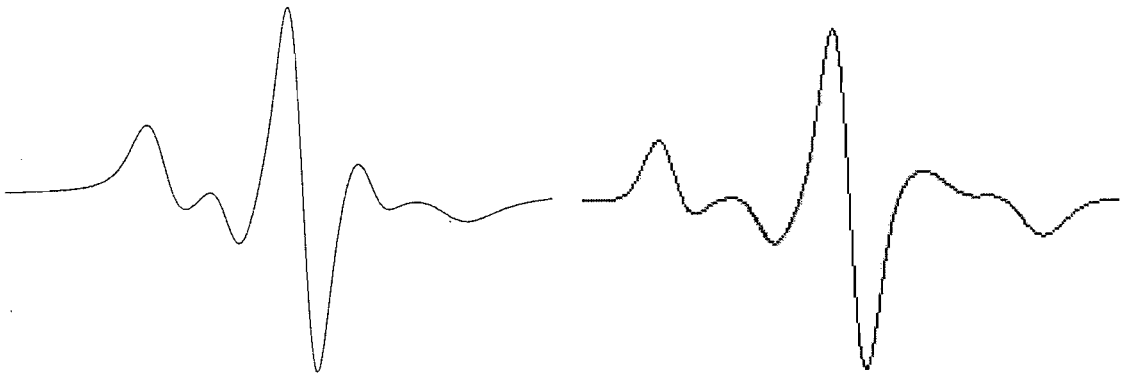

experiment *simulation*

$\tilde{A}_{\parallel} = 7.20G, \tilde{A}_{\perp} = 17.10G, T_2^{-1}(-1) = 1.50G, T_2^{-1}(0) = 1.60G, T_2^{-1}(1) = 2.20G, a = 1.8$

MBBA + 1.0wt% Claytone

experiment *simulation*

$\tilde{A}_{\parallel} = 8.44G, \tilde{A}_{\perp} = 18.34G, T_2^{-1}(-1) = 2.00G, T_2^{-1}(0) = 1.55G, T_2^{-1}(1) = 1.90G, a = 4.0$

Figure 21: The experimental ESR spectra for different systems with the associated simulation and the parameters used to simulate them.

Spectral simulations which attempt to mimic the real ESR spectrum give the information that is hard to determine by a direct measurement from the ESR spectra. We have now seen how a affects the orientational order of the director via the form of the ESR powder patterns spectra. In addition it is related to the director distribution function. It is also a factor that controls the linewidth and the lineshape of the spectral lines. The parameter a which controls the distribution function is unity for a random distribution, and infinity for a perfectly ordered director. The extent of the director orientational order is reflected by the director order parameter, $\overline{P}_2^d$; this is clearly related to the distribution function by

$$\overline{P}_2^d = \int P_2(\cos\theta) f_d(\theta) d\theta. \qquad (4.10)$$

However as we have seen in Chapter II with this particular form of the distribution function there is an analytical form for the order parameter. Figure 22 shows a series of plots for the director distribution function, for each sample that we have examined, including the a values and also the second rank director orientational order parameter, $\overline{P}_2^d$. For each plot, the x-axis represents of $\cos\theta$, so that $x = 1$ corresponds to the director parallel to the field while y-axis represents the magnitude of probability for director being at an angle of θ to the field to be seen.

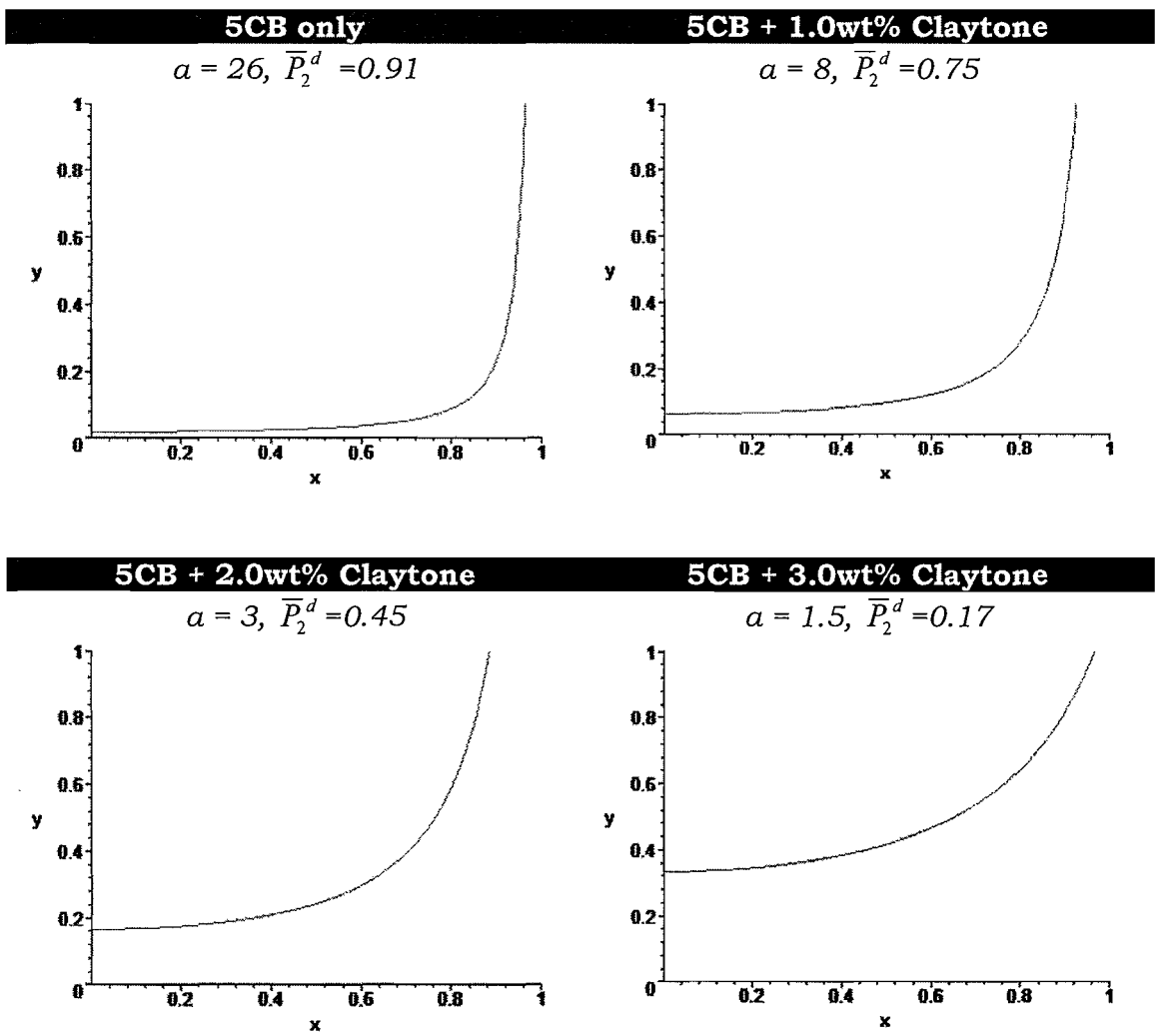

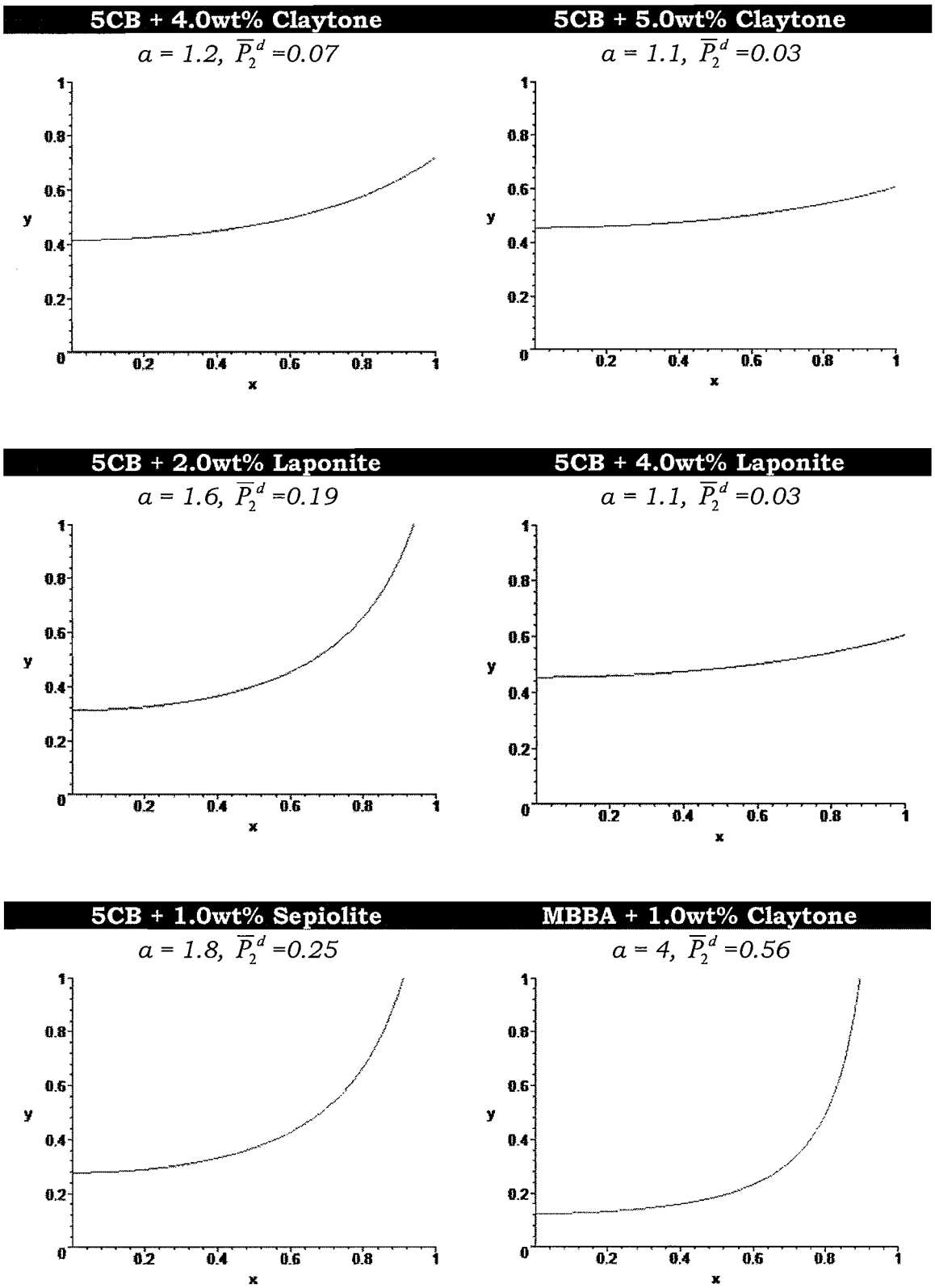

Figure 22: *The director orientational distribution function for different values of a together with the second rank director order parameter, $\overline{P}_2^d$. x-axis represents $\cos\theta$, while y-axis represents $f(\theta)$.*

The value of a provides a measure of the ordering or disordering of the nematic director in our samples. The relationship between the value of a and the second rank director order parameter, $\overline{P}_2^d$ gives us the director ordering. The relationship is shown graphically in Figure 23 where the director order parameter is plotted against the parameter a. We can see that as a increases from the limiting value of unity so the director order parameter grows rapidly from its limiting value of zero until it reaches a value of about 0.7 and then it grows far less rapidly towards its limiting value of unity as a increases.

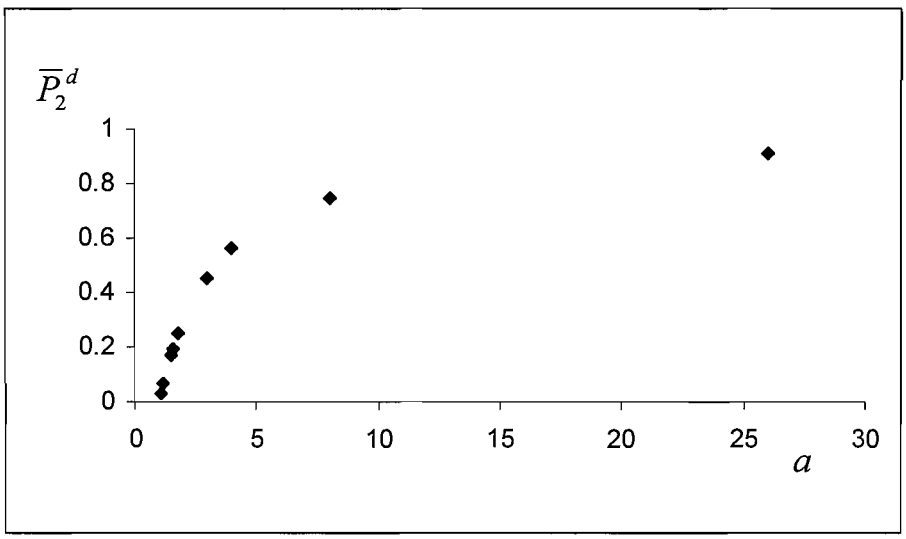

Figure 23: Plot of second rank director order parameter, $\overline{P}_2^d$ versus the a value from the distribution function.

We have found that the liquid crystal director is highly ordered by the magnetic field for a sample with no clay particles or the smallest concentration of clay in the nematic host. That is the director distribution function is highly peaked as x tends to unity; however, it might have been expected that the director order would have been perfect with an order parameter of 1.00 rather than the value that is found of 0.91. It is possible that the difference is caused by factors, other than the director distribution, produce similar spectral changes. Figure 24 shows the plot giving the variation of $\overline{P}_2^d$ with the changing the clay particle concentration in the nematic sample for Claytone in 5CB at room temperature. It is seen that as the concentration of Claytone grows so the director order parameter tends, almost linearly, to its limiting value of zero when the director is randomly

distributed even though there is a weak magnetic field. This limit is reached when the concentration of Claytone is between 4.0 and 5.0wt%.

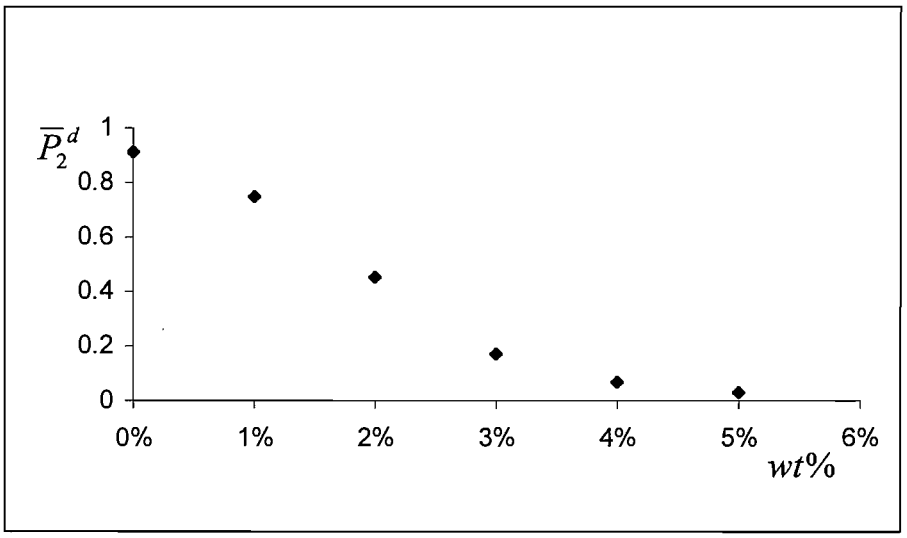

Figure 24: The dependence of the director order parameter, $\overline{P}_2^d$, on the Claytone concentration in nematic 5CB at room temperature.

4.6.2 Dynamic Experiments for Colloidal Nematic Sample

It is of interest to study the influence of the colloidal particles on the director dynamics induced by the magnetic field of the ESR spectrometer. To do this we have applied the method developed by *Becker* et al. of using ESR spectroscopy to monitor the director orientation as a function of time following rotation of the sample with respect to the magnetic field [25]. The sample chosen for this investigation is that with the smallest concentration of clay particles, as high concentration of clays made the sample quite viscous, hard to handle with and probably hard to show any dynamics in the director alignment. The experiment involves rotation of the sample in the magnetic field using a rotary solenoid, while the ESR measurement is performed to determine the director alignment essentially before and after the rotation of the sample. The interesting information that could be observed from this experiment was the time-dependence of the field-scanned ESR spectrum which allows the determination of the director orientation with respect to the magnetic field at certain times during the scan. However, this experiment requires the uniform alignment of the director and so, as we have

indicated, it was only applicable for liquid crystal samples with low clay concentrations.

In this ESR measurement, the parameters that were considered are the *sweep time* (ST) which is the time taken to acquire a complete spectrum and the *pulse time* (PT) which is the time at which the sample is rotated after the scanning process has started. These two parameters are interrelated and we could determine from the ESR spectrum at what point the sample actually starts to rotate. This experiment is related to the studies for the determination of the field-induced alignment of the director to explore the rotational viscosity coefficient of nematics. The dynamic behaviour predicted by continuum theory for this experiment can be obtained by solving the torque-balance equation for the director orientation. This involves a balance of the magnetic and viscous torques and the solution to the resultant differential equation is

$$\tan\theta(t) = \tan\theta_0 \exp\left(\frac{-t}{\tau}\right). \tag{4.11}$$

Here θ_0 denotes $\theta(t=0)$, which is the initial director orientation with respect to the magnetic field and τ is the field-induced relaxation time

$$\tau = \frac{\mu_0 \gamma_1}{\Delta\tilde{\chi} B^2}, \tag{4.12}$$

where γ_1 is the rotational viscosity coefficient.

From a single dynamic spectrum that is one recorded while the field is being scanned, we can determine the information shown in Figure 25. This ESR spectrum is compared to the static ESR spectrum which is the ESR spectrum recorded just before the sample was rotated and gives the parallel component of the hyperfine tensor which together with the isotropic coupling allows the perpendicular component to be determined. This and the data in the dynamic spectrum (x_1, x_2, t_1 *and* t_2) can measure the relaxation time of the

liquid crystal sample. We shall discuss this determination shortly but first we consider how the experiment was performed.

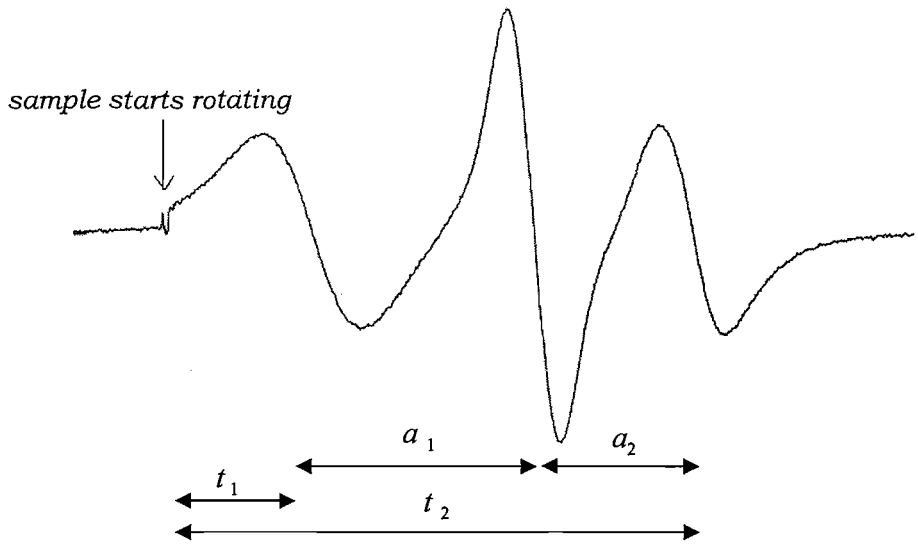

Figure 25: Basic data from a single dynamic ESR spectrum.

We considered two ways of generating the initial non-equilibrium state with the director at an angle to the field following the director rotation after it was aligned parallel to the magnetic field. A rotary solenoid (giving rotation of either 45° or 90°) rotates the sample tube following a trigger pulse (the director rotates as well as the tube because of the interaction of the nematic with the surface) and the ESR spectrum is recorded to measure the director orientation as a function of time. There is a major difference between the director alignment from an initial orientation of 45° or 90°. With the initial 90° state the director can return to being parallel to the magnetic field by rotating either clock-wise or anti clock-wise, as shown in Figure 26.

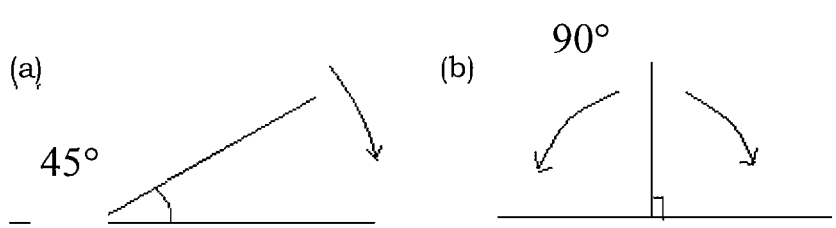

Figure 26: The directions of director alignment for (a) the 45° and (b) the 90° rotation experiment.

The rotation in both directions causes the director to be disordered and so not to align as a monodomain; in contrast for the 45° rotation the director realignment does proceed as a monodomain. We can use equation (4.11), for the determination of the relaxation times for the director; time t_1 corresponds to the position of the low-field peak

$$\tan\theta_1 = \tan\theta_0 \exp\left(\frac{-t_1}{\tau}\right) \tag{4.13}$$

and at t_2 for the position of the high-field peak,

$$\tan\theta_2 = \tan\theta_0 \exp\left(\frac{-t_2}{\tau}\right). \tag{4.14}$$

Equation (4.13) divided by equation (4.14) gives,

$$\left(\frac{\tan\theta_1}{\tan\theta_2}\right) = \exp\left(\frac{-(t_1 - t_2)}{\tau}\right), \tag{4.15}$$

which can be rearranged to give

$$\tau = \frac{-(t_1 - t_2)}{\ln\tan\theta_2 - \ln\tan\theta_1}. \tag{4.16}$$

To determine the director relaxation time, τ , we need to know θ_1 and θ_2 from the experiment

$$\tan\theta_1 = \left(\frac{a_1^2 - \tilde{A}_{\|}^2}{\tilde{A}_{\perp}^2 - a_1^2}\right)^{\frac{1}{2}}, \tag{4.17}$$

and

$$\tan\theta_2 = \left(\frac{a_2^2 - \tilde{A}_{\parallel}^2}{\tilde{A}_{\perp}^2 - a_2^2}\right)^{\frac{1}{2}}. \tag{4.18}$$

This can be written in terms of the experimental two hyperfine splittings, a_1 and a_2; rearrangement of the equation then gives the relaxation time as

$$\tau = \frac{2(a_1 + a_2)}{b \ln\left[\frac{(a_1^2 - \tilde{A}_{\parallel}^2)(\tilde{A}_{\perp}^2 - a_2^2)}{(\tilde{A}_{\perp}^2 - a_1^2)(a_2^2 - \tilde{A}_{\parallel}^2)}\right]}, \tag{4.19}$$

where b is the rate at which the field is scanned. Here the difference in the two times has been replaced by the field separation between the two peaks divided by the scan rate. Figure 27 shows a sketch of θ is changes with time as the director is being pulled back parallel to the magnetic field. θ_1 and θ_2 are the angles at times t_1 and t_2. The difference of these two points can be used to determine the relaxation time of the director.

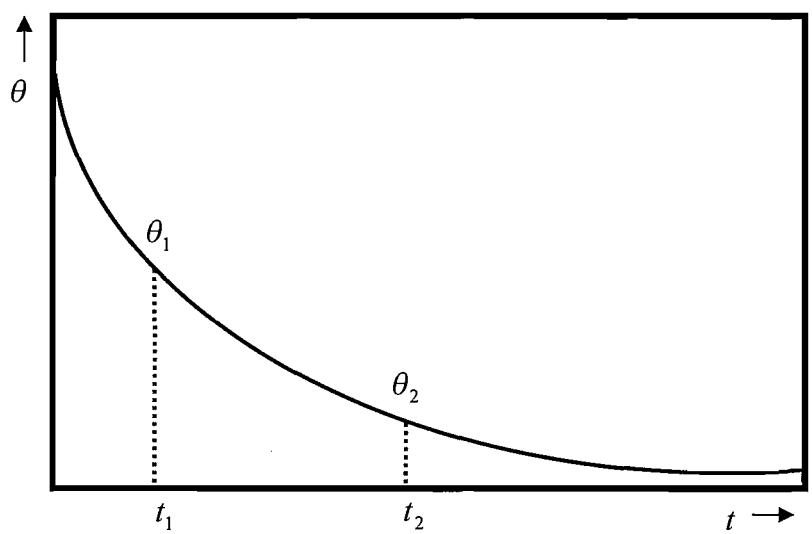

Figure 27: Director orientation starts at 45° (after rotation) and is pulled back to be parallel to the field.

We found the best sweep time to measure the field-induced director dynamics for nematic 5CB was 5.12s while the pulse time was 0.46s. The rotation angles also influence the observed results which are optimal if the

director has only just started to realign at t_1 after sample rotation and is not quite aligned, at t_2, parallel to the magnetic field. The results for this experiment are shown in Figure 28, as both the spectra, the parameters determined from them and the field-induced director relaxation time determined from these parameters.

5CB

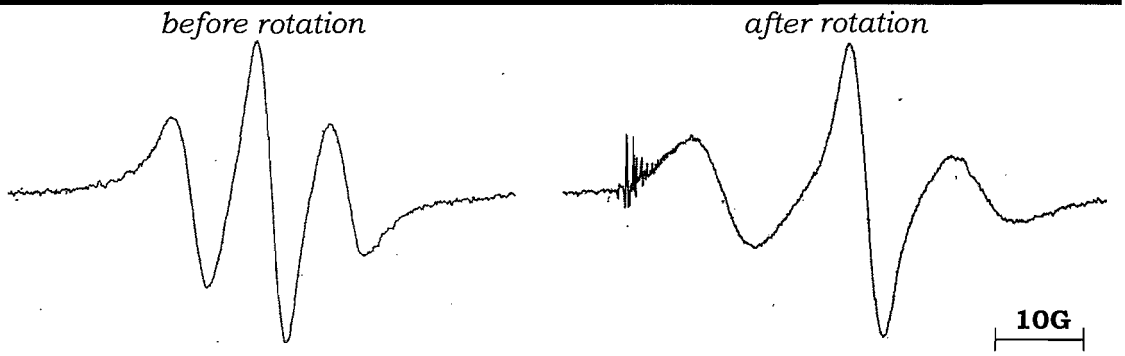

$\tilde{A}_{\parallel}/G$	$\tilde{A}_{\perp}/G$	a_1/G	a_2/G	ST/s	$\theta_1/^{o}$	$\theta_2/^{o}$	τ/s
9.13	17.34	13.40	9.80	1.31	41.7	13.9	0.48

This experiment was carried out with a 45° rotation.

5CB + 1.0wt% Claytone

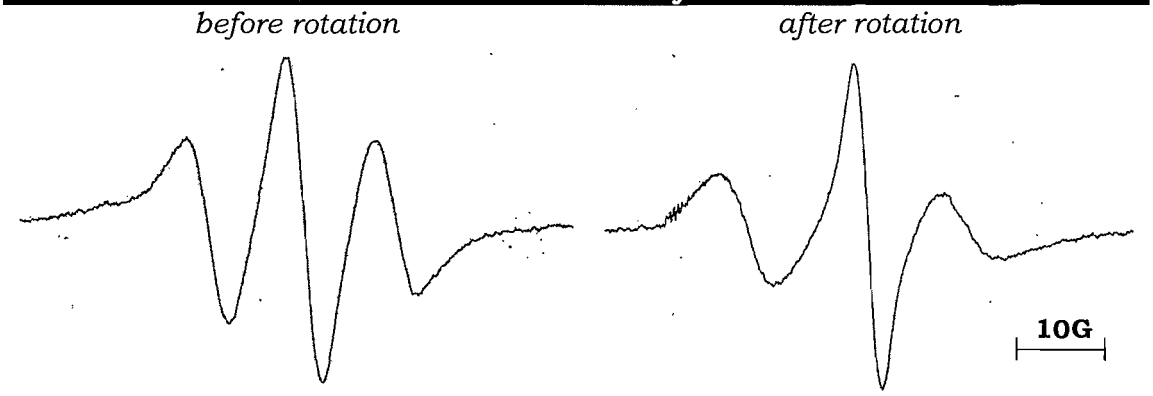

$\tilde{A}_{\parallel}/G$	$\tilde{A}_{\perp}/G$	a_1/G	a_2/G	ST/s	$\theta_1/^{o}$	$\theta_2/^{o}$	τ/s
8.59	17.60	12.60	9.82	1.31	36.8	18.0	0.70

This experiment was carried out with a 45° rotation.

5CB + 2.0wt% Laponite

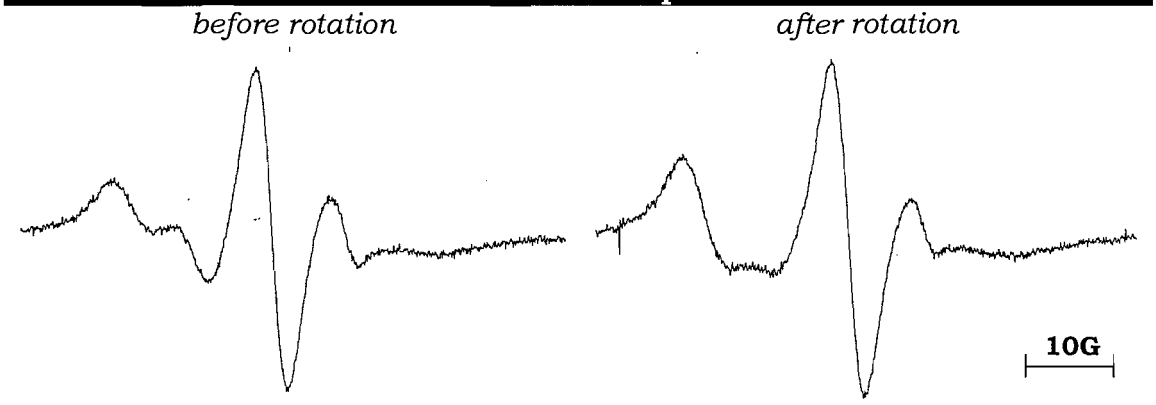

$\tilde{A}_{\parallel}/G$	$\tilde{A}_{\perp}/G$	a_1/G	a_2/G	ST/s	$\theta_1/^{o}$	$\theta_2/^{o}$	τ/s
8.10	18.20	15.96	8.90	5.24	81.2	14.4	0.81

This experiment was carried out with a 90° rotation.

5CB + 1.0wt% Sepiolite

$\tilde{A}_{\parallel}/G$	$\tilde{A}_{\perp}/G$	a_1/G	a_2/G	ST/s	$\theta_1/^{o}$	$\theta_2/^{o}$	τ/s
7.80	19.18	16.57	9.21	5.24	74.2	21.7	1.24

This experiment was carried out with a 90° rotation.

MBBA + 1.0wt% Claytone

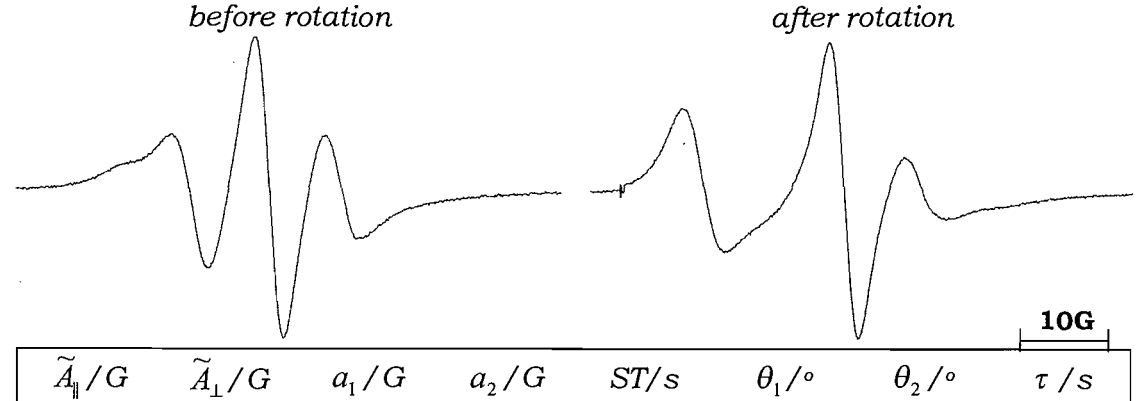

$\tilde{A}_{\parallel}/G$	$\tilde{A}_{\perp}/G$	a_1/G	a_2/G	ST/s	$\theta_1/^{o}$	$\theta_2/^{o}$	τ/s
8.40	18.13	16.27	9.21	5.24	58.6	13.1	1.37

This experiment was carried out with a 90° rotation.

Figure 28: The dynamic ESR spectra for the colloidal nematics.

The director dynamic experiments have been performed under a wide variety of conditions different nematic hosts, colloidal clays and rotation angles; it is not surprising that a rich variety of behaviour is observed. The simplest experiment involves low clay concentrations and a rotation angle of 45°. Thus the spectra in Figure 28 for pure 5CB and 5CB doped with 1.0wt% of Claytone shown initial spectrum containing essentially three lines with equal spacings between them corresponding to the director parallel to the magnetic field. Then after rotation through 45° the spectrum still contains three lines but they are no longer equally spaced corresponding to the director being aligned at different angles to the field at different times. From these spacings and times, we estimate the field-induced relaxation time for pure 5CB to be 0.48s and for Claytone-doped 5CB it has increased slightly to 0.70s. It seems reasonable that the field-induced relaxation time has increased with addition of Claytone. In a second series of experiments, the rotation angle was increased to 90° and different systems were studied. For MBBA with 1.0wt% Claytone, the initial spectrum approximates to three hyperfine lines indicating that the director is largely parallel to the magnetic field. After rotation through 90° the spectrum still contains three but not equally spaced, corresponding to the different director orientations. The fact that the lines are relatively sharp shows that the director has remained uniformly aligned during its rotation. The field-induced relaxation time calculated from our results is 1.37s which is larger than for 5CB in keeping with the larger rotational viscosity for MBBA. The initial spectrum for the other two systems, with 1.0wt% Laponite and Sepiolite, contain five hyperfine lines showing quite clearly that surface forces from the clay particles have randomized the director. Under such conditions, it is not expected that the rotation experiment can give the field-induced relaxation times. However, the spectra after rotation are of interest as the initial line shows that the director is predominantly at 90° to the field. Two spectral lines observed at larger times showing that the director has returned to being partially disordered.

4.6.3 Nematic-Isotropic Transition Temperature

It is likely that the addition of the clay to the nematic will change its transitional properties and so to investigate this we have determined T_{NI} for a variety of samples. The nematic-isotropic transition temperature, T_{NI} was determined by two quite different methods; ESR spectroscopy and optical microscopy. We first started with ESR spectroscopy since this is the main characterization method used in our investigation. For ESR, we could see the changes in the ESR spectrum and hence the hyperfine spacing when the nematic changes its phase, but we are not able to measure the ESR spectra for very small and accurate temperature changes. This might be a weakness of ESR as the method for determining phase transition temperature. However, in this experiment, the microscopic method could confirm the results that we acquire from the ESR spectra. Undoubtedly, the microscopic method was actually much more accurate than ESR. This because of the high birefringence for the liquid crystals which results in an optical texture from which we could clearly observe the changes in the liquid crystal textures when its phase changes from nematic to isotropic. The combination of microscope and the heater in a single unit helps us to record accurately the transition temperature as we observe the phase changing.

Normally with ESR spectroscopy, for Cholestane spin probe in nematic liquid crystal with $\Delta\tilde{\chi} > 0$, the hyperfine spacing in the ESR spectrum is about 8.0 to 10.0G, depending on their order parameter which is determined by the temperature. For a nitroxide spin probe, when the phase changes to isotropic, the spacing becomes larger than the parallel component of the partially averaged hyperfine tensor, the scalar hyperfine splitting is about 15.0G. Even for a powder spectrum which contains five hyperfine lines, when it reaches the isotropic phase, then the hyperfine spacing is going to be about 15.0G but more significantly the number of hyperfine lines will decrease to three. The temperature when the isotropic phase starts to appear is recorded as T_{NI} and was determined when there was a drastic change in hyperfine spacing using the plots such as those shown in Figure 29. While Figure 30 shows the ESR spectra for 5CB with 1.0wt% Claytone as the sample was heated into the isotropic phase.

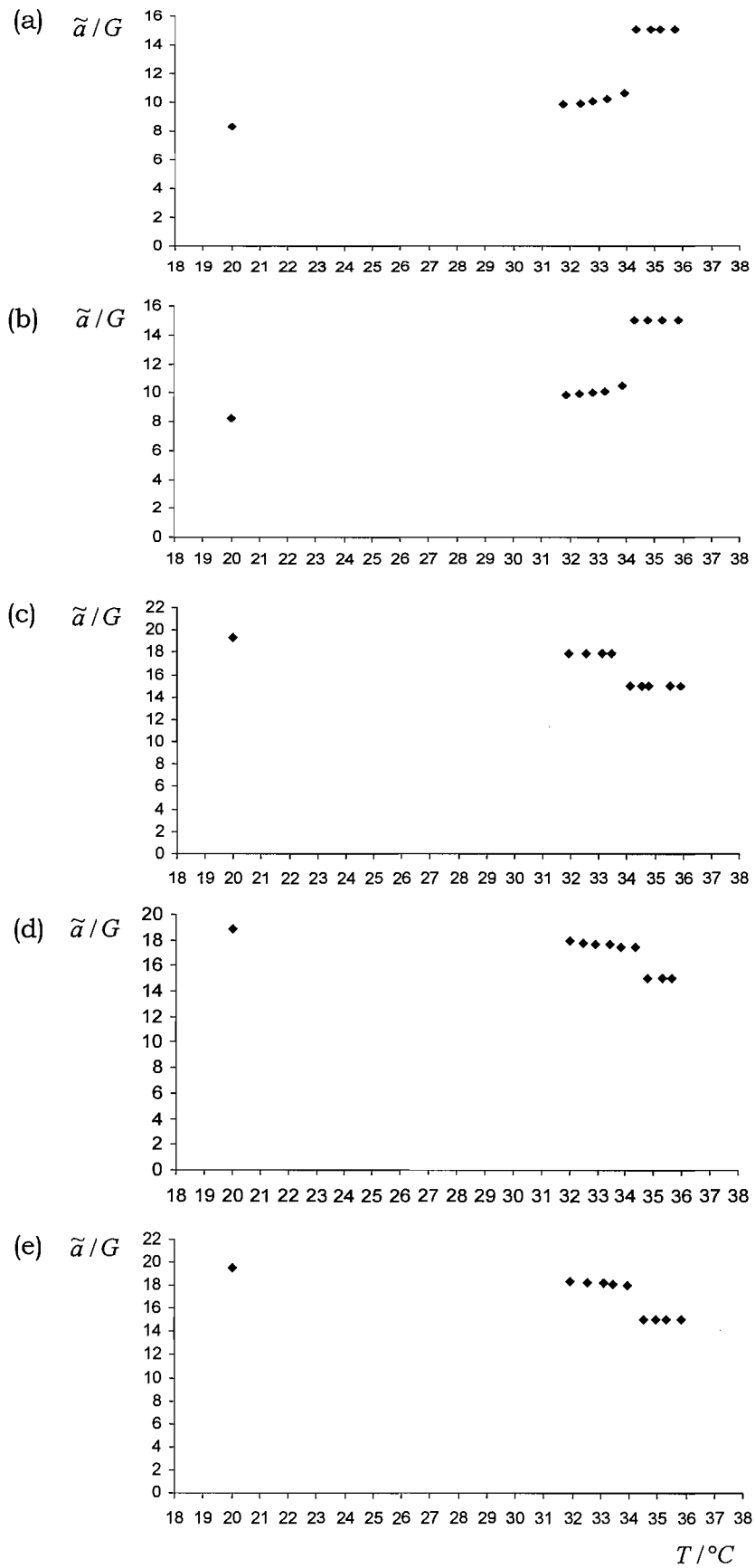

Figure 29: The results for the determination of T_{NI} using ESR method for (a) 0wt%, (b) 1.0wt%, (c) 2.0wt%, (d) 3.0wt%, (e) 4.0wt% of Claytone concentrations in nematic 5CB.

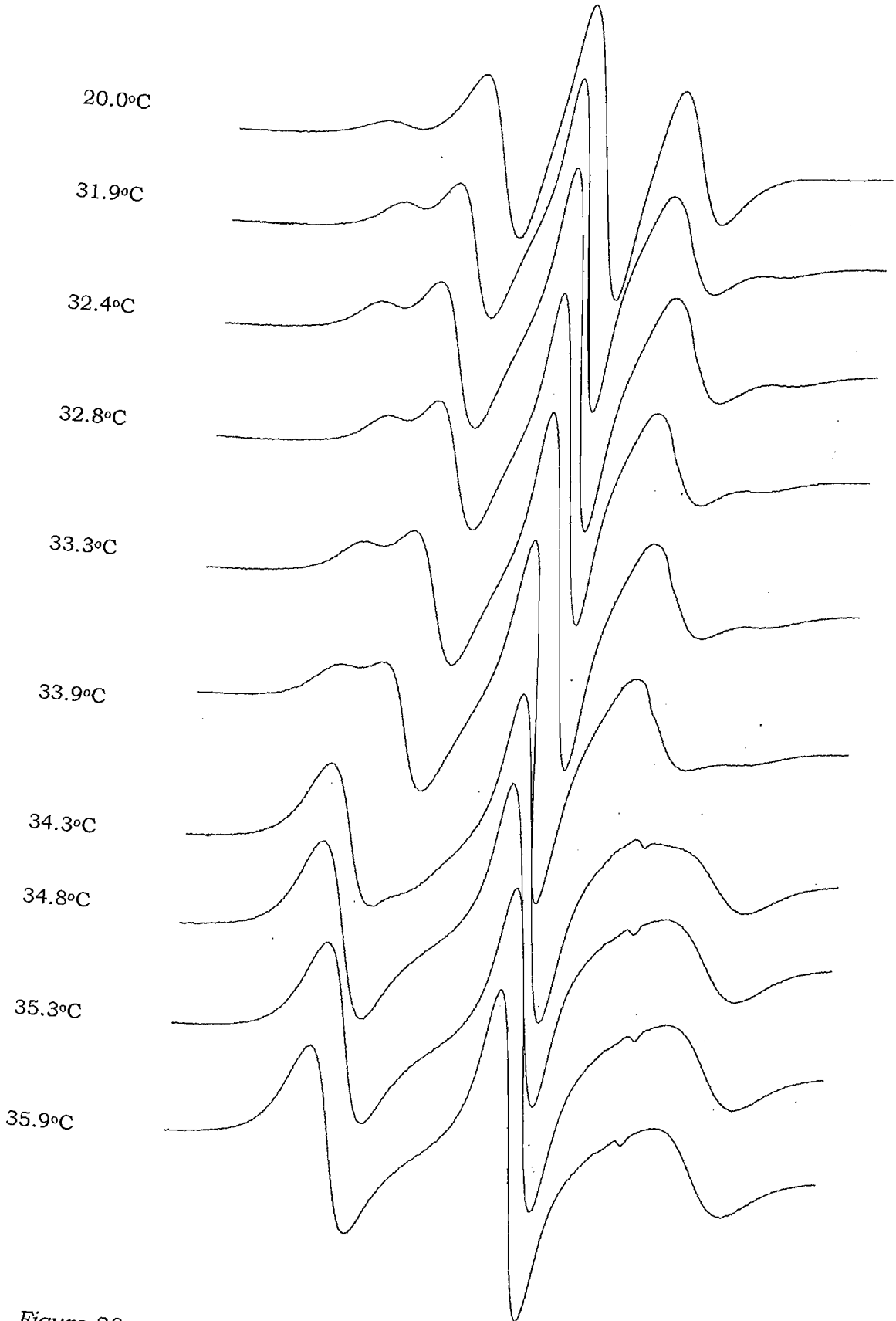

Figure 30: *The ESR spectra as a function of temperature for 1.0wt% Claytone in 5CB.*

As we have mentioned, the optical microscopy method is potentially more convenient and accurate to determine T_{NI}, as well as being less expensive. The temperature controller was attached to the microscope and we could determine the T_{NI} by recording the temperature when there is a change in the optical textures, some of which are dramatic. These can be clearly seen under the microscope. In the nematic phase, the image is coloured (this is caused by the birefringence of the liquid crystal for pure 5CB) and also some dispersed points of colloids (caused by the colloidal particles). Once the sample has become isotropic, then the image becomes black (except when Claytone produces optical defects resulting from the aggregation of the clay). The images of the microscopic textures observed under the optical microscope with crossed polarizers are shown in Figure 31.

Temp. /°C	20.7	33.4	34.5
5CB			

Temp. /°C	23.3	34.0	34.5
5CB + 1.0wt% Claytone	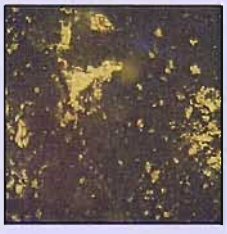		

Temp. /°C	20.7	33.4	34.3
5CB + 2.0wt% Claytone	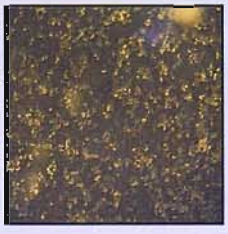		

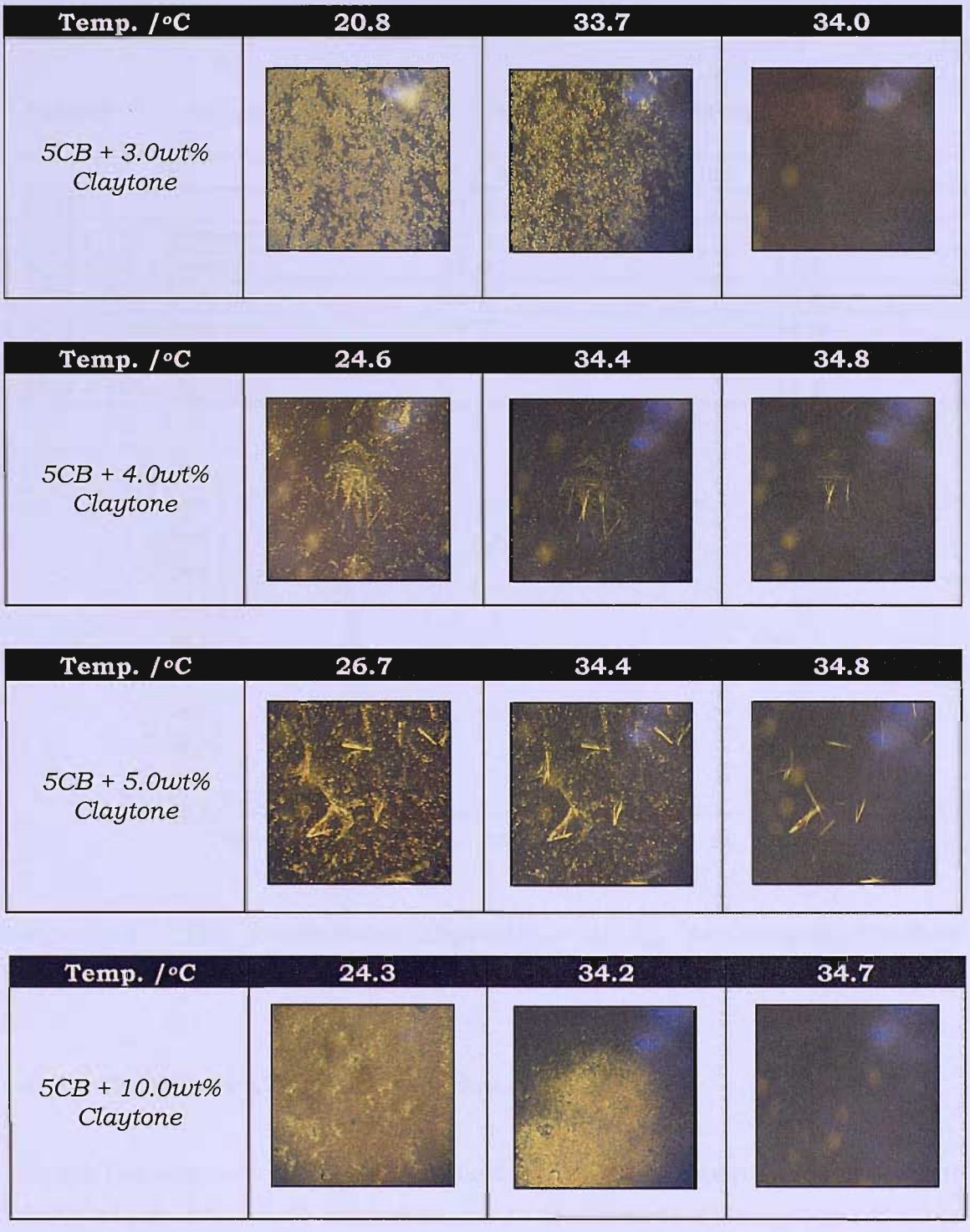

Figure 31: Optical textures of colloidal nematic (5CB + Claytone) under an optical microscope at different temperatures.

We have compared the T_{NI} results obtained using ESR spectroscopy and optical microscopy in Table 2, and the T_{NI} plot for the different concentrations is shown in Figure 32. The sample of 5CB with 3.0wt%

Claytone shows a small difference to the other T_{NI} as we expected the sample was not pure at the time we used it.

Table 2: T_{NI} value of colloidal nematics using different method.

	ESR / °C	Optical Microscope / °C
5CB	34.2	34.3
5CB + 1% Claytone	34.5	34.4
5CB + 2% Claytone	34.6	34.5
5CB + 3% Claytone	33.8	33.8
5CB + 4% Claytone	34.2	34.4
5CB + 5% Claytone	34.5	34.5
5CB + 10% Claytone	-	34.2

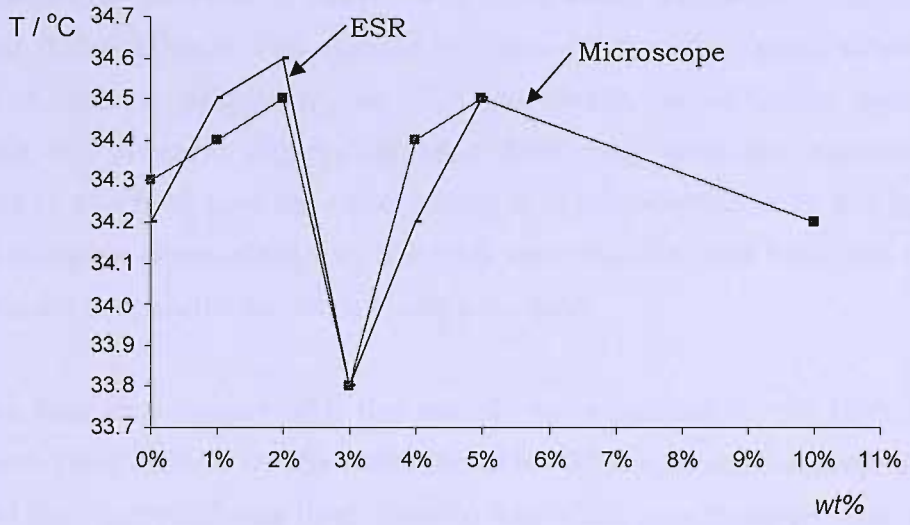

Figure 32: The concentration dependence of T_{NI} for samples Claytone dispersed in 5CB.

4.6.4 High-Field Alignment Experiment

So far the magnetic field strength used in all of our experiments was about 0.3T, which is the field needed to record the X-band ESR spectra. Also we have seen so far the director that for colloidal nematic samples with the smallest concentration of clay could align well, but not when the clay concentration is higher than maybe 4.0wt%. It produces a random director distribution as we have already mentioned in Section 4.6.3.

In this Section, we use a higher strength magnetic field to align the director of the colloidal samples. The greater magnetic torque would align the nematic director into a monodomain or uniform state, with the ability to exceed the surface and elastic forces that result from the interaction of the nematic with the surface of the colloid. To do this, we shall use the magnetic field of a 300MHz Varian NMR spectrometer which is about 7.05T and we shall refer to this as high-field. It is used in combination with ESR spectroscopy, after the sample is aligned by the high-field for about 20min, it is then removed from the NMR spectrometer and placed into the ESR spectrometer to measure the ESR spectrum which will provide information on the director distribution. We chose the most viscous sample, namely a colloidal nematic with a high concentration, 5.0wt%, of Claytone in 5CB since we clearly seen a random director distribution in this sample. In these studies, we expect to see the two types of director alignment, so that we create two different methods for aligning the nematic director at high field. One with the sample tube is parallel to the field and the other when it is perpendicular to the high field. These samples when placed in the ESR spectrometer will have the tube axis necessarily perpendicular to the magnetic field.

For the first experiment with the sample tube parallel to the high field, the tube was held vertical by the NMR probe for 20min in the magnetic field. The aligned liquid crystal was then studied with ESR spectroscopy just after that within about 3min which is the minimum time to transfer the sample between the spectrometers. The orientation of the magnetic field of the NMR is parallel to the ESR tube and so, we should observe perpendicular director signal for the ESR spectra, since the ESR magnetic field orientation is perpendicular to the axis of the ESR tube. This is shown schematically in Figure 33.

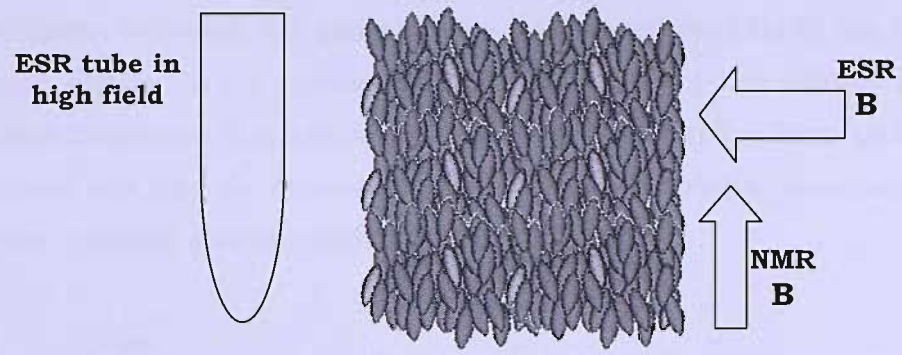

Figure 33: ESR tube was placed vertically in both spectrometers the director is initially parallel to the high NMR field and so perpendicular to the ESR field.

Then for the second case, the sample tube is perpendicular to the NMR magnetic field. First, the ESR tube with sample inside it has to be cut to a length of 3cm; this has to be done because the NMR probe is not wide enough to take a longer ESR tube perpendicular to the high field. The tube was again kept in the NMR probe for 20min. Finally, this short ESR tube was placed into an NMR tube just before the ESR measurement. In this case, the ESR tube was perpendicular to the high field, so the director will be parallel to the ESR field (see Figure 34). This allows us to measure the angle dependence of liquid crystal alignment and goniometer was used to perform the experiment. The ESR tube is marked on its surface upon alignment at high NMR field, so that we could determine the director orientation as the tube is move to the ESR spectrometer.

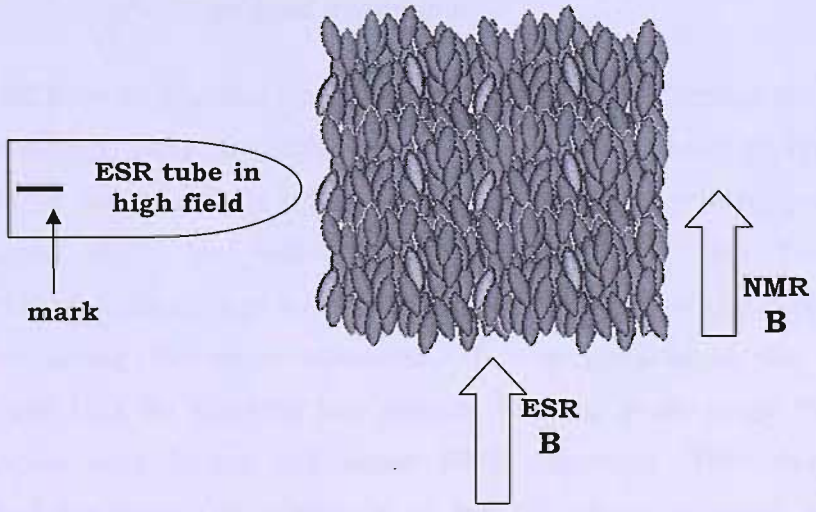

Figure 34: The ESR tube was placed vertically and the director is aligned parallel to the high field and so parallel to the ESR field.

Here we discuss the results from these experiments. We start with the experiment in which the sample tube was placed parallel to the high field for 20min. Figure 35 (a) shows the ESR spectrum for the sample of 5CB with 5.0wt% Claytone. This spectrum contains five hyperfine lines but the parallel features are not so obvious, which represent peaks associated with the director parallel and perpendicular to the field.

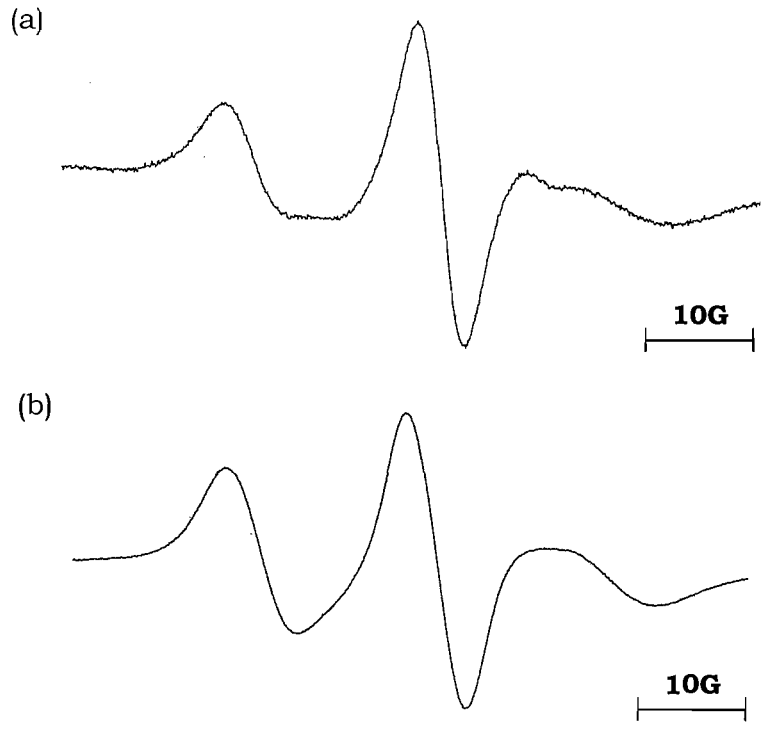

Figure 35: *(a) ESR spectrum for Cholestane in 5CB with 5.0wt% Claytone before high field alignment.*
(b) ESR spectrum for Cholestane in 5CB with 5.0wt% Claytone after high field alignment.

We shall now look at the spectrum in Figure 35 (b). This is the ESR spectrum measured just after the high field alignment of the director. The liquid crystal director is now partially aligned as seen from the relatively intense signals associated with the director perpendicular to the ESR field. This perpendicular alignment looks almost perfect as all of the director is actually oriented along the same direction, that is parallel to the tube axis. We confirmed this by rotating the sample tube to some angle from its original orientation and found the same ESR spectrum. This might have been expected because the distribution for the director must be cylindrically symmetric about the tube axis which was the direction of alignment for the high magnetic field.

It is also of interest that the sample is able to retain its alignment for a quite long time after removal from the high field. This happened to the sample that we aligned in the high field and this preserved alignment is also known as a memory effect. This sample of the colloidal nematic seems to have the ability to keep the alignment (in our case, 3 days) and this memory is a very good property for liquid crystal display devices. Figure 36 shows a series of ESR spectra recorded at different times but still showing the same form for the ESR spectra which represents the same director distribution. The spectra have not changed even after four hours which indicates a relatively long memory.

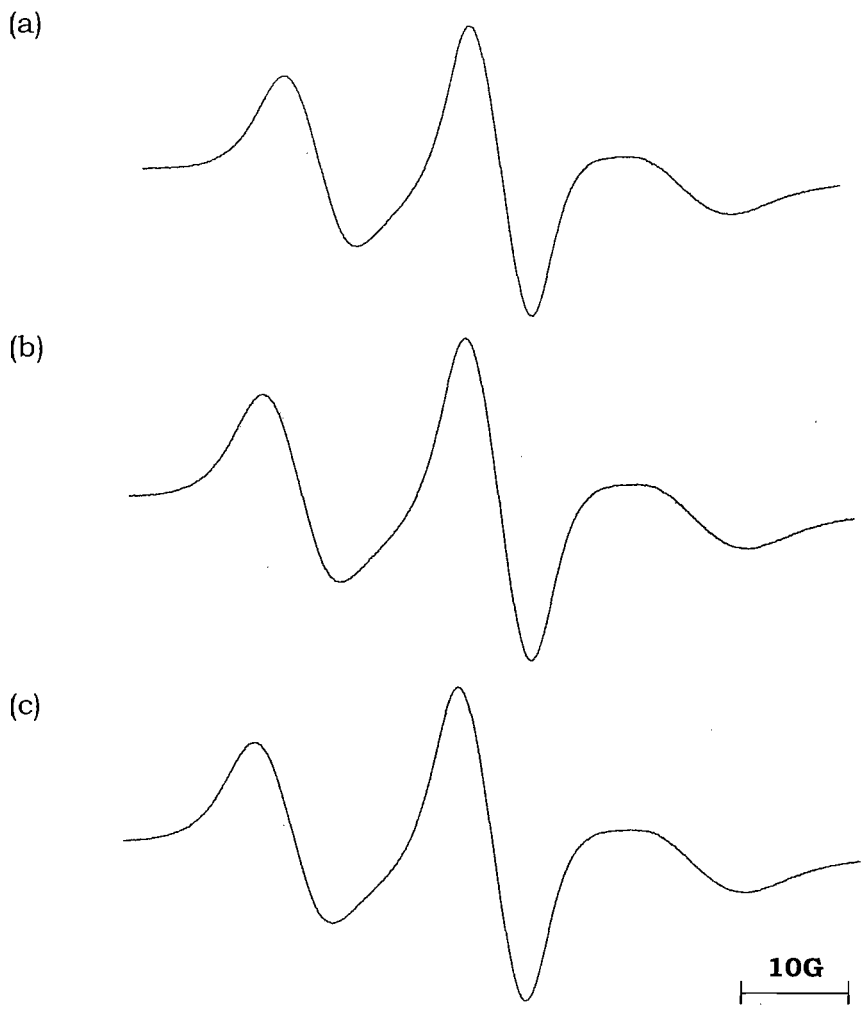

Figure 36: *(a) ESR spectrum for Cholestane in 5CB with 5.0wt% Claytone recorded 0.17h after high-field alignment.*
(b) ESR spectrum for Cholestane in 5CB with 5.0wt% Claytone recorded 1.35h after high-field alignment.
(c) ESR spectrum for Cholestane in 5CB with 5.0wt% Claytone recorded 4.02h after high-field alignment.

We expected to see analogous results for the second experiment, in which the ESR tube is held horizontal in the high field, so that in the ESR measurements the director should be parallel to the field. Surprisingly, this did not happen since we observed almost the same spectra as in Figure 35 (b). The high field, should of course, have aligned the director perpendicular to the tube axis. The ESR results are shown in Figure 37 and show that the alignment by the high field has occurred but the director is clearly orthogonal to the field of the ESR spectrometer.

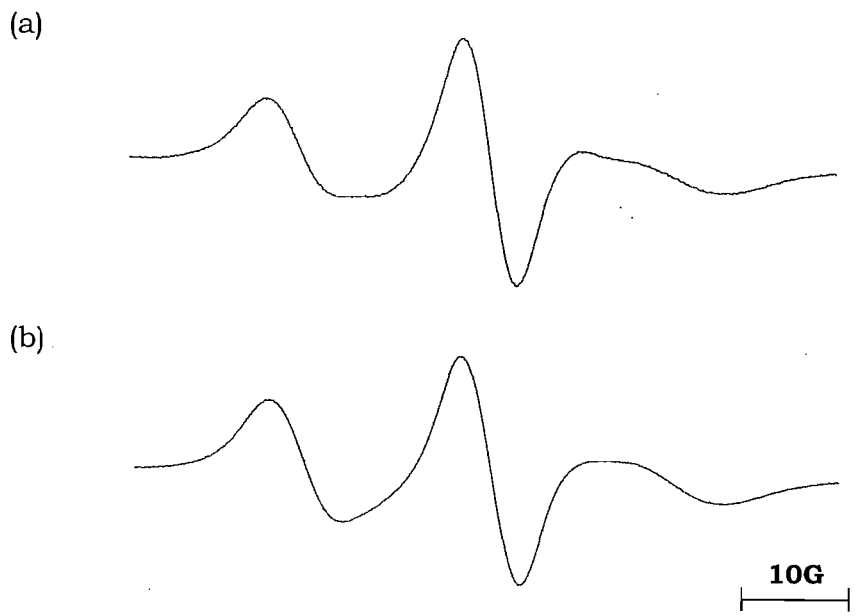

Figure 37: *(a) ESR spectrum for Cholestane in 5CB with 5.0wt% Claytone recorded before high field alignment.*
(b) ESR spectrum for Cholestane in 5CB with 5.0wt% Claytone recorded after high field alignment.

It is the best to simulate the ESR spectra that we observed to understand the changes in the spectra, before and after high field alignment. We shall now take an example of the ESR spectra in Figure 37 for the second experiment. The first ESR spectrum results from a random director distribution in which the parameter *a* takes, the value of unity. But the second spectrum should be simulated and its simulated spectrum is shown in Figure 38.

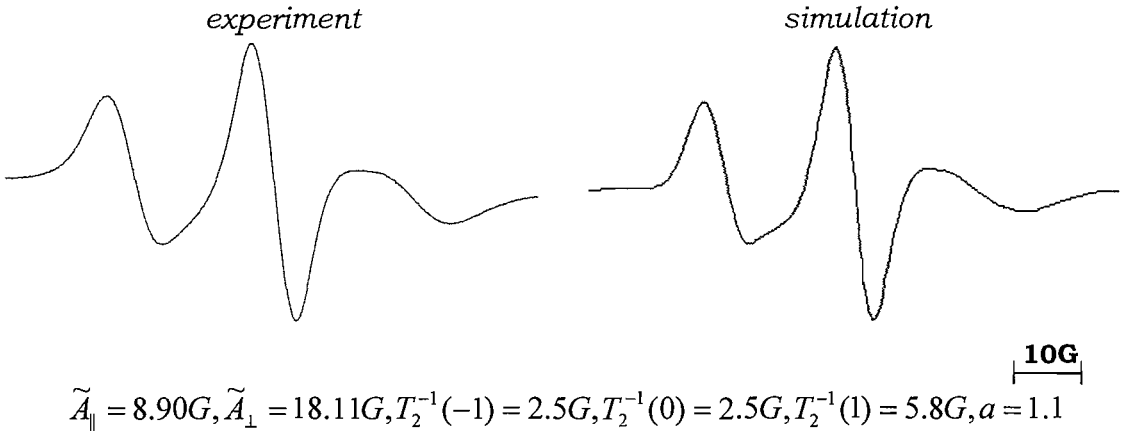

Figure 38: ESR spectrum for Cholestane in 5CB with 5.0wt% Claytone after high field alignment; the director should be parallel to the field, and its simulation.

The ESR spectra simulation for the spectrum recorded after high-field alignment used a value for a is 1.1. Bear in mind, before the alignment with the high magnetic field, the a value was 1, which means the director was randomly ordered. Therefore, we have found that the director orientation changes in this experiment and that the distribution was frozen in the magnetic field, which indicates that the clay particles are aligned. Before this, we know that the powder-like pattern ESR spectra was caused by the clay particles that made the director randomly ordered. But, after the high field alignment, we think that the clay particles are also aligned, when we could see the parallel signal is partially reduced, but the perpendicular signal has become more intense. This could be referring to Figure 38 for an example.

At this point, we have already know that the high-field of the NMR spectrometer could align the nematic director. The weaker ESR field could not align the director and we understand this because of the surfaces of the colloidal platelets which might have some degree of disorder. We found these colloidal nematics show analogous properties as smectic phases as it also has a memory effect and the alignment behaviour is interesting. The smectic does exhibit a memory effect because of its high viscosity, while for the colloidal nematics it was caused by the dispersal of large clay particles in the medium of a low viscosity nematic liquid crystal which increases the viscosity as seen by our dynamic experiments.

4.6.5 Isotropic at High-Field

We designed this experiment to study the possible alignment of the clay particles when the nematic was isotropic in the high field. This experiment was carried out for samples of 5CB with 5.0wt% and 10.0wt% Claytone. The experimental setup is as follows: the ESR tube was cut to a shorter piece of 3cm length, to make sure the ESR tube could be held horizontally into the NMR probe. The temperature in the NMR probe was set to 70° C, to keep the sample of 5CB well in the isotropic phase (n.b. its nematic-isotropic transition temperature is 35° C) and the sample was kept in the isotropic phase for 20min. Just after that, the sample tube then removed from magnetic while sample is still at the high temperature so that the sample does not return to nematic phase after the magnetic phase has fallen to zero. In this way, any director alignment must be due to the alignment of colloidal particles. The sample then was characterized with ESR spectrometer. Figure 39 shows the ESR spectra recorded for 5CB with 10.0wt% of Claytone. Surprisingly, there was no difference or change made between spectra (a) and (b). It shows the cooling step of the sample from isotropic phase in the high-field seems not to result in the alignment of the nematic director.

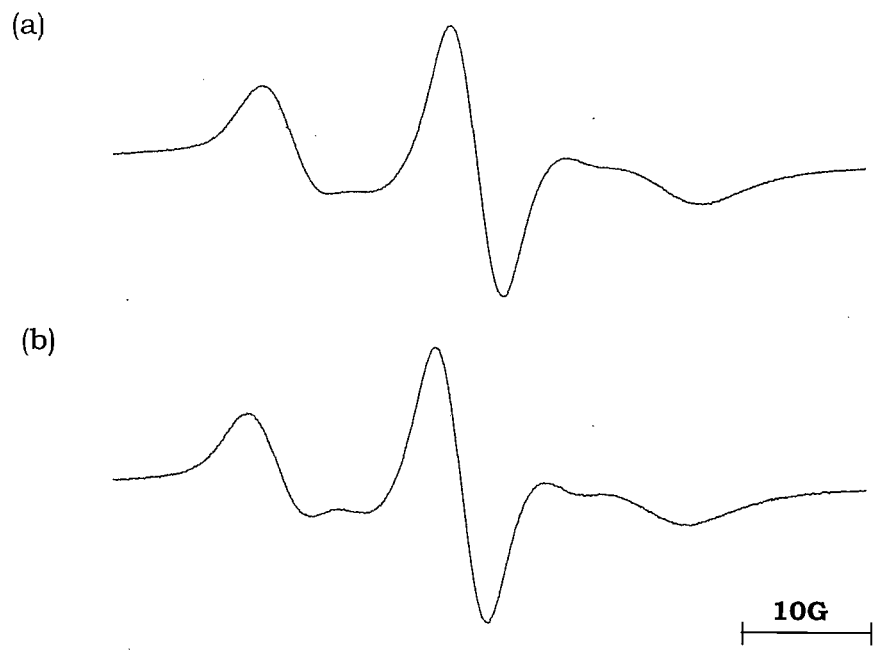

Figure 39: *(a) ESR spectrum for Cholestane in sample of 5CB with 10.0wt% Claytone recorded before being held in the isotropic phase at high field, (b) ESR spectrum for Cholestane in sample of 5CB with 10.0wt% Claytone recorded after being held in the isotropic phase at high field.*

The same results were found for sample 5CB with 5.0wt% Claytone. There was no change in the spectra recorded before and after high-field alignment, showing that the director of liquid crystal did not align after alignment of the colloidal particles in the isotropic at high field had been attempted. This emphasizes that it is actually the liquid crystal interaction with the clay particles that is responsible for their alignment. Figure 40 shows the ESR spectra for 5CB with 5.0wt% Claytone before and after alignment in the isotropic phase at high field.

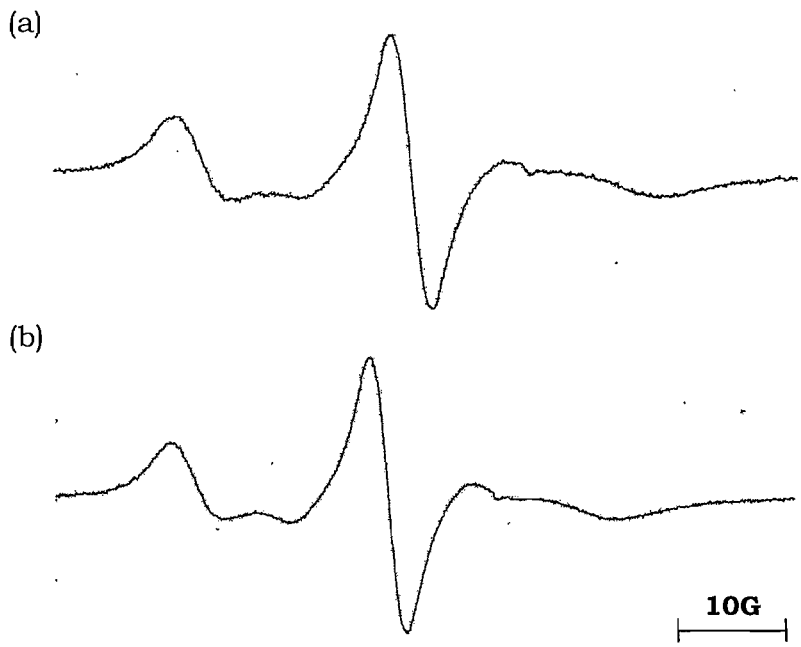

Figure 40: *(a) ESR spectrum for Cholestane in 5CB with 5.0wt% Claytone recorded before being held in the isotropic phase at high field. (b) ESR spectrum for Cholestane in 5CB with 5.0wt% Claytone recorded after being held in the isotropic phase at high field.*

4.6.6 Memory Effect: Discussion

We did describe the memory effect when we performed the ESR experiment for director alignment at high field. However, there is not much explanation that can be made to describe the condition, so we come out with a calculation on the clay particles alignment and motion in the sample to some extent could explain how the director could retain alignment for some long period of time without any disturbance of magnetic field or mechanical perturbation.

The effect implies that the time taken for a colloidal particle to rotate is long. Factors which influence this relaxation time are the size of the particle itself and the viscosity of the host. To see if this is sufficient to explain our results, we have estimated the rotational correlation time, τ_R, in the following way [26]. We start with the rotational diffusion coefficient, D_R, which according to theory is given by

$$D_R = 3k_BT/32\eta r^3, \tag{4.20}$$

for disc-shaped particle, and

$$D_R = k_BT/8\pi\eta r^3, \tag{4.21}$$

for a spherical object; here r is the radius of the clay particles and η is the viscosity of the solvent.

The relaxation time is related to the diffusion constant by

$$\tau_R = \frac{1}{6D_R}. \tag{4.22}$$

To estimate the rotational relaxation time for a colloid dispersed in a nematic host, we have used the following values for the various parameters

$$r = 1000\times10^{-9}\,m,$$

$$T = 298K.$$

$$k_BT = 1.3806\times10^{-23}\,J/K,$$

$$\eta = 0.03Pa.S,$$

These give τ_R, for the disc-shaped particle as 129s and for the spherical object, τ_R is 30s. As to be expected, the rotation of a sphere is faster than for the tumbling motion of the anisotropic disc. From our experimental results, for 5CB containing 5.0wt% Claytone, we found that the colloidal system keeps its alignment for at least three days.

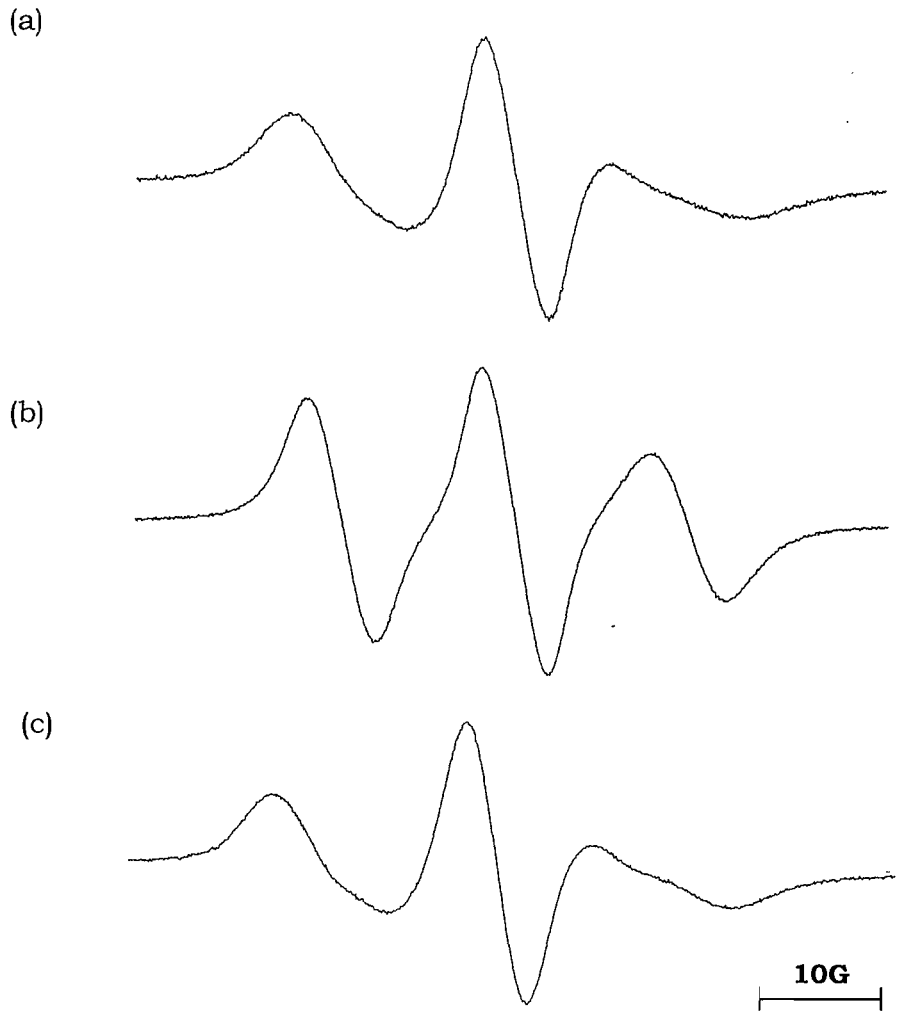

Figure 47 : *(a) ESR spectrum for Cholestane in 5CB with 5.0wt% Claytone after high field alignment; before the sample was heated - nematic.*
(b) ESR spectrum for Cholestane in 5CB with 5.0wt% Claytone after high field alignment; the sample was in the isotropic phase.
(c) ESR spectrum for Cholestane in 5CB with 5.0wt% Claytone after high field alignment; after the sample was cooled back into the nematic phase.

We measured the ESR spectrum for the same sample without any change to its position, and we have confirmed this result. However, this is in contrast to with the theoretical calculations we have made, which indicate that the clay

particle should take only 129s to make a complete rotation and so randomize the alignment of the particles and hence that of the nematic. If this motion did happen on this fast time scale, we would see a powder-like ESR spectrum in a very short time. In fact, there was no randomization of the sample when we heated the same sample after the high-field alignment, which had been aligned by the high-field to the isotropic phase, ~38° C and then cooled it back to the nematic. We measured the ESR spectrum both before and after the sample had been heated. The results, shown in Figure 47, indicate that heating and cooling the sample does not disturb the director alignment. This suggests that the orientational distribution for the colloidal particles has not changed on reforming the nematic.

One solution to this conflict between the observed and predicted relaxation time would be if one or more of the parameters used in the calculation were in error, for example larger values of the viscosity or the particle size would increase the relaxation time independently and that there is a network effect where locking of the particles increases the relaxation time significantly. However, the error would need to be enormous to explain the different between the observed and predicted relaxation times. It seems more likely therefore that the particles do not move.

4.6.7 Flow Alignment

Our collaborators from the University of Bristol had claimed that the clay particles could be aligned by flow forces, while the sample is being prepared. We wished to test this claim which in itself is not surprising because flowing a nematic can cause the director to be aligned.

There are several sensitive steps that need to be taken into consideration while performing this experiment. The colloidal nematic that is used for this experiment was that prepared for the ESR experiments with the sample in the ESR tube. The sample then is moved to a capillary tube with a narrower diameter. To fill the capillary, we have to make sure there were no air bubbles neither in the syringe nor in the needle. Then, the needle has to be placed at the bottom of the capillary tube. As the sample starts to fill the

capillary, the needle has to be brought up gradually so that it is just below the liquid level at all times because removing the needle from the sample might disturb the director. The sample was filled until the length of the sample is 1cm from the bottom of the capillary, with constant pressure on the syringe. Then, the needle is completely removed from the capillary tube. While performing this experiment, there will be no heating and the needle will not be reinserted into the capillary tube.

We have used a syringe to give a gentle flow to the sample in a capillary tube and ESR is used to characterize the director distribution in the sample. We used two types of capillary tube; one was a particular one used for the SAXS experiments (*tube 1*), and the other was a normal capillary tube (*tube 2*). Both tubes are differ in the diameter of the tubes; *tube 1* is larger than *tube 2*. In addition, *tube 1* was the one used for SAXS measurements while *tube 2* was a normal capillary tube. To perform an ESR measurement, the capillary was placed into an empty ESR tube and then in the microwave cavity of the ESR spectrometer. Figures 41 to 43 show the apparatus used in this experiment.

Figure 41: Syringe that was used to introduce the sample into the capillary tube. The size of needle can be important as it controls shear on nematic.

Figure 42: Picture of tube 1.

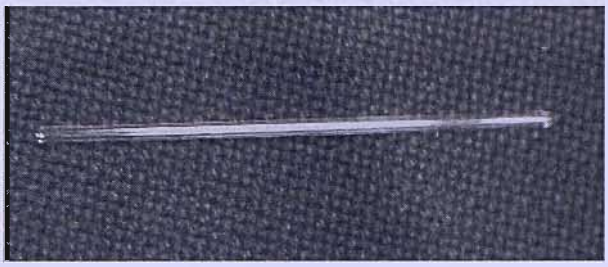

Figure 43: Picture of tube 2.

The flow experiment was first performed for a sample of 5CB with 4.0wt% Claytone using *tube 1* and the ESR spectra are shown in Figure 44.

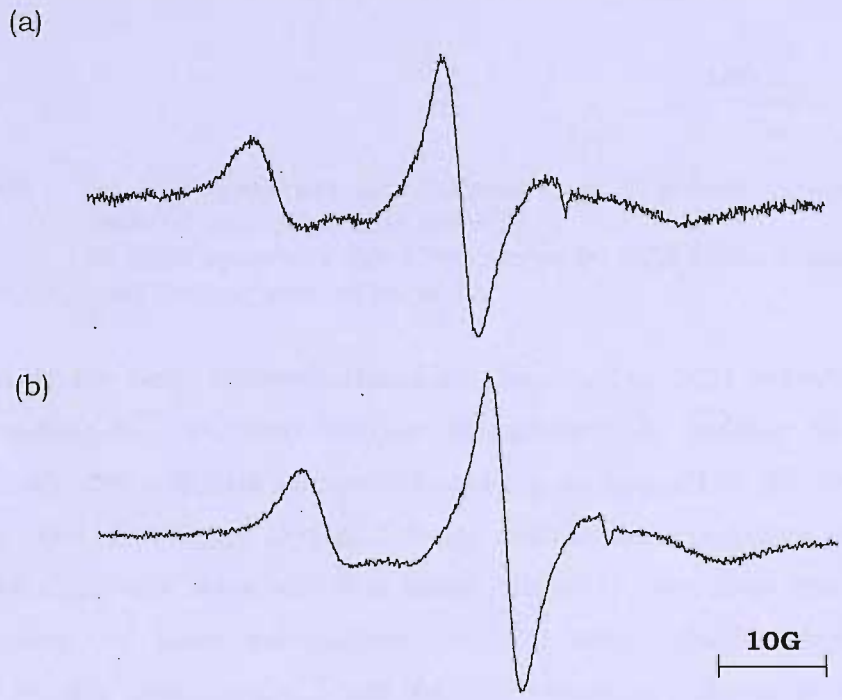

Figure 44: (a) ESR spectrum for Cholestane in 5CB with 4.0wt% Claytone without flow alignment (tube1).
(b) ESR spectrum for Cholestane in 5CB with 4.0wt% Claytone with flow alignment (tube 1).

Since the two ESR spectra with and without flow are so similar, we conclude that the flow field does not align the clay particles, or the director of the liquid crystal host. We then repeated the same experiment for a sample of 5CB with 5.0wt% Claytone and the analogous ESR spectra are shown in Figure 45.

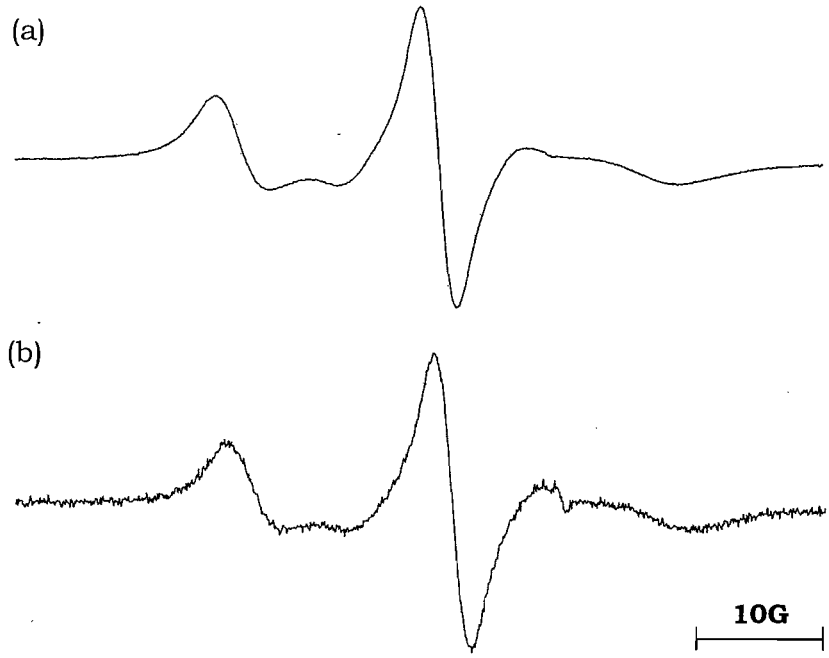

Figure 45: *(a) ESR spectrum for Cholestane in 5CB with 5.0wt% Claytone without flow alignment (tube 1).*
(b) ESR spectrum for Cholestane in 5CB with 5.0wt% Claytone with flow alignment (tube 1).

The results for both concentrations of Claytone in 5CB seem very similar corresponding to a random director distribution. In another words, in our experiments, the colloidal nematics could not be aligned by the flow field that we have used. The liquid crystal director distributions of before and after the flow field alignment were still the same, which is randomly distributed. We then repeat the same experiment for 5CB with 5.0wt% Claytone, using another sample holder, tube 2 and the ESR results are shown in Figure 46.

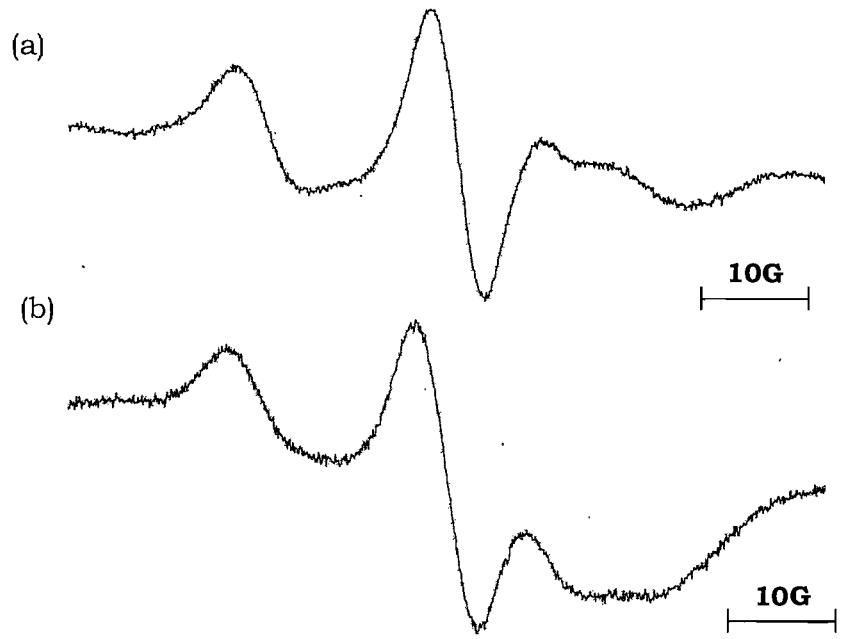

Figure 46: *(a) ESR spectrum for Cholestane in 5CB with 5.0wt% Claytone without flow alignment.*
(b) ESR spectrum for Cholestane in 5CB with 5.0wt% Claytone with flow alignment and using normal capillary tube.

From Figure 46, the ESR spectra for with and without flow alignment show some difference with each other, but the director are still randomly ordered. These results emphasized that the flow alignment is not occur in our experiments. We have repeated these experiments several times as we believed the detail of the sample injection into the capillary tube might strongly influenced the alignment behaviour. Nevertheless, despite these attempts, we still could not align the director in colloidal nematics. All of these results do not convince us of the flow alignment of the colloidal nematic occurs when placed in a tube with a syringe. The director seem and hence the colloidal particles to keep its random orientation after the flow alignment.

4.7 Colloidal Nematics: NMR Studies

The ^2H NMR studies in this section were kindly performed by Dr. Azizah Mainal from the University of Southampton.

Our aim was to examine the ordering of the director at a much higher field then used in ESR experiments as well as to see if the presence of the colloid influences the orientational order at the molecular level. However, our ESR results suggest that the order parameter of the Cholestane spin probe is not changed by the colloidal particles. The systems studied were pure 5CB to act as a baseline comparison, 5CB with 1.0wt% and 10.0wt% of Claytone, 5CB with 1.0wt% of Laponite, and 5CB with 10.0wt% of Sepiolite. In the ^2H NMR experiments, p-xylene-d_{10} was used as a source of deuterium (see Figure 48), and it was the orientational order of this guest molecule that was determined. A previous study by *Emsley* et al. [27] on the orientational order of p-xylene-d_{10} dissolved in a series of 4-alkyloxy-4'-cyanobiphenyls, has shown that the orientational order of the guest reflected that of the host in agreement with theory. *p-xylene-d_{10}* was chosen as a probe molecule was because it gave a well-resolved NMR spectrum and it was commercially available. In addition, the two splittings observed in the NMR spectrum of p-xylene-d_{10} provide information on the major and biaxial components of the *Saupe* ordering matrix. The form of the NMR spectrum also provides information on the director distribution function as in the ESR experiments.

Approximately 2mg p-xylene-d_{10} was inserted in a 3.5cm length of a 5mm o.d. 4mm i.d. NMR glass tube. The liquid crystal colloid contained in a sample vial was slowly heated into the isotropic phase and stirred using a hot plate/magnetic stirrer. This was followed by sonication in order to homogenize the sample. After adding the sample to the NMR tube, the mixture was mixed mechanically and heated with a hot-air gun to ensure the homogeneity of the sample. A Teflon vortex plug was used to prevent the sample from escaping, before finally inserting the shortened NMR tube into the probe. The ^2H NMR measurements were performed on a *Varian Infinity Plus 300* spectrometer with SPINSIGHT software for data acquisition and processing, using the Solaris Operating Environment on a SUN *Microsystem* workstation. The spectra were recorded using a quadrupolar echo sequence

$(\pi/2-\tau_1-\pi/2-\tau_2)$, where both τ_1 and τ_2 were 30μs, while the length of the $\pi/2$ pulse was 5μs. Each sample was first heated into the isotropic phase before the FID was recorded as the sample was cooled down into the nematic phase. The temperature was controlled, via a thermocouple in the probe head connected to a *Varian* temperature control unit, with an accuracy of 0.1°C.

In the ^{2}H NMR spectra, two pairs of quadrupolar split peaks were observed; the inner peaks correspond to the aromatic deuterons, while the outer peaks correspond to the methyl deuterons (see Figures 48 and 49). This assignment could be determined from the integration of the respective peaks; the area under the peaks for the six methyl deuterons is larger than that of the four aromatic deuterons. In addition, this assignment of the peaks in consistent with the fine splittings on the peaks in the spectra which were a consequence of dipolar couplings between nearest neighbour deuterons. The splitting of the outer peaks originated from the dipolar coupling from the three deuterons of the methyl group, while the splitting of the inner peaks come from the nearest two deuterons of the aromatic group. The quadrupolar splittings for the methyl and aromatic group were measured from the largest of their splittings. These splittings are related to the orientational order of the probe according to the following equations

$$\Delta\tilde{\nu}_{Me} = \frac{3}{4} q_{CD}^{Me} S_{zz} \left(3\cos^2\alpha - 1\right) \tag{4.23}$$

and

$$\Delta\tilde{\nu}_{Ar} = \frac{3}{4} q_{CD}^{Ar} \left[S_{zz} \left(3\cos^2\theta - 1\right) + \left(S_{xx} - S_{yy}\right)\sin^2\theta \right], \tag{4.24}$$

where the quadrupolar coupling constants are 168kHz for the methyl group and 186kHz for the aromatic group. α is the angle between the C-D bonds in the CD_3 group and z, which is 70.5°, assuming a tetrahedral geometry, while θ is the angle that the C-D bonds in the aromatic ring make with the z axis, which is 60°, assuming a regular hexagonal structure.

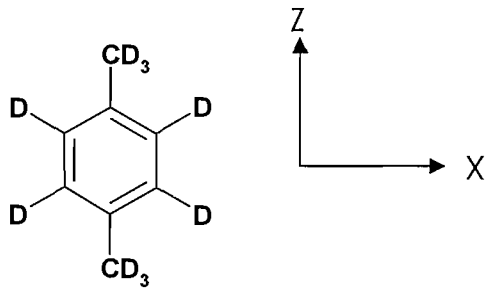

Figure 48: The molecular structure of p-xylene-d_{10} showing the effective symmetry axes.

From the ^2H NMR spectra and the plots of the quadrupolar splittings against the shifted temperatures in Figures 49 and 50, it is apparent that the orientational order of the probe in all the colloidal suspensions are, in essence, the same. The colloidal particles seem to have a negligible effect on the orientational order of the host, provided that the comparison allows for the small shift in the transition temperature. In addition, the NMR experiments also show that as in the pure 5CB, the director alignment by the magnetic field (7.05T) of the spectrometer for the colloidal samples is complete due to similar lineshape of the peaks in the NMR spectra.

Our results have shown the presence of the suspended clay particles had no significant effect on the orientational order in nematic 5CB. In addition, all the samples were well-aligned by the magnetic field. This suggested that the magnetic field (7.05T) employed in this NMR studies was too large to observe any effect of the clay suspension resulting from surface alignment.

5CB

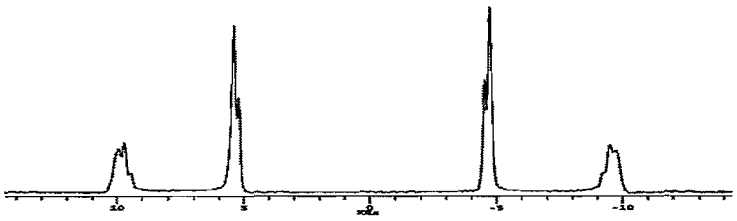

5CB + 1.0wt% Claytone

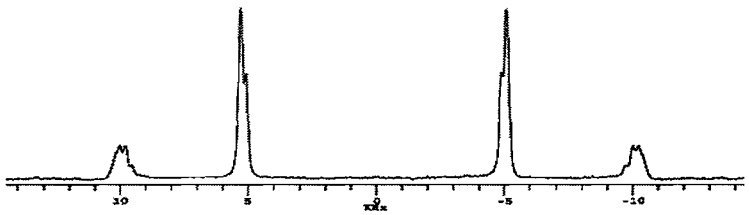

5CB + 10.0wt% Claytone

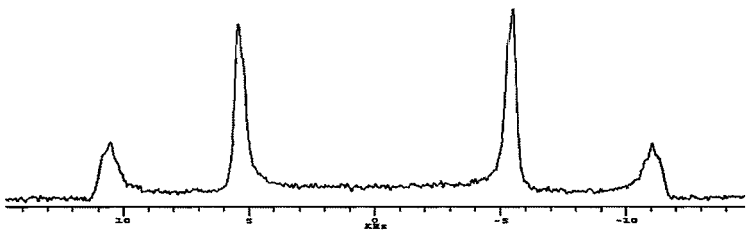

5CB + 1.0wt% Laponite

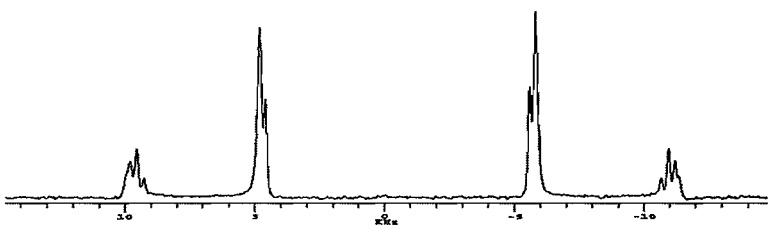

5CB + 10.0wt% Sepiolite

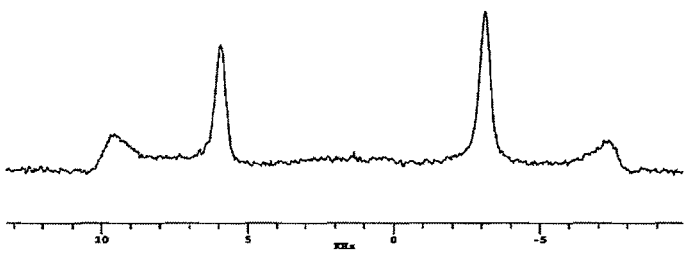

Figure 49: *^2H NMR spectra of the p-xylene-d_{10} in the pure host 5CB and in the colloidal suspensions in 5CB at 25°C. The quadrupolar splittings for the methyl and aromatic group were measured from the largest of their splittings.*

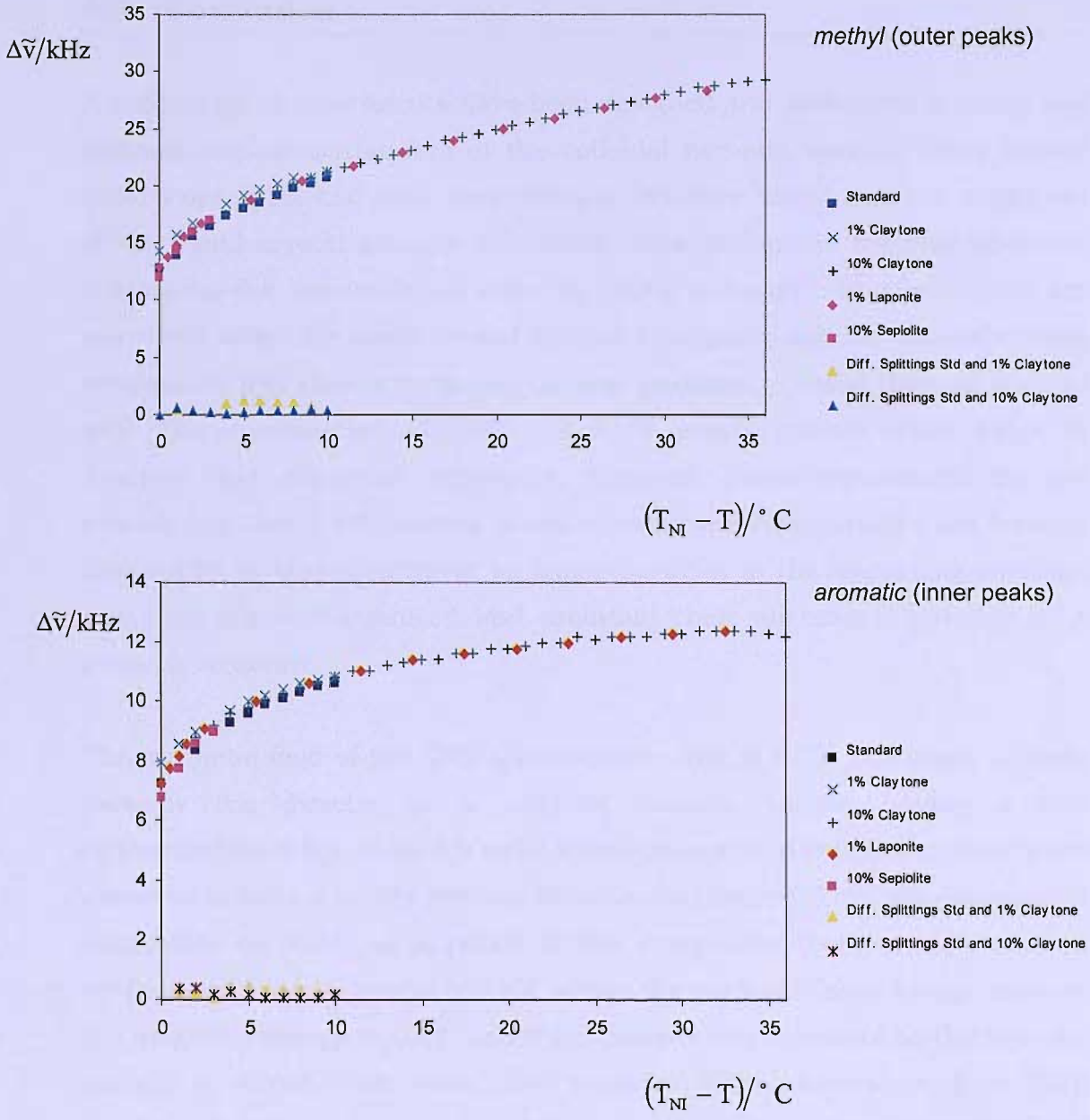

Figure 50: *The plots show the shifted temperature dependence of the quadrupolar splittings for the aromatic and methyl deuterons of p-xylene-d_{10} in 5CB, 1.0wt% and 10wt% Claytone suspensions, the 1.0wt% Laponite suspension, and the 10.0wt% Sepiolite suspension. Also included is the difference in quadrupolar splittings between the standard 5CB and the 1.0wt% and 10.0wt% Claytone suspensions at the same shifted temperatures.*

4.8 Conclusion

A wide range of experiments have been designed and performed to study and increase our understanding of the colloidal nematic system, using optical microscopy, ESR and NMR spectroscopy. We have found that the alignment of the liquid crystal actually influences the alignment of the clay particles, confirming the results found with the SAXS technique. Elastic torques are generated when the liquid crystal director is aligned, and because of surface interaction, this gives a torque on the clay particles to assist them to align as well. The combination of ESR and NMR measurements really helps to describe this alignment behaviour. However, these experiments do not provide any direct information about whether the clay particles are forming into stacks or stay distributed as single particles in the dispersing medium, but they are well-organized and maintain their alignment, possibly in a network structure.

The magnetic field of the ESR spectrometer, that is 0.3T, can align, at least partially the director in a colloidal nematic sample having a clay concentration of less than 3.0 wt%. More concentrated colloidal nematics are observed to have a totally random director distribution. This misalignment is considered to occur as a result of the competition between the random surface and uniform magnetic field, where the surface/elastic energy exceeds the magnetic energy at 0.3T, and this becomes more obvious as the nematic sample is doped with more clay particles. Our observation from ESR experiments inspired us to study the competition between the surface and magnetic field in order to align the liquid crystal director. The magnetic field at 0.3T could not align the director in a colloidal nematic sample for clay concentrations higher than 4.0 wt%. Our calculations based on the theory for the Freedericksz experiment found the critical distance, d_c, between the clay particles in order to align the liquid crystal director should be more than 22μm. Our model for a disc-like particle found the distance between these neighbouring stacks of plates, for a clay concentration of 4.0 wt%, is 13μm, which is smaller than d_c. Therefore, a random director distribution is produced. The surface/elastic force is greater when the distance between the stacks is small, so the magnetic field of 0.3T cannot align the liquid crystal director. Clearly a higher strength of the magnetic field is needed for the

alignment of the director in the colloidal nematic sample and this is practically shown with NMR studies where the field strength is 7.05T.
The rotational dynamics experiment for a colloidal nematic determines the field-induced relaxation time for the director in the sample. Compared with the pure nematic sample, the addition of the clay is seen to increase the rotational viscosity coefficient for the sample itself. But this could only be observed for the samples with low concentrations of clay particles in the nematic because with higher concentrations the director is randomly oriented and the experiment is not valid for such systems. The high-field (7.05T) experiment opened more discussions to the origin of the alignment of the clay particles. We made a final conclusion that the high-field of the NMR spectrometer could align the nematic director. However, this director alignment is not influenced by the clay particles alignment, and we confirmed this with results from our experiment when the sample is heated to the isotropic phase in high-field, which has shown that the nematic director before and after the sample is kept isotropic in high-field, are still randomly distributed. This adds to the fact that the clay stacks are not aligned, which finally resolves the speculation as to how the alignment of the director influences the alignment of the clay particles. Lastly, we still wonder about whether and to what extent our colloidal nematics could exhibit memory effects although the calculation of rotational relaxation times for single clay particles suggest that this memory effect cannot result from the slow motion of single particles and that there must be some other mechanism impeding their rotation, for example as a result of the formation of network structures, as in a gel.

The combination of information gained from several characterization methods (SAXS, ESR and NMR) gives us the following conclusions concerning the structure of a system of clay particles in nematic liquid crystals. SAXS tells us about the formation of small stacks, which are formed by disc-like clay particles of ~5 sheets. For 1.0 wt% Claytone in 5CB, the stacks are formed with a repeat distance of 37Å. While ESR, with a magnetic field of 0.3T, gives information on the ordering of the liquid crystal director. This director ordering is dependent to the concentration of the clay particles, which is related to the distance between the stacks of clay particles. The small distance between the stacks makes it harder for the magnetic field to align

the liquid crystal director. For 1.0 wt% of Claytone in 5CB, we have seen some misalignment of the director since the clay stacks are randomly distributed in the sample. While NMR results shows a complete alignment of the liquid crystal director even for a high concentration of clay particles in 5CB (e.g. 10.0 wt%). This is because NMR has the highest magnetic field strength (7.05T), of all the characterization methods used in this investigation, which allows the magnetic field to align the clay particles [28] as well as the liquid crystal director.

The combination of information gained from all of these characterization methods is presented pictorially in Figure 51. This sketch demonstrates that the variation of

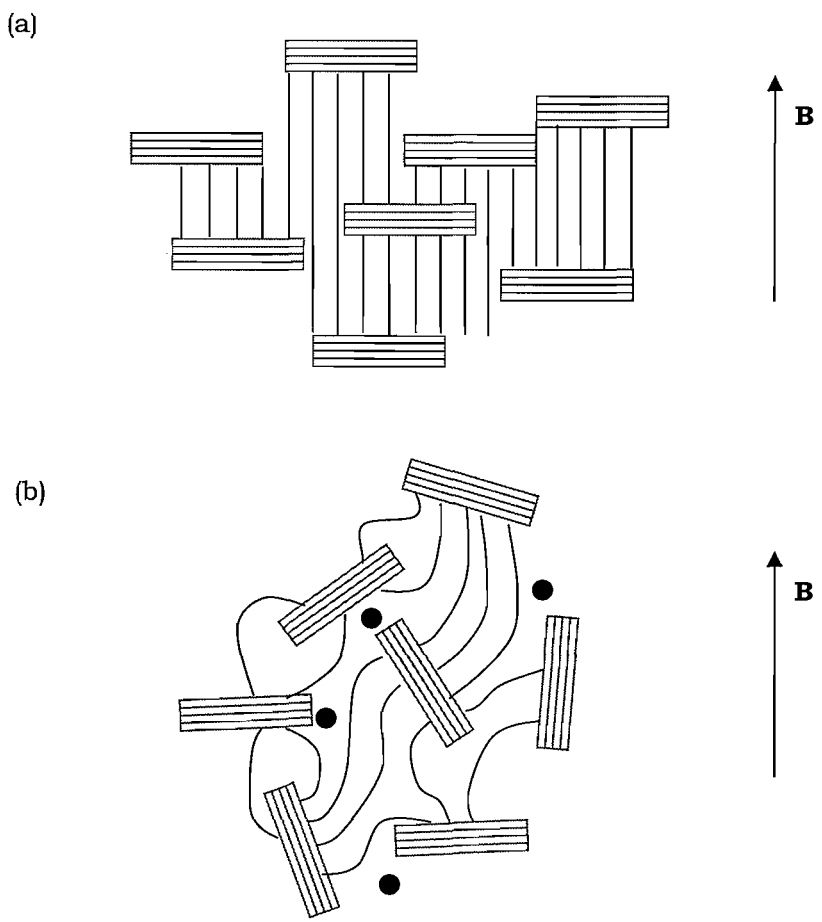

Figure 51: The orientation of liquid crystal director between the stacks of clay particles influenced by the magnetic field, (a) 7.05T and (b) 0.3T. Black dots represent the occurrence of defects.

the magnetic field strength influences the ordering of the liquid crystal director differently. The clay particles are ordered in stacks of 3 to 5 discs, aligned with their normals parallel [28] to the magnetic field strength of 7.05T. On the other hand, in a low magnetic field (0.3T), these clay stacks are randomly distributed which produces a random director distribution of liquid crystal and so may well form defects around the stacks.

4.9 References

[1] A. G. Ward; *Colloids: Their Properties and Applications*, Blackie & Son Ltd, London (1945).

[2] J. W. Goodwin; *Colloidal Dispersions*, Henry Ling Ltd, Dorset (1982).

[3] B. Jirgensons, M. E. Straumanis; *A Short Textbook of Colloid Chemistry*, Pergamon Press Ltd, London (1954).

[4] E. Hatschek; *An Introduction to the Physics and Chemistry of Colloids*, J & A. Churchill, London (1925).

[5] M. Kawasumi, N. Hasegawa, A. Usuki, A. Okada; *Appl. Clay Sci.*, **15**, 93 (1999).

[6] P. Poulin, H. Stark, T. C. Lubensky, D. A. Weitz; *Science.*, **275**, 1770 (1997).

[7] A. M. Zhivkov, S. P. Stoylov; *Coll. Surf. A.*, **209**, 315 (2002).

[8] L. Almásy, A. Jákli, L. Rosta, G. Pépy; *Physica B.*, **241-243**, 996 (1998).

[9] A. Usuki; *United States Patent.*, **4**, 889, 885 (1989).

[10] X. P. Kelly, A. Akelah, S. Qutubuddin, A. Moet; *J. Mater. Sci.*, **29**, 2274 (1994).

[11] A. S. Moet, A. Akelah; *Mater. Lett.*, **18**, 97 (1993).

[12] R. A. Vaia, H. Ishiim, E. P. Giannelis; *Angew. Chem. Mater.*, **5**, 1694 (1993).

[13] A. Borštnik, H. Stark, S. Žumer, *Phys. Rev. E*, **61**, 2831 (2000).

[14] H. Stark; *Phys. Rep.*, **351**, 387 (2001).

[15] M. Kawasumi, A. Usuki, A, Okada, T. Kurauchi; *Mol. Cryst. Liq. Cryst.*, **281**, 91 (1996).

[16] H. van Olphen; *Colloids: An Introduction to Clay Colloid Chemistry 2nd Ed*, Wiley, New York (1977).

[17] Rockwood Additives Product Information, (2003).

[18] A. P. P. Cione, M. G. Neumann, F. Gessner; *J. Coll. Interface Sci.*, **198**, 106 (1998).

[19] E. Balnois, S. Durand-Vidal, P. Levitz; *Langmuir*, **19**, 6633 (2003).

[20] A. M. Zhivkov, S. P. Stoylov; *Coll. Surf. A*, **209**, 315 (2002).

[21] C. Pizzey, S. Klein, E. Leach, J. S. van Duijneveldt, R. M. Richardson; *J. Phys. Condens. Matter*, **16**, 2479 (2004).

[22] E. M. Levin, S. –S. Hou, S. L. Budko, K. Schmidt-Rohr; *J. Appl. Phys.*, **96**, 5085 (2004).

[23] C. Uyeda, T. Takeuchi, A. Yamagishi, M. Date; *J. Phys. Soc. Japan*, **60**, 3234 (1991).

[24] S. R. Wilson, P. J. Ridler, B. R. Jennings; *IEEE Trans. Magn.*, **33**, 4349 (1997).

[25] J. Becker, D. A. Dunmur, C. J. Dunn, G. R. Luckhurst, S. E. Marchant-Lane, B. A. Timimi; *Mol. Cryst. Liq. Cryst.*, **394**, 45 (2003).

[26] M. B. McBride, P. Baveye, *J. Soil Sci. Soc. of Ame.*, **66**, 1207 (2002).

[27] J. W. Emsley, G. R. Luckhurst, and H. S. Sachdev, *Liq. Cryst.*, **5**, 953 (1989).

[28] J. Connoly, J. S. van Duijneveldt, S. Klein, C. Pizzey, R. M. Richardson; *J. Phys. Condens. Matter*, **19**, 156103 (2007).

Chapter V

Nematic Gels and Phase Biaxiality

5.1 Introduction

When potato starch is heated below a high temperature (~ 70° C), it becomes a sticky paste, colourless but interestingly it smells delicious. Before the discovery of modern adhesives, the paste which is the so-called starch glue, was one of the vegetable-based glues that were used in the post office to stick the stamp on the envelope, or to hang a poster on the wall. Starch of a polysaccharide material is a relatively complex carbohydrate, made up of many monosaccharides or glucose, joined together in a structure by glycosidic linkages. Nowadays, beside its importance in cooking and the food industry, starch is also valuable for making natural adhesives.

Adhesives are compounds that commonly work to adhere or bond two items together, for example two pieces of paper. The strength of attachment between an adhesive and a substrate depends on many factors, including the means by which the attachment occurs. Adhesion may occur either by mechanical means, in which the adhesive penetrates small pores of the

substrate, or by one of several chemical mechanisms. In some cases, a chemical bond is formed between the adhesive and the substrate. Electrostatic forces, as in static electricity, might also hold the substances together. We might also consider the chemical method which involves van der Waals' forces develops between each substance. Finally yet importantly, the moisture-aided diffusion of the glue into the substrate, followed by hardening.

Introduction on the idea of adhesives, glues, and attachment between substrates brings us to understand the mechanism of a simple gelation process. Starch, for example is a thickening agent in the food industry, in a way we employ it as a gelator to make the sauces thicker. What are we trying to understand here is how a gelling agent is actually able to make the structure of a fluid become stiff and harder. We are interested in the study of the gel systems, however in this Chapter, we are not looking into gels used in the food industry, but in their potential technological application in liquid crystal devices, for which liquid crystal gels have been proved to show considerable promise in electro-optical devices. The next Section introduces the basic knowledge of gels, this is then followed by information on nematic gels in Section 5.3. Afterwards, in Section 5.4, we shall discuss liquid crystal phase biaxiality. Our presentation for the experimental findings of ESR spectroscopy measurements which includes spectral simulations can be found in Section 5.5.

5.2 The Science of Gels

Sol comes from the word *hydrosol* which means colloidal suspensions in water and the solid form obtained from it, is the Gel. This solid could be as mundane as the epoxy glue which can be used to mend a child's toy, or it can be as sublime as the jellies or custards that delight the haute cuisine, at least for children. The ancient Latins called gel '*gelu*' which means freezing, cold, ice, or '*gelatus*' for a frozen and immobile state of matter. Gels are defined as a colloidal system in which a porous network of interconnected molecules spans the volume of a liquid medium. In general, we see gels as an apparent solid such as jelly-like materials. However, by weight and volume,

gels are mostly liquid in composition and thus exhibit densities similar to the liquids but actually have the structural coherence of a solid.

Gel formation or *gelation* is the conversion of a liquid to a disordered solid by construction of a network of chemical or physical bonds between the molecules or particles composing the liquid [1]. These networks can be presented as polymer branching structures which are shown in Figure 1.

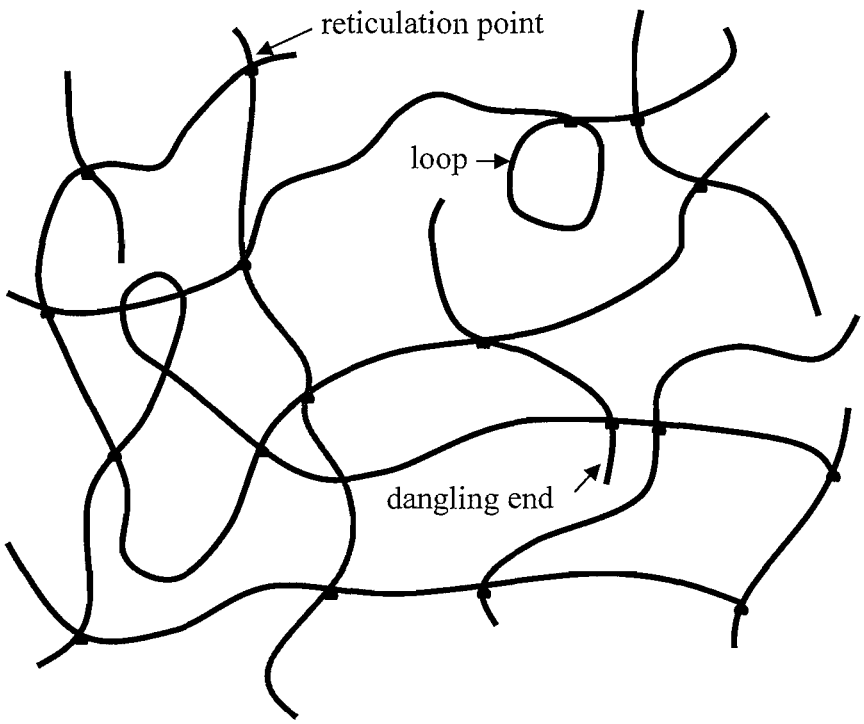

Figure 1: Schematic of a typical cross-linked polymer gel network.

This branching network is crucial for the formation of gels, especially for *chemical gels* which are formed by the dispersion of covalently cross-linked networks. On the other hand, the other class of gels, namely *physical gels* are formed via non-covalent interactions such as hydrogen bonding. Due to *de Gennes* [2], at least three generic types of *chemical* reaction that can produce this gel branching structure are recognized. One of them is a condensation reaction, and it occurs when a molecule with three or more reactive groups such as OH groups, react with a *cross-linker*. The second type of branching reaction is additional polymerization, which contributes a free-radical reaction to open the double bond, then creating additional bonds that link the monomers together. This type of reaction will produce linear chains

if there is only one double bond per monomer but branching could also occur if there are two or more double bonds. Finally, yet importantly, branching also could be created by cross-linked or vulcanization of the linear polymeric precursors with chemical links that bond them together.

Physical gelation as has been mentioned earlier, is related to the non-covalent interactions, which occur because of intermolecular association to form a network (see Figure 2).

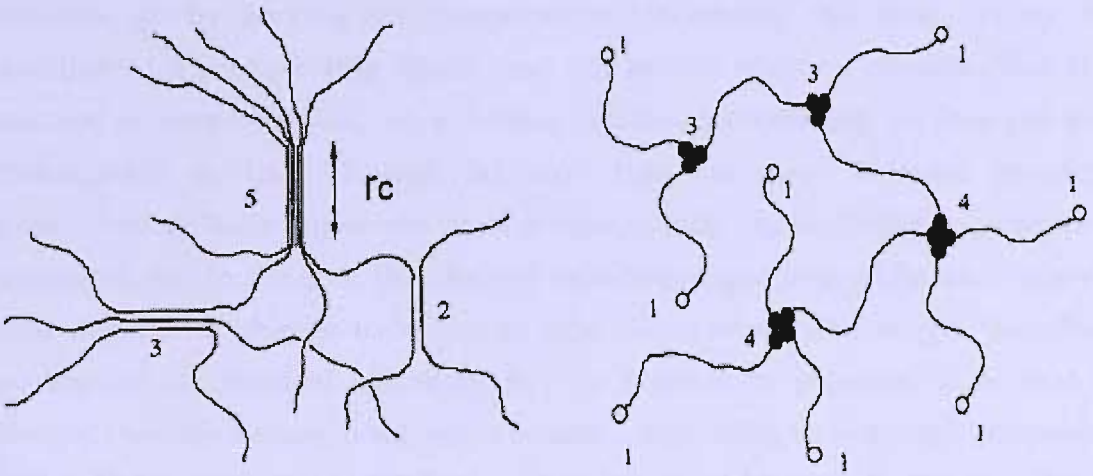

Figure 2: *Illustration of two typical physical gels with junctions of variable multiplicity, (a) junctions are formed by microcrystallites, and (b) junctions are formed by the end groups of telechelic polymers.*

These intermolecular associations are weak, reversible bonds or clusters produced by *van der Waals* forces, electrostatic attractions or hydrogen bonding. The physical association here differs from chemical bonds in that the latter are covalent attachments between two atoms. This association is producing gelation, whereby it is crucial that junctions between molecules that are formed by such associations do not grow too large. *de Gennes* had identified three types of interactions that can lead to physical gelation: (i) local *helical structures* which one molecule winds around each other, (ii) *microcrystallites*, and (iii) *nodular domains* in which the chain is chemically heterogeneous, and association only occurs at preferred sites along the chain. Polymers that form nodular domains such as water-soluble associative thickeners are useful for additives in foods and personal care

products because at low concentrations, such thickeners greatly enhance the viscosity of water.

Gels are disordered materials that are kinetically frozen. The method of preparation strongly influences the properties of the gels. As has been said earlier, gels are formed from colloidal suspensions, by reducing the solubility of the colloidal material sufficiently to enable the particles to be linked together, forming a weak solid mass which is distributed uniformly within a dispersion medium [3]. In order to reduce the solubility, several ways are possible: (i) by varying the temperature (or cooling the sols), (ii) by the addition of a precipitating liquid, and (iii) by the addition of salts. The first method is very common for a simple gelation process [4], in fact the gels investigated in this Chapter fall into this category. Gelation involving precipitant or salts which act as a gelator, needs rapid mixing to produce a saturated sol. In the end, they form a thixotropic (property of fluids to show a time-dependent change in viscosity) gels [5], in which the sol-gel transition occurs via mechanical agitation. In any process of gelation, it is vital to ensure that the gelator does not crystallize on cooling in order for gelation to occur. The formation of crystals could be inhibited by introducing chirality to the gelator compounds [6].

Gelators or gelling agents are compounds used to thicken and stabilize sols. Examples of natural gelators are natural gums, starches, pectin, agar-agar and gelatine. In this modern world, there are many present and maybe future synthetic gelators produced from organic compounds which are very important in several industries. For example, low molecular weight amino acid derivatives could be used for gelation not only in the food industry but also for liquid crystal materials. Previous research has shown the disordering of the nematic liquid crystal director and so the gelation process seems very useful for display device technologies [7].

5.3 Nematic Gels

Most gels are isotropic especially gels that we find as foods, or toys or any jelly-like materials in our environment. They are also called *normal gels*. The opposite of isotropic, which is the anisotropic phase, also produce gels with properties similar to those of normal gels, but different to some extent in their physical properties. It has been reported that the gelation of anisotropic materials of organic solvents by low molecular weight compounds has attracted much attention and research has rapidly developed for this topic, since it shows great potential for electro-optical applications such as PDLC devices [8, 9, 10]. Polymer-dispersed liquid crystals (PDLCs) have utilized liquid-crystalline chemical gels, prepared by the dispersion of covalently cross-linked polymers, in which droplets of nematic liquid crystal (20 – 70wt%) on the scale of micrometers or less are dispersed in polymer matrices (30 – 80wt%).

Liquid crystalline materials are also endowed with additional functionality from the gels by phase segregation and self-assembly. Both actions control the ordering through weak interactions to create more complex structures, and this self-assembled structure formed from a variety of different molecules has been employed for many approaches in supramolecular chemistry [11, 12]. One common benefit for these supramolecular materials is that they can respond to external stimuli and to different environments by changing their self-assembled structures [13] and by the association and dissociation of non-covalent interactions [14, 15]. In the formation of self-assembled liquid crystal structures, specific intermolecular interactions such as hydrogen bonding and ionic interactions play key roles.

Kato et al. [16], are among the pioneers in the creation and investigation of liquid crystal physical gels; they have reported findings on the self-aggregation of *trans*-(1R,2R)-bis(dodeconoylamino)-cyclohexane. This system was prepared by adding the gelator (a low molecular weight compound) to a room temperature nematic at the desired concentration. It was considered as a new class of gel since low molecular weight compounds had not yet been used to prepare anisotropic gels. The gelator compounds or gelling agents used are all amino acid derivatives which are able to form the hydrogen

bond, necessary to create the network of fibres which traps the liquid crystal host. These fibres act as a network structure which can pin the director at its surface and this pinning can actually compete with the alignment by an applied electric or magnetic field for the director alignment. The work by *Kato et al.* found that physical gelation of liquid crystals by the fibrous aggregation of small molecules (gelators) could exhibit faster electro-optic response times in TN cells, than that of the corresponding pure host, providing the concentration of the gelator is below 1.0wt%. Higher concentrations than that cannot be used in TN cells due to the increase in light scattering caused by the increased amount of segregated gelators. Figure 3 shows the chemical structure of the gelators used by *Kato et al.* to gel liquid crystals, while Figure 4 shows the perspective of micro-scale phase segregation of liquid-crystalline physical gels and the pinned nematogenic molecules.

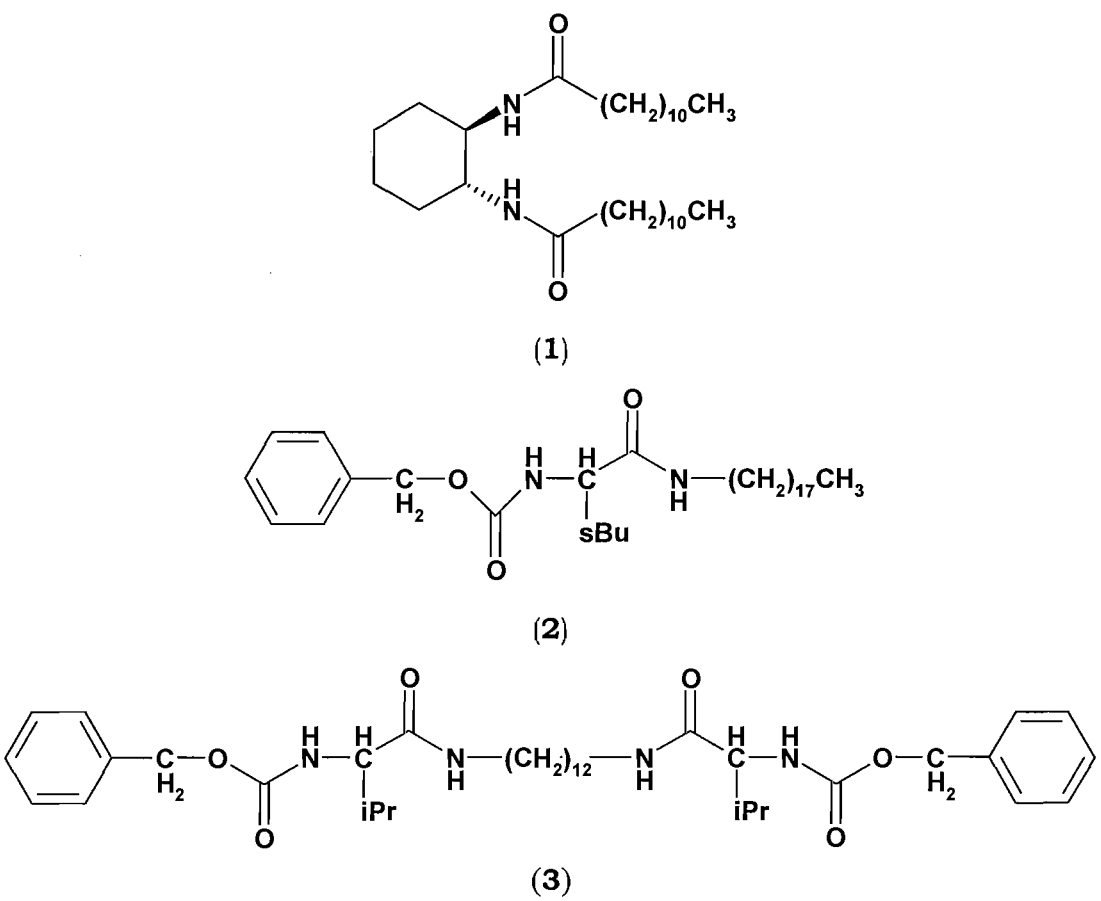

Figure 3: *Chemical structures of amino acid derivatives which act as gelators to gel nematic liquid crystal.*

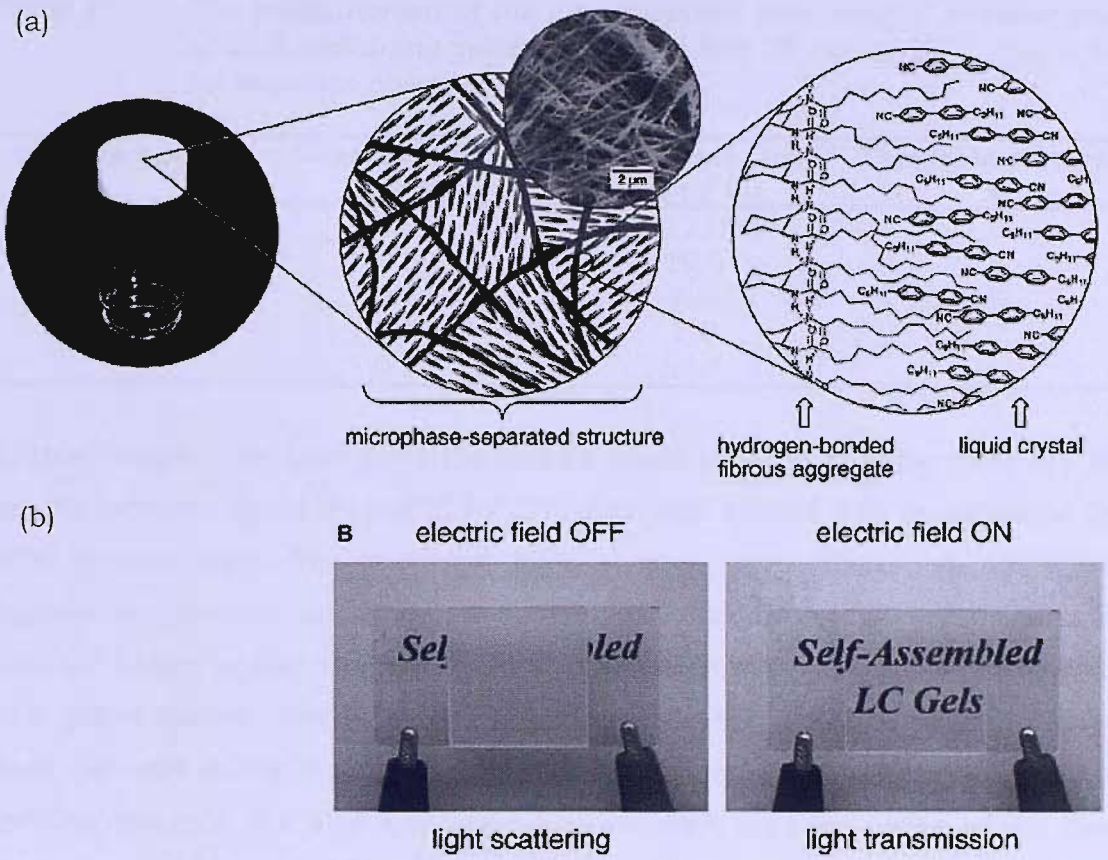

Figure 4: *Micrometer-scale phase segregation of liquid-crystalline physical gels, (a) hierarchy of structures consisting of self-assembled fibres and conventional rod-like mesogenic molecules, (b) left – light scattering state (electric field off); right – light transmission state (electric field on) [11].*

In TN cells, the segregated structures containing less than 0.5wt% of the gelator has been found to lead to a faster switching of the director due to the presence of the electric field. However, the key role here in such dynamic behaviour is the balance of the interactions of the mesogenic molecules with the electrode surfaces and fibrous aggregates [11]. This simple self-assembly not only enables the system to give a faster response but also to exhibit a lower driving voltage and higher contrast with an even smaller amount of gelator. The electro-optic response times for the gelled system made up of gelators (1), (2), and (3) in 5CB in a TN cell were obtained using an applied voltage of 10.0V, with a cell thickness of 16μm, and a frequency of 300Hz for the electric field [9]. The results are given in Table 1.

Table 1: *The measurement of the electro-optical behaviour of nematic gels of 5CB containing gelators 1,2 and 3 in TN cell at 20° C. * n/a for no response observed.*

Gelling Agent	Concentration / mol%	Turn-off response time / ms	Threshold voltage / V
None	0.00	12.0	1.0
1	0.50	19.0	1.5
2	0.25	6.0	0.8
2	0.50	7.0	1.7
3	0.25	n/a*	n/a*

In this Chapter, we have used the gelator made by *Kato* (numbered as **(1)**) to gel the nematic liquid crystal ZLI-4792, then this system was investigated by ESR spectroscopy. The recorded ESR spectra were simulated using an appropriate director orientational distribution function to give some insight into the ability of the magnetic field of the spectrometer to align the director of a gelled system. The gels were found to exhibit a novel behaviour with a high viscosity and strong interaction of the director with the fibrous network forming the gels. We also synthesized a cinnamic acid derivative which had been claimed to show a biaxial nematic phase and this has also been gelled by the gelator [25]. ESR spectroscopy has been employed to investigate this system as well.

5.4 Biaxiality and Phase Symmetry

Scientists have predicted that the biaxial nematic phase could be employed in display device technology, potentially with a faster response, based-on in-plane switching [17, 18]. This is because the rotation of the minor directors $\hat{l}$ and $\hat{m}$, might be relatively rapid and possibly faster than the motion of the main director, $\hat{n}$ (see Figure 5). Claims to have discovered this phase have been widely discussed and many attempts have been made to synthesize thermotropic biaxial materials, and more importantly, to obtain unambiguous evidence of the phase symmetry using different characterization methods.

(a)

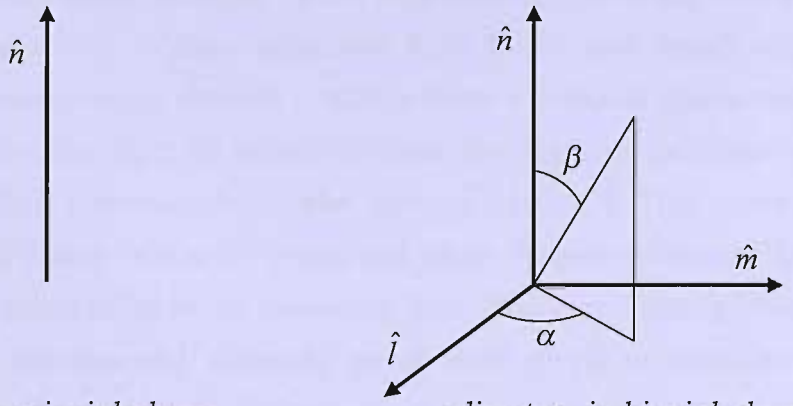

director in uniaxial phase *directors in biaxial phase*

(b)

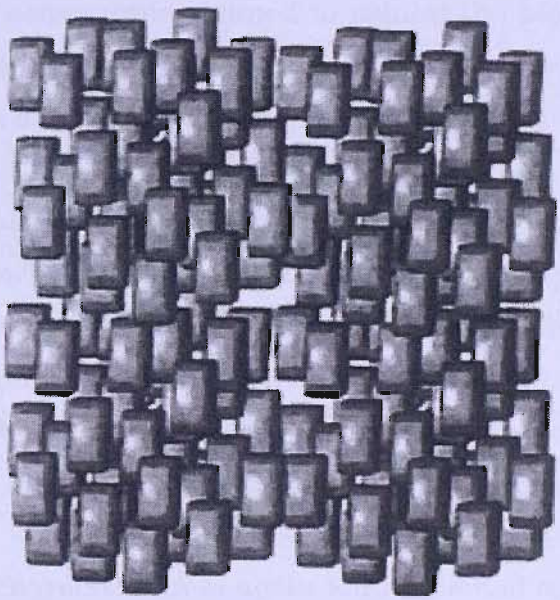

(c)

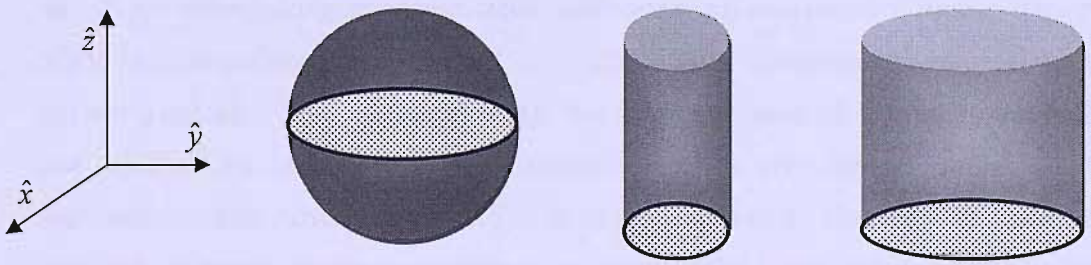

isotropic *uniaxial nematic* *biaxial nematic*

Figure 5: *(a) The three directors are denoted by $\hat{l}$, $\hat{m}$ and $\hat{n}$, (b) molecular organization in a biaxial nematic phase composed of lozenge-shaped molecules, (c) a schematic representation of phase symmetries for isotropic, uniaxial and biaxial nematic phases.*

The word biaxial comes from the optics expression, indicating that there are two axes along which a plane-polarised light beam can travel without its state of polarization being altered. It differs from a uniaxial phase which only has one axis for the light to travel without the state of polarization being changed and this corresponds to the director [19, 20]. The history of the biaxial nematic phase began 30 years ago when *Freiser* published his paper predicting the probability of its existence [21]. However, during that period, no convincing studies and scientific proof were given to demonstrate the existence of the biaxial nematic because no thermotropic biaxial materials had yet been found. Then in 1986, a paper was published by *Malthete et al.*, on the synthesis of compounds claimed to exhibit the biaxial nematic phase [22]. However, the phase that was thought to be nematic actually possessed some properties of a smectic C phase.

Following the original claim by *Malthete*, two years later, *Chandrasekhar et al.* reported their work, in which the nematic exhibited by a copper complex was found to exhibit a weak optical biaxiality [23]. The study of biaxial nematics has exhibited a rapid growth during this period. However, the optical textures and conoscopic observations that have been used to identify the phase were not convincing enough and still can in be doubt. *Praefcke et al.* had synthesized some materials that might be expected to exhibit phase biaxiality [24]. The characterization again found a small optical biaxiality and it was still not convincing to confirm the existence of the biaxial nematic phase for these materials. One of those materials synthesized by *Praefcke et al.*, *2,3,4-trihexyloxycinnamic acid* has been characterized using deuterium NMR spectroscopy by *Fan et al.* [25]. The compound was specifically deuteriated and the results showed that the nematic phase was uniaxial and not biaxial as claimed. This emphasized that the investigation of phase biaxiality is still unresolved and is quite challenging. Not all compounds can form or possess phase biaxiality even though the constituent molecules are clearly biaxial. The ability of the material to form a biaxial nematic depends on the magnitude of the molecular biaxiality. One of the ways to define molecular biaxiality is achieved within the context of the molecular field approach that can predict the phase behaviour of the biaxial system [26]. At the heart of this is how the potential energy of the molecule changes with its orientation with respect to the directors. This change is determined by the

tensor strength and this is related to the molecular anisotropy and the long-range orientational order parameters. Molecular field theory approach can be used to determine the transition temperature for uniaxial nematic-isotropic transition, as well as the biaxial-uniaxial nematic transition. Such determinations have been made by *Boccara et al.* where they presented a mathematical treatment for an investigation of the transitions to ordered uniaxial and biaxial phases in an assembly of asymmetric ellipsoids coupled by a constant infinite-range isotropic interaction [30]. Although the systems studied are not directly related to liquid crystal phases, but it is applicable to these system. Figure 6 shows the phase diagram from the work by *Boccara et al.*

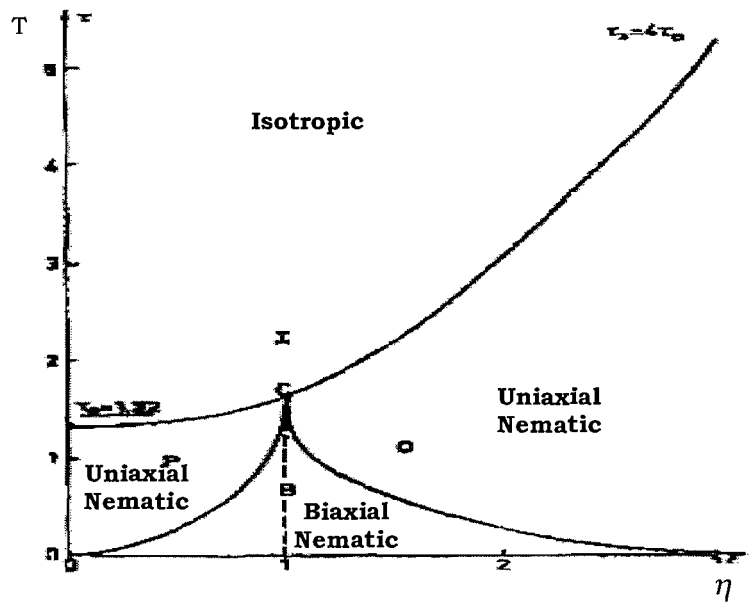

Figure 6: *Phase diagram predicted by Boccara et al. [30] of the transition between uniaxial, biaxial and isotropic phases of liquid crystals.*

To identify the biaxial nematic phase, optical textures observed under a polarising microscope are commonly used since it is thought to reflect, albeit indirectly, the optical biaxiality and is, in general, very useful at the first stage of identifying a liquid crystal phase. It was suggested that, uniaxial and biaxial nematic phases could be identified by the form of the *Schlieren* texture [28]. In the case of a uniaxial nematic, it is known to show both two-fold and four-fold brushes while for a biaxial nematic, it has been suggested that the *Schlieren* texture only has two-fold brushes, as can be seen in Figure 7. However, there is concern that the optical texture does not provide

definitive evidence for biaxiality because there are other reasons for the absence of four-fold brushes, including their higher energy [27, 31].

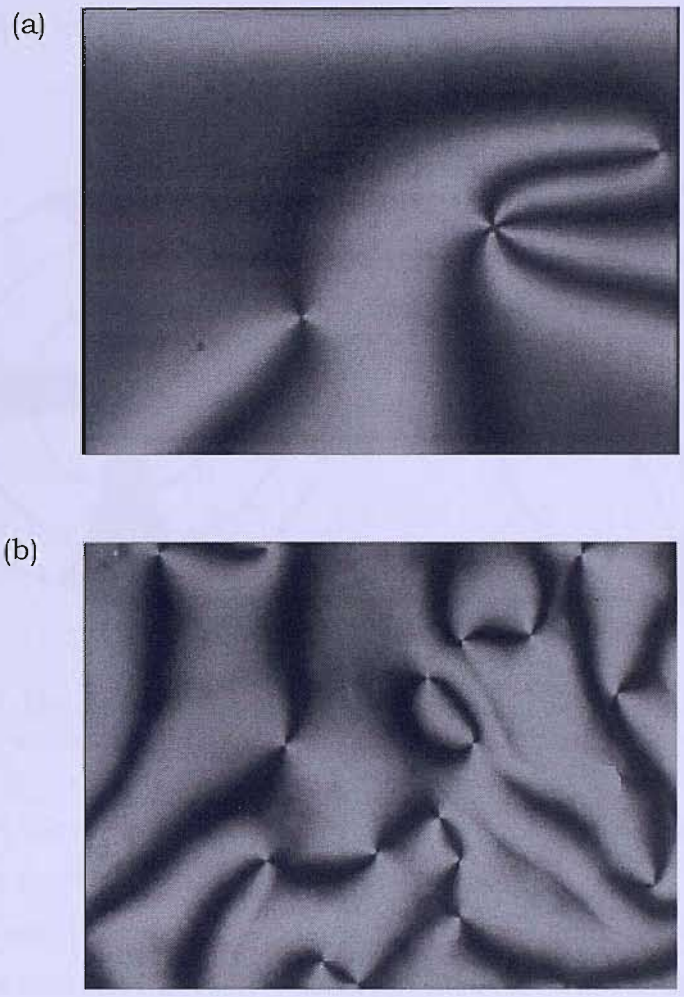

Figure 7: *The Schlieren textures observed for a nematic exhibiting (a) two-fold and four-fold brushes for a uniaxial nematic and (b) only two-fold brushes for nematic thought to be biaxial [28].*

A more recognized and sensitive technique to determine the spherical biaxiality of a material is *conoscopy* which provides information on the symmetry of the components of the refractive index [29]. In this method, a thin film of nematic is aligned with the main director orthogonal to the substrate and with the minor directors aligned in the plane and for a biaxial nematic clearly two constraints are needed to align the three directors, these are usually an electric field and surface torque. Then using convergent polarised light, an interference feature like a Maltese cross is observed for a uniaxial nematic. While for biaxial nematic, the arms of the cross or isogyres open to an extent that depends on the optical biaxiality, as shown in Figure

8. However, this technique has its own disadvantage since the surface torque can also tilt the director of the thin film and this can induce a small biaxiality in the director distribution. As a result even for a uniaxial nematic, the image observed is one in which the isogyres are open.

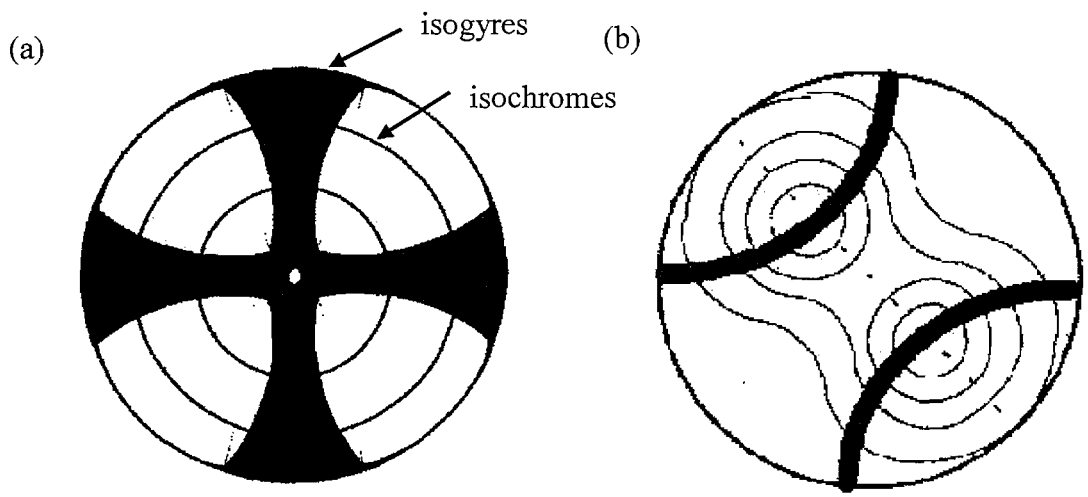

Figure 8: *The conoscopic interference images expected for (a) an optically uniaxial, and (b) and optically biaxial nematic phase.*

Among all of these techniques, NMR spectroscopy has been found to be one of the most powerful characterization methods to study the symmetry of nematic phases. NMR can investigate a bulk sample and so the surface of the container cannot influence the director distribution for the majority of the sample and hence the symmetry of the measured magnetic tensor. The tensor is usually the quadrupolar tensor, $\tilde{q}$, which is determined from the spectral doublets associated with a deuteron. The single line in the deuterium NMR spectrum for the isotropic phase is split into a doublet on entering the liquid crystal phase. This occurs because of the long-range orientational order and so the anisotropy in the quadrupolar interaction for the deuteron is no longer averaged to zero by the rotational motion. The magnitude of the splitting depends on the second rank orientational order parameters for the molecule and the orientation of the director with respect to the magnetic field. The angular variation of the spectrum depends on the angle, θ made by the director with the field and this angular variation of the quadrupolar splitting, $\Delta\tilde{\nu}$, is given by

$$\Delta\tilde{\nu}(\theta) = \Delta\tilde{\nu}(0)(3\cos^2\theta - 1)/2 \qquad (5.1)$$

for a uniaxial phase. The difference between uniaxial and biaxial nematic splittings is that for a uniaxial nematic, the modulus of the ratio of quadrupolar splitting when the director is parallel to the field to that when it is perpendicular is 2:1. On the contrary, for a biaxial nematic the ratio of the splitting when the magnetic field is along director $\hat{n}$ to that when it is parallel to $\hat{l}$ or $\hat{m}$ is different from 2:1. In other words the components of the partially averaged quadrupolar tensor along the three directors are different whereas for a uniaxial phase the components orthogonal to the main director are equal and minus one-half that parallel to the main director. This method is actually more powerful because it is not necessary to study a monodomain and so the director alignment can be randomised; this can be achieved by spinning the sample about an axis orthogonal to the magnetic field. This is found to randomise the director in a plane perpendicular to the spinning axis above a certain angular velocity. It provides a spectrum with a two-dimensional powder pattern because it comes from a sum of spectra; that is from each orientation of the director with respect to the magnetic field from 0° to 90°. Simulated NMR spectra for uniaxial and biaxial quadrupolar tensors illustrate how the real spectra should be look for the different symmetries of the phase being characterized. Figure 9 shows the simulated spectra for uniaxial and biaxial nematic phase for a three-dimensional distribution of the directors. We can see that in the uniaxial phase there are just two features; the outer shoulders and the inner horns which are associated with the main director being parallel and perpendicular to the magnetic field, respectively. For the biaxial phase there are as might be expected, three features associated with the NMR spectrum, the shoulders and horns as found for the uniaxial phase but now there is an additional pair of shoulders associated with one of the minor directors parallel to the magnetic field.

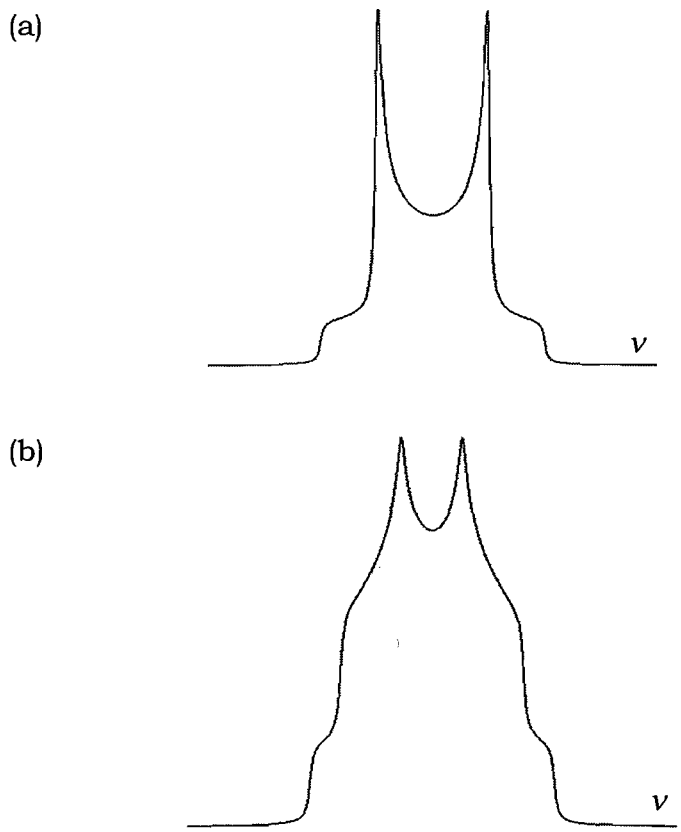

Figure 9: *The deuterium NMR spectra expected for (a) a uniaxial nematic and (b) a biaxial nematic; in both cases the directors are randomly distributed in three dimensions and the molecules contain a single deuteron.*

It has been shown that NMR spectroscopy is one of the most powerful techniques to identify symmetry of a biaxial nematic phase. However, alongside NMR, there is another branch of magnetic resonance spectroscopy which can be used to characterize a material, this is ESR spectroscopy. Here we describe the potential use of ESR spectroscopy in characterizing biaxial nematic phases.

Such identification using ESR spectroscopy would tend to show three-dimensional ESR spectra since the small magnitude of the magnetic field of an X-band spectrometer is an advantage because it would not perturb the random director distribution. Compared to NMR spectroscopy, ESR is actually more sensitive, owing to the fact that electrons have a greater magnetic moment than the nuclei. However, there is the potential disadvantage that a spin probe has to be added to the liquid crystal because

these are not paramagnetic. Although deuteriated probes have been used in NMR studies of phase symmetry.

The idea of characterizing the biaxial nematic phase using ESR spectroscopy is related to the ease of disordering of the nematic directors in the presence of a magnetic field. In our case, gelled liquid crystals are used, so that a three-dimensional powder pattern ESR spectrum would be obtained. This is thought to be the first theoretical attempt to see how the ESR spectra should appear and how sensitive they are to the biaxiality of the nematic phase. As we have seen, the biaxial phase has three principal components of a second rank tensor that would all be different, unlike a uniaxial nematic. The dominant interaction in ESR using nitroxide spin probes is the nitrogen hyperfine interaction. The components of the partially averaged hyperfine tensor are denoted by $\widetilde{A}_{XX}$, $\widetilde{A}_{YY}$ and $\widetilde{A}_{ZZ}$ where $\hat{X}$, $\hat{Y}$ and $\hat{Z}$ are parallel to the three directors for a biaxial nematic. Simulation of ESR spectra for biaxial splitting would help to understand under what conditions ESR spectroscopy could be used to identify and determine the biaxiality of a biaxial nematic phase.

The line position for a biaxial hyperfine interaction in ESR spectrum for an isotropic g factor that is $\widetilde{g}_{XX} = \widetilde{g}_{YY} = \widetilde{g}_{ZZ}$, is determined by

$$K(\beta,\alpha) = (\widetilde{A}_{ZZ}{}^2 \cos^2\beta + (\sin^2\beta)(\widetilde{A}_{XX}{}^2 \cos^2\alpha + \widetilde{A}_{YY}{}^2 \sin^2\alpha))^{1/2}. \qquad (5.2)$$

The dependence of this hyperfine interaction on the two angles, β and α, is important since these describe the orientation of the magnetic field with respect to the three directors. The simulation of the ESR spectra will show how the biaxiality in $\widetilde{A}$, influences the three-dimensional powder pattern of the ESR spectrum. The biaxiality in the hyperfine tensor, $\widetilde{\eta}$, is defined by

$$\widetilde{\eta} = \frac{(\widetilde{A}_{XX} - \widetilde{A}_{YY})}{(\widetilde{A}_{ZZ} - \widetilde{a}_{iso})}, \qquad (5.3)$$

where

$$\tilde{A}_{XX} + \tilde{A}_{YY} + \tilde{A}_{ZZ} = 3\tilde{a}_{iso}. \tag{5.4}$$

In our case, $\tilde{\eta}$ takes the limiting values of 0 and 1. The phase biaxiality is zero when two components of the hyperfine tensor are equal; for example when $\tilde{A}_{XX} = \tilde{A}_{YY}$. It is unity when $\tilde{A}_{XX} = a_{iso}$ and $\tilde{A}_{YY} + a_{iso} = -\tilde{A}_{ZZ} + a_{iso}$. These results follow from equation (5.3), when the biaxiality is unity then

$$\begin{aligned} \tilde{A}_{ZZ} - \tilde{a}_{iso} &= \tilde{A}_{XX} - \tilde{A}_{YY}, \\ &= (\tilde{A}_{XX} - \tilde{a}_{iso}) - (\tilde{A}_{YY} - \tilde{a}_{iso}). \end{aligned} \tag{5.5}$$

From equation (5.4),

$$(\tilde{A}_{XX} - \tilde{a}_{iso}) + (\tilde{A}_{YY} - \tilde{a}_{iso}) + (\tilde{A}_{ZZ} - \tilde{a}_{iso}) = 0, \tag{5.6}$$

that is the trace of the anisotropic hyperfine tensor is zero.

Writing the components $(\tilde{A}_{XX} - \tilde{a}_{iso})$, $(\tilde{A}_{YY} - \tilde{a}_{iso})$ and $(\tilde{A}_{ZZ} - \tilde{a}_{iso})$ as $(\tilde{A}'_{XX})$, $(\tilde{A}'_{YY})$ and $(\tilde{A}'_{ZZ})$, allows us to write equation (5.5) as

$$\tilde{A}'_{ZZ} = \tilde{A}'_{XX} - \tilde{A}'_{YY}, \tag{5.7}$$

but $\tilde{A}'_{ZZ} + \tilde{A}'_{YY} = -\tilde{A}'_{XX}$, so that we require

$$\tilde{A}'_{XX} = -\tilde{A}'_{XX}, \tag{5.8}$$

which has the solution that $\widetilde{A}'_{XX} = 0$. This means that the X component of the hyperfine tensor is just the scalar hyperfine coupling constant, a_{iso}. With $\widetilde{A}'_{XX}$ equal to zero, it follows from equation (5.7) that

$$\widetilde{A}'_{ZZ} = -\widetilde{A}'_{YY}, \tag{5.9}$$

that is the remaining two principal components of the anisotropic hyperfine tensor are equal and opposite in sign. The total tensor components are then $(\widetilde{a}_{iso}, \widetilde{a}_{iso} - \widetilde{A}'_{ZZ}, \widetilde{a}_{iso} + \widetilde{A}'_{ZZ})$ in the limit of maximum biaxiality.

Simulations of the ESR spectra for the biaxiality from 0 to 1 are shown in Figure 10. To perform this simulation, first we have to decide on the parameters $\widetilde{A}_{XX}$, $\widetilde{A}_{YY}$ and $\widetilde{A}_{ZZ}$ in equation (5.2) where the line positions for the biaxial ESR spectrum is determined. The ESR spectra for Cholestane spin probe in uniaxial ZLI-4792 in the nematic and isotropic phases are the primary input for this simulation. From there we determine $\widetilde{A}_{ZZ}$ and $\widetilde{a}_{iso}$ which take the values of 7.71G and 14.71G. Using equations (5.3) and (5.4), we can calculate the two principal components, $\widetilde{A}_{XX}$ and $\widetilde{A}_{YY}$. The three linewidths, $T_2^{-1}(-1)$, $T_2^{-1}(0)$ and $T_2^{-1}(1)$ for the three hyperfine peaks in the biaxial ESR spectrum were hard to decide since we do not have an experimental biaxial ESR spectrum yet. However, we do know that the simulated spectrum should look like a 3D powder pattern, so we finally chose 0.5G (Tempone) and 1.5G (Cholestane) as the linewidths for those three peaks. Table 2 shows the parameters used to simulate the biaxial ESR spectrum for biaxiality from 0 to 1. The simulation was presented for two different spin probes; Tempone and Cholestane.

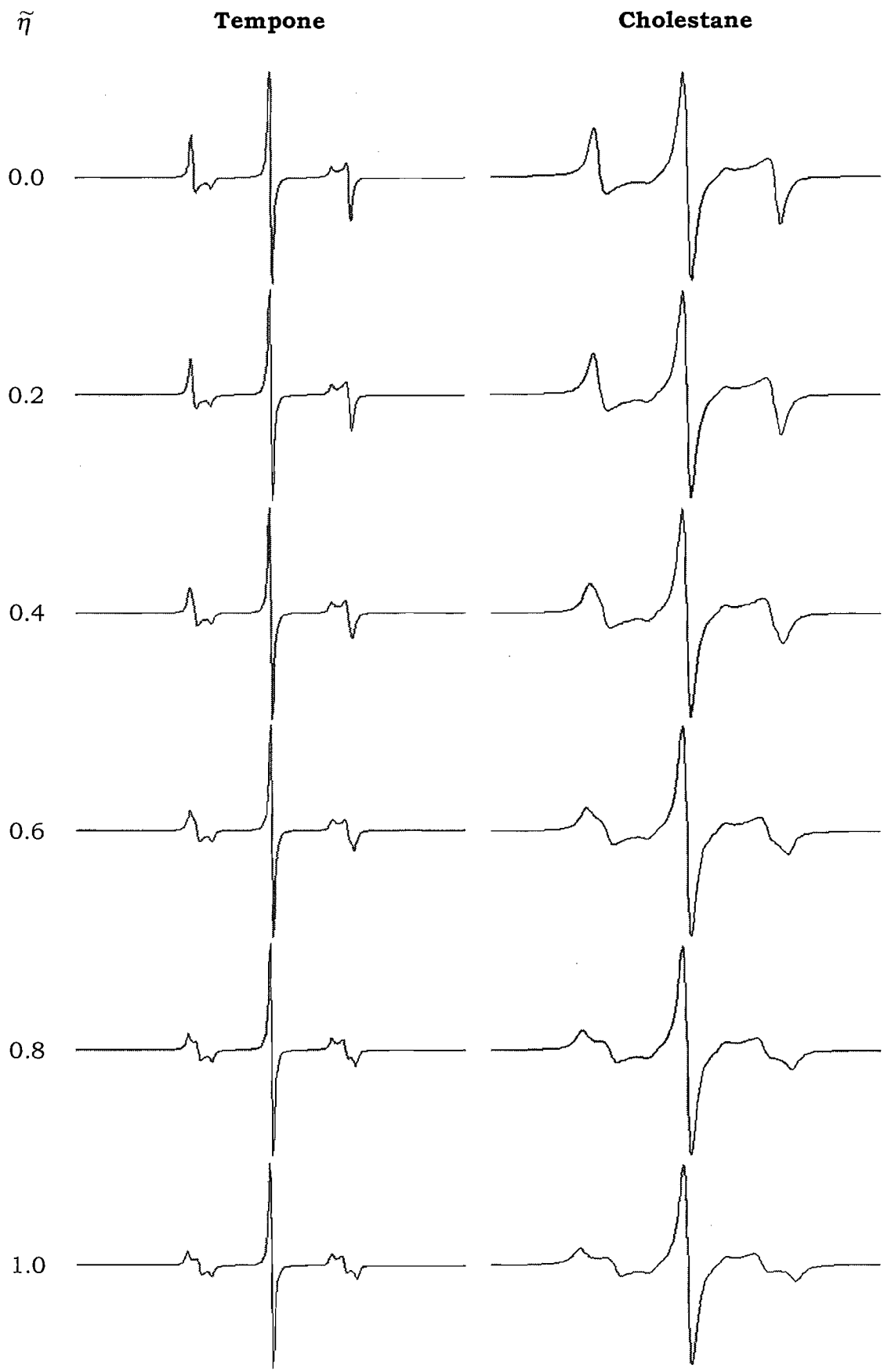

Figure 10: The simulated biaxial ESR spectra for the different biaxiality, $\widetilde{\eta}$ in $\widetilde{A}$.

Table 2: The parameters and data used to simulate the ESR spectra for Tempone and Cholestane spin probe shown in Figure 10 for the biaxial nematic phase.

Tempone spin probe

$\tilde{\eta}$	$\tilde{A}_{XX}/G$	$\tilde{A}_{YY}/G$	$\tilde{A}_{ZZ}/G$	$T_2^{-1}(-1)/G$	$T_2^{-1}(0)/G$	$T_2^{-1}(1)/G$
0.0	15.88	15.88	12.16	0.5	0.5	0.5
0.2	15.63	16.13	12.16	0.5	0.5	0.5
0.4	15.38	16.38	12.16	0.5	0.5	0.5
0.6	15.14	16.62	12.16	0.5	0.5	0.5
0.8	14.89	16.87	12.16	0.5	0.5	0.5
1.0	14.64	17.12	12.16	0.5	0.5	0.5

Cholestane spin probe

$\tilde{\eta}$	$\tilde{A}_{XX}/G$	$\tilde{A}_{YY}/G$	$\tilde{A}_{ZZ}/G$	$T_2^{-1}(-1)/G$	$T_2^{-1}(0)/G$	$T_2^{-1}(1)/G$
0.0	18.21	18.21	7.71	1.5	1.5	1.5
0.2	17.51	18.91	7.71	1.5	1.5	1.5
0.4	16.81	19.61	7.71	1.5	1.5	1.5
0.6	16.11	20.31	7.71	1.5	1.5	1.5
0.8	15.41	21.01	7.71	1.5	1.5	1.5
1.0	14.71	21.71	7.71	1.5	1.5	1.5

Cholestane gives broader lineshapes than Tempone, as we already discussed in Chapter IV. From the simulated biaxial ESR spectra in Figure 10, the all the seven peaks for a biaxial nematic are clearly seen especially for the ESR spectrum with the highest biaxiality. The simulated ESR spectra for the small biaxialities ($\tilde{\eta} < 0.4$), do not show any significant changes compared to that with no biaxiality, ($\tilde{\eta} = 0$). We could say all the three hyperfine splittings, $\tilde{A}_{XX}$, $\tilde{A}_{YY}$ and $\tilde{A}_{ZZ}$ first appear when $\tilde{\eta}$ is 0.4. Therefore, this could suggest that ESR spectroscopy could only be used to characterise materials that have higher biaxiality value, which is more than 0.4. It is apparent that, as the biaxiality increases, the three hyperfine splittings, could be clearly recognized and the best powder pattern simulation occurs when the biaxiality takes the value of one, which shown all the three directions of the directors. These three splittings can be measured from ESR spectra and signifies the biaxiality in the hyperfine tensor which is related to that of the nematic determined using ESR spectroscopy.

5.5 ESR Spectroscopy and Spectral Simulations

From the Introduction and theories of gels, gelators, gelation and phase biaxiality, we now proceed to a series of ESR experiments that we have performed for nematic gels. There are several types of experiments that we have made, based on the variation of the nematic liquid crystal and the gelling agents used to produce the nematic gel. The experimental setup and ESR spectrometer settings are reported in Chapter III. We used nematic ZLI-4792 as the nematic host to be gelled by the effective gelator based on the amino acid derivative introduced by *Kato* from the University of Tokyo [16]. The chemical structure of this low molecular weight compound, *trans-(1R,2R)-bis(dodecanoylamino)cyclohexane* is shown in Figure 3 (labelled as 1) in the previous Section, (after this it is called simply the *Kato* gelator).

Since the anisotropic gels that we are making are classified as physical gels, we expect that the gelation of room temperature nematic liquid crystals is by self-aggregation of gelator molecules through hydrogen bonding. Once the gel is formed, on cooling the sample tube can be turned upside down without flow, a typical characteristic of a gel, and when the mixture is heated, it becomes a fluid isotropic liquid. We also measured the ESR spectra as a function of temperature on heating and cooling the sample. The transition of sol-gel is thermally reversible and the gels are stable at room temperature.

In addition to nematic ZLI-4792 ($T_{NI} = 92°\,\mathrm{C}$), our group here had also synthesized an organic compound which is claimed to be biaxial due to the discovery from conventional methods. It is compound *2,3,4-trihexyloxycinnamic acid* and the *Kato* gelator has, again, been used to gel this liquid crystal. The results of this experiment are described in the Sub-section 5.5.2.

5.5.1 Gelation of Nematic ZLI-4792

To start our study on gelation, we examined the commercial nematic ZLI-4792, ungelled and gelled to be characterized with ESR spectroscopy. Figure

11 shows the ESR spectrum for the Tempone spin probe dissolved in ungelled ZLI-4792 in its nematic phase.

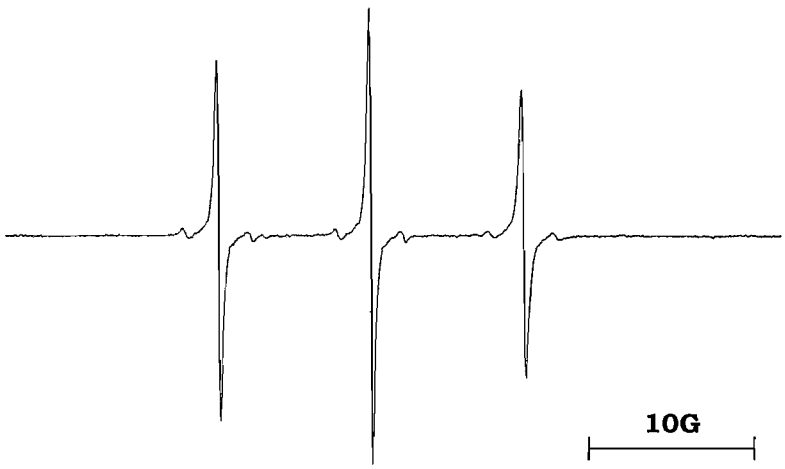

Figure 11 : The ESR spectrum for the Tempone spin probe in ZLI-4792 at 300K.

From Figure 11, we see that the ESR spectrum contains three sharp and intense hyperfine lines from the Tempone spin probe, and for each lines which occurs from the interaction between the free electron and the ^{14}N nuclei, there appear two satellite peaks, which come from the presence of ^{13}C (spin ½) atoms. These peaks are small and low in intensity due to the small natural abundance of carbon-13 which is about 1%. There are six ^{13}C atoms in the Tempone molecules, which contributed to the 3% for each satellite peak height compared to the height of the main peak. Not only carbon-13 peaks, but also additional small peaks could be seen between the three main peaks, which originate from ^{15}N (spin ½). There are two peaks, with a large spacing but they have as a small intensity compared to the others as its natural abundance is also relatively small, ~0.5%. Of the three main peaks, the spacing between the two outer peaks is 24.86G, so that the value of $\tilde{A}_{\parallel}$ is 12.43G. From here, we could determine the order parameter for the probe in this liquid crystal to be 0.13. This experiment was performed at room temperature while the sample was in the nematic phase of ZLI-4792. So that, this spectrum shows the ESR splittings when the nematic director is parallel to the magnetic field, since $\Delta\tilde{\chi} > 0$ for ZLI-4792.

The idea of this experiment is to obtain a gelled nematic and to study how ESR spectra would change with the disruption of the director ordering found in the original aligned system. The physical gel that we obtained in this experiment was characterized with ESR spectroscopy and it has been shown that gelation is a good method to disrupt the director alignment. The sample with disordered director kept its disordered condition for several months without the presence of magnetic field [16] and this is a very good result for this subject research since the nematic gel that was produced is stable in time. The amount of gelator that we used to gel the liquid crystal in this experiment was only 0.5wt%. However, as we have seen this small amount of gelator could randomize the director completely. For this experiment, the amount of gelator used is around 1.0mg. It is not easy to prepare a nematic gel using less than 1.0mg gelator, with the equipment that we had in the laboratory. On the other hand, besides using Tempone spin probe, the Cholestane spin probe could show interesting results since $\left|\widetilde{A}_{\parallel}-\widetilde{A}_{\perp}\right|$ is much bigger than Tempone, so that the difference between ESR signals for director parallel and perpendicular to the magnetic field should be more clearly observed. However, it is also expected that the linewidths for Cholestane will be larger than for Tempone.

When nematic ZLI-4792 had been gelled with the Kato gelator, as predicted the nematic director will be disordered in three dimensions and so its ESR spectrum should corresponds to a three-dimensional powder pattern. Figure 12 shows the spectrum for gelled ZLI-4792 and we can clearly see its powder-like form which comes from the sum of spectra of director parallel (labelled 2) and perpendicular (labelled 1) to the field and intermediate of its all orientations. The perpendicular peaks are more intense than the parallel, indicating that more of the director is perpendicular to the magnetic field, or in other words, a random three-dimensional disordering of the director has been achieved. Under consideration with director distribution function (explained in Chapter II), the value of a which corresponds to the parameter controlling the director order parameter, takes value of unity.

To simulate the ESR spectrum, some important parameters have to be measured first. From the original ESR spectrum, we could obtain the values

for $\tilde{A}_{\parallel}$, $\tilde{A}_{\perp}$ and the three linewidths, each represents the three main peaks. The a value is a variable parameter and is up to be amended to control the director distribution function employed to simulate the ESR spectrum. These values are included in calculations involving the lineposition and lineshape equations that have been mentioned in Chapter II. The simulation of this spectrum is shown in Figure 13 and the parameters used in order to simulate the spectrum are included in its caption.

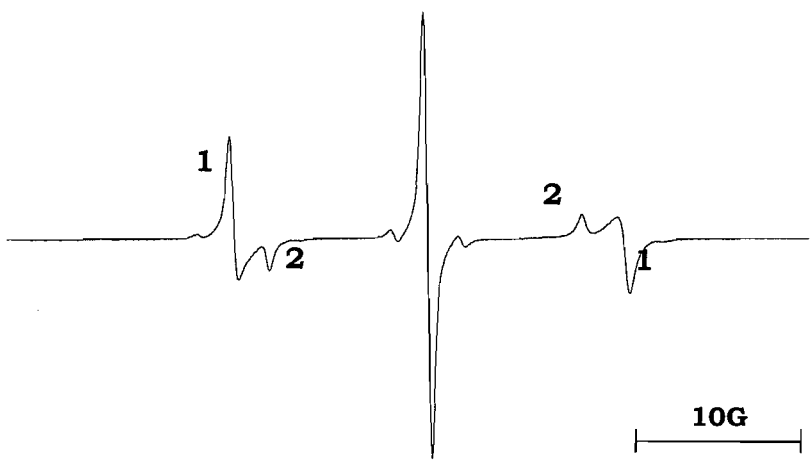

Figure 12 : The ESR spectrum for Tempone in gelled ZLI-4792 at room temperature. The satellite peaks originating from ^{13}C and ^{15}N isotopes still could be seen.

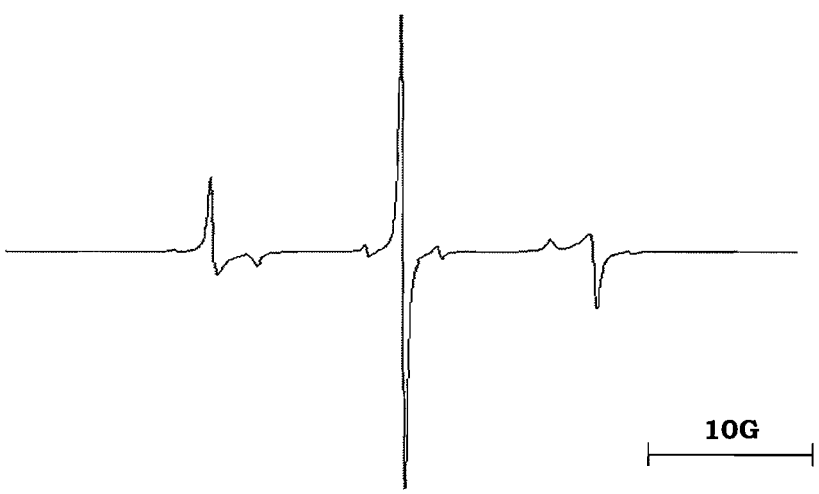

$$\tilde{A}_{\parallel} = 12.16G, \tilde{A}_{\perp} = 15.88G, T_2^{-1}(-1) = 0.30G, T_2^{-1}(0) = 0.30G, T_2^{-1}(1) = 0.36G, a = 1.0$$

Figure 13 : The simulated ESR spectrum for a uniaxial-gelled ZLI-4792 based on Lorentzian lineshape.

The simulated ESR spectrum shows a good agreement with the experimental spectrum. From here we could conclude that the director ordering is disrupted to give a random director distribution in a gel nematic system. The parameter which controls the director ordering, *a*, is unity for the simulated spectrum in Figure 13. The values of $\widetilde{A}_{\|}$ and $\widetilde{A}_{\perp}$ for this gelled system, if compared with the non-gelled system are not really different, and this small difference might result from the dissimilarity in the director ordering between the initial system of perfectly director alignment to the random director alignment.

The gelled ZLI-4792 then was heated from room temperature (~300K) to the nematic-isotropic transition temperature (~380K). Figure 14 shows the ESR spectra of the Tempone spin probe in gelled ZLI-4792 as temperature increases from 300K to 380K every 10K. The order parameter, $\overline{P}_2$, varies with temperatures and we do see the associated changes in the ESR spectra as the temperature increases. The parameter, *a*, in the director distribution increases with temperature, so that the director distribution becomes more ordered by the magnetic field. The ESR spectrum changes gradually with temperature from 300K to 340K where we clearly see the changes in the value of $\widetilde{A}_{\|}$ and $\widetilde{A}_{\perp}$. As it reaches 350K, the ESR spectrum shows a two-dimensional like pattern in that the parallel and perpendicular peaks have similar intensities before it transforms to a three lines spectrum at 360K corresponding to the formation of the isotropic phase.

This two-dimensional ESR spectrum is recognized when the parallel and perpendicular peaks are similar in height and these are related to the probability of finding the director parallel and perpendicular to the field is equal. At 360K, the three main peaks are broader than before, which might be caused by the presence of a biphasic region for ZLI-4792. This liquid crystal is a mixture of several components, as a consequence, the transition from the nematic to the isotropic phase occurs through a biphasic region where nematic and isotropic phases necessarily coexist with the amount of nematic phase decreasing with increasing temperature. From ESR spectra in Figure 14, the isotropic phase is clearly seen when the sample is heated to

370K and 380K. The hyperfine spacing between two outer peaks of ESR spectrum for isotropic phase is 29.5G.

We let the sample stay in the isotropic phase at 380K for 10min before we cooled it back to the nematic phase. Figure 15 shows the ESR spectra measured for every 10K during the cooling process. The powder pattern ESR spectra are gradually seen when the sample becomes nematic. However, the clear observation here is the ESR spectra starts to show the two-dimensional distribution, from 360K decreasing to 300K. In addition, the approximation of $\tilde{g}_{\parallel} = \tilde{g}_{\perp}$ is no more accurate since the difference, $\left|\tilde{A}_{\parallel} - \tilde{A}_{\perp}\right|$ at higher ESR field is greater than that of lower ESR field. At 300K, the ESR spectrum still shows the 2D distribution, which is totally different to the ESR spectrum recorded when the sample just started to be heated. We do not, so far have an explanation for the strong hysteresis in the director distribution function. However, the cooling process are performed in the presence of the magnetic field. Therefore, the magnetic field might be responsible for the alignment of the liquid crystal director, which keeps the director distribution to be 2D, and not 3D as expected.

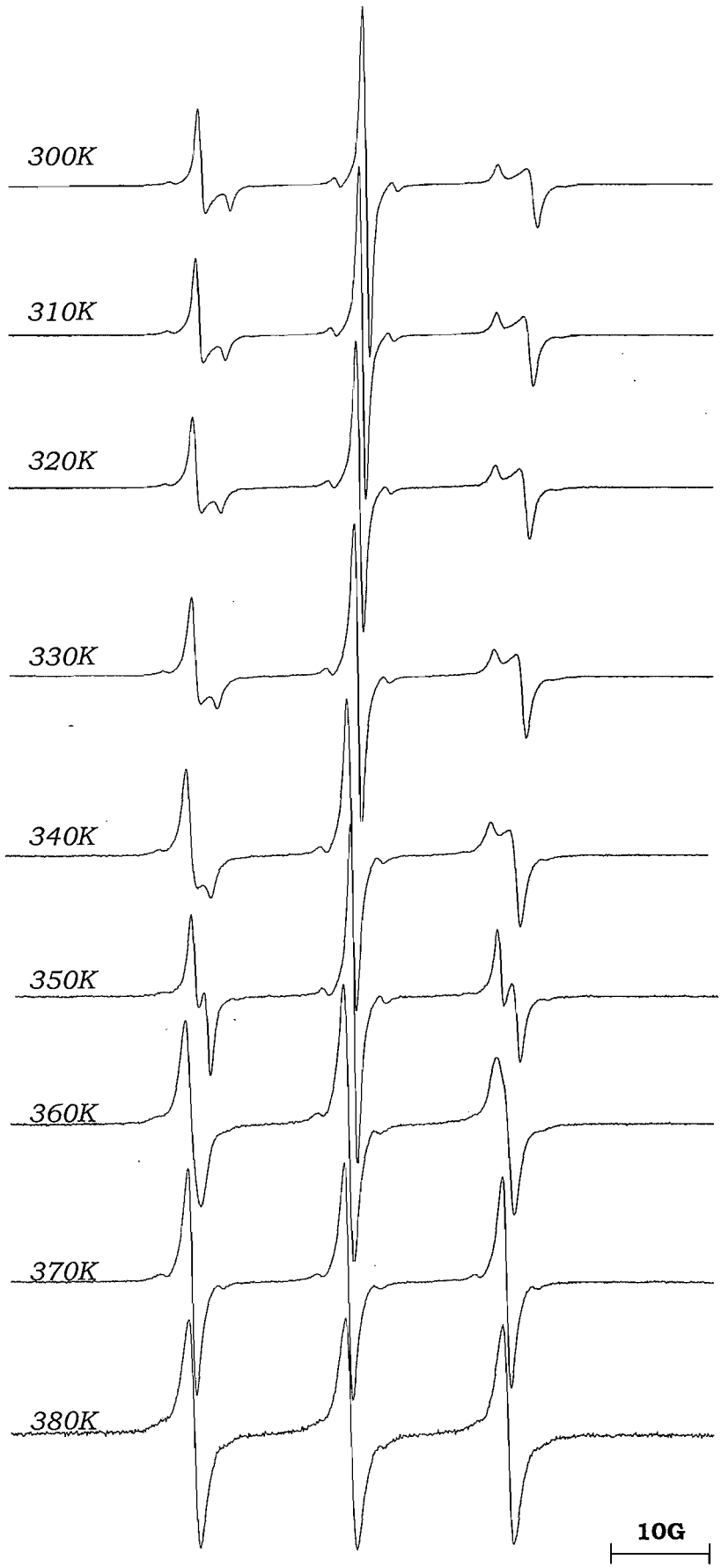

Figure 14 : The temperature dependence of the ESR spectra for the Tempone spin probe in gelled ZLI-4792 (heating).

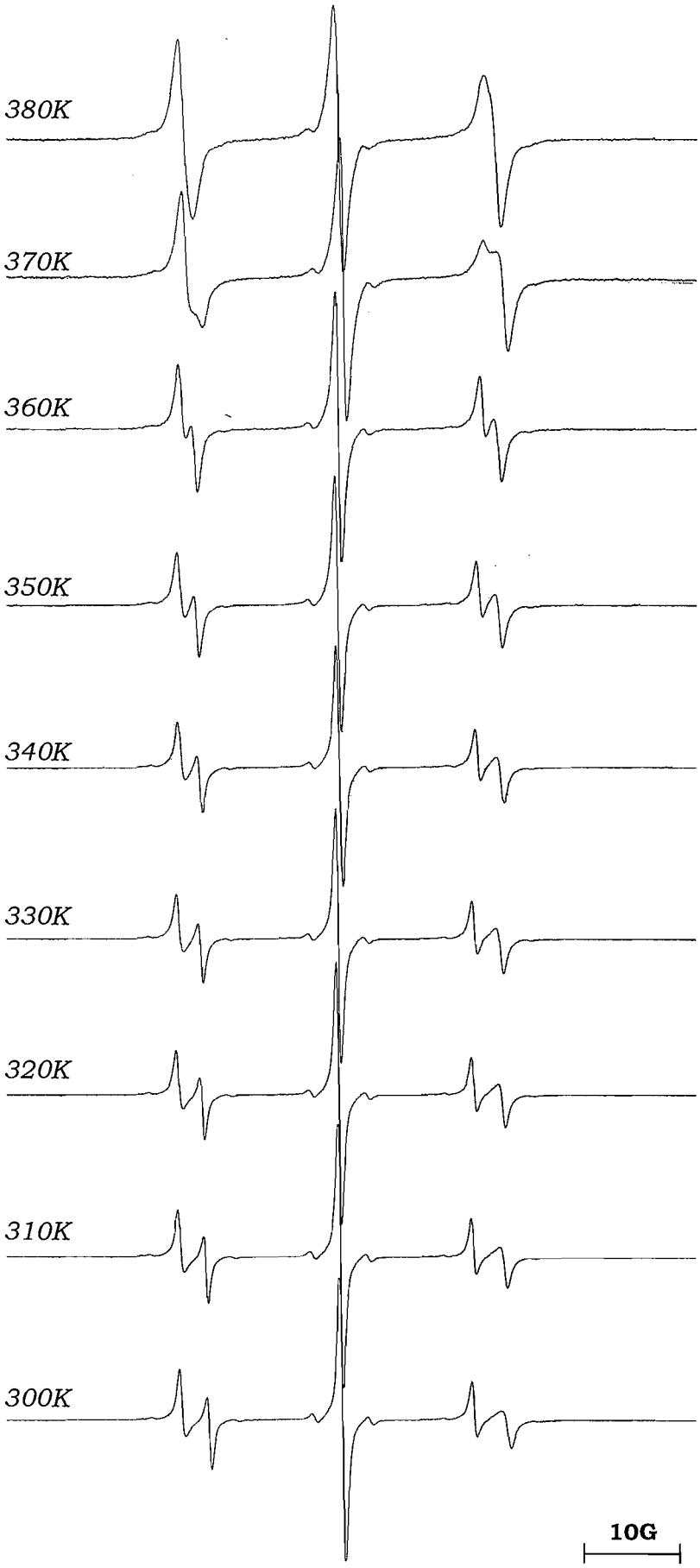

Figure 15: The temperature dependence of the ESR spectra for the Tempone spin probe in gelled ZLI-4792 (cooling).

5.5.2 Gelation of Nematic 2,3,4-trihexyloxycinnamic Acid

The mesogen *2,3,4-trihexyloxycinnamic acid* (compound C) was synthesized by Mr. Richard Parker, following the preparation methods reported by *Fan et al.* [25].

Originally, this cinnamic acid derivative was designed by *Praefcke* from the Institute of Organic Chemistry, Technische Universitat Berlin. Classified as a thermotropic liquid crystal, compound C was reported to exhibit biaxial nematic phase based on conoscopic and X-ray diffraction experiments. This compound had been claimed to form a biaxial nematic [25] phase with transition temperatures, $T_{CrN_B} = 51.2°\,C$ and $T_{N_BI} = 59.7°\,C$, but studies using deuterium NMR spectroscopy had shown that the nematic phase was in fact uniaxial. During this period, there were several thermotropic liquid crystals which were claimed to form biaxial nematic phase according to conventional methods, but they were all strongly disagree with the results of deuterium NMR experiments (see Section 5.4).

2,3,4-trihexyloxycinnamic acid was prepared in a simple two-step process. The compound *2,3,4-trihydroxybenzaldehyde*, was first alkylated on the hydroxyl groups (Figure 16), then reacted with *malonic acid* (Figure 17) to produce compound C.

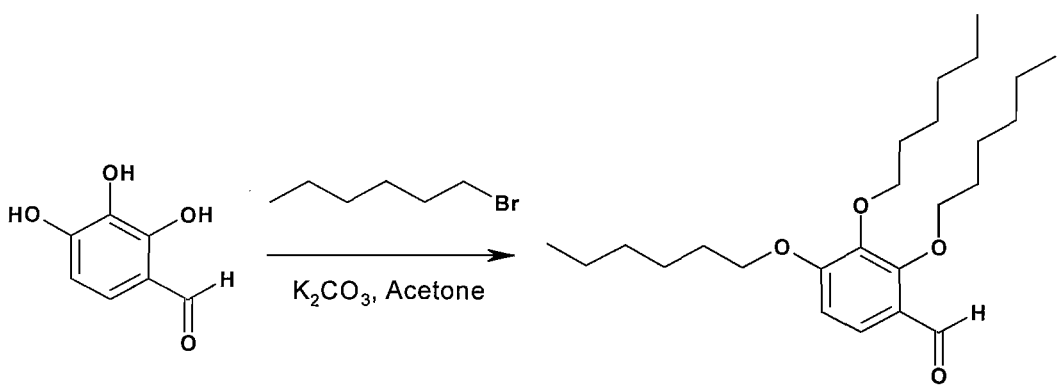

Figure 16: Preparation of 2,3,4-trihexyloxybenzaldehyde.

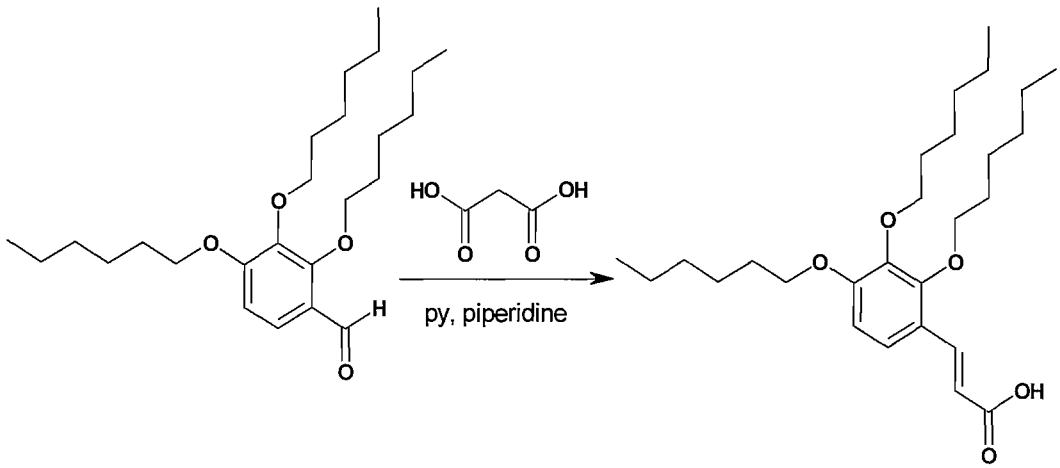

Figure 17: Preparation of 2,3,4-trihexyloxycinnamic acid.

In this reaction, *piperidine* was added to initiate the reaction, while 2,3,4-trihexyloxybenzaldehyde and *malonic acid* were dissolved in *pyridine*. Then, the mixture was heated at 100° C for 5h in an oil bath. Afterwards, the reaction mixture was cooled and then poured onto a mixture of ice and concentrated *hydrochloric acid,* until the mixture had a pH of 2, before being left to stir for another 30min. The solid product was collected by filtration and it was recrystallized using *acetonitrile* as the solvent to give a white crystalline solid.

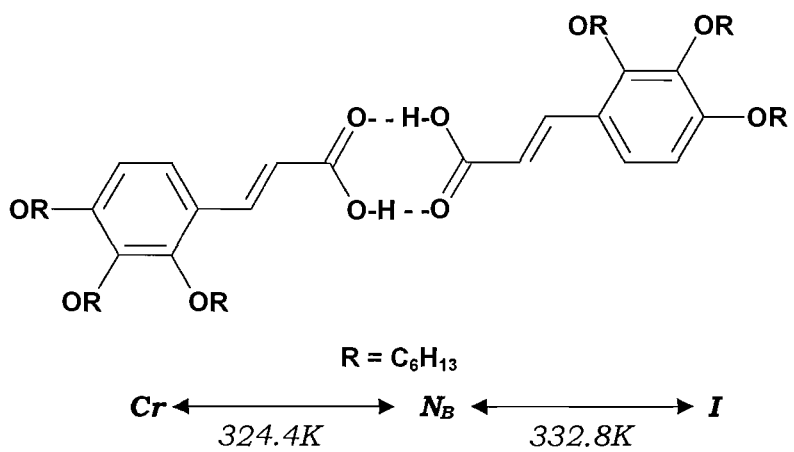

Figure 18: Chemical structure of 2,3,4-trihexyloxycinnamic acid with its transition temperatures, T_{CrN_B} and T_{N_BI}.

Since the NMR technique with the director randomly distributed failed to observe a phase biaxiality for this nematogen [25], so that we are looking for an alternative method which we think quite convincing, but only works if the examined compound has a high degree of biaxiality, $\tilde{\eta} > 0.4$. ESR spectroscopy is the other method that we meant for determining the phase biaxiality.

We used the *Kato* gelator to gel this compound. The methods and amount of chemicals used in this experiment were the same as those used to gel nematic ZLI-4792. However as a spin probe, we used Cholestane for this ESR experiment instead of Tempone. This because Cholestane gives a greater difference between parallel and perpendicular peaks in the spectrum, so we could use this opportunity to see the signals for the three director orientations to characterize a biaxial phase. However, it does not mean that Cholestane is better spin probe than Tempone for this study because the linewidths for Cholestane are far broader than Tempone, so the resolution may be reduced. The gelled nematic compound C was a colourless jelly-like material which physically looked static and does not flow inside the sample tube, since it has a high viscosity. The gelled compound C was heated from the nematic gel phase at 318K until all compound turned to isotropic phase. The ESR spectra were recorded as increasing temperature and each spectrum was simulated in order to find the agreement between the experimental results and theory. ESR spectra with its spectral simulation are shown in Figure 19. The parameters used in the simulations are listed in Table 3.

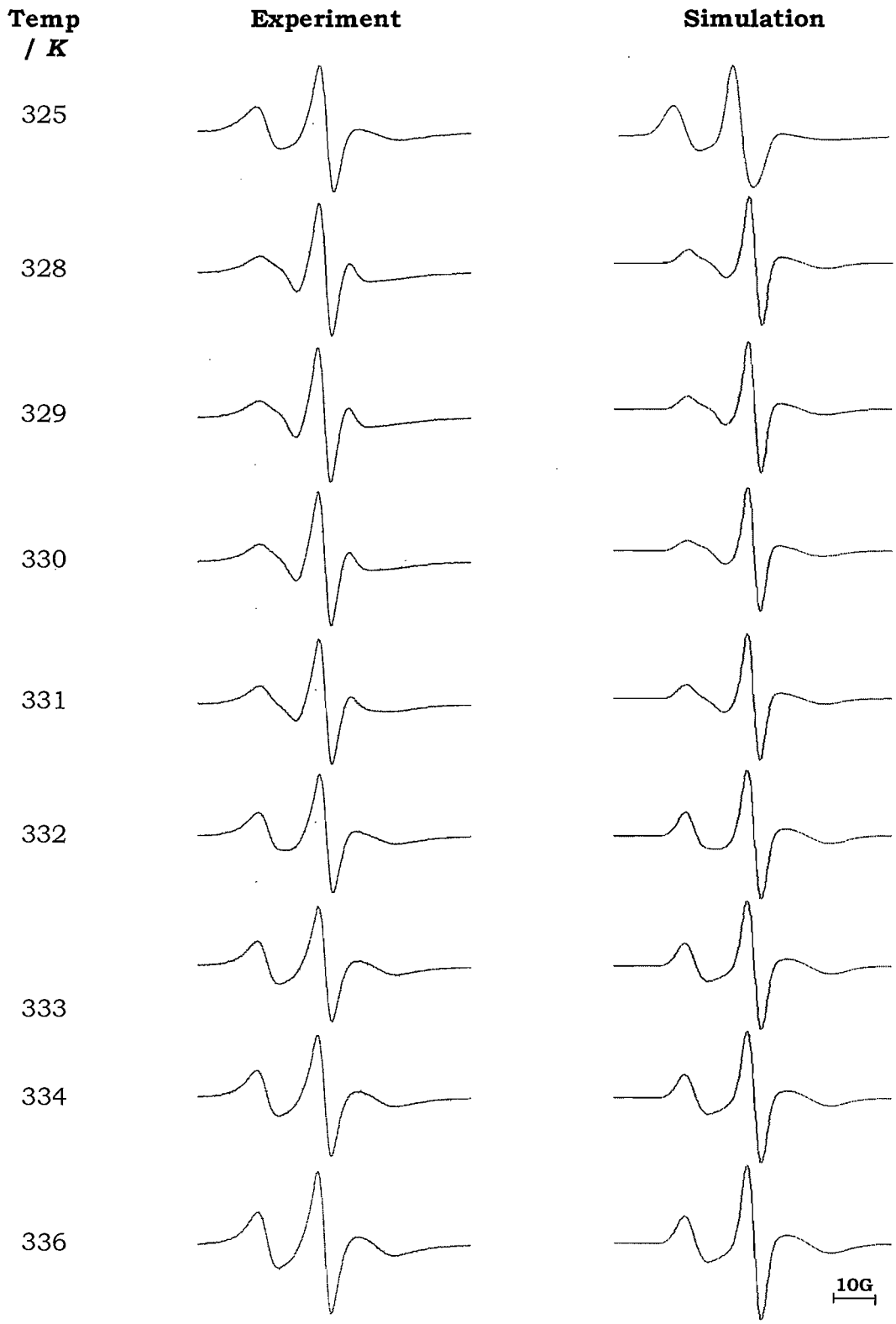

Figure 19: The temperature dependence of the ESR spectra for the spin probe in the gelled mesogen 2,3,4-trihexyloxycinnamic acid with the simulated ESR spectra.

Table 3: The parameters and data used to simulate the ESR spectra shown in Figure 19.

Temp / K	$\widetilde{A}_{\parallel}/G$	$\widetilde{A}_{\perp}/G$	$T_2^{-1}(-1)$ /G	$T_2^{-1}(0)$ /G	$T_2^{-1}(1)$ /G	a	$\widetilde{g}_{\parallel}/G$	$\widetilde{g}_{\perp}/G$
325	12.0	21.0	4.2	2.8	15.0	1.0	2.0027	2.0075
328	9.0	18.0	2.5	1.8	5.5	2.1	2.0027	2.0027
329	9.0	18.0	2.5	1.8	5.5	2.2	2.0027	2.0027
330	9.0	18.0	2.8	1.8	5.5	2.3	2.0027	2.0027
331	9.0	18.0	2.5	1.8	5.5	1.9	2.0027	2.0027
332	9.0	18.0	2.5	2.0	5.5	1.2	2.0027	2.0027
333	9.0	18.0	2.7	2.0	5.5	1.0	2.0027	2.0027
334	9.0	18.0	2.7	2.0	5.5	1.0	2.0027	2.0027
336	9.0	18.0	2.7	2.0	5.5	1.0	2.0027	2.0027

We measured the ESR spectrum as a function of increasing temperature, starting when the mixture was in the nematic phase. At 325K, the ESR spectrum looks like a solid powder pattern distribution, so at this stage, the sample might be in the mixture of the crystal and nematic phase. The real change in the ESR spectra of the mesogen occurs when the temperature reached 328K. The changes includes those in $\widetilde{A}_{\parallel}$, $\widetilde{A}_{\perp}$, the three linewidths and the value of *a*. The nematic phase is reached at 328K where we see the appearance of five peaks in the ESR spectrum which come from director parallel and perpendicular to the magnetic field, with some director alignment by the magnetic field; the value of *a* is certainly larger than 1. As the sample temperature increased from 329K to 331K, we do not see the obvious changes in the ESR spectrum but at 332K, from the simulated ESR spectra, we know that the value of *a* has decreased, showing that the nematic phase is approaching the transition to the isotropic phase. We believed the whole sample becomes isotropic at 333K, due to the hyperfine spacing between the two outer peaks, ~30G.

For a uniaxial liquid crystal, a random director alignment would show an ESR spectrum containing five main peaks, where four of them are corresponding to the director being parallel and perpendicular to the field. Nevertheless, in biaxial liquid crystal, we expected to observe seven main peaks in the ESR spectrum, since in the biaxial system, there are three director orientations, so that the signal could come from the X, Y or Z-axis. From this experiment, we do not observe more than five signals from the ESR spectra, which meant ESR does not give any evidence of biaxiality for this

compound. This experiment is kind of confirming the report made by *Fan et al.* The method for determining biaxiality using ESR spectroscopy might be novel but can be developed to at least confirm the experimental results that have been performed by other characterization methods. Compound C or 2,3,4-trihexyloxycinnamic acid, so far is classified as uniaxial nematic compound.

5.6 Conclusion

The gelator has produced gels in the liquid crystal host, forming fibrous networks which held together by hydrogen bonds between the gelator molecules. Upon heating and cooling, these hydrogen-bonded gelators do not dissolve and the fibrous network remains present until it reaches the isotropic phase. This stable gelled nematic phase also can keep its disordering system for months without any disruption in the absence of magnetic field. The strong interaction in the gels system suggests the pure gelator is actually trapping the liquid crystal to form the physical gels.

ESR spectroscopy has confirmed the disruption of liquid crystal alignment by the formation for these gel structures. The amount of 0.5wt% of gelator could abruptly disturb the director alignment, which we demonstrated with the studies on gelled nematic ZLI-4792. The random director alignment confirmed our prediction of the nematic being trapped in the pockets of the gel network. Upon heating and cooling, the gelled ZLI-4792 shows quite an interesting results where we found a strong hysteresis for ESR spectra for cooling process; they do not match with the spectra for heating process at the same temperature; they change from 3D to a 2D director distribution. The alignment by magnetic field might be responsible for this behaviour.

Our approach to determine the biaxiality in the mesogen 2,3,4-trihexyloxycinnamic acid was unsuccessful, in the sense, we observed the same ESR signals as for the uniaxial nematic. However, this confirms the findings obtained by *Fan et al.* where the NMR technique also found the biaxiality for the same compound as zero. The ESR technique might be novel for the biaxiality confirmation, but could help to determine biaxiality. At least

for a high degree of biaxiality, $\eta > 0.4$ which the ESR spectrum starts to show the seven hyperfine peaks from the three different director orientations.

5.7 References

[1] R. G. Larson; *The Structure and Rheology of Complex Fluids*, Oxford University Press, New York (1999).

[2] P. G. de Gennes; *Scaling Concepts in Polymer Physics*, Cornell University Press, Ithaca (1979).

[3] A. E. Alexander, P. Johnson; *Colloid Science*, Clarendon Press, Oxford (1949).

[4] E. Hatschek; *An Introduction to the Physics and Chemistry of Colloids*, J & A. Churchill, London (1925).

[5] A. G. Ward; *Colloids: Their Properties and Applications*, Blackie & Son Ltd, London (1945).

[6] A. Aggeli, I. A. Nyrkova, M. Bell, R. Handing, L. Carrick, T. C. B. McLeish, A. N. Semenov, N. Boden; *PNAS,*. **98**, 11857 (2001).

[7] G. W. Gray; *Thermotropic Liquid Crystals*, Wiley, Chichester (1987).

[8] G. P. Crawford, S. Žumer; *Liquid Crystals in Complex Geometries: Formed by Polymer and Porous Network,* Taylor and Francis, London (1996).

[9] N. Mizoshita, K. Hanabusa, T. Kato; *Adv. Mater.*, **11**, 392 (1999).

[10] N. Mizoshita, T. Kutsuna, K. Hanabusa, T. Kato; *Chem. Commun.*, **1999**, 781 (1999).

[11] T. Kato; *Science.*, **295**, 2414 (1997).

[12] T. Kato, N. Mizoshita, K. Kishimoto; *Angew. Chem. Int. Ed.*, **45**, 38 (2006).

[13] K. Kanie; *J. Mater. Chem.*, **11**, 2875 (2001).

[14] T. Kato; *Struct. Bonding (Berlin)*, **96**, 95 (2000).

[15] T. Kato, H. Kihara, U. Kumar, T. Uryu, J. M. J. Fréchet; *Angew. Chem. Int. Ed. Eng.*, **33**, 1644 (1994).

[16] T. Kato, T. Kutsuna, K. Hanabusa, M. Ukon; *Adv. Mater.*, **10**, 606 (1998).

[17] G. R. Luckhurst; *Thin Solid. Films.*, **393**, 40 (2001).

[18] G. R. Luckhurst; *Thin Solid Films,*. **506**, 36 (2006).

[19] G. R. Luckhurst; *Angew. Chem. Int. Ed.*, **44**, 2 (2005).

[20] G. R. Luckhurst; *Nature.*, **430**, 413 (2004).

[21] M. J. Freiser; *Phys. Rev. Lett.*, **24**, 1041 (1970).

[22] J. Malthete, H. T. Nguyen, A. M. Levelut; *J. Chem. Soc. Chem. Commun.*, 1548 (1986).

[23] S. Chandrasekhar, B. R. Ratna, B. K. Sadashiva, V. N. Raja; *Mol. Cryst. Liq. Cryst.*, **165**, 123 (1988).

[24] K. Praefcke, B. Kohne, B. Gundogan, D. Singer, D. Demus, S. Diele, G. Pelzl, U. Bakowski; *Mol. Cryst. Liq. Cryst.*, **198**, 393 (1991).

[25] S. M. Fan, I. D. Fletcher, B. Gundogan, N. J. Heaton, G. Kothe, G. R. Luckhurst, K. Praefcke; *Chem. Phys. Lett.*, **204**, 517 (1993).

[26] A. Ferrarini, G. R. Luckhurst, P. L. Nordio, E. Spolaore; *J. Chem. Soc. Faraday Trans.*, **91**, 3177 (1995).

[27] G. R. Luckhurst; *British Liquid Crystal Society Bulletin Aug. 2005*, http://www-g.eng.cam.ac.uk/photonics/blcs/blcsnew.html (2005).

[28] I. Dierking; *Textures of Liquid Crystal*, Wiley-VCH, Weinheim, 171 (2003).

[29] L. A. Madsen, T. J. Dingemans, M. Nakata, E. T. Samulski; *Phys. Rev. Lett.*, **92**, 145505 (2004).

[30] N. Boccara, R. Medjani, L. de Seze; *J. Phys.*, **38**, 149 (1977).

[31] B. Berardi, C. Zannoni; *J. Chem. Phys.*, **113**, 5971 (2000).

Chapter VI

Nematics in Confined Geometries

6.1 Introduction

The term porous is used to describe a material with pores, while porosity is a measure of the void spaces in a material. A porous medium or a porous material is a solid (often called frame or matrix) permeated by an interconnected network of pores (voids) filled with a fluid (liquid or gas). Both the solid matrix and the pore network (also known as the pore space) are assumed to be continuous, so as to form two interpenetrating continua such as in a sponge.

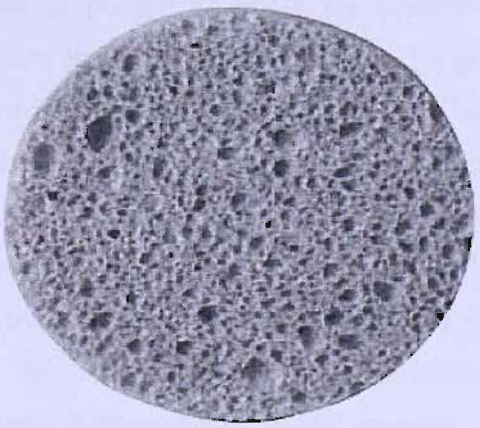

The concept of porous media with confined geometries is used in many areas of applied science and engineering such as mechanics (acoustics, geomechanics, soil mechanics, rock mechanics), engineering (petroleum engineering, construction engineering), geosciences (hydrogeology, petroleum geology, geophysics), biology and biophysics as well as in material science [1].

Not only that, fluid flows through porous media has becoming a topic of most common interest and has emerged a separate field of study. The physics of fluids in confined geometries has become an extraordinarily rich subject to date. The structure and ordering, phase transitions, order parameter fluctuations and dynamics of molecular motion have been effectively studied during the past decade. At the same time, liquid crystals in confined geometries have turned out to give the most significant developments in this field. It is difficult to anticipate how any fluid or liquid crystal would behave when it is infused into a porous host. One thing for sure, their behaviour in the confined matrix will be totally different with that when they are in the bulk. This had been confirmed with the previous studies on the state of these fluids when they were in the constraining pores [1].

In this Chapter, we are interested in the study of the liquid crystal phase in a porous glass as the host matrix, employing electron spin resonance (ESR) spectroscopy to investigate the phase behaviour and the director alignment of the liquid crystal in the presence of the ESR magnetic field. All of the results presented in this Chapter are novel for ESR measurements on the confined system. Nevertheless, the field of confined systems is not new but has generated such a promising and appealing results from previous studies. These investigations are of potential value for display devices. In fact, the field of liquid crystals in confined geometries is largely responsible to the discovery and development of polymer-dispersed liquid crystals (PDLC) display device [2] which is simply described in the next Section. Section 6.3 and 6.4 present information of liquid crystals in porous materials and ESR spectroscopy of confined mesogens, respectively. The experimental ESR spectra and their spectral simulations can be found in Section 6.5. Lastly, Section 6.6 discusses the results of deuterium NMR studies which were carried out for deuteriated 8CB confined in the porous material.

6.2 Polymer Dispersed Liquid Crystals

There have been intense research studies on materials of polymer-dispersed liquid crystals (PDLCs) since 1980s. In principle, PDLCs provide a wide range of new applications beyond existing liquid crystal technologies include large-scale flexible displays and switchable coatings for windows, to be used for controlling daylight or interior lighting, privacy, cosmetics, solar heat gains, security, etc [3].

In a PDLC device, liquid crystal droplets are dispersed in a solid polymer matrix and this results a sort of *'Swiss cheese'* polymer with isolated liquid crystal droplets filling in the holes of the cheese. These micron-size droplets are responsible for the unique behaviour of the material and the intensity of transmitted light throughout the polymer varied by changing the orientations of the nematic director with an electric field. Figure 1 shows a construction of a 10 – 25μm thick film of PDLC material between transparent conducting electrodes [4]. In the opaque state, nematic droplets with positive dielectric anisotropy are randomly oriented as can be seen in Figure 1(a) where the film has a translucent white appearance because of the light scattering properties of the droplets. Upon application of the electric field, the nematic droplets align in a direction parallel to the field (Figure 1 (b)). The light scattering then stops provided the refractive index, $n_{\perp}$ (index perpendicular to the nematic director) approximately matches the refractive index of the polymer matrix. Upon removal of the field, the droplets return to their original random orientation and the film returns to its opaque state. The opaque state can be switched to the clear state by changing the temperature across the film to a value above the nematic-isotropic phase transition, as shown in Figure 1(d).

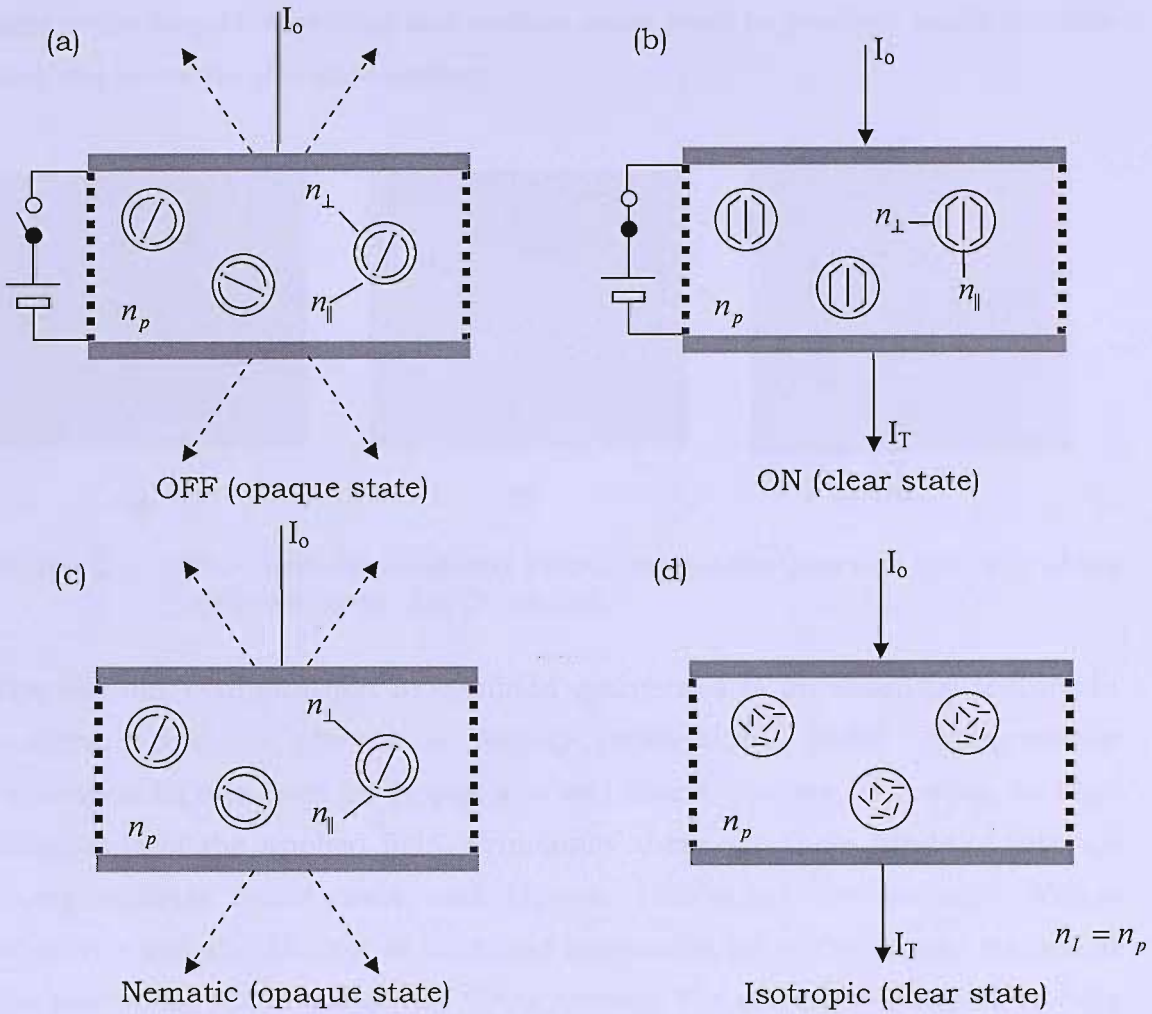

Figure 1: *Schematic for PDLC light shutter illustrating the opaque state (a) and (c), the electro optically switched transparent state, (b), with droplets and the thermally switched transparent state, (d), with the droplets in the isotropic phase.*

PDLCs materials can be prepared in several different ways but phase separation methods are the most convenient to do that. There are three common ways for separation methods; polymerization, thermal processes and solvent evaporation. Each method is possible to produce liquid crystal droplets of a uniform and predetermined size and shape in order to optimize the specific electro-optic properties. Figure 2 shows the pictures of liquid crystal droplets obtained by phase separation using thermal processes. In this method, a homogeneous mixture of the melted polymer and a liquid crystal is formed. To induce phase separation, the mixture is cooled at a specific rate and then the liquid crystal droplets begin to form as the polymer hardens. The cooling rate of the polymer melt and liquid crystal mixture

affects the droplet size. The fast cooling rates tend to produce small droplets and vice versa for the slow cooling.

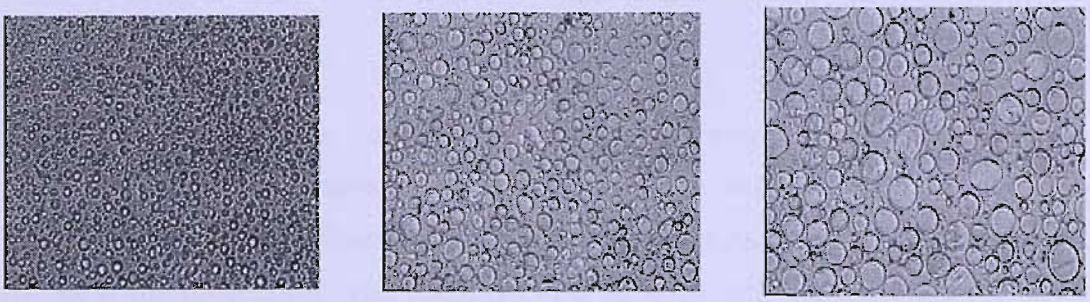

(a) (b) (c)

Figure 2: The thermally induced phase separation process taken at three different times, (a), (b) and (c).

The director configuration in confined geometries is an essential feature in understanding the physics of display applications. These configurations depend on factors such as droplet size and shape, surface anchoring, and the magnitude of the applied field. Principally there are three kinds of director configurations; radial, axial and bipolar. The radial configuration occurs when the nematic director is anchored perpendicular to the droplet walls and the point defect is in the centre of the droplet. The axial configuration results when the director is oriented perpendicular to the droplet wall, with a weak surface anchoring. It creates a line defect that runs along the equator of the spherical droplet. The bipolar configuration is obtained with tangential anchoring of director and this creates two point defects at each pole of the droplet. This is the most dominant configuration studied to date. These three director configurations in the droplets are shown in Figure 3.

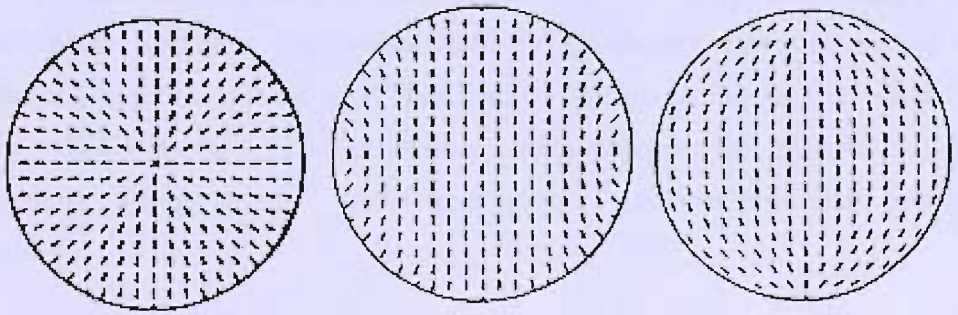

(a) (b) (c)

Figure 3: Types of director configuration in the spherical droplets, (a) radial, (b) axial, and (c) bipolar.

Even though there are many types of director configuration for a droplet of a typical PDLC sample, when an electric field is applied, the director within the droplets aligns along the field ($\Delta\tilde{\varepsilon} > 0$) and the systems have analogous optical properties.

Nowadays, PDLC films have features such as capability for sub-millisecond switching times, operation at low driving power, specifically less than $1\mu W/cm^2$, which is achievable with thermoplastics. It is also believed to be the best for projection type displays and in large flexible displays for outdoor and indoor use. The use of nematics in confined geometries is in fact becoming competitive with existing liquid crystal display technologies.

6.3 Liquid Crystals in Porous Glass Materials

The porous glass systems can be produced with definite pore diameters between a few nanometres up to several hundred nanometres and a narrow cavity size distribution. Porous materials, used as hosts for liquid crystals include controlled porous glass (CPG) [5], Anapore and Nucleopore membranes [6-8], Vycor glass [9], aerogels [10-14], or similar porous glass [15,16]. In CPG, the voids are cylindrically shaped, but are strongly curved and interconnected. While for Anapore and Nucleopore materials, the voids are long, straight and non-interconnected cylinders. CPG, Anapore and Nucleopore matrices are porous glass with a relatively narrow distribution of pore sizes. The construction of the Vycor glass is reminiscent of that of the CPG but with relatively large local departures from the cylindrical geometry. The voids for aerogels are separated by randomly interconnected silica strands forming the matrix, and this makes the geometry of the voids highly irregular. Of all these porous materials, aerogels have the highest degrees of randomness. Figure 5 to 7 show examples of porous materials previously described.

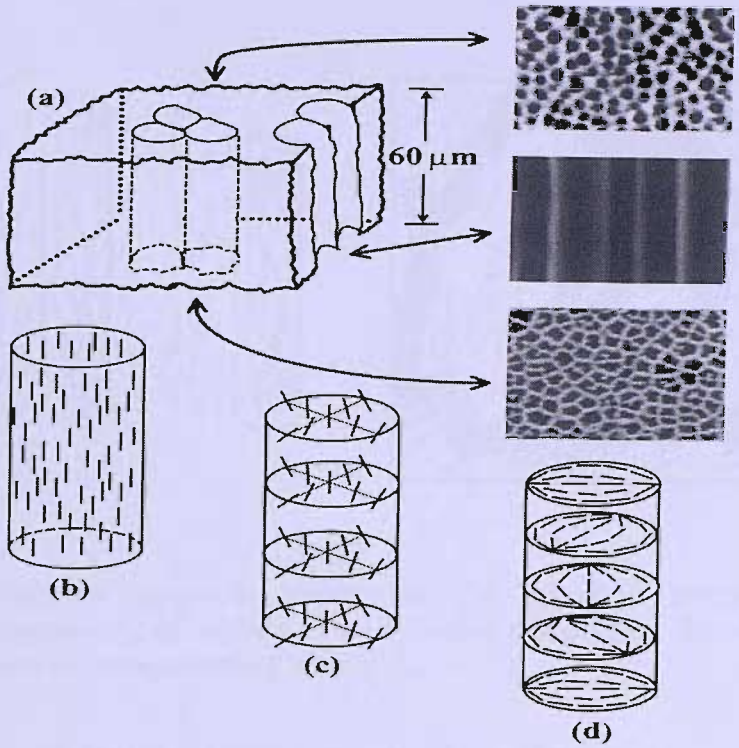

Figure 5: *Scanning electron microscope (SEM) photographs (a) of the Anapore microporous membrane with possible director configurations, (b) the parallel axial, (c) the tilted axial, and (d) the twisted bipolar in a channel.*

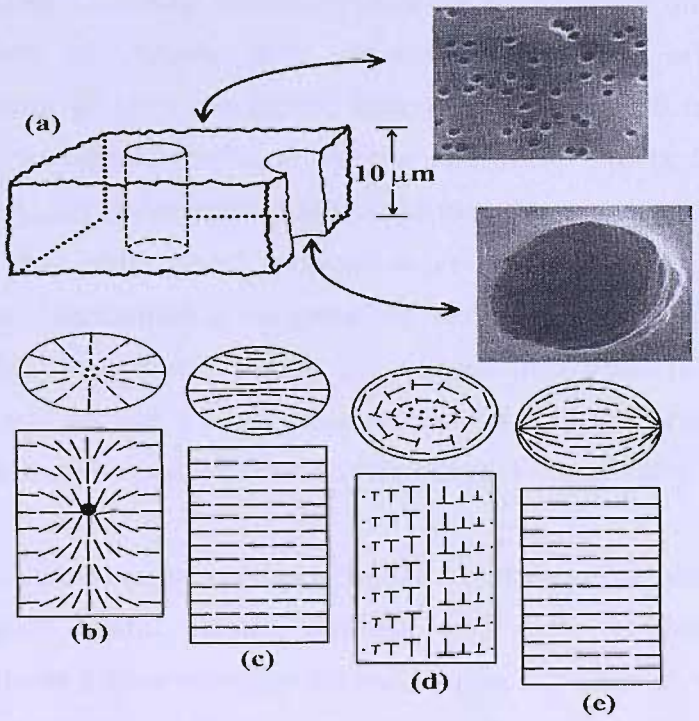

Figure 6: *Scanning electron microscope photograph (a) of a microporous Nucleopore membrane with various nematic director fields within a channel, (b) the escaped radial with point defects, (c) the planar-polar, (d) the escaped-twisted, and (e) the planar bipolar.*

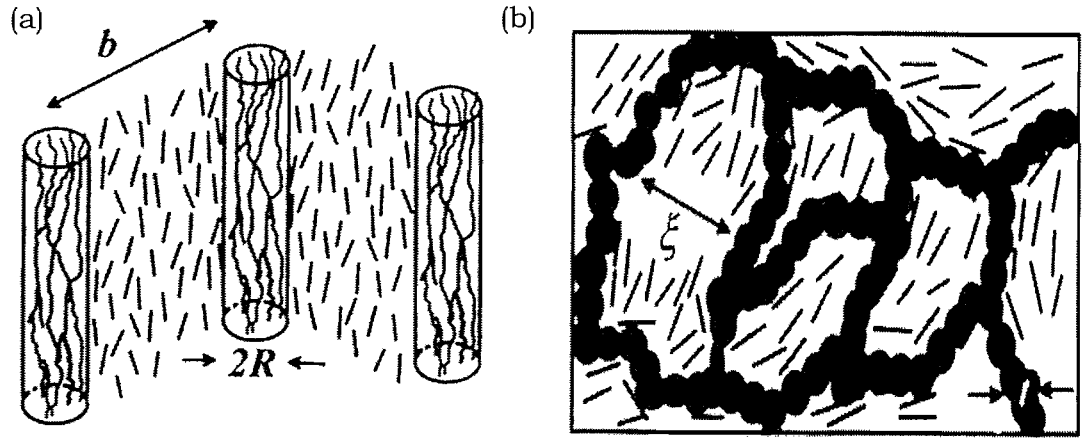

Figure 7: *Polymer network assemblies for (a) fibril morphology (pore segments) of radius R and lattice spacing b, (b) silica aerogels with a compartment size of ξ .*

The behaviour of liquid crystals immersed in the various geometries are actually complex, however they exhibit a richness of physical phenomena and their susceptibility to variations in geometry and size of the confining cavity is large due to the interaction between the liquid crystal and the surface of the host. Confined liquid crystals are particularly useful as (i) they exhibit a variety of phases with different degrees of orientational or translational order, (ii) they are typical representatives of soft materials (their response to perturbations induced by the confining matrix is pronounced and long ranged), (iii) there exist different kinds of transitions between these phases (e.g., first-order and second-order phase transitions in the orientational or translational degrees of order) specifically due to the curvature of the cavity walls and steric effects that tend to suppress the nematic phase and induce a large number of defects in the director field, and (iv) nematogens and the host matrix do not interact chemically.

The phase and structure of confined liquid crystals reflect the competition among the liquid crystal elastic, surface, and external field forces. The strength of all these forces strongly depends upon the size, d , characterizing the confining cavity. Figure 8 shows a cartoon for the confining cavity filled with liquid crystal. The earliest studies on nematics in confined geometries found homeotropic alignment for the liquid crystal director. This has been studied in detail by *Cladis* [17], *Meyer* [18] and *Saupe* [19]. However, there

are many possibilities for the nematic director fields in cylindrical cavities and the common configuration is designated as planar polar (PP) and planar radial (PR). The existence of this structure is expected to be stable but can vary depending on the cavity sizes as well as their shape. Figures 8 to 10 show sketches of the nematic director in random confinements.

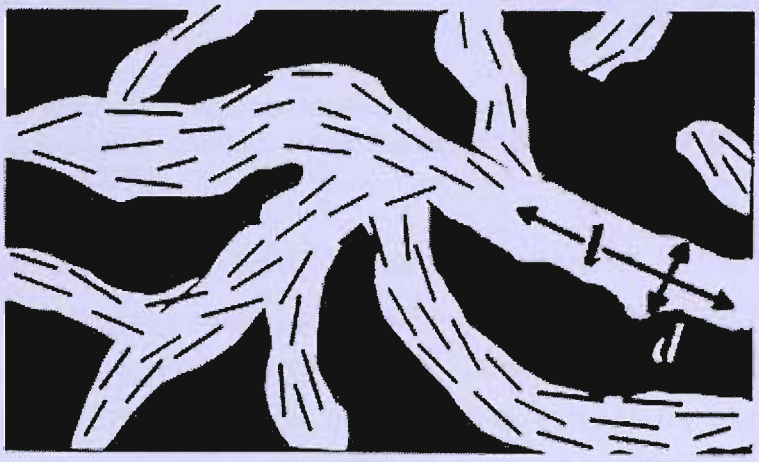

Figure 8: *A nematic under random confinement, with mean diameter, d, and length, l.*

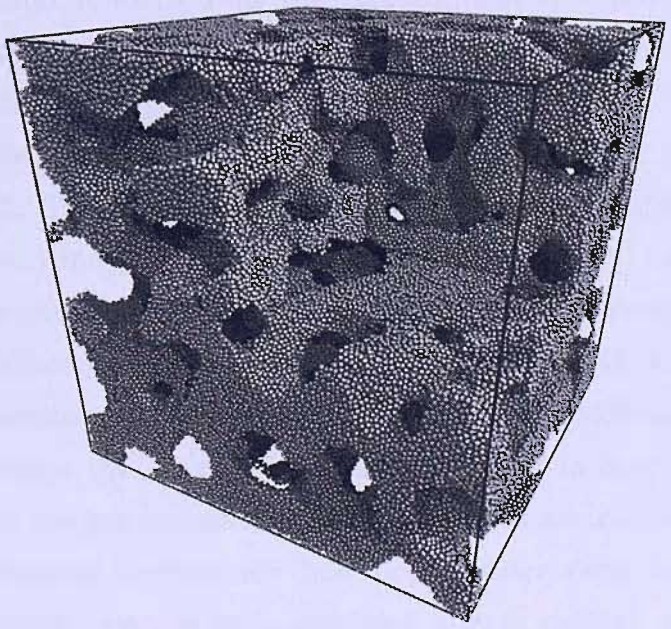

Figure 9: *A model of a controlled porous glass showing the intricately interconnected pore network running through the material [20].*

Figure 10: A schematic representation of possible nematic director fields in cylindrical cavities designated as planar polar (PP) and planar radial (PR).

From previous studies of liquid crystals distributed in various porous materials, there are some important results that are interesting for informing further investigations. For example, there exists a weak residual nematic ordering at the enclosing surface even at temperatures far above the bulk isotropic–nematic phase transition. This is caused by different competitive effects of the confining geometry which influence the formation of nematic order. A surface-induced nematic alignment can increase the nematic order in the cavities and tend to shift the nematic-isotropic phase transition to higher temperatures. It is appropriate to call the corresponding phase a paranematic rather than isotropic; similar order is induced by a magnetic field although the field here is homogeneous unlike that in a porous medium. Other than that, the nematic-isotropic transition temperature seems to be gradual for porous matrices with cavity sizes less than 0.1μm [21]. In these restricted geometries, the transition from nematic to smectic A phase is usually more affected by confinement rather than the nematic-isotropic transition. In addition, an additional slow relaxation mechanism is observed in confined samples that is not really seen when it is in the bulk. Most of these results are not yet completely understood and an intense research with different experimental techniques has been undertaken in the past and present since liquid crystals in a confined matrix exhibit such fascinating behaviour.

Different experimental techniques such as deuterium NMR [22-27], light scattering [10, 28], X-ray scattering [12], precision calorimetry [10, 29], and time-resolved grating optical Kerr effect experiments [30] have been used in

studies of confined liquid crystals in porous materials. Most of these techniques led essentially to the same conclusion that the behaviour of liquid crystals in porous matrices strongly depends on the mean characteristic pore sizes and their shapes as well as the anchoring properties of the internal surfaces for the director. Among the various techniques, deuterium NMR has been proved valuable and in combination with other experimental methods, to be very useful for this system to probe the orientational order and dynamics in confined systems, basically to study the director distributions, and probe the surface-induced order above the bulk transition [27].

The conclusions on the local molecular order from the measurement of macroscopic observation in random porous media actually are not straightforward. In a system of disordered nanometre pores, the orientation of the nematic director is determined by the geometry of the cavity walls, and in the simplest cases is either axial or radial to the pores. The influence of external fields on the director alignment can be neglected when the magnetic or electric coherence lengths of the nematogen at a reasonable field strengths are much larger than the cavity sizes [23]. This is in contrast to the measurement in the disordered porous materials for which NMR spectroscopic experiments yield powder pattern, which is a superposition of random orientations of the director inside the pores. From this powder pattern spectra, the director order parameter could be measured. NMR seems to be a tool well suited to probe director ordering and this has been reported in many publications. We present some of the NMR measurements on a CPG system at the end of this Chapter. We note that, we are interested in investigating the behaviour of liquid crystals distributed in porous materials using another form of magnetic resonance spectroscopy, namely electron spin resonance spectroscopy.

6.4 ESR Spectroscopy of Confined Mesogens

The nematic director in confined geometries such as CPG is not uniformly oriented, given that the topology of the porous structure is random. This is the hypothesis of this experiment under such conditions, the ESR spectrum will show a weighted sum of spectra from all director orientations with respect to the field. This has been explained in the Chapter II where the spectral analysis in terms of director distribution function is applicable; the lineshape is then given by

$$I(B) = \sum_m \int f(\theta) L(B, B_m(\theta), T_2^{-1}) \sin\theta d\theta, \tag{6.1}$$

where $f(\theta)\sin\theta d\theta$ is the probability of finding the director with an orientation between $\cos\theta$ and $\cos\theta + d\cos\theta$, and is given by

$$f(x) = \frac{a}{\left\{a^2 - \left(a^2 - 1\right)x^2\right\}^{\frac{3}{2}}}, \tag{6.2}$$

where $x = \cos\theta$ and θ is the angle made by the director with the field. a is the parameter which controls the orientational order of the director; it is infinite for a perfectly aligned system and unity for a director randomly distributed in three dimensions. Thus for nematic system dispersed in the pores, there is no doubt that the director distribution has a as 1, showing that the orientations of the director are random and a powder pattern ESR spectrum will be observed. This is equivalent to assuming that the magnetic field is unable to effect the random director distribution which as we shall see proves to be the case.

The other factor which influences the appearance of the ESR spectrum is the rate at which the molecular orientation of the spin probes with respect to the director changes. In the so-called fast motion limit when the rotational correlation time is smaller than 10^{-8}s the spectrum of the nitroxide spin probe will contain three lines with the hyperfine spacing being equal to the average of the total hyperfine tensor. This is normally the situation observed

in the bulk liquid crystal when the director is uniformly aligned. However, when the director is not uniformly aligned, the ESR spectrum of the spin probe will depend on how fast the director orientation and hence that of the probe changes with respect to the magnetic field. It is usually case that the director motion is slow so that the observed spectrum will be a sum of the spectra from all director orientations. At the other extreme in the slow motion limit when the correlation time is larger than 10^{-8}s the spectrum contains a weighted sum of spectra from all orientations. This is the so-called powder-pattern whose form is also determined by the orientational distribution function for the probe.

It is not possible to decide in advance of observing the ESR spectrum what form it will take since the rotational correlation times are not known. As on example of the influence of the correlation time on the spectrum we have measured the ESR spectrum of Cholestane in the conventional solvent *ortho-terphenyl* as a function of temperature; in this way we have been able to change the bulk viscosity which also changes the correlation time. The observed spectra are shown in Figure 11. At the highest temperature, of 333.1K, the ESR spectrum contains just three relatively sharp hyperfine lines with a hyperfine spacing of about 14.5G which is the isotropic average of the total hyperfine tensor. From this observation, it would seem that the system is in the fast motion limit with the correlation time for the spin probe being smaller than 10^{-8}s. At the other extreme temperature namely 299.1K the spectrum is quite different. First the linewidths are much larger and secondly the spacing between the outer two spectral lines is about 70G corresponding to a hyperfine spacing of 35G. This value is essentially the value of the component, of the total hyperfine tensor perpendicular to the oxazolidine ring. These results show that the motion of the spin probe is in the slow motion limit. This decrease in the rate at which the spin probe rotates is in keeping with the increase in the viscosity on lowering the temperature and passing into the glass phase. The growth in the linewidths and the increase in the hyperfine spacing are in keeping with the slowing down of the rate of rotation.

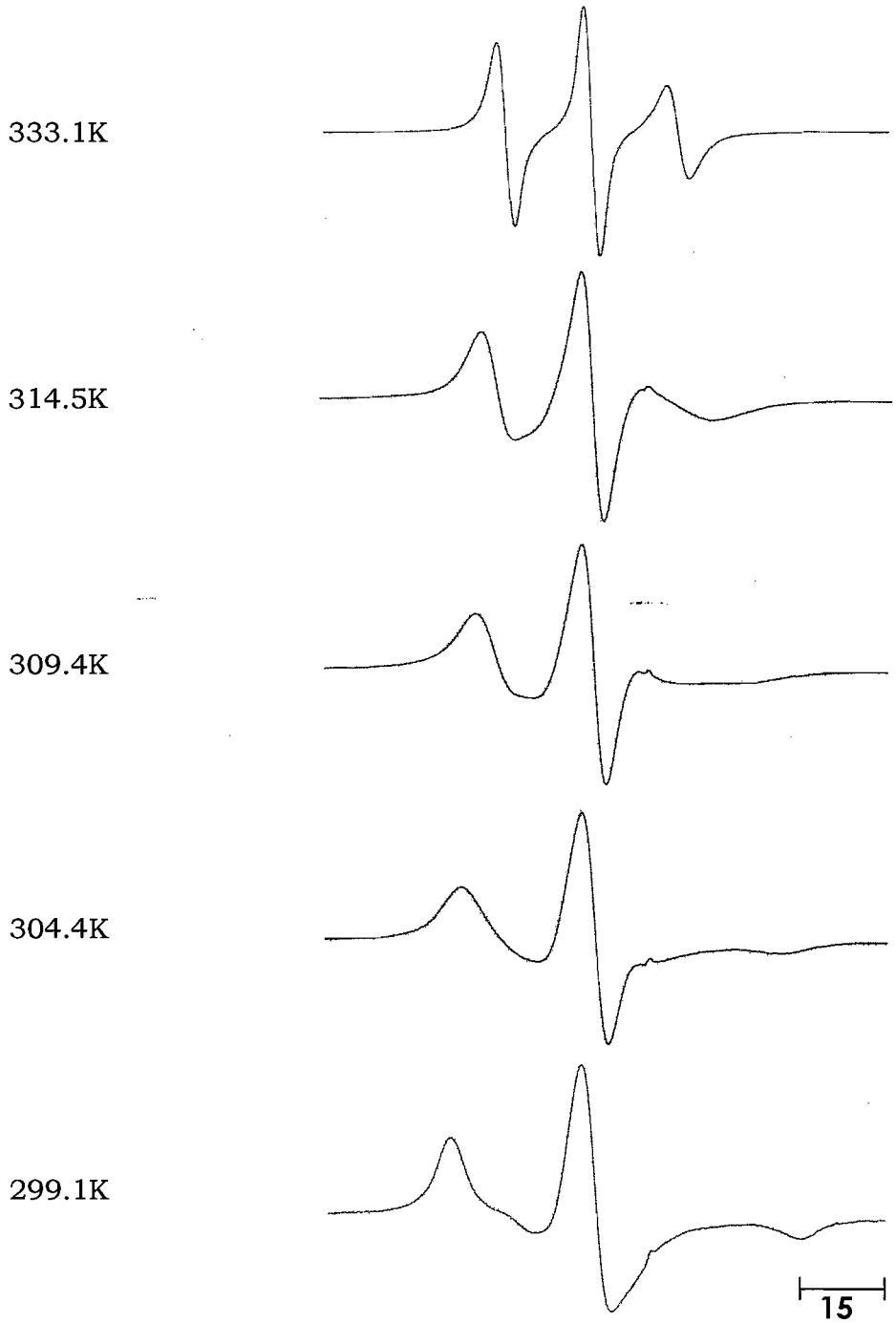

Figure 11: The ESR spectra for the Cholestane spin probe dissolved in o-terphenyl as the temperature is lowered from the liquid to the glassy phase.

There have been several studies of the theoretical analysis of ESR lineshapes in the slow or intermediate rotational region [32-35] which corresponds to rotational correlation times, τ_R, in the range 10^{-9}s to 10^{-6}s.

The slow tumbling theoretical method was developed for anisotropic liquids, starting with the stochastic Liouville equation of motion for the spin-density matrix. It is possible to interpret the ESR lineshape in terms of the relevant spin parameters to obtain information about the dynamics of the molecular reorientation process. The results of this theory, from a study by *Freed et al.* [36], are shown in Figure 12 for a range of rotational correlation times. It can be seen that for the smallest correlation time the simulated spectrum contains three relatively sharp lines. Then as the correlation time grows so new rather broad peaks appear in the spectrum and as the correlation time increases further so the lines sharpen and move further apart; at the largest correlation time of 3×10^{-7}s, the linepositions correspond to the parallel and perpendicular components of the total nitrogen hyperfine tensor.

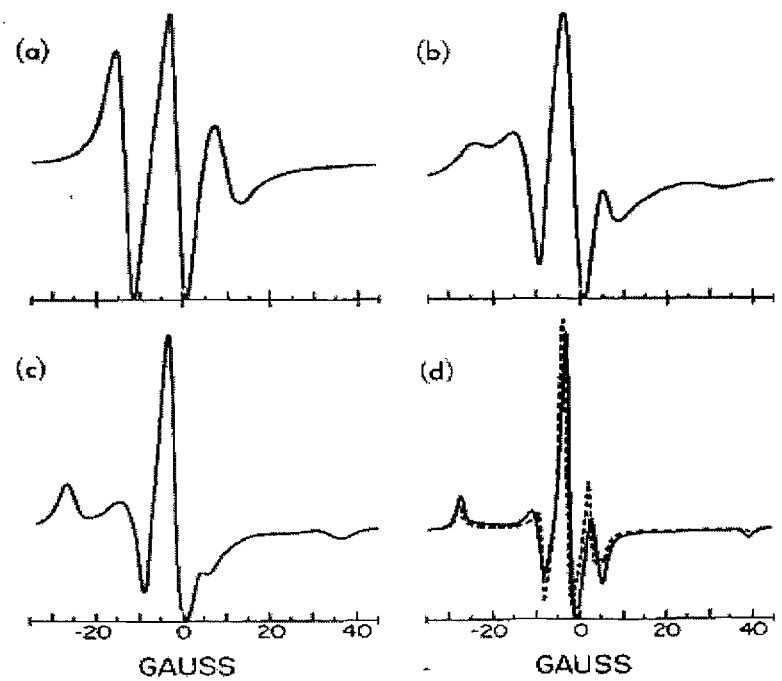

Figure 12: The theoretical ESR spectra for an axially symmetric nitroxide spin probe in the case of low ordering as function of the rotational correlation time, τ_R, for Brownian diffusion: (a) $\tau_R = 3 \times 10^{-9}$s, (b) $\tau_R = 10^{-8}$s, (c) $\tau_R = 3 \times 10^{-8}$s, and (d) $\tau_R = 3 \times 10^{-7}$s.

6.5 ESR Spectroscopy and Spectral Simulations

This Section will describe a novel ESR experiment on the behaviour of nematics in the porous glass host, especially for the investigation of director alignment by the magnetic field. The novelty of this investigation is because this confined system has not been explored before by ESR spectroscopy. Although another branch of magnetic resonance spectroscopy, i.e. NMR, has been used to explore many cases of confined liquid crystal systems, but ESR is using a different mechanism and most important, a different magnitude of the magnetic field which makes the system behave differently. Our literature reviews have shown that liquid crystals in confined geometries behave differently compared with when they are in the bulk. Besides shifting T_{NI}, the motion of the mesogenic molecules is getting slower in the restricted cavities. ESR could not give all information on how this happens, but the changes in the spectral lineshapes and the occurrence of the resonance signals could confirm all of our hypotheses. All of these results come from the spectra of the spin probe doped in nematic contained in porous materials, i.e. CPG.

The sample preparation methods have been described in Chapter III for the nematic ZLI-4792 in the randomly oriented pores of controlled porous glass media. Controlled Porous Glass (CPG) was chosen to host the nematic in our experiments. This rigid glass structure, obtained from Millipore USA, is manufactured from a borosilicate base material and is well-known as an inorganic support for use in the phase separation method such as liquid chromatography (stationary phase). CPG media are thought to be non-absorptive and are unaffected by changes in a solvent system or by pressure. CPG, with their excellent mechanical properties, can be prepared with a wide range of porosities and average pore sizes. Figure 13 shows the SEM photograph of a CPG matrix.

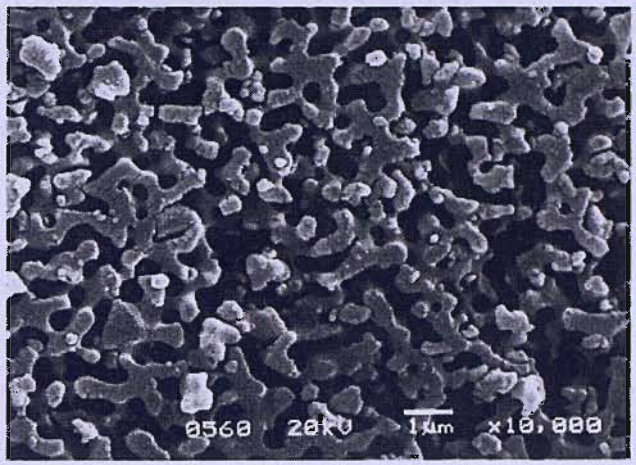

Figure 13: Scanning electron micrograph of a CPG grain with pore radius, R=2000Å [21].

Nematic ZLI-4792 was dispersed into the CPG matrix by mechanical mixing in the ESR sample tube. We know that it is mixed properly when we found the CPG can flow inside the tube with no indication of liquid crystals inside the tube, i.e. on the outside of the CPG. This meant that all of the liquid crystal is inside the pores. For all ESR measurements, two types of spin probes have been used. The details of their structure and the importance in our studies have been described in Chapter III. Tempone and Cholestane spin probes, are both nitroxide-based molecules but differ in their shape anisotropies. Therefore we expected to see some dissimilarity of the ESR signals for each spin probe.

6.5.1 Tempone Spin Probe

ESR measurements for Tempone in ZLI-4792 dispersed in CPG pores are described later. Five different pore-size diameter CPGs have been used in these measurements: 500Å, 700Å, 1000Å, 1400Å and 3000Å. For each of these, the ESR measurement was performed as a function of increasing temperature starting at room temperature, ~300K to the nematic-isotropic transition of ZLI-4792 of ~380K.

6.5.1.1 Temperature Dependent Study: Pore Size 500Å

Due to the properties of its size, shape anisotropy and resultant rotational correlation time, the Tempone spin probe gives a very sharp and so intense hyperfine lines for low viscosity bulk nematics measured with ESR spectroscopy. However, in the CPG experiments, the ESR spectra are very broad and less intense. From Figure 14, we see that when the temperature is 300K, the ESR spectrum contains three broad hyperfine lines, but the signal is not that expected for parallel alignment of the director with respect to the magnetic field. Since the porous media that we have used is random in its geometry, we expect to observe a powder pattern ESR spectra for a weighted sum of spectra from all director orientations. The hyperfine spacing for Tempone in this case is relatively large compared to the spacing for an aligned bulk sample. Meanwhile, the spacing from the maximum peak at the low ESR field to the minimum peak at the high ESR field is almost the same as for a polycrystalline sample or powder spectrum (this will be explained in the next sub-section). This result signifies the surprising observation of a slow molecular motion for the probe and hence the mesogenic molecules inside the pores. As the temperature increases, these slow motion powder spectra gradually transform to just three hyperfine lines with an isotropic splitting of ~15G although the lines remain extremely broad which is also indicative of slow molecular rotation (see Figure 12 (a)). The ESR spectra do not change much with temperature, but we can see the noticeable difference between the spectrum at 300K and 390K. We believe that the splittings for spectrum at 390K come from the isotropic phase, but certainly not for the 300K. We claim that the 300K spectrum actually contains five hyperfine lines, but the line broadening makes it harder for these to be defined. We shall want to see the results for CPG with bigger pore sizes before we make any conclusion for these results for the 500Å CPG.

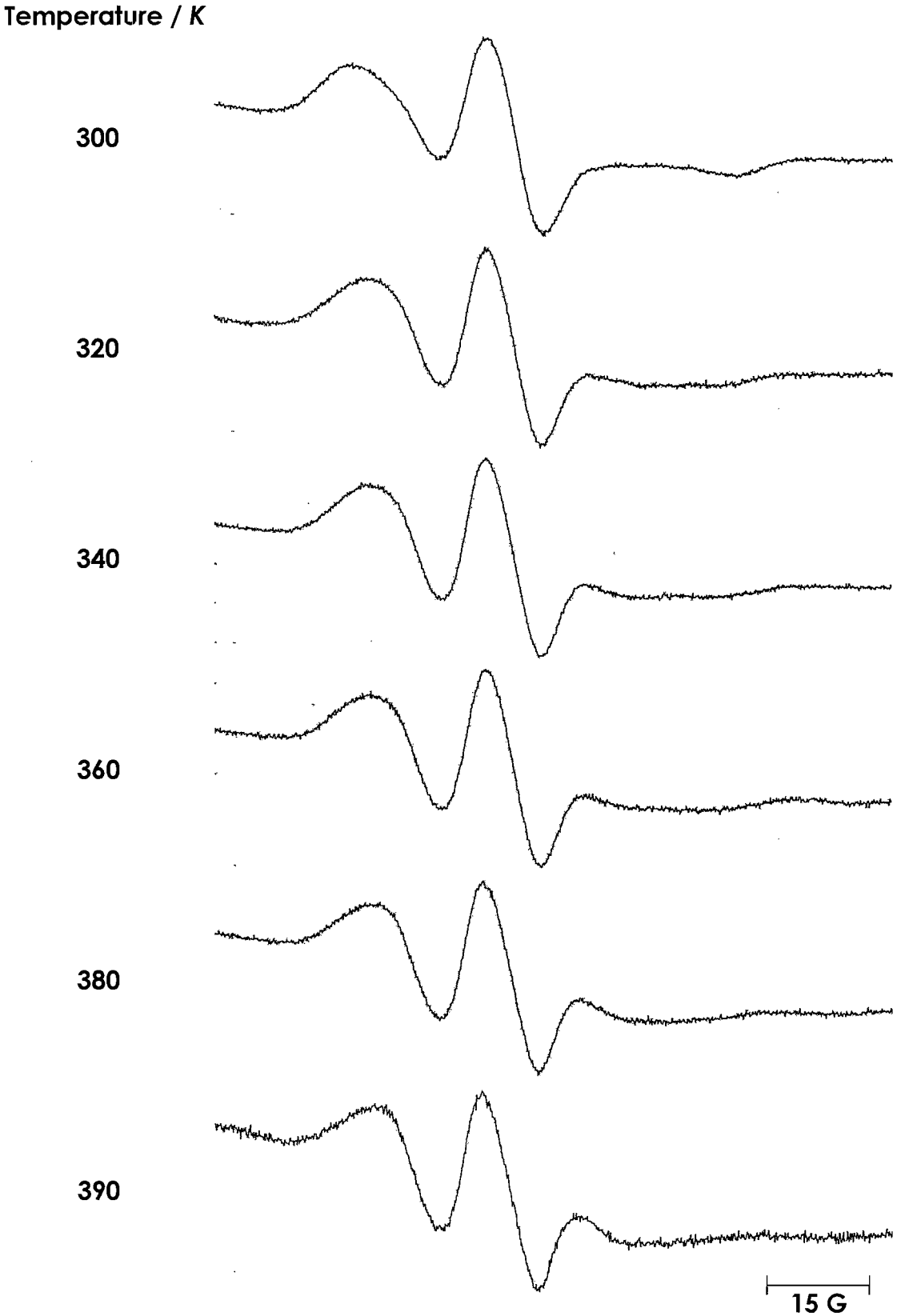

Figure 14: ESR spectra for Tempone in ZLI-4792 confined in a CPG matrix with a pore size of 500Å at increasing temperatures.

6.5.1.2 Temperature Dependent Study: Pore Size 700Å

Figure 15 shows the ESR spectra for Tempone in ZLI-4792 dispersed in the CPG with 700Å pore size. This CPG has a 30% larger pore size compared to the previous CPG, so the ESR spectra for pore size 700Å are different than those at 500Å. Clearly we expect and do see a powder pattern spectrum for the sample at room temperature ~300K, indicating that the molecular motion is in the slow regime. This is quite similar to what we have found for 500Å pore size. However, some of the lines seem sharper than for the 500Å, therefore we assumed that this is an indication for some fast motion component in the sample. This fast motion spectrum also shows a powder-like pattern since the director is randomly oriented by the random pores. As the temperature increases, the changes in the ESR spectra occur gradually but cannot really be analysed in detail since the lines are still broad. In this experiment, the ESR spectrum at 390K has a small signal to noise ratio and this happened because of decomposition of the spin probe after the sample was heated at high temperatures. It has happened to this sample since the amount of the spin probe in the liquid crystal host was very small.

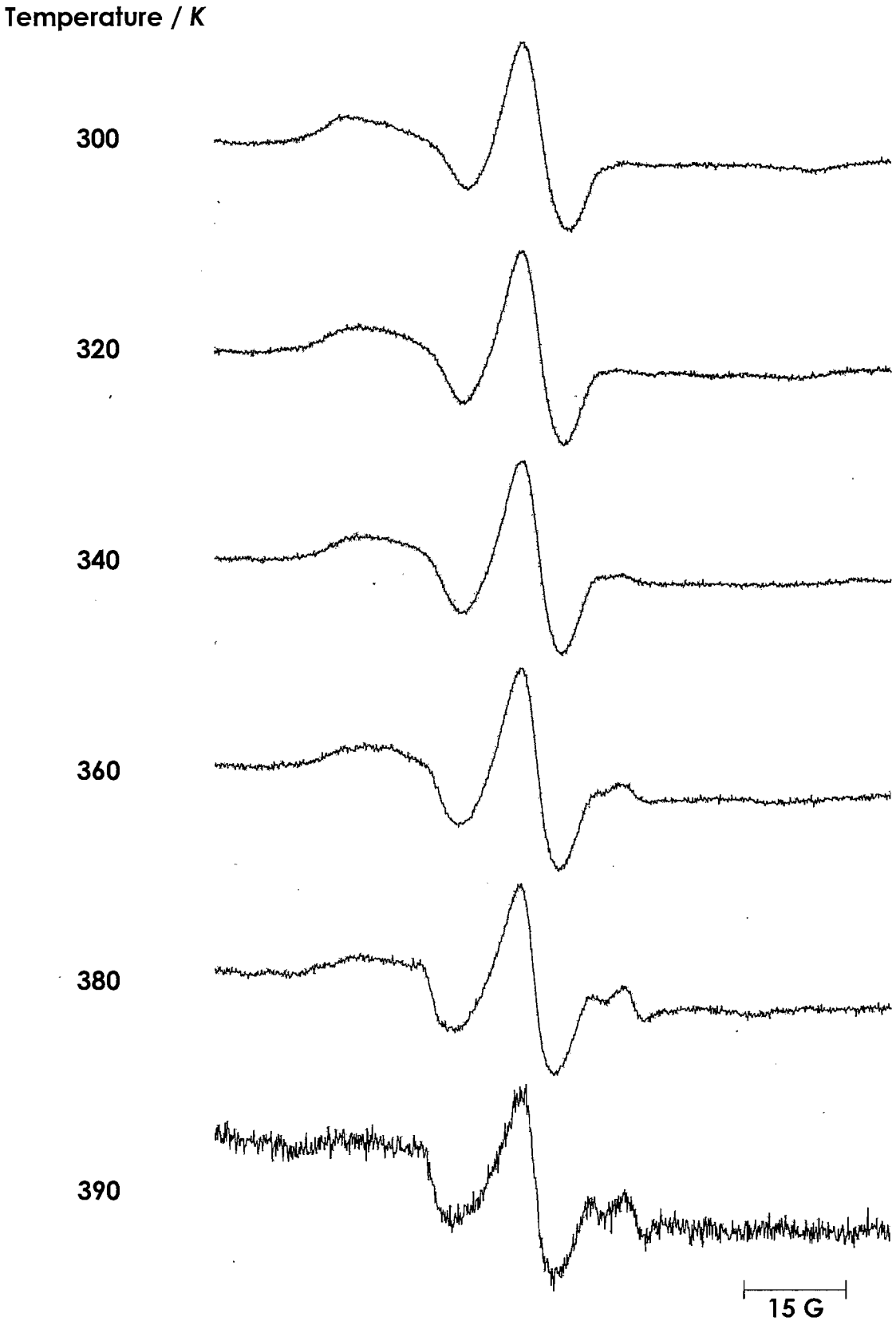

Figure 15: ESR spectra for Tempone in ZLI-4792 confined in a CPG matrix with a pore size of 700Å at increasing temperatures.

6.5.1.3 Temperature Dependent Study: Pore Size 1000Å

The signal-to-noise (S/N) ratios for these spectra are getting better as the pore size increases. From the ESR spectra shown in Figure 16, of the spectrum at 300K, we can say, with confidence, that there is a mixture of slow and fast molecular motion spectra observed even at the lowest temperature. The hyperfine splitting at low field in the ESR spectra at 300K represents the slow motion components while the next smaller peak originates from the fast motion region. Our first interpretation was that the slow motion peaks are coming from part of the spin probe close to the pores surface while the fast motion signals come from the spin probe in the bulk region of liquid crystals. As the temperature increases, the signals for the slow and fast motion components seem more obvious (320K), and we could also see the growth of the high field fast motion peak especially as the sample reaches the isotropic phase. Our studies so far, on increasing the pore size, the intensity of the fast motion signals become bigger and so the intensities of the slow motion signals tends to decrease; this is especially apparent for the ESR spectra at 300K.

6.5.1.4 Temperature Dependent Study: Pore Size 1400Å

Figure 17 shows the ESR spectra for Tempone in ZLI-4792 confined in the 1400Å pores of a CPG. We observed the same qualitative results in terms of the mixture of the fast and slow molecular rotation of the spin probe in this sample. Nevertheless these results seem peculiar since the intensity of the fast motion signal is too low compared to the signal for the slow motion. It should be the opposite since the pores are now bigger which should result in the rotation of more molecules in the fast motion region. This expectation would seem correct for the smaller pore sizes. Again, these changes are especially apparent from the peak at high field.

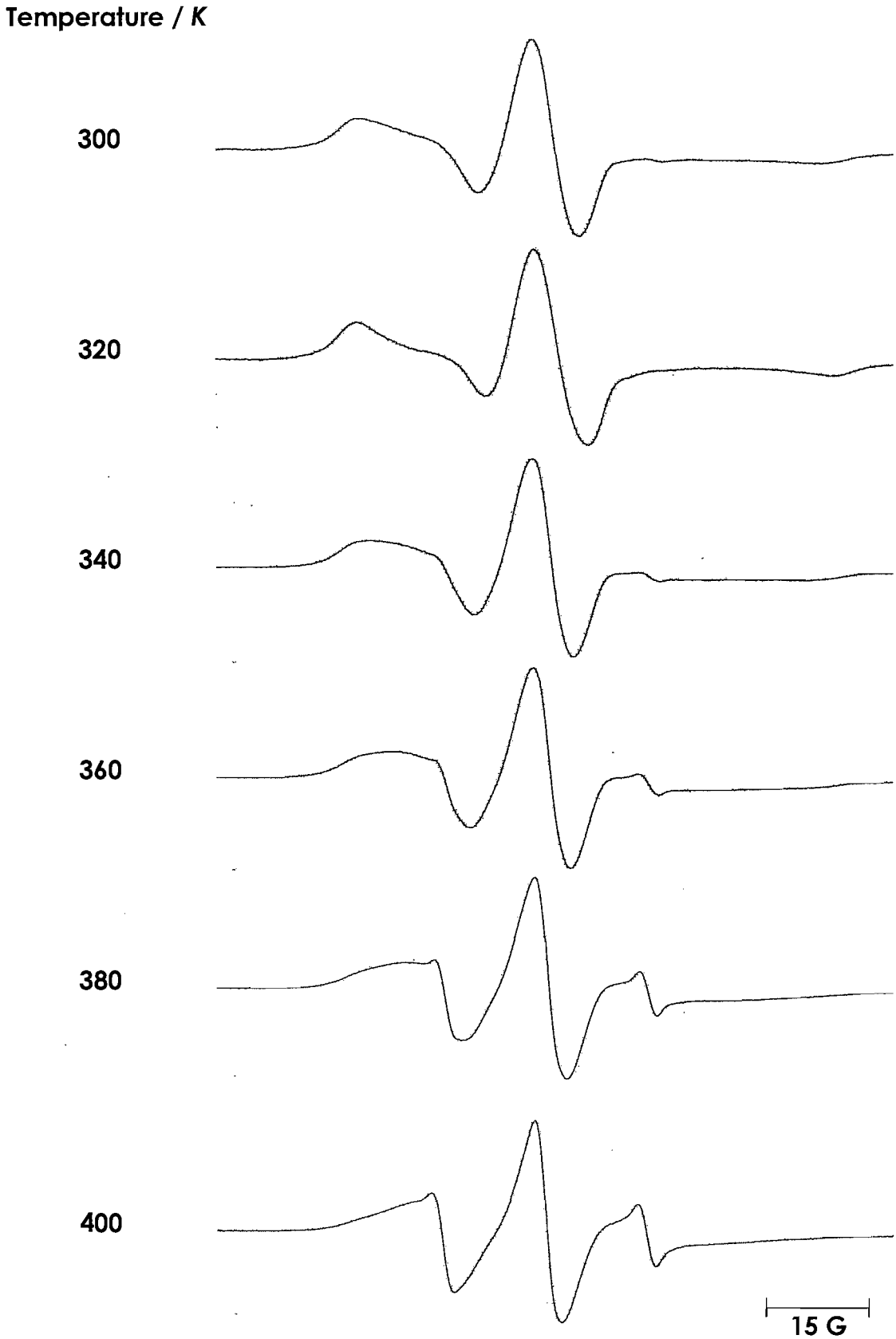

Figure 16: ESR spectra for Tempone in ZLI-4792 confined in a CPG matrix with a pore size of 1000Å at increasing temperatures.

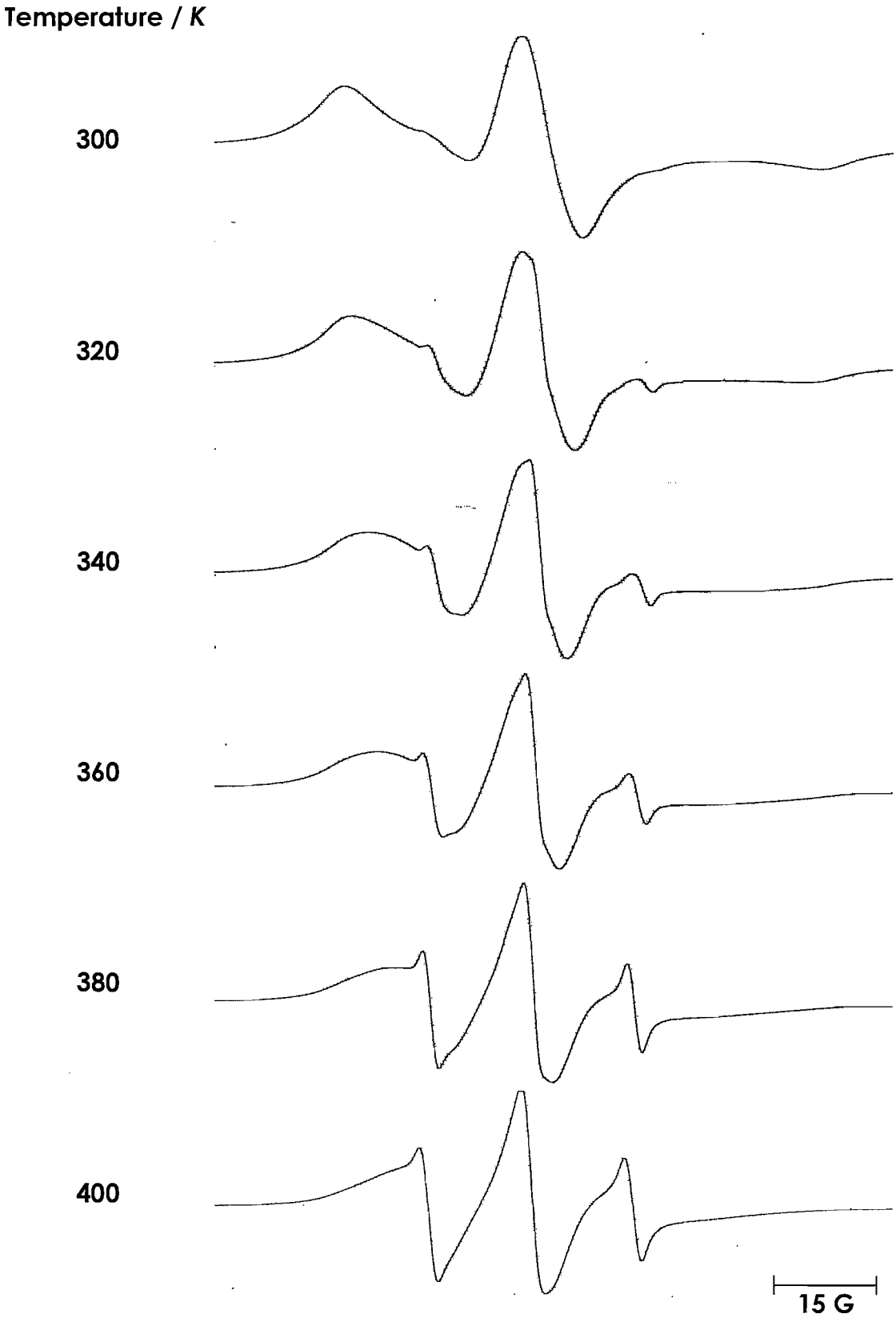

Figure 17: ESR spectra for Tempone in ZLI-4792 confined in a CPG matrix with a pore size of 1400Å at increasing temperatures.

6.5.1.5 Temperature Dependent Study: Pore Size 3000Å

We now consider our results for the CPG with the largest pore size that we have studied; these spectra are shown in Figure 18. Three sharp hyperfine lines appear in the spectra coming from the fast motion of the spin probe. The slow motion signal still appears in the spectra but with a much lower intensity in comparison with the largest motion. For the fast motion signal, the lineshape is expected to be powder-like but clearly, this is not seen because of the value for $\widetilde{A}_{\parallel}$ and $\widetilde{A}_{\perp}$ are quite close even for the Tempone in the bulk nematic at low temperature. Our expectation of more of the sample being in the fast motion region as the pore size increases is supported by this experiment.

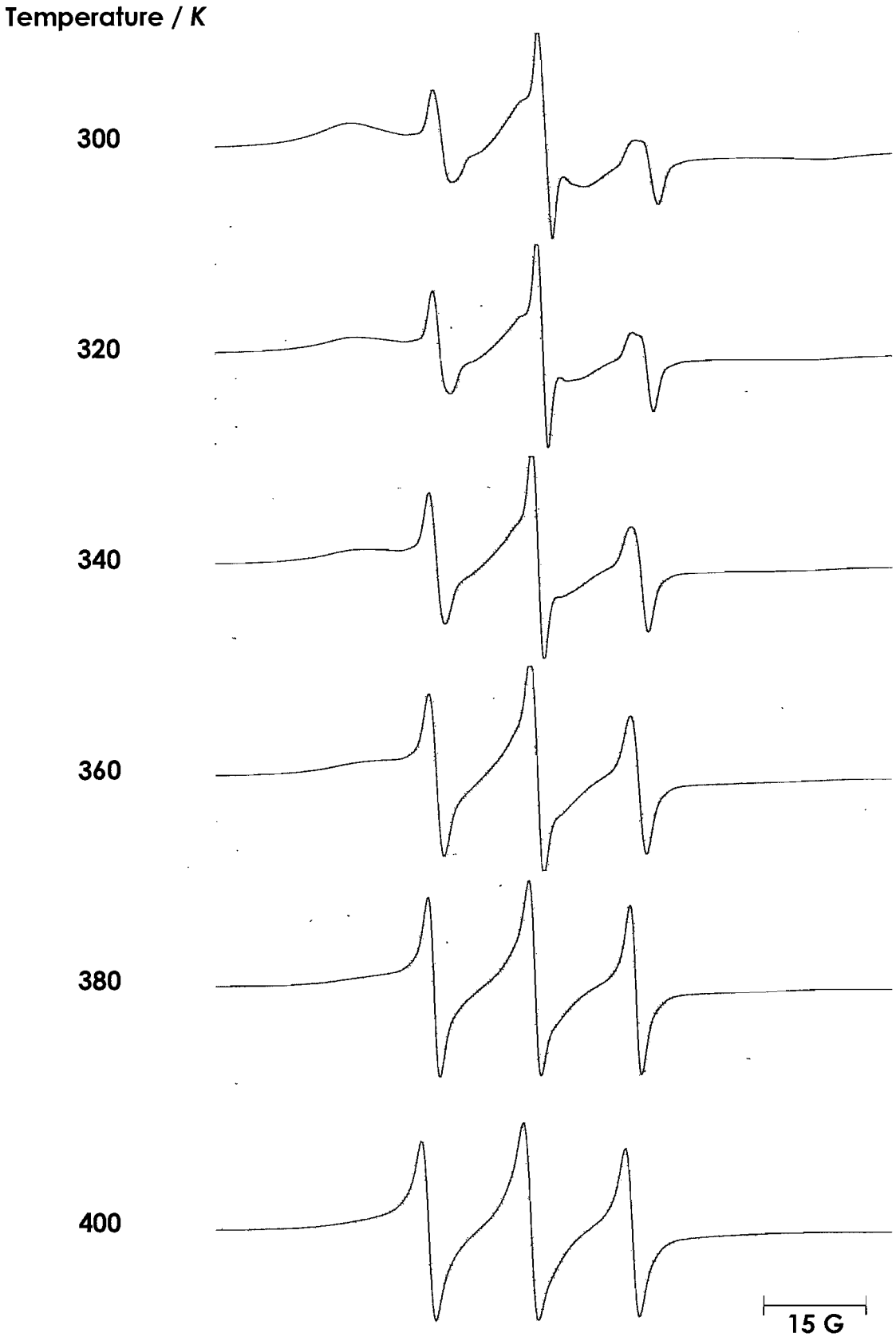

Figure 18: ESR spectra for Tempone in ZLI-4792 confined in a CPG matrix with a pore size of 3000Å at increasing temperatures.

6.5.2 Cholestane Spin Probe

To check these observations and their explanation, we have repeated the studies but using the Cholestane spin probe. The Cholestane spin probe was doped into nematic ZLI-4792 and the mixture was dispersed in the CPG media. The major difference between Cholestane and Tempone is that Cholestane has a larger molecular size, therefore slower rotational motion is expected at least for the end-over-end rotation. It should, therefore, make the lines much broaden in the ESR spectrum compared to Tempone.

6.5.2.1 Temperature Dependent Study: Pore Size 500Å

Figure 19 shows the ESR spectra for Cholestane in ZLI-4792, dispersed in the CPG with a pore size of 500Å. The slow motion signal seems dominant and intense while for the fast motion spectrum, we observed slightly broad lines which come from the region where director is randomly distributed. As the temperature increases, the slow motion signals gradually decrease in intensity while the fast motion signal becomes more intense, until a strong three line spectrum with weak slow motion features appear when the sample enters the isotropic phase. For this sample, the slow motion signals still appear even on the ESR spectrum for the isotropic sample which suggests that some of the slow motion components are hidden in the pores and the rotation is very slow.

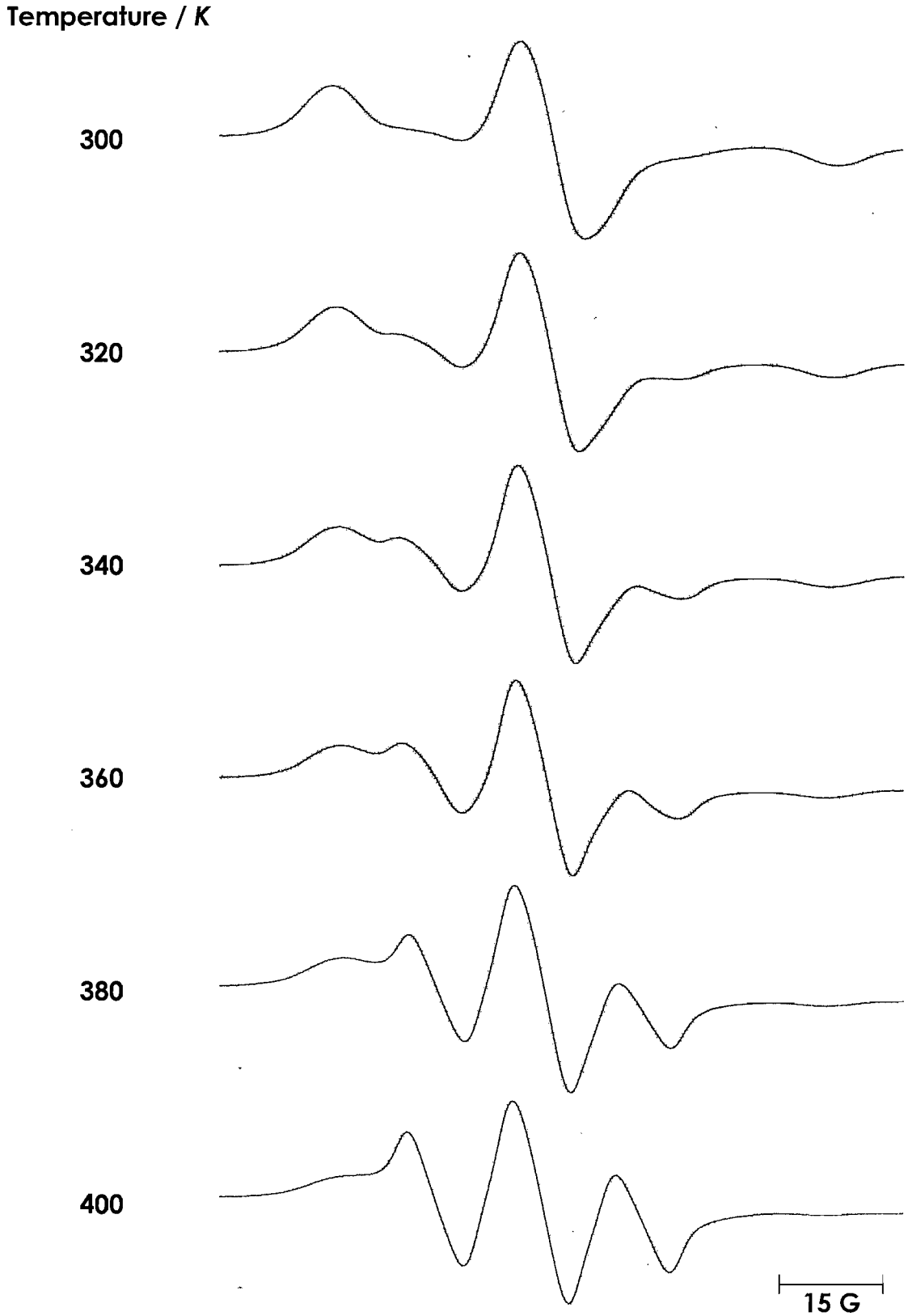

Figure 19: *ESR spectra for Cholestane in ZLI-4792 confined in a CPG matrix with a pore size of 500Å at increasing temperatures.*

6.5.2.2 Temperature Dependent Study: Pore Size 700Å

The increase in the pore size for the CPG with 700Å pores has increased the amount of the fast motion component in the ESR spectra. Here, the powder-like spectrum for the fast motion contribution becomes more apparent which clearly shows spectral features for the director both parallel and perpendicular to the magnetic field in the fast motion spectral region (see Figure 20 for temperature 300K). The increase in pore size has also decreased the relative intensities of the slow motion features of the ESR spectra. Again, the fast motion spectrum dominates the isotropic phase ESR spectrum with just very weak features coming from the Cholestane moving in the slow motion region, which are less intense than those found with pore size 500Å. Surprisingly, this behaviour contrasts with that found for the Tempone spin probe where essentially all of the spectra are in the slow motion regime, we are surprised because with its smaller size, Tempone should have a faster rotation.

6.5.2.3 Temperature Dependent Study: Pore Size 1000Å

The ESR spectra for this experiment with the CPG having the larger pore size of 1000Å are shown in Figure 21. These spectra seem to be very similar to the results found for 700Å, but the ESR contribution to the spectra for the fast motion regime are slightly more significant and so more intense than the slow motion. This change in behaviour is to be expected for increase in the pore size. As for the CPG with pore size of 700Å the change from nematic to isotropic is clearly apparent from the spectra recorded in the range from 360K to 380K.

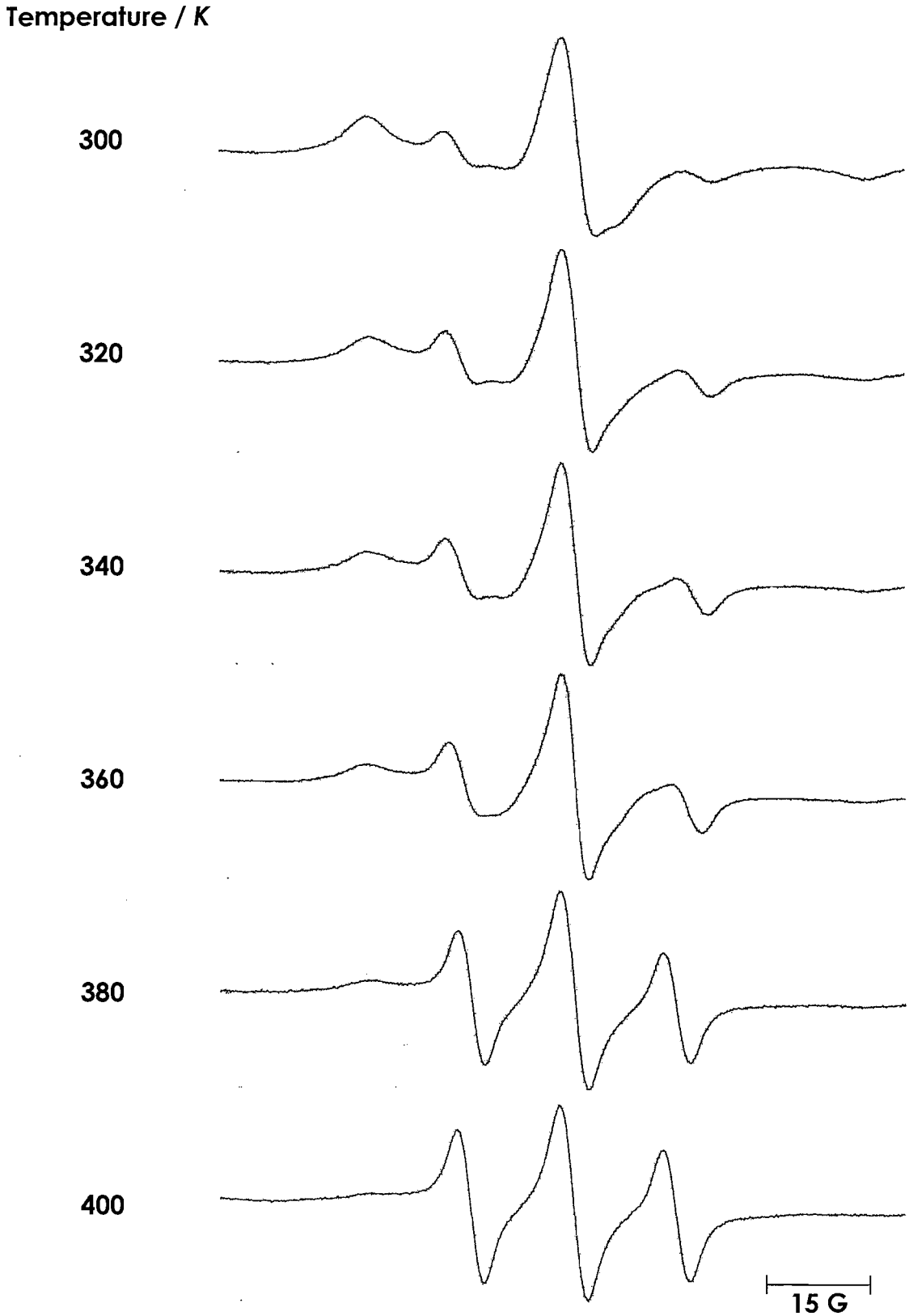

Figure 20: *ESR spectra for Cholestane in ZLI-4792 confined in a CPG matrix with a pore size of 700Å at increasing temperatures.*

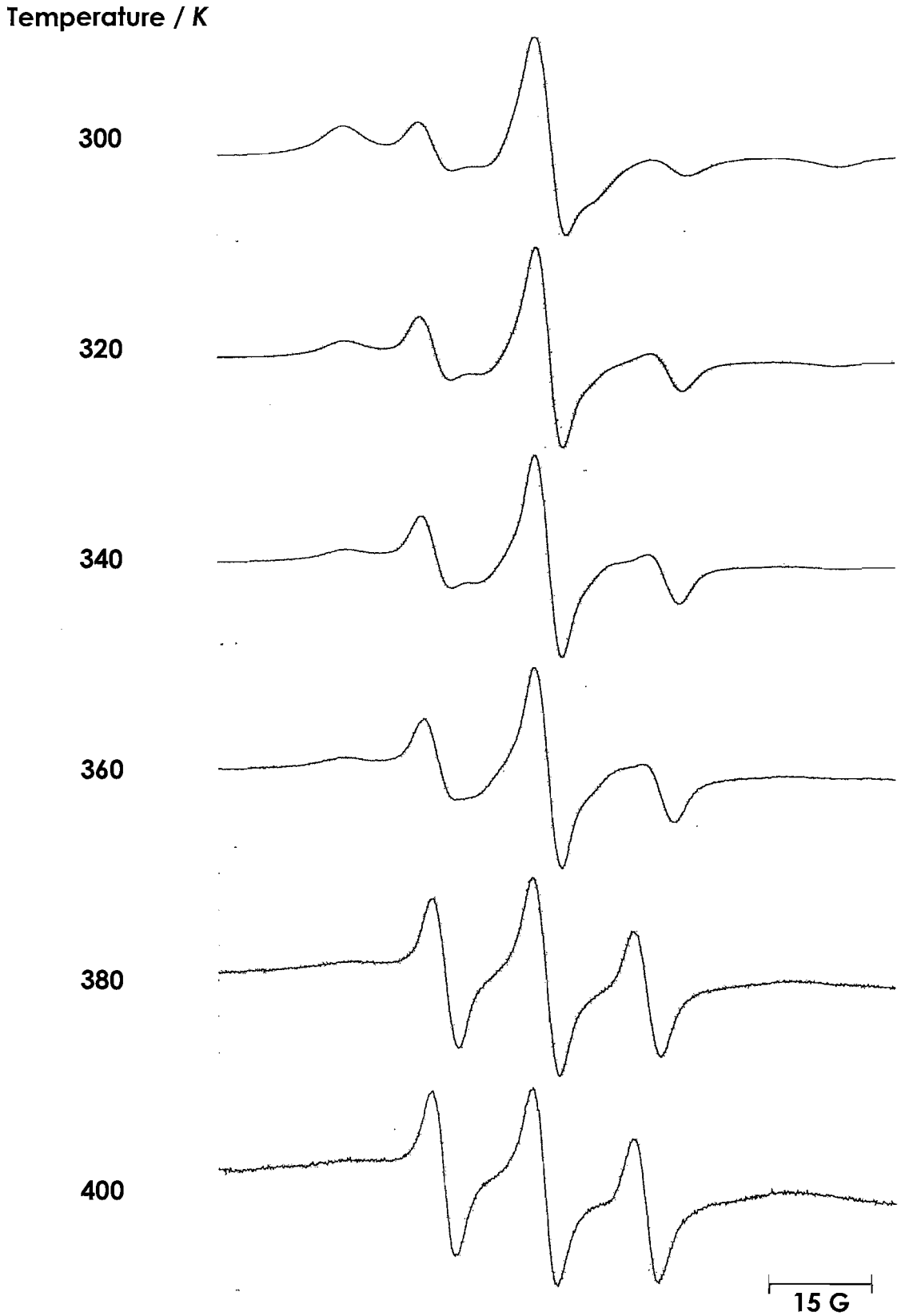

Figure 21: *ESR spectra for Cholestane in ZLI-4792 confined in a CPG matrix with a pore size of 1000Å at increasing temperatures.*

6.5.2.4 Temperature Dependent Study: Pore Size 1400Å

The increase in the pore size to 1400Å should have resulted in an increase in the relative amount of the fast motion spectral component. However, the ESR spectra found for this and the other CPGs suggest that the pore size is, in fact, about ~700Å. Thus, there is a reduction in the intensities of the fast motion component as is apparent from the spectra shown in Figure 22 when compared with those in Figure 21. The same phenomena was observed with Tempone spin probe for the CPG with the same pore size diameter. This suggests that the pore sizes given by the supplier might not be correct.

6.5.2.5 Temperature Dependent Study: Pore Size 3000Å

This system has the largest pore size of all of the CPG available to us, so we expect that the fast motion spectral components should have a larger relative intensity. As we can see from the spectra in Figure 23, this is indeed the case, the fraction of fast motion components has increased with respect to the slow motion components. However, the slow motion component still appears but with small intensities especially at low temperatures.

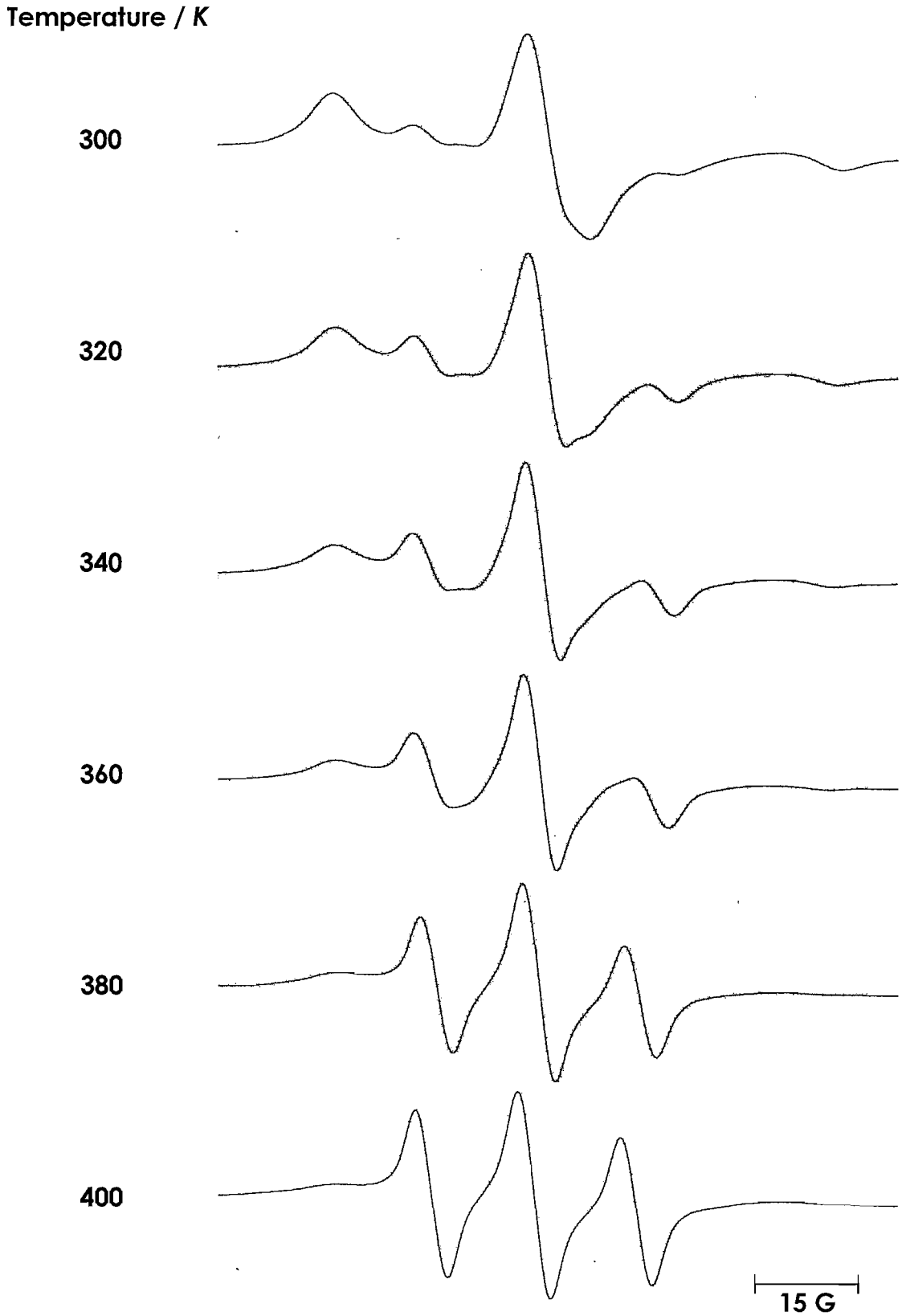

Figure 22: *ESR spectra for Cholestane in ZLI-4792 confined in a CPG matrix with a pore size of 1400Å at increasing temperatures.*

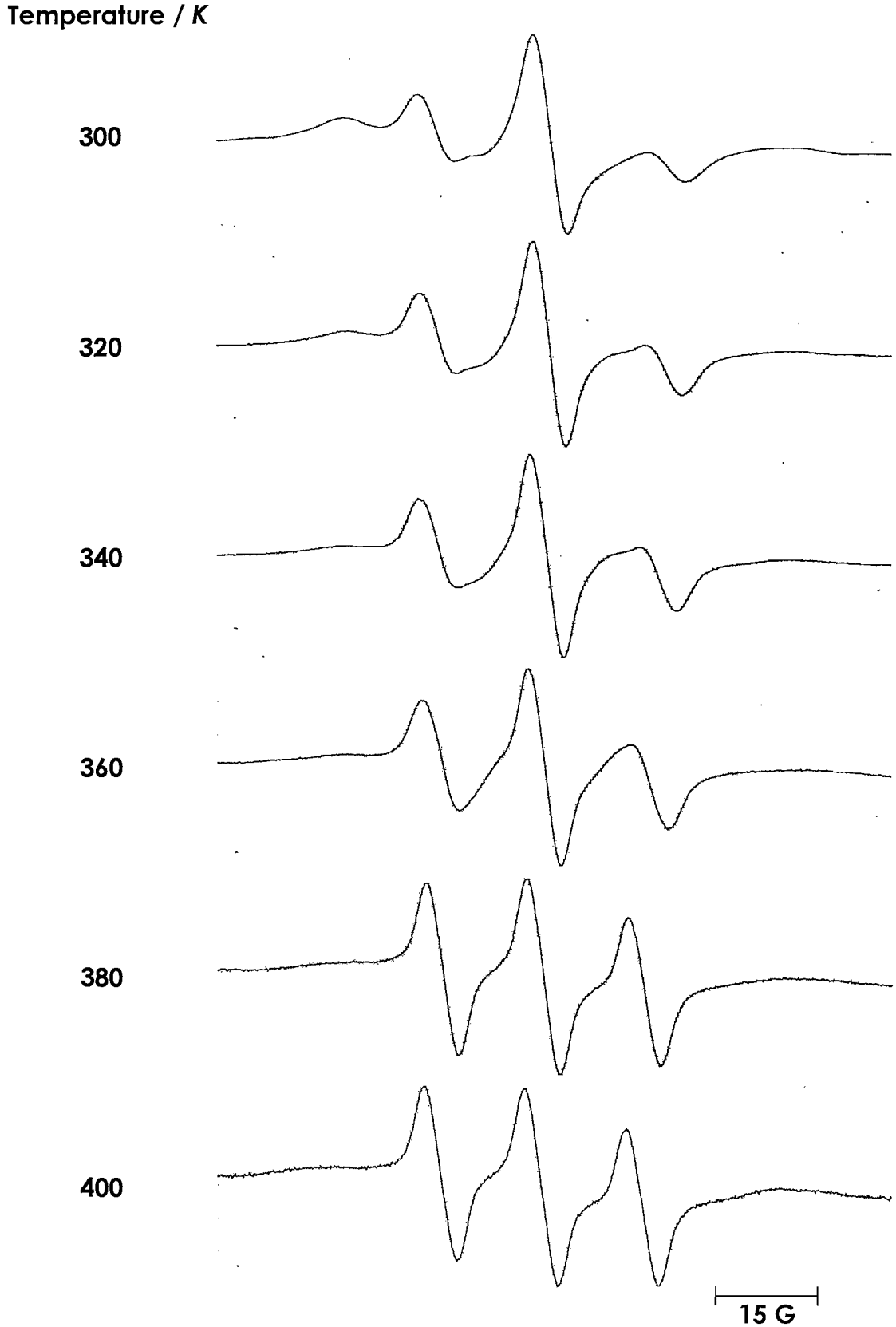

Figure 23: ESR spectra for Cholestane in ZLI-4792 confined in a CPG matrix with a pore size of 3000Å at increasing temperatures.

6.5.3 Discussion of the Measurement of the ESR Spectra

From all ESR spectra with the two different spin probes and the five pore diameters of CPG, many of them looked different from a conventional ESR spectrum in the bulk, in terms of both the symmetries and lineshapes. For example, some of the first derivative signals are very broad for most of the spectra. In addition, the samples are in a disordered state, which gave a broad linewidth. Since the molecular rotational motion is slow, then in some of the ESR measurements we have used a high magnitude of modulation amplitude to increase the signal intensity. This however, can distort the lineshape as well as making the line broader, similarly if excess microwave power is used in the measurement; then the lines are also broadened which impair the spectral resolution.

The slow motion ESR spectra are believed to originate from the liquid crystal region, where the director are frozen in the sample. While the fast motion spectra are coming from the director which adopts all orientations with respect to the field, because of the randomness of the pore structure. As a result, this gave a powder pattern spectrum with partially averaged $\boldsymbol{g}$ and hyperfine tensors, both having cylindrical symmetry which is the symmetry of the nematic phase. For every ESR spectrum (non-isotropic), we found that the hyperfine spacings from the central peak to the other peaks at high field seem larger than to the low field side. This difference almost certainly originates from the second order correction to the energy levels and hence hyperfine spacings [38], which is an extension of the ESR linepositions, described in the second Chapter. Thus, the difference in the energy of the spin levels for the allowed transitions are

$$h\nu = \tilde{g}\mu_B B_m + \tilde{K}hm + \frac{h^2\tilde{A}_\perp^2}{4}\frac{(\tilde{A}_\parallel^2 + \tilde{K}^2)[I(I+1)-m^2]}{\tilde{K}^2\tilde{g}\mu_B B_m}, \qquad (6.3)$$

where

$$\tilde{g} = \left(\tilde{g}_{\perp}^2 \sin^2\theta + \tilde{g}_{\parallel}^2 \cos^2\theta\right)^{1/2}, \tag{6.4}$$

and

$$\tilde{K} = \left(\tilde{A}_{\perp}^2 \tilde{g}_{\perp}^2 \sin^2\theta + \tilde{A}_{\parallel}^2 \tilde{g}_{\parallel}^2 \cos^2\theta\right)^{1/2} / \tilde{g}. \tag{6.5}$$

The importance of these second order corrections to the linepositions depends on the relative magnitude of the hyperfine spacing to the Zeeman splitting. The correction, ∂ can be explained in more detail in the drawings shown in Figure 24.

In the isotropic phase, equation (6.5) is simplified because $\tilde{g}_{\parallel} = \tilde{g}_{\perp} = g$, $\tilde{K} = a/g$ and $\tilde{A}_{\parallel} = \tilde{A}_{\perp} = a$. This gives

$$h\nu = \tilde{g}\mu_B B_m + ahm + \frac{h^2 a^2 [I(I+1) - m^2]}{g^2 \mu_B B_0}. \tag{6.6}$$

For zeroth order,

$$B_0 = \frac{h\nu}{g\mu_B}, \tag{6.7}$$

and for the first order,

$$\frac{h\nu}{g\mu_B} = B_0 + \frac{ahm}{g\mu_B}. \tag{6.8}$$

$\frac{h\nu}{g\mu_B}$ converts frequency to field, so that we can write $B_{-1} = B_0 + am$, $B_0 = B_0$ and $B_1 = B_0 - am$.

The second order correction can be derived from,

$$B_0 = B_m + am + \frac{h^2 a^2 [I(I+1) - m^2]}{2g^2 \mu_B B_0}, \tag{6.9}$$

then B_{-1}, B_0 and B_1 are define as, $B_{-1} = B_0 + a - \frac{a^2}{2B_0}$, $B_0 = B_0 - \frac{a^2}{2B_0}$, and $B_1 = B_0 - a - \frac{a^2}{2B_0}$.

Therefore, the spacing between adjacent lines are, $a - \frac{a^2}{2B_0}$ and $a + \frac{a^2}{2B_0}$. Figure 24 (a) shows the illustration for the second order shift in the isotropic phase.

Powder pattern ESR spectra is a contribution by the weighted sum of the director from all orientations, between direction parallel and perpendicular to the magnetic field. For these ESR spectra, the spacing between signals parallel and perpendicular at high field is far larger than the low field. This corresponds to the difference in the $\tilde{g}_{\parallel}$ and $\tilde{g}_{\perp}$ as shown in Figure 24 (b). The central peak is broader and shifted as a result for the difference in both g-values.

(a) Isotropic sample, ($\partial = \frac{a^2}{2B_0}$).

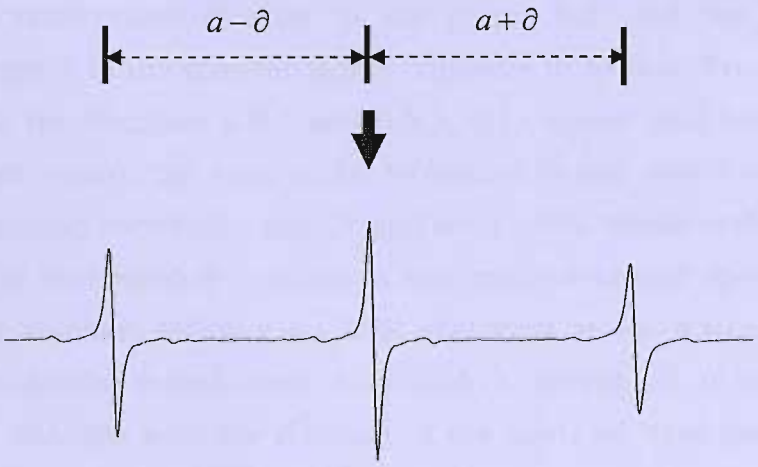

(b) Powder sample (contribution of g-values and second order shifts)

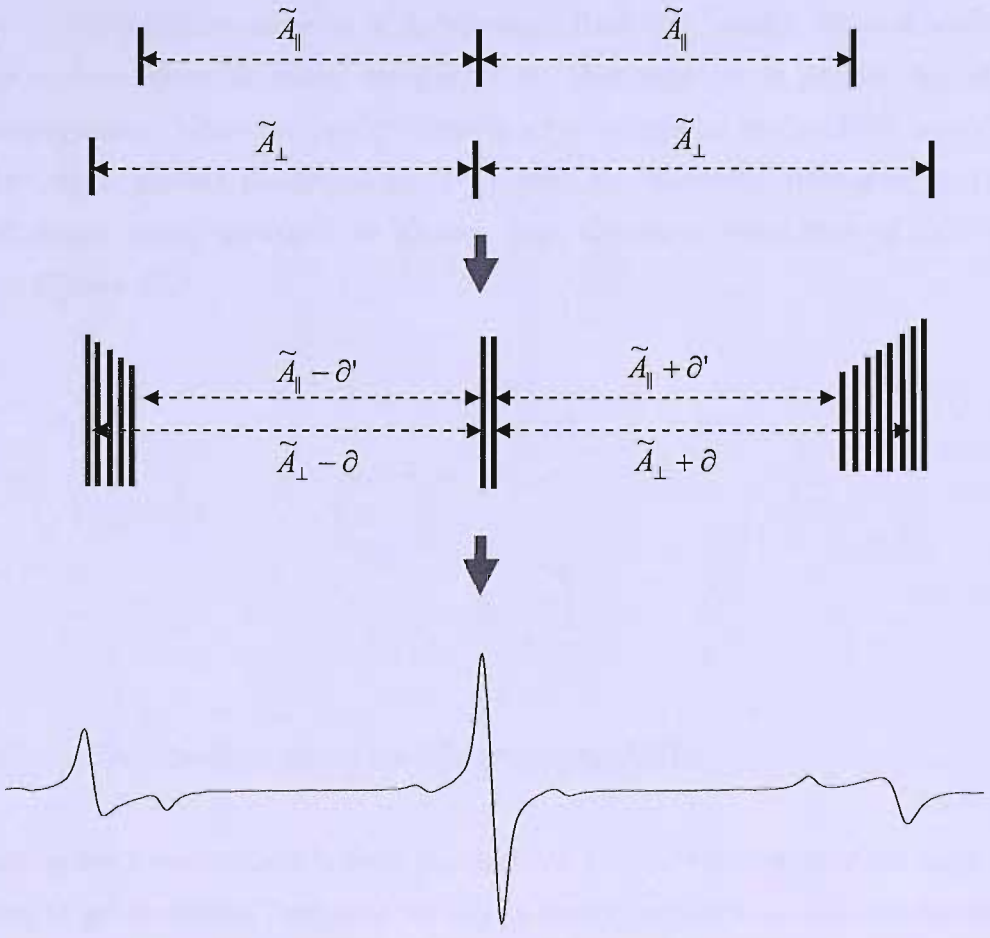

Figure 24: *The drawings of the use of (a) the second order correction for the linepositions of the ESR spectra for an isotropic sample, (b) powder pattern spectrum and the influence of the g-values.*

6.5.4 Spin Probes in Viscous Materials

We had expected that the nematics when dispersed in porous materials would have a randomized director in the pores, but that the molecular motion with respect to the director would continue to be fast. From the ESR results given in the Sections 6.5.1 and 6.5.2, it is shown that unexpectedly there is a region where the spin probe molecules rotate slowly on an ESR timescale, in fact the correlation time is less than 10^{-8}s, which is the smallest time for the ESR time window to record a motionally averaged spectrum. The slow molecular rotation will give an ESR spectrum as for a frozen sample with random molecular orientations. As a control experiment, to see how the ESR spectrum changes with the viscosity of the host, we have used the two spin probes dissolved in *o-terphenyl* (OTP) which has a high viscosity that increases rapidly with decreasing temperature.

OTP or *1,2-diphenylbenzene* is a compound that can easily form a stable glassy structure even at room temperature. Therefore, it is perfect for our ESR investigation, since we could observe what happens to the ESR spectra of the two spin probes dissolved in OTP when its viscosity increases as the phase changes from isotropic to glassy. The chemical structure of OTP is shown in Figure 25.

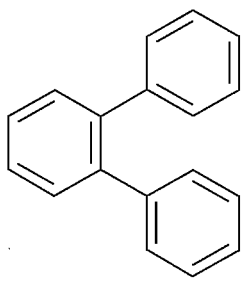

Figure 25: The chemical structure of o-terphenyl (OTP).

Two spin probes were used which are known to be reasonably rigid and to have simple geometries; Tempone which is nearly spherical and Cholestane which approximates to a cylindrically symmetric shape. With concentrations of 10^{-3}mol/l, corresponding to 200ppm, they were dissolved in OTP and the ESR spectra measured at 350K and 300K are shown in Figure 26.

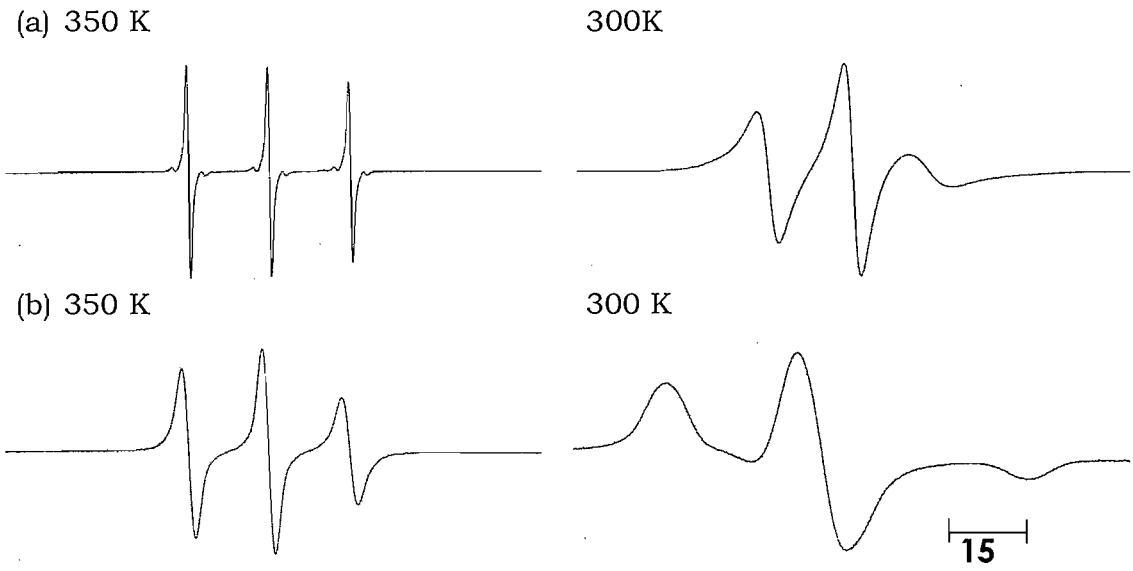

Figure 26: (a) ESR spectra for Tempone in OTP at different temperature (b) ESR spectra for Cholestane in OTP at different temperature.

The ESR spectrum for Tempone at 350K shows three sharp lines expected for the fast motion limit together with the carbon-13 satellite lines. On cooling to 300K, in the glassy phase of OTP the spectrum retains the three strong lines but their widths have increased and this has obscured the carbon-13 satellite lines. The clear fact here is that although the lines have broadened, the motion is still fast, since the hyperfine spacing is still 15G and the lineshapes are symmetric, and that the slow motion limit has yet to be reached. In contrast, although the ESR spectrum for Cholestane at 350K also shows three hyperfine lines as expected for the fast motion limit. However, on cooling to 300K, the spectrum changes totally to a new spectrum which contains broad lines, with the extreme lines not equally separated from the central peak. For both spin probes in OTP, the clear observation here is the change that occur in the ESR lineshape when the sample changes from isotropic to the glassy state. In the isotropic state, the molecular tumbling is rapid so the ESR spectrum is in the fast motion limit and there are three hyperfine lines with a spacing of ~15G, expected for the isotropic phase.

The behaviour of these ESR spectra can be explained in terms of the rotational correlation time, τ, of the molecules. This is related to the viscosity of the solvent, η, and on a basis of the Stokes-Einstein equation [39]

$$\tau = \frac{4\pi r^3 \eta}{3k_B T}, \qquad (6.10)$$

where r is the hydrodynamic radius of the molecule, k_B is the Boltzmann constant and T is the absolute temperature. The ESR linewidths and ultimately the lineshape for a spin probe depend on the magnetic tensors and the rotational correlation time. Therefore, a cylindrically symmetric molecule like Cholestane with its larger size takes a longer time to rotate and this is the explanation for the very broad and asymmetric ESR signals for Cholestane spin probe. In contrast, Tempone is a more spherical molecule and is smaller in size, so it rotates faster which results in the narrower ESR lines. In conclusion, we note that the behaviour observed in OTP is well understood, it does however contrast with our observations for spin probes in the liquid crystals confined in the porous media which is difficult to rationalise.

6.5.4 Isotropic Solution in Porous Media

At an early stage of our studies of confined nematic system, we wondered if the slow motion component of the observed ESR spectra for nematics in porous media might result from the absorption of the spin probe on the CPG surfaces. Therefore, in order to test this assumption, we devised a control experiment using toluene doped with spin probes and dispersed in the CPG with a pore size of 1000Å. Figure 27 shows the ESR spectra for this experiment.

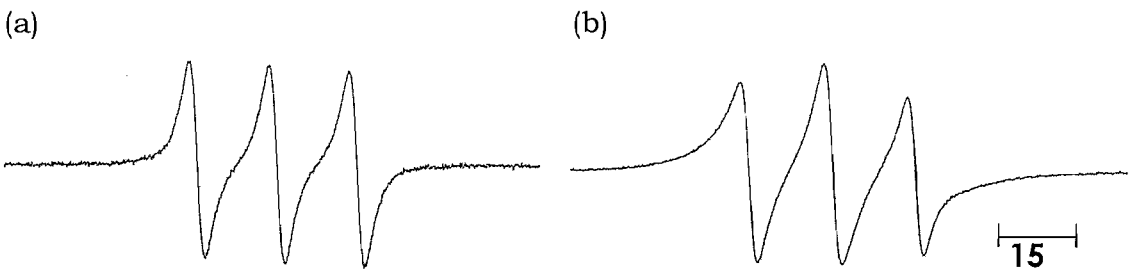

Figure 27: (a) ESR spectrum for Tempone in toluene, (b) ESR spectrum for Tempone in toluene confined in CPG matrix of pore size 1000Å.

Clearly, there is no significant difference between both ESR spectra. Bear in mind that both spectra actually belong to the Tempone spin probe, but the broad lines have resulted from the oxygen that was not well removed for this experiment. However, the most important result here is that we have shown that the spin probe is not absorbed by the CPG surface since the ESR spectra for the spin probes with CPG and without CPG show basically the same form. Another point in favour of this explanation, i.e. no absorption is that for liquid crystal samples once in the isotropic phase, then slow motion component is significantly reduced, i.e. the effect is something to do with the nematic phase and its interaction with CPG surface.

6.5.5 Simulation for Fast and Slow Motion ESR Spectra

There are two types of ESR spectra that have been measured throughout these experiments; slow and fast motion spectrum, respectively come from components with slow and fast molecular tumbling. As mentioned earlier, the fast motion ESR spectra represents the powder-like pattern with a weighted sum of random director orientations in the nematic. The simulation of this kind of spectra has been described in detail in the two previous Chapters (colloidal and gel nematic systems). In these simulation, director orientational distribution function is described by the director distribution function, $f(\theta)$ (Chapter II, equation (2.16)) whereas in the CPG the director is randomly distributed in three dimensions. The simulated ESR spectra for this fast motion spectral component is shown in Figure 28. This was obtained with the parameter which controls the director ordering, a, set to unity. The hyperfine tensor components, $\tilde{A}_{\parallel}$ and $\tilde{A}_{\perp}$ are set to 8.0G and 18.0G, typical for the spin probe, Cholestane. While the three linewidths, $T_2^{-1}(-1)$, $T_2^{-1}(0)$ and $T_2^{-1}(1)$ are set to 1.0G each.

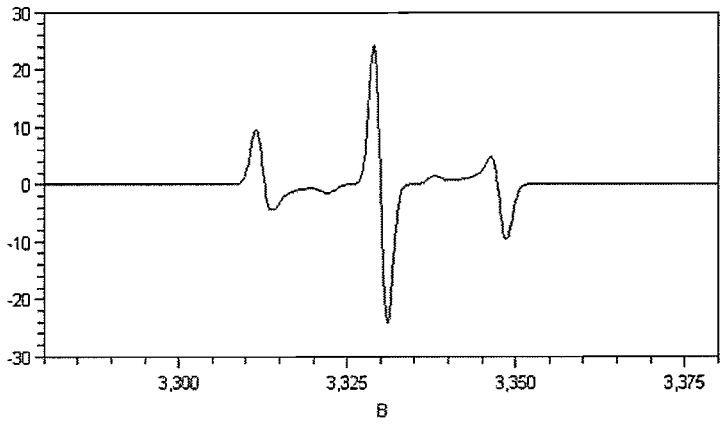

$$\widetilde{A}_{\|} = 8.0G, \widetilde{A}_{\perp} = 18.0G, T_2^{-1}(-1) = 1.0G, T_2^{-1}(0) = 1.0G, T_2^{-1}(1) = 1.0G, a = 1.0$$

Figure 28: Simulated ESR spectrum for powder-like pattern for a fast molecular motion.

For the slow motion spectra, the values for $A_{\|}$ and $A_{\perp}$ are different to the fast motion spectrum, since they are no longer averaged by the molecular rotation but they correspond to the total hyperfine tensor. The a value is still unity because the molecular orientation in this case is also considered to be random in three dimensions. The linewidths used are larger since the width for the experimental ESR spectra for slow motion sample are observed to be quite broad. However, this broadening varies with the different pore size of the CPGs. Figure 29 shows the simulated ESR spectra for slow motion components. This simulated ESR spectrum looks similar to the ESR spectrum for Cholestane in OTP at 300K (see Figure 26 (b)).

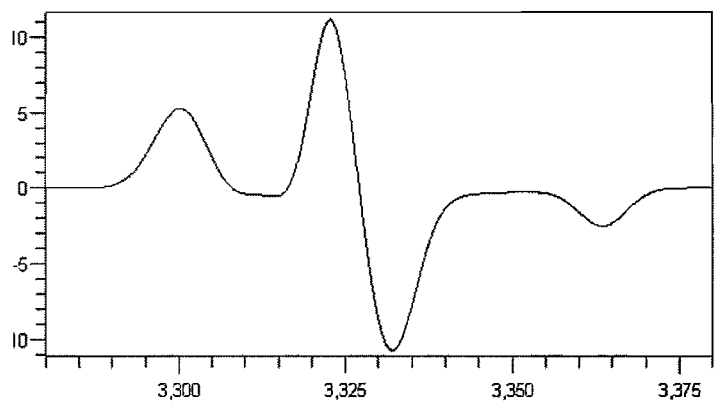

$$A_{\|} = 31.1G, A_{\perp} = 5.0G, \widetilde{g}_{\|} = 2.0054, \widetilde{g}_{\perp} = 2.0057, T_2^{-1}(-1) = 3.5G, T_2^{-1}(0) = 3.5G, T_2^{-1}(1) = 4.1G.$$

Figure 29: Simulated ESR spectrum for powder-like pattern for slow molecular motion.

6.6 Deuterium NMR of 8CB-d_2 Confined in a CPG

The d_2-8CB NMR experiments in this Section were kindly carried out by Dr. Bakir A. Timimi from the University of Southampton.

The ESR spectra reveal a slowing down of the molecular rotation which results in part of the spectra corresponding to the slow motion regime. This may not occur for deuterium NMR spectroscopy where the rotational correlation time needed for slow motion should be greater than 10^{-6}s. It is to be expected, therefore, that we might see fast motion spectra in deuterium NMR corresponding to a random director distribution. To test this idea, the porous media used in the NMR experiment were chosen to be the same as those used for the ESR measurements; that is controlled porous glasses with pore sizes of 500Å, 700Å, 1000Å and 3000Å. However for the dispersed liquid crystal, we chose 4-octyl-4'-cyanobiphenyl (8CB) deuteriated in the α-position of the *octyl* chain. Both deuteriated 8CB (8CB-d_2) and the porous media were mixed mechanically, by using a small spatula inside the NMR tube, until the 8CB-d_2 sample was totally dispersed in the pores of the CPG. Then, the mixture was investigated by variable temperature deuterium NMR spectroscopy. However, in this Section we only present the results for NMR measurements at room temperature to show the difference to the behaviour observed with ESR.

For a uniaxial liquid crystal phase, a macroscopic aligned bulk sample will yield a spectrum having two lines separated by the frequency [40, 41, 42]

$$\Delta\tilde{\nu} = \frac{3}{2}\frac{e^2qQ}{h}\frac{1}{2}(3\cos^2\theta_n - 1)S, \qquad (6.11)$$

where θ_n is the angle between the magnetic field and the nematic director, S is the orientational order parameter for the C-D bond which is averaged by molecular conformational changes and by fast reorientation of the mesogenic molecule and e^2qQ/h is the quadrupole coupling constant. The recorded quadrupole splitting, $\Delta\tilde{\nu}$, indicates how the director is aligned in the liquid crystal phase with respect to the magnetic field. If the director is aligned

parallel to the field, then it produces a larger splitting compared to the perpendicular alignment. The large magnetic field of the NMR spectrometer could possibly align the liquid crystal director into a single domain, depending on the sign of the magnetic anisotropy of the compounds ($\Delta\tilde{\chi} > 0$ or $\Delta\tilde{\chi} < 0$). In the case of when all director orientations occur, the observed powder spectrum is dominated by the perpendicular peaks with weaker parallel features. In general the NMR spectrum will show a powder pattern form corresponding to the weighted sum of all orientations and so can give information on the director distribution.

Compared to ESR spectroscopy, NMR could measure systems with a slower molecular tumbling in the sample that is 10^{-6}s or smaller for its rotational correlation times. In NMR spectroscopy, the quadrupolar interaction is smaller than the hyperfine tensor in ESR, which accounts for the difference in the correlation times needed to achieve the fast motion limit. The hypothesis of this experiment is the director to be randomly aligned inside the pores because of the randomness of the pores. Therefore, we expected that the NMR spectra would be a powder pattern and will contain both parallel and perpendicular features. Figures 30 to 33 show the NMR spectra for 8CB-d_2 dispersed in CPG with different pore diameters.

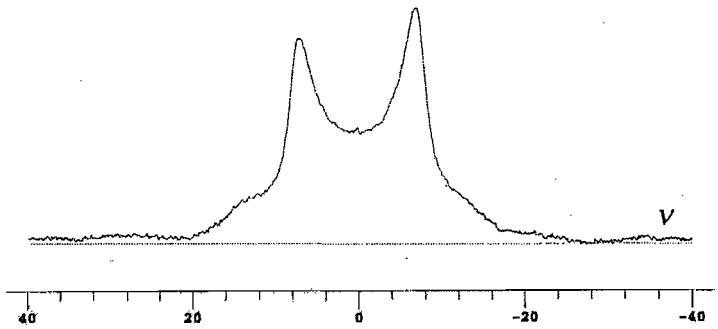

Figure 30: NMR spectrum for 8CB-d_2 confined in a CPG matrix with a pore diameter of 500Å at 300K in the smectic A phase.

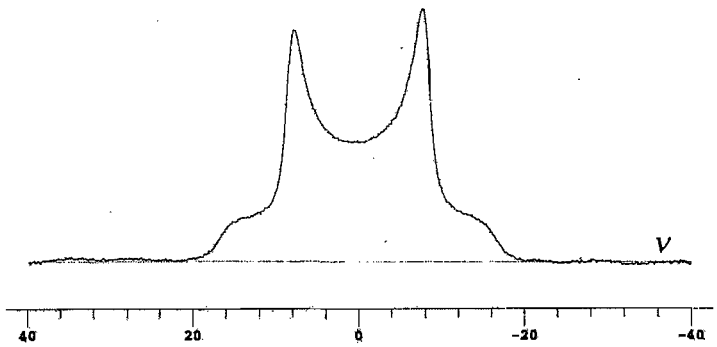

Figure 31: NMR spectrum for 8CB-d_2 confined in a CPG matrix with a pore diameter of 700Å at 300K in the smectic A phase.

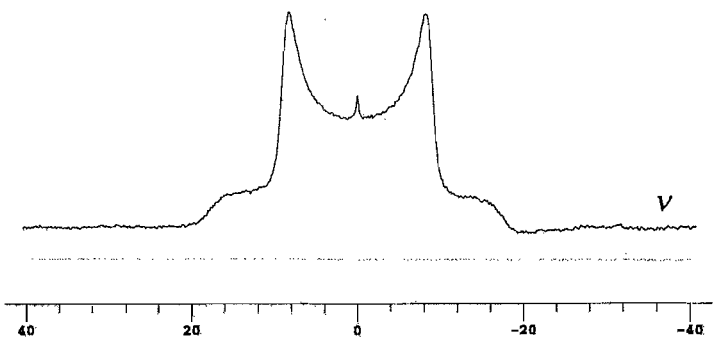

Figure 32: NMR spectrum for 8CB-d_2 confined in a CPG matrix with a pore diameter of 1000Å at 300K in the smectic A phase.

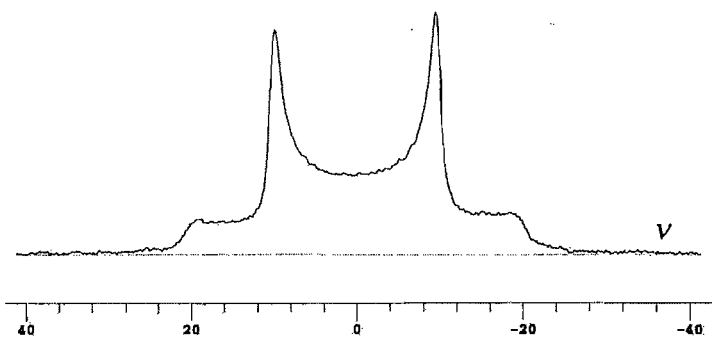

Figure 33: NMR spectrum for 8CB-d_2 confined in a CPG matrix with a pore diameter of 3000Å at 300K in the smectic A phase.

The outer shoulders on the NMR spectra correspond to the director being parallel to the magnetic field while the inner horns are associated with the director perpendicular to the field. It is of interest that for the largest pores the parallel features are sharper and more intense which suggests that the strong magnetic field has produced some small alignment of the director. For all systems with different pore diameters, we found the molecular motion is still fast because the quadrupolar splitting is comparable to that found in the bulk phase and is partially averaged by the rotational and conformational motion. It is to be expected that the motion becomes faster as the pore diameters increase. Certainly the linewidths decrease with increasing pore size which supports the ESR results that the rotational motion (or director fluctuations) become faster as the pore size increases. The signal for this powder pattern spectra is far narrower lines for the widest pore size, and this is related to the ability for the molecules to rotate faster in the widest pores or for more rapid director fluctuations. From the NMR observations, it is concluded that the dispersed smectic 8CB-d_2 in the confined geometries produces a randomly aligned director, therefore with these results our hypothesis earlier based on the ESR experiments is confirmed.

6.7 Conclusion

ESR as well as NMR spectroscopy are both powerful spectroscopic techniques for the qualitative and quantitative study of the director distribution in confined materials. In our studies, we have managed to perform ESR and NMR measurements for sample liquid crystals, doped with spin probes and dispersed in the pores of the CPG materials. Various controlled porous glasses with different pore diameters have been used, each produced interesting results that has been described and explained earlier in this Chapter.

To summarise and conclude, we have found that slow motion ESR spectra are observed for a nematic dispersed in both the smallest pores for 500Å, and even in the largest pore size of 3000Å. This contrasts with the behaviour in the bulk where the rotational motion is fast on the ESR timescale. The slow molecular motion spectra are actually similar to the ESR spectrum for a

glassy sample and we have confirmed this with our measurements of spin probes dissolved in the highly viscous OTP. However the behaviour for the two spin probes, Tempone and Cholestane, are, curiously reversed on going from the CPG to the OTP. The ESR spectra also contained powder patterns indicating part of the sample was in the fast molecular motion spectra, and confirmed that the director was randomly distributed through its interaction with the pore surface. The fast motion spectra might correspond to the spin probes inside the pores while the slow motion spectra come from the probes near the surface of the CPG pores which had the restricted movements. ESR can measure a spectrum for molecular motion of at least 10^{-8} s, therefore the observed results differentiate between regions of molecular motion of at least 10^{-8}s and also the one slower than that. Slower molecular rotation makes ESR linewidth broader and we have seen this in almost all the ESR spectra. The magnetic interaction, $\boldsymbol{g}$ and $\boldsymbol{A}$, for the slow motion components are non-averaged and take the values for a fixed spin probe. Experimental setup for toluene in the CPG media confirms that the spin probes are not absorbed by the CPG surfaces. It is to be expected, therefore, that for the nematic in CPG, the slow motion spectral component but actually comes from the spin probe doped in the liquid crystal.

NMR can be used to observe fast motion spectra when the molecular motion is slower of up to 10^{-6}s. In this situation, we have observed a randomly aligned powder pattern NMR spectra, however, the linewidths decreased with increasing pore diameter, suggesting that the molecular motion of the liquid crystal is becomes faster as the pore diameter is increased. Compared to ESR, NMR technique could only observe the fast motion components but these are consistent with the ESR results for the random director alignment in the random pores of CPG. The magnitude of the director randomness varies with the changes in the pore sizes, and this is similar for both ESR and NMR spectroscopies.

6.8 References

[1] G. P. Crawford, S. Žumer; *Liquid Crystals in Complex Geometries: Formed by Polymer and Porous Network,* Taylor and Francis, London (1996).

[2] J. W. Doane, A. Golemme, J. L. West, J. B. Whitehead, B. G. Wu; *Mol. Cryst. Liq. Cryst.*, **165**, 511 (1988).

[3] J. Pirs, S. Žumer, R. Blinc, J. W. Doane, J. West; *Proceedings of the Society for Information Display*, Anaheim (1988).

[4] J. W. Doane, N. A. Vaz, B. –G. Wu, S. Žumer; *Appl. Phys. Lett.,* **48**, 269 (1986).

[5] M. D. Dadmun, M. Muthukumar; *J. Chem. Phys.*, **98**, 4850 (1993).

[6] G. P. Crawford, R. Stannarius, J. W. Doane; *Phys. Rev. E.*, **44**, 2558 (1991).

[7] G. P. Crawford, L. M. Steele, R. J. Ondris-Crawford, G. S. Iannacchione, C. J. Yeager, J. W. Doane, D. Finotello; *J. Chem. Phys.,* **96**, 7788 (1992).

[8] G. P. Crawford, D. W. Allender, J. W. Doane; *Phys. Rev. A,* **45**, 8693 (1992).

[9] G. S. Iannacchione, G. P. Crawford, S. Žumer, J. W. Doane, D. Finotello; *Phys. Rev. Lett.,* **71**, 2595 (1993).

[10] T. Bellini, N.A. Clark, C. D. Muzny, L. Wu, C. W. Garland, D. W. Schaefar, B. Olivier; *Phys. Rev. Lett.*, **69**, 788 (1992).

[11] L. Wu, B. Zhou, C. W. Garland, T. Bellini, D. W. Schaefar, B. Olivier; *Phys. Rev. E.*, **51**, 2157 (1995).

[12] N.A. Clark, T. Bellini, R. M. Malzbender, B. N. Thomas, A. G. Rappaport, C. D. Muzny, D. W. Schaefar, L. Hrubesh; *Phys. Rev. Lett.*, **71**, 3505 (1993).

[13] S. Kralj, G. Lahajnar, A. Zidanšek, N. Vrbančič-Kopač, M. Vilfan, R. Blinc, M. Kosec; *Phys. Rev. E.*, **48**, 340 (1993).

[14] A. Zidanšek, S. Kralj, G. Lahajnar, R. Blinc; *Phys. Rev. E.*, **51**, 3332 (1995).

[15] F. M. Aliev; *Sov. Phys. Crystallogr.,* **33**, 573 (1988).

[16] F. M. Aliev, M. N. Breganov; *Sov. Phys. JETP.*, **68**, 70 (1989).

[17] P. E. Cladis, M. Kleman; *J. Phys. (Paris).*, **33**, 591 (1972).

[18] R. B. Meyer; *Philos. Mag.*, **27**, 405 (1973).

[19] A. Saupe; *Mol. Cryst. Liq. Cryst.*, **21**, 211 (1973).

[20] *National Partnership for Advanced Computational Infrastructure: Archive.*, **4 (11)** (2000).

[21] S. Kralj, A. Zidanšek, G. Lahajnar, S. Žumer, R. Blinc; *Phys. Rev. E.*, **57**, 3021 (1998).

[22] R. J. Ondris-Crawford, G. P. Crawford, J. W. Doane, S. Žumer, M. Vilfan, I. Vilfan; *Phys. Rev. E,* **48**, 1998 (1993).

[23] C. Cramer, T. Cramer, F. Kremer, R. Stannarius; *J. Chem. Phys.*, **106**, 3730 (1997).

[24] S. Kralj, A. Zidanšek, G. Lahajnar, I. Muševič, S. Žumer, R. Blinc, M. M. Pintar; *Phys. Rev. E.*, **53**, 3629 (1996).

[25] M. Vilfan, T. Apih, A. Gregorovič, B. Zalar, G. Lahajnar, S. Žumer, G. Hinze, R. Böhmer, G. Althoff; *Mag. Res. Imag.*, **19**, 433 (2001).

[26] G. P. Crawford, R. Ondris-Crawford, S. Žumer, J. W. Doane; *Phys. Rev. Lett.*, **70**, 1838 (1993).

[27] G. P. Crawford, D. K. Yang, S. Žumer, D. Finotello, J. W. Doane; *Phys. Rev. Lett.*, **66**, 723 (1991).

[28] X. Wu, W. I. Goldburg, M. X. Liu; *Phys. Rev. Lett.*, **69**, 470 (1992).

[29] L. Wu, B. Zhou, C. W. Garland, T. Bellini, D. W. Schaefer; *Phys. Rev. E.*, **51**, 2157 (1995).

[30] G. Schwalb, F. W. Deeg; *Phys. Rev. Lett.*, **74**, 1383 (1995).

[31] D. W. Allender, G. P. Crawford, J. W. Doane; *Phys. Rev. Lett.*, **67**, 1442 (1991).

[32] S. A. Goldman, G. V. Bruno, J. H. Freed; *J. Phys. Chem.,* **76**, 1858 (1972).

[33] J. H. Freed, G. V. Bruno, C. F. Polnaszek; *J. Phys. Chem.*, **75**, 3385 (1971).

[34] S. A. Goldman, G. V. Bruno, C. F. Polnaszek, J. H. Freed; *J. Chem. Phys.,* **56**, 716 (1972).

[35] J. H. Freed; *Ann. Rev. Phys. Chem.*, **23**, 265 (1972).

[36] C. F. Polnaszek, G. V. Bruno, J. H. Freed; *J. Chem. Phys.,* **58**, 3185 (1973).

[37] B. Rånby, J. F. Rabek; *ESR Spectroscopy in Polymer Research,* Springer-Verlag, Berlin (1997).

[38] N. M. Atherton; *Electron Spin Resonance Theory and Applications,* Ellis Horwood Ltd, Chichester (1973).

[39] Y. Ito; *J. Chem. Phys.*, **79**, 2650 (1983).

[40] G. R. Luckhurst; in *Magnetic Resonance Spectroscopy of Liquid Crystals – Non-Amphiphilic Systems,* Ed. by G. W. Gray, P. A. Winsor, Vol. 2, Chapt. 7, Ellis Horwood Ltd, Chichester (1974).

[41] J. W. Doane; in *Magnetic Resonance of Phase Transitions,* Ed. by F. J. Owens et al., Chapt. 4, Academic, New York (1979).

[42] R. Y. Dong; *Nuclear Magnetic Resonance of Liquid Crystals,* Springer, Berlin (1994).

Chapter VII

Magnetic Field Alignment of Chiral Nematics

7.1 Introduction

Have we ever realized that the word '*ambulance*' is in fact reversely spelled on the front of its vehicle? It is one of many international standards and all the countries in the world apply this convention. It must be a strong motive as to why the words and letters have to spell in reverse order. Yes, it is made to

make sure the other drivers on a busy road could easily identify an approaching ambulance in their rear view mirrors. This mirror will generate a two dimensional figure which is very similar to the original object that was placed in front of its surface. Both words are different in their appearance,

but they share the same meaning. There is a term in Chemistry which is called *chirality*, means two objects or compounds, both are important and

meaningful, both look very similar but are mirror images to each other, that is the object in this case a molecule is not superimposable on its mirror image [1]. Therefore, from the chemistry view, the word *ambulance* is one of a chiral object, just like our own hands!

The opposite of chiral is achiral and a simple example for this term is a pen or a cube. A mirror image of a pen can be imposed on the original object or in another word, we could tell it has mirror symmetry. Chirality is employed in chemistry to denote a molecular structure is asymmetric and handed. Mostly but not exclusively, molecular chirality is generated when four different structural moieties are attached to a tetrahedral, sp^3 carbon atom; this unit is often described as a chiral centre. These two mirror images are called enantiomers, which are non-superimposable and complete mirror image to each other. It has two stereochemical configurations which are termed *S* and *R*, as shown below for molecule *2-octanol*. The chiral centres are labelled with the stars. This chirality is responsible for optical activity,

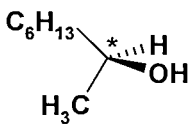

(S)-2-octanol

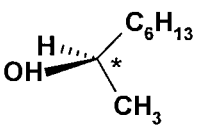

(R)-2-octanol

as evidenced by the rotation of the plane of plane polarised light and many other properties. Such chiral compounds usually are natural products and their chirality is responsible for with some special ability especially their biology activity.

Since our Thesis is mainly about liquid crystal, we are interested with liquid crystal compounds that could exhibit chirality behaviour. However, this type of compound is very special and unusual. Nevertheless, that is not a problem since structurally chiral liquid crystals can be formed by doping an achiral liquid crystal with any chiral molecule [2]. As we are fascinated with the simple nematic liquid crystal, the material that we study here is the chiral nematic phase and this phase will be explained more in the next Section. The chiral dopant changes the arrangement of the liquid crystal director to arrange it in a helical structure. We are quite familiar with this behaviour so

that this Chapter will go into further details to investigate the magnetic field alignment of chiral nematic phase, using ESR spectroscopy. That is the main aim for this Chapter. The next Section introduces our basic understanding of chiral nematics, followed by the Section on the perturbation of the helix, induced by a magnetic field. Then Section 7.4 presents the experimental findings of ESR measurement for a series of chiral nematic samples, together with the spectral simulations. While Section 7.5 discusses the quantitative studies from the ESR measurement and lastly Section 7.6 gives the details on the isotropic to chiral nematic cooling experiment.

7.2 Chiral Nematics

Nematic liquid crystals are widely recognised for their wide use in display devices. However, chiral nematics are even more fascinating; they have an array of special properties enabling them to be used in some of the latest technological applications, especially in the ferroelectric displays. In the first Chapter of this Thesis, we already presented a topic on liquid crystal display devices, and for these chiral materials are often added to the nematic mixtures employed. For example, in super twisted nematic (STN), a chiral material is used to create a proper pitch, P, is chosen in order to induce a total twist angle of $3\pi/2$ within a given cell spacing. Also, in the twisted nematic display, in order to obtain the same twist direction throughout the device (when there are two possible directions caused by the perpendicular alignment at the top and bottom plate), a small quantity of chiral material plays a major role for the device. Since it avoids the mosaic texture which could spoil the appearance of the display.

Chiral nematic phase was originally called cholesteric phase since most of compounds exhibiting chiral properties were from cholesterol derivatives. Hence, the first thermotropic liquid crystalline material, *cholesteryl benzoate*, discovered by Austrian botanist *Reinitzer*, exhibited a chiral nematic phase. Its chemical structure is shown in Figure 1.

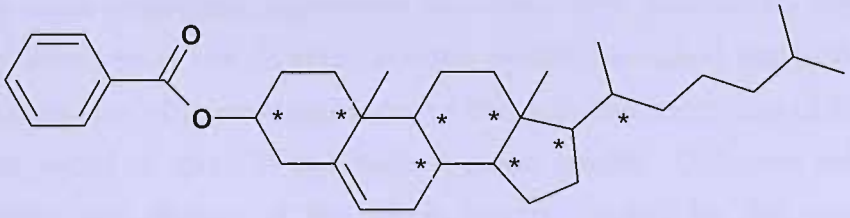

Figure 1: *Chemical structure of cholesteryl benzoate; Cr* 146° C *N** 178° C *I. The stars denote the chiral centres.*

However, not all chiral nematic compounds have to originate from cholesterol derivatives. Most nematic liquid crystals can produce a chiral nematic phase by adding a small quantity of chiral materials (chiral dopants) which are not necessarily liquid crystalline, into the nematic material. These chiral dopants have the ability to create a chiral environment in the nematic matrix through the construction of a helical macrostructure for the director. The ability to do this is measured by the helical twisting power, HTP details of which are described later in this Section. Figure 2 shows the helical structure of the director in the chiral nematic phase. The helical structure in which the director rotates about the axis of the helix is produced by a small uniform torsion caused by enantiomorphic molecules about an axis perpendicular to the director axis [3].

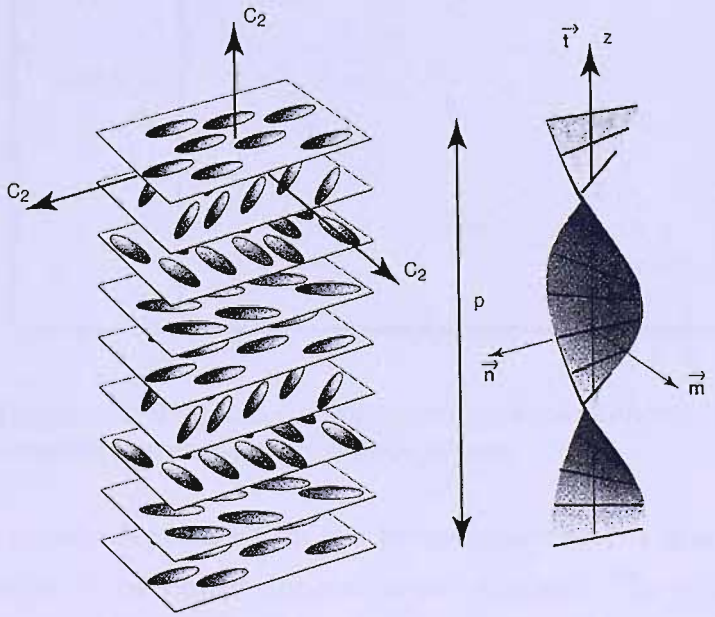

Figure 2: *Director arrangement in the chiral nematic phase (left-handed helix, P<0). The planes depicted here are fictitious as there is no positional order in the chiral nematic phase [4].*

One of the most important parameter that describes this helical structure is the length over which the director rotates by 2π , is called the pitch, *P*. The periodic structures of the helix results in the selective reflective of light, for a wavelength equal to that of the helical pitch length. Different colours are reflected with the change of the pitch length caused by the temperature dependence of the pitch [5]. The changes of the pitch length have proved to be useful to create a device to replace mercury thermometers for applications especially in the medical area. A thermometer whose colour changes with temperature is also safer to the patient and cheaper.

Figure 3 describes the behaviour of pitch-temperature dependent for one class of chiral nematic possessing a smectic phase. The pitch length increases with reducing temperature as the chiral nematic phase approaches a smectic A phase when it is converted to a layered and untwisted smectic phase. With increasing temperature, the pitch length for chiral nematic is tighter until the isotropic phase is reached so the helix is destroyed. More effects on increasing the temperature will be discussed in the next section with the experimental results obtained from the ESR spectra.

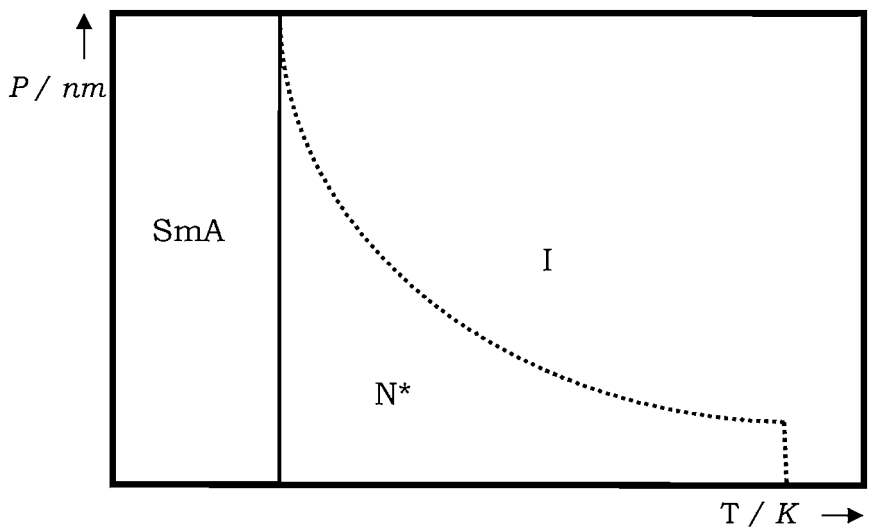

Figure 3: *The phase diagram for temperature dependence of pitch for chiral nematic materials with a SmA phase.*

The pitch is not only dependent on the temperature but is also controlled by the concentration of the chiral dopant in the nematic. The pitch is found to be inversely proportional to the number of chiral 'objects', i.e. the concentration of the chiral dopants; this can be measured in a variety of

ways but the correct measure is as the mole fraction. Different dopants have widely different capabilities to twist the director in a nematic phase. The ability of a chiral material to generate a helix is defined by helical twisting power (HTP), β_M which is unique for every dopant and host combination [6].

$$P = (x\beta_M)^{-1}, \tag{7.1}$$

where x is the mole fraction of the dopant material [2]. The sign of β_M can either be positive (right-handed helix) or negative (left-handed helix) depending on the chiral dopant. The pure enantiomers of the same chiral dopant should have the same magnitude of β_M but with the opposite signs.

There has been a considerable interest of chiral dopants with high β_M values for use in display devices [7]. But to achieve that is extremely difficult since there are no easy rules to predict a molecular structure of chiral dopant which can be related to its ability to induce a helical structure. Some molecules have large HTPs but some do not. Small changes in molecular structure of chiral compounds can actually create significant changes in their HTP [8,9]. In addition, there is also a limit on the solubility of the chiral dopants; this means that only a small concentration of chiral dopant can be employed. So there is no way to decrease P by adding large amount of chiral dopants to the nematic matrix. In addition, chiral dopants could reduce T_{NI} which is undesirable in applications.

According to theory, the term K_2 (twist elastic constant) in the Oseen-Zöcher-Frank equation for the free energy density (see Chapter I) is actually related to β_M for the nematic [11]. In fact,

$$\beta_M = -RT\Im\varepsilon / 2\pi K_2 V_m, \tag{7.2}$$

where $\Im$ is a chirality order parameter (depend on the ordering matrix of the dopant and its shape chirality), ε is a scaling parameter which is proportional to the orientational order of the nematic solvent [12] and V_m is the molar volume of the dopant. Usually the HTP is measured in units of

μm^{-1} and different chiral dopants and nematic solvents exhibit different β_M values; in Table 1 we give values for HTPs measured for chiral dopants in nematic poly(hexyl isocyanate) (PHIC) and 4-pentyl-4'-cyanobiphenyl [13].

Table 1: Helical twisting power of various chiral dopants.

dopant	in toluene solution of PHIC[a] w^c	in toluene solution of PHIC[a] $\beta_M/\mu m^{-1}$	in PCB[b] $\beta_M/\mu m^{-1}$	in isotropic solution $[\theta]_{237\,nm}/C_{dope}$[d]
BN-1	0.30	-0.48 ± 0.02 (-0.46 ± 0.02)	+85 ± 4	
BN-2	0.30	0.00 (0.00)		
BN-3	0.30	(+0.69 ± 0.03)	+80 ± 3	
BN-4	0.32	+0.22 ± 0.02 (+0.57 ± 0.04)	+79 ± 4	
cholesterol	0.30	+0.32 ± 0.01	-5.6 ± 0.5	
cholesteryl chloride	0.29	+0.28 ± 0.02	-3.5 ± 0.4	-64
cholesteryl propionate	0.40	+0.20 ± 0.01	-9.5 ± 0.7	-63
cholesteryl nonanoate	0.23	+0.027 ± 0.001	-9.6 ± 0.6	not detectable
cholestane	0.27	-0.055 ± 0.002		11
MPC	0.30	-0.26 ± 0.01		
camphor	0.28	+0.062 ± 0.002		-24
HIC/NIC (85/15)	0.30	1.2 ± 0.1		
	0.40	1.7 ± 0.1		

[a] MW 73 000 (MW 133 000). [b] 4-Cyano 4'-*n*-pentylbiphenyl. [c] PHIC weight fraction in toluene solution. [d] Molar ellipticity of the PHIC monomer unit per unit molar concentration of the dopant in the units of deg/cm·M^2.

In our measurements, we chose *cholesteryl propionate* as the chiral dopant and nematic ZLI-4792 as the nematic host. From the results in Table 1, we see that compared to the other dopants, *cholesteryl propionate* is quite powerful to create a small pitch in the chiral nematic phase. The chemical structure of this chiral dopant is shown in Figure 4, while the structural details for ZLI-4792 are described in Chapter III.

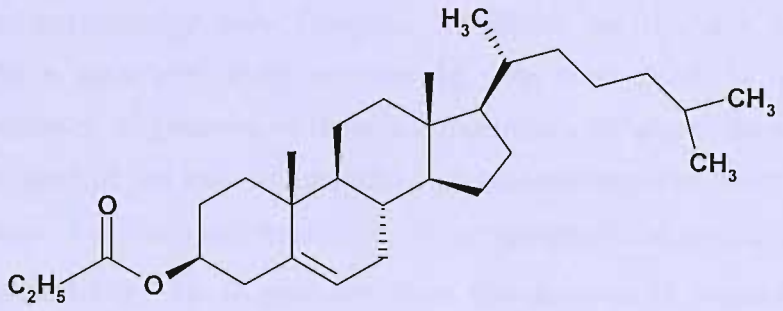

Figure 4: Chemical structure of cholesteryl propionate, $C_{30}H_{50}O_2$.

The facts that have been described here are mostly regarding the chiral nematic phase. However, there are many more chiral liquid crystalline phases such as chiral smectic C, chiral discotic phases and chiral polymeric mesogens each of which has its own characteristic and special properties. In addition, there are so-called frustrated phases such as the blue phases.

However, we are not going to discuss them in detail here. The studies on weak chiral nematics were performed long ago. One of the principal researchers in this area is *Meyer* [14] who presented the results for the effect of electric and magnetic fields on the structure of a chiral nematic phase in 1968 and then a year later he confirmed the theory for the distortion of a chiral nematic structure by a magnetic field [15]. Magnetic resonance studies of this phase to investigate the field induced chiral nematic-to-nematic transition has been introduced by *Luckhurst* and *Smith* in 1972 in their investigation of the nematic *4,4'-dimethoxyazoxybenzene* doped with *cholesteryl chloride* [16]. Their studies were then followed by those of *Zannoni et al.* in 1981 [17], here they reported a more detailed version of method to provide a rapid and reliable determination of both the pitch and handedness of induced chiral nematic mesophases. In their studies, the experimental technique was crosschecked by the *Grandjean-Cano* method. Since then, many more publications on chiral nematic studies have appeared.

7.3 Perturbation of the Helix Induced by a Magnetic Field

The application of a magnetic or an electric field to any mesophase produces a uniform alignment because of the anisotropy in the magnetic susceptibility or dielectric permittivity (see Chapter I). When we discuss the director alignment by a magnetic field, we should note that there is a significant difference between alignment of uniaxial nematic and chiral nematic phase, certainly because of the existing regular helical arrangement within the chiral nematic phase. For uniaxial nematics, if the magnetic susceptibility, $\Delta\tilde{\chi}$ or dielectric permittivity, $\Delta\tilde{\varepsilon}$ is positive, then the director is aligned parallel to field, and vice versa if the sign is negative. For a chiral nematic phase, if the anisotropic diamagnetic susceptibility is negative then the helix axis is aligned parallel to the magnetic field [15]. We shall discuss the more unusual behaviour if it is positive shortly.

In the absence of the magnetic field, the helix axes are randomly distributed possibly with some defects forming between the structures. When the magnetic field is applied to this system, these helixes are united into a

greater helical arrangement and the orientation of helix axis is actually aligned perpendicular to the magnetic field (for $\Delta\tilde{\chi} > 0$). Figure 5 shows the structure of helixes with no preferred direction before the field is applied and then the alignment of the helix axis perpendicular to the magnetic field after the field alignment. The black dots denote the defects between helixes.

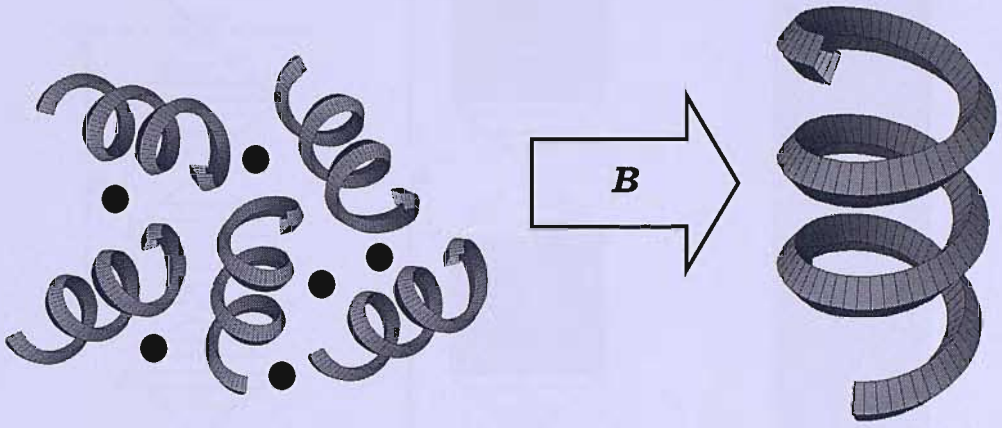

Figure 5: *Helical arrangement in chiral nematics before and after the application of magnetic field, giving* $\Delta\tilde{\chi} > 0$.

According to continuum theory [14, 18], the helix will undergo a distortion in the presence of the magnetic field which increases the probability to find director parallel to the magnetic field [16]. This could happen as the field strength is increased where the helical structure is distorted. The distortion only involves the changes in the pitch length and not the periodic structure of the chiral nematic mesophase. The pitch length is increased with the increasing field strength until at a certain limit, a critical field is reached and at this point, the pitch diverges logarithmically and the helical structure is destroyed, that is the structure is converted to a nematic structure [19]. The field-induced conversion from a chiral nematic to nematic phase does correspond to a continuous phase transition since there is no discontinuity in the gradient of the free energy at the critical field [20]. The structural changes occurring in this phenomenon are illustrated in Figures 6 and 7. The helical structure (white blocks) are dominant without the application of magnetic field. But as the field is applied, some of the helixes are destroyed in the helical arrangement to become a uniformly aligned director (black blocks). As the field is increased, more helixes are destroyed until the threshold field is reach, where the chiral nematic phase is totally converted

to a nematic phase. Figure 7 represents the phase diagram for this transition.

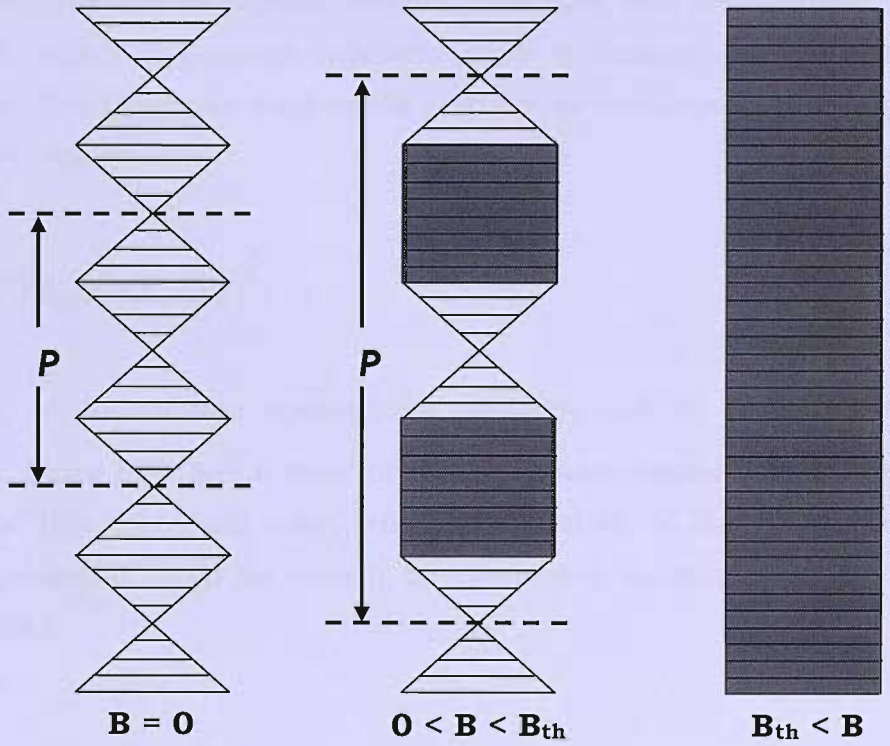

Figure 6: *Schematic representation of magnetic field effects for a chiral nematic with* $\Delta\tilde{\chi} > 0$.

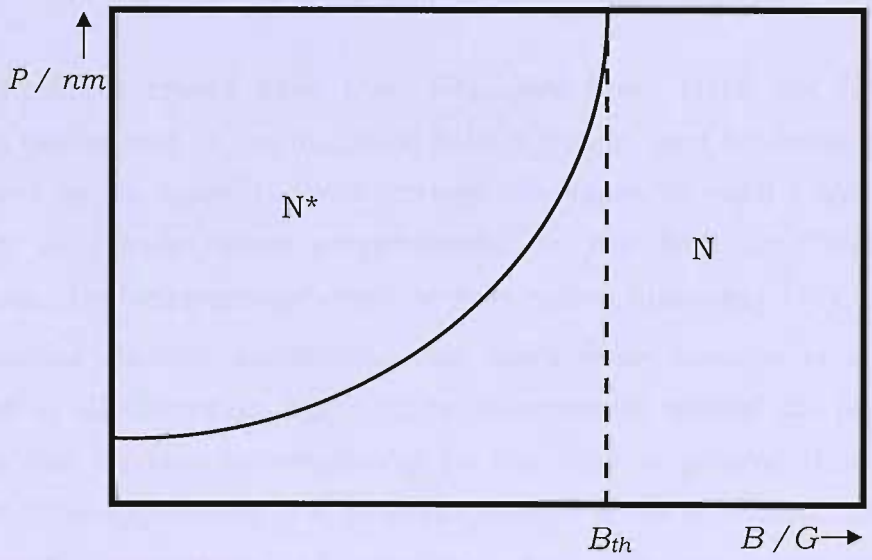

Figure 7: *Dependence of pitch on the magnetic field strength, B.*

In our case, we could not measure the threshold field, B_{th}, although we could achieve it if we use a different dopant with lower HTP, or maybe a lower concentration of chiral dopant. However, the ESR field is essentially fixed at just 3kG, which is perhaps relatively weak to destroy the chiral nematic structure. The threshold field could actually be measured according to the theory [14, 18]

$$B_{th} = (x\pi^2 / \beta_M)(\mu_0 K_2 / \Delta\tilde{\chi})^{\frac{1}{2}}, \tag{7.3}$$

where μ_0 is the vacuum permeability constant and K_2 is the twist elastic constant. Since ESR has a more or less constant magnetic field, in order to determine this threshold value, the concentration of chiral dopant in the nematic material could be varied; by combining equations (7.1), (7.2) and (7.3) we find

$$x_{th} = (B / \pi^2 \beta_M)(\Delta\tilde{\chi} / \mu_0 K_2)^{\frac{1}{2}}, \tag{7.4}$$

this gives the threshold concentration of chiral dopant needed to induce a chiral nematic state at a given field strength.

Two important effects have been described here. First, the helix axis is aligned orthogonal to the magnetic field direction, and secondly the pitch is increased as the magnetic field strength increases, in such a way that more director is parallel than perpendicular to the field. In Chapter I, we mentioned the orientational director distribution function, $f(\theta)$, for a three-dimensional director distribution, for cases when director is in randomly ordered in all directions. For a three dimensional system the probability of finding the director perpendicular to the field is greater than finding it parallel. The application of a magnetic field to a chiral nematic with positive diamagnetic anisotropy, $\Delta\tilde{\chi}$, produces both director being parallel and perpendicular to the field. Since the helix axis is cylindrically symmetry, the director has a cylindrical distribution with parallel and perpendicular director orientations being equivalent. The director distribution for this case

is called a two dimensional orientational distribution function, $p(\theta)$, and for an arbitrary field strength the orientational probability of the director with respect to the field is predicted to be [14,18]

$$p(\theta) = \frac{(1-k^2\cos^2\theta)^{-\frac{1}{2}}}{\int_0^{2\pi}(1-k^2\cos^2\theta)^{-\frac{1}{2}}d\theta}. \tag{7.5}$$

Here k is a parameter which determines the distribution function for a particular material and at a given field is

$$k = (PB/\pi^2)(\Delta\tilde{\chi}/\mu_0 K_2)^{\frac{1}{2}} E(k), \tag{7.6}$$

where $E(k)$ is an elliptic integral of the second kind

$$E(k) = \int_0^{\pi/2}(1-k^2\sin^2\theta)^{\frac{1}{2}}d\theta. \tag{7.7}$$

The parameter k can take values from zero to unity. Zero means an unperturbed helical structure with the helix axis perpendicular to the field while unity means the director is fully aligned parallel to the magnetic field direction. Figure 8 shows examples for the distribution function calculated for values of k from 0 to 0.99. The plots are shown in the range for θ from 0° – 90° only because of the symmetry of the system.

From the director distribution function, we can simulate the ESR spectra we expect to observe in the experiments using different concentrations of chiral dopant. These simulate spectra are shown together with the director distribution function in Figure 8. We can see significant changes in the intensity of both parallel peaks, that is those with the smaller splitting, occur when k is relatively close to unity, which corresponds to an increase in the probability to find the director parallel to the magnetic field. The changes in k from 0 up to about 0.5 do not have a significant effect on the ESR

spectra as expected from the weak dependence of the director probability on its orientation [21].

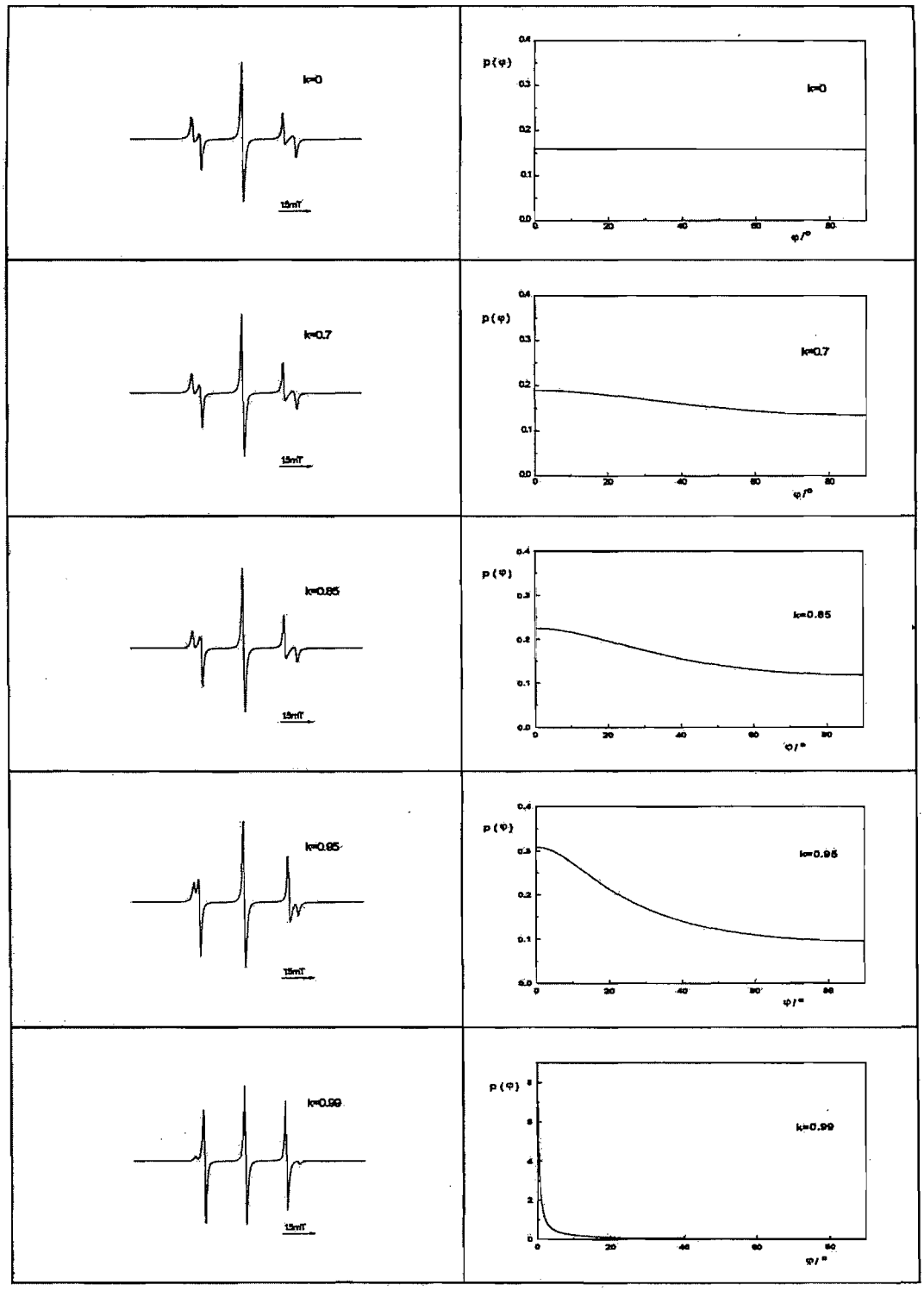

Figure 8: *Simulated ESR spectra of the Tempone spin probe using the director distribution function, $p(\theta)$, given in equation (7.4) for different values of k.*

As the concentration of chiral dopant in the chiral nematic increases, so the helical pitch length decreases and so to some extent, the parameter k will decrease. In the limit that k vanishes the distribution function in equation (7.4) becomes

$$p(\theta)=\frac{1}{2}\pi, \tag{7.8}$$

corresponding to an isotropic two dimensional director distribution with respect to the magnetic field.

If the concentration keeps increasing, *2D* director distribution is removed completely then all director orientations are observed to be equally probable which gives the *3D* isotropic distribution function

$$p(\theta)=\frac{\sin\theta}{4\pi}, \tag{7.9}$$

that is used to calculate the ESR spectrum for a 3D director distribution. In 3D ESR spectrum (see Figure 11), the outer $\widetilde{A}_{\perp}$ lines increase in intensity while that of the $\widetilde{A}_{\parallel}$ lines are diminished. The increase of intensity of the $\widetilde{A}_{\perp}$ lines indicated that there is a greater probability of finding the director perpendicular rather than parallel to the field, when the concentration of chiral dopants reaches its critical value. Such this behaviour can only occur if there is no longer helix axis to be constrained perpendicular to the magnetic field.

So far, we have gone through two types of distribution function, two-dimensional (2D) and three-dimensional (3D) distribution function which characterize the director distribution in the liquid crystal. Actually there is one more director distribution which characterize the liquid crystal, and this is the one dimensional (1D) distribution function. This function is applied when the liquid crystal director is fully aligned, whether parallel or perpendicular to the magnetic field.

7.4 ESR Spectroscopy and Spectral Simulations

Generally, when a spin probe (e.g. Cholestane) is added to a nematic liquid crystal the nematic phase is actually converted to a weakly chiral nematic phase even for low concentrations. That is it has the same capability as other chiral dopants to induce a chiral nematic phase. However, the initial pitch in the chiral nematic phase for this very low concentration of spin probe is sufficiently large for the helix to be completely unwound by the magnetic field of the ESR spectrometer. However, in our ESR measurements, the spin probe employed was 2,2,6,6-tetramethyl-4-piperidone-N-oxide (Tempone) which is achiral so it will not produce any chiral nematic phase. Compared to the highly anisotropic Cholestane spin probe, Tempone presents a better ratio of the hyperfine splitting to the linewidth, which allows a better spectral resolution and so a more sensitive study of the director distribution.

The ESR spectrum for Tempone in nematic ZLI-4792 without any chiral dopant is expected to contain three hyperfine lines with approximately equal hyperfine spacings. It represents a uniformly aligned nematic with the director parallel to the magnetic field, since $\Delta\tilde{\chi}$ is positive for ZLI-4792. Figure 9 shows the ESR spectrum for the Tempone spin probe in the nematic ZLI-4792.

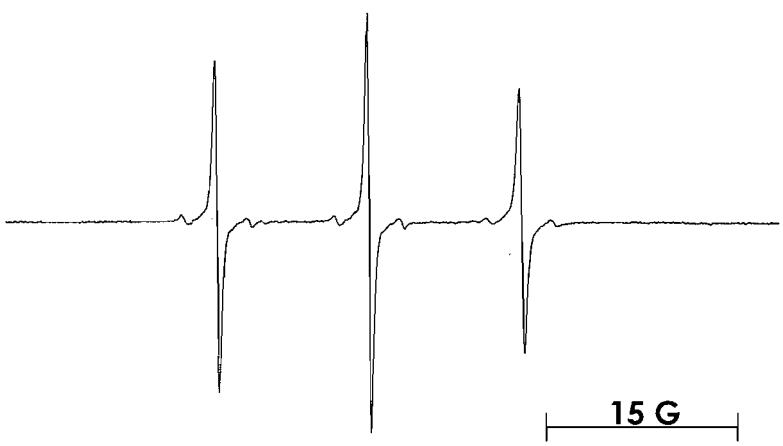

Figure 9: ESR spectrum for the Tempone spin probe in nematic ZLI-4792.

For each nitrogen hyperfine line, there are two additional weak peaks on either side of the main peaks, which result from carbon-13 isotopes in the

spin probe. These satellite lines do not contain any information relevant to the director alignment or director distribution because the carbon-13 hyperfine interaction is essentially a scalar. Therefore, in the remainder of the analysis, we shall ignore them.

In the presence of the chiral dopant in the nematic, there are more than three lines in the ESR spectrum, indicating that the director is not uniformly oriented with respect to the magnetic field. The nematic is now converted to a weakly or highly chiral nematic phase, depending on the concentration of chiral dopant in the nematic. For a low concentration of chiral dopant, we expect the spectrum to show a one dimensional director distribution with respect to the field. The magnetic field of the ESR spectrometer could possibly destroy the weakly chiral nematic phase, as mentioned before. As the concentration of chiral dopant increases, certainly the chiral nematic phase is produced. Provided $\Delta\widetilde{\chi} > 0$ the helical structure is aligned to give a 2D director distribution with respect to the magnetic field and an associated ESR spectrum similar to the simulated spectrum shown in Figure 10. This shows five nitrogen hyperfine lines corresponding to the director both parallel and perpendicular to the magnetic field. In the study of the field alignment of a chiral nematic, we expect to find an ESR spectrum characteristic of 2D director distribution for high concentrations of chiral dopant. To perform this simulation, the parameters $\widetilde{A}_{\parallel}$ and $\widetilde{A}_{\perp}$ are determined from the spectrum shown in Figure 9, while $T_2^{-1}(-1)$, $T_2^{-1}(0)$ and $T_2^{-1}(1)$ were set equal to 0.40G, 0.33G and 0.40G, respectively. The central line does not change its position and actually,

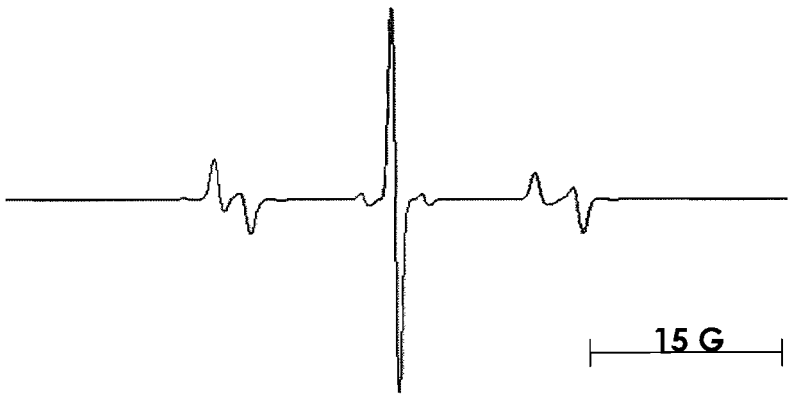

Figure 10: Simulated ESR spectrum for a two-dimensional director distribution with equal probability of finding the director both parallel and perpendicular to the magnetic field.

it is a sum of two lines since we assume that $\widetilde{g}_{\parallel} = \widetilde{g}_{\perp}$. The two inner peaks (near to the central peak) in the spectrum originate from the director parallel to the field with a hyperfine splitting, $\widetilde{A}_{\parallel}$, while the outer peaks are from the director perpendicular to the magnetic field, with a hyperfine splitting, $\widetilde{A}_{\perp}$. The difference, $\widetilde{A}_{\parallel} - \widetilde{A}_{\perp}$ is small for Tempone spin probe due to its low molecular anisotropy [22] but the parallel and perpendicular peaks are readily seen because their linewidths are small.

In the chiral nematic phase, external forces, such as the magnetic field, can unwind the helical structure. It means some part of the phase could be aligned parallel to the magnetic field and so produces a larger pitch. If this happens, the ESR spectrum would have the form shown in Figure 11, the intensities of the parallel peaks are increased in intensity while those of the perpendicular are decreased. The helix is partially unwound as indicated by the greater intensity of the parallel peaks.

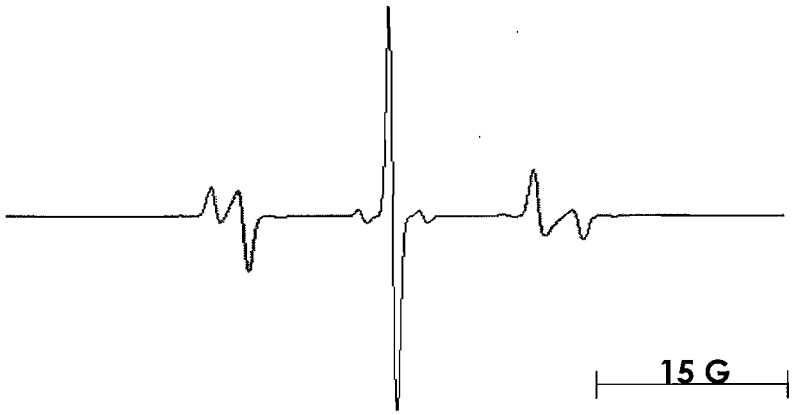

Figure 11: Simulated ESR spectrum for a two-dimensional director distribution showing the helix of the chiral nematic is partially unwound.

In several cases, experiment suggests that the director distribution can go beyond 2D and this should happen if we keep increasing the amount of chiral dopant in the nematic host. High concentrations of dopant decrease the pitch length, which makes the helical structure less distorted and aligned by the magnetic field. Therefore, the outer lines in the ESR spectrum increase in intensity while that of the inner lines diminish. The large intensity of the outer spectral lines with respect to the inner suggests to a three dimensional director distribution. This behaviour suggests that the helix axis is no longer constrained to be orthogonal to the magnetic field. In this case, the 3D distribution function can be used to simulate the ESR spectrum associated with this distribution. Figure 12 shows the simulated ESR spectrum for a three-dimensional distribution function, for a high chiral dopant concentration in the nematic host.

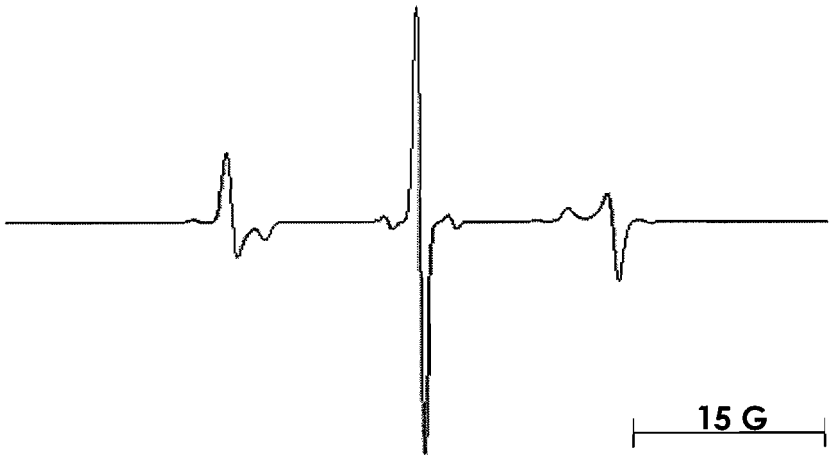

Figure 12: *Simulated ESR spectrum for a 3D director distribution in a chiral nematic.*

Figures 9 to 12 have describe the range of ESR spectra for a chiral nematic phase expected to be found in a chiral nematic, depending on the director distribution in the helical structures.

Our studies on the chiral nematic phase involve several samples of Tempone spin probe dissolved in nematic ZLI-4792, doped with *cholesteryl propionate* for a range of concentrations (see Table 1). The lowest concentration of chiral

Table 1: *The series chiral nematic mixtures used in the ESR study of chiral nematics.*

Label	**A**	**B**	**C**	**D**	**E**	**F**	**G**
Weight percentage (wt%)	0.50	1.0	1.0	1.5	1.5	2.0	5.0
Mole fraction, x (mol%)	0.39	0.77	0.77	1.14	1.15	1.54	3.77

dopant in the host is 0.5wt% while the highest is 5.0wt%. We made duplicate samples for the 1.0wt% and 1.5wt% mixtures, in order to study the reproducibility and consistency of our results. For each sample, we recorded their spectra from room temperature until the chiral nematic phase undergoes a transition to the isotropic phase. The ESR measurement methods are described in Chapter III and we followed the method used by *Luckhurst* and *Smith* [16]. As the temperature is increased, we have studied the changes in the hyperfine splittings and the appearance of new peaks for

each ESR spectrum. Qualitative and quantitative analysis of these ESR spectra are described later.

7.4.1 Concentration of Chiral Dopant in Chiral Nematic: 0.5wt%

The ESR spectra for this experiment are shown in Figure 13 (a) while the simulated spectra along with the corresponding director distribution function are shown in Figure 13 (b). The mole fraction of *cholesteryl propionate* in ZLI-4792 for this sample is 0.39%, so make it the smallest concentration of chiral dopant that we have studied. As expected, the ESR spectrum at 300K shows a 2D director distribution, confirming the existing of helical structure in the chiral nematic phase. The parallel and perpendicular peaks seem equal in intensity, which gives the intensity ratio for the two peaks as 1. As the temperature increases, the parallel peaks become more intense and as do the perpendicular peaks. However, the parallel peaks seem more intense which suggests that the helix is being unwound by the magnetic field. We can also see the difference, $\left|\tilde{A}_{\parallel} - \tilde{A}_{\perp}\right|$ is getting smaller as the temperature increases from 300K to 360K. The inner parallel and outer perpendicular peaks are gradually shifted closer to each other corresponding to a decrease in the orientational order and finally meet at 380K, showing the phase is isotropic. The gradual changes of $\tilde{A}_{\parallel}$ and $\tilde{A}_{\perp}$ values for each spectrum demonstrate the changes of the molecular orientational order of the chiral nematic phase as the temperature is increased. Other than that, we could also notice the difference in the separation of the parallel and perpendicular peaks at high field and low field for each spectrum. At high field, the spacing between these two peaks seems bigger than that of at low field. This phenomena occurs as a result of the difference in the $\tilde{g}_{\parallel}$ and $\tilde{g}_{\perp}$; details of this phenomena are mentioned in Chapter VI. For the spectral simulations, we have used the value of 2.0057 for $\tilde{g}_{\parallel}$ and 2.0054 for $\tilde{g}_{\perp}$. Although the difference between them is very small the effects on the ESR separations is quite significant. The parameters used for the ESR spectral simulation for this study are shown in Table 2. How and why these parameters are chosen is described in Chapter IV. The distribution parameter, a, only increases slightly over the 50K

temperature range, therefore the director order parameters only change slightly indicating poor alignment by the magnetic field. The molecular order parameter for the chiral nematic phase decreased as a function of increasing temperature. The simulated spectra are in good agreement with the equivalent experimental spectra.

Table 2: *The hyperfine spacings, linewidths, and distribution parameter used to simulate the ESR spectra for Tempone in ZLI-4792 doped with 0.5wt% cholesteryl propionate.*

Temp. / K	$\tilde{A}_{\parallel}/G$	$\tilde{A}_{\perp}/G$	$T_2^{-1}(-1)/G$	$T_2^{-1}(0)/G$	$T_2^{-1}(1)/G$	a
300	12.58	15.13	0.40	0.30	0.40	1.8
320	12.96	14.98	0.40	0.28	0.40	1.9
340	13.17	14.89	0.25	0.30	0.30	2.0
350	13.47	14.98	0.27	0.28	0.27	2.0
360	13.50	14.95	0.27	0.28	0.35	1.8
380	14.42	14.42	0.32	0.28	0.38	-

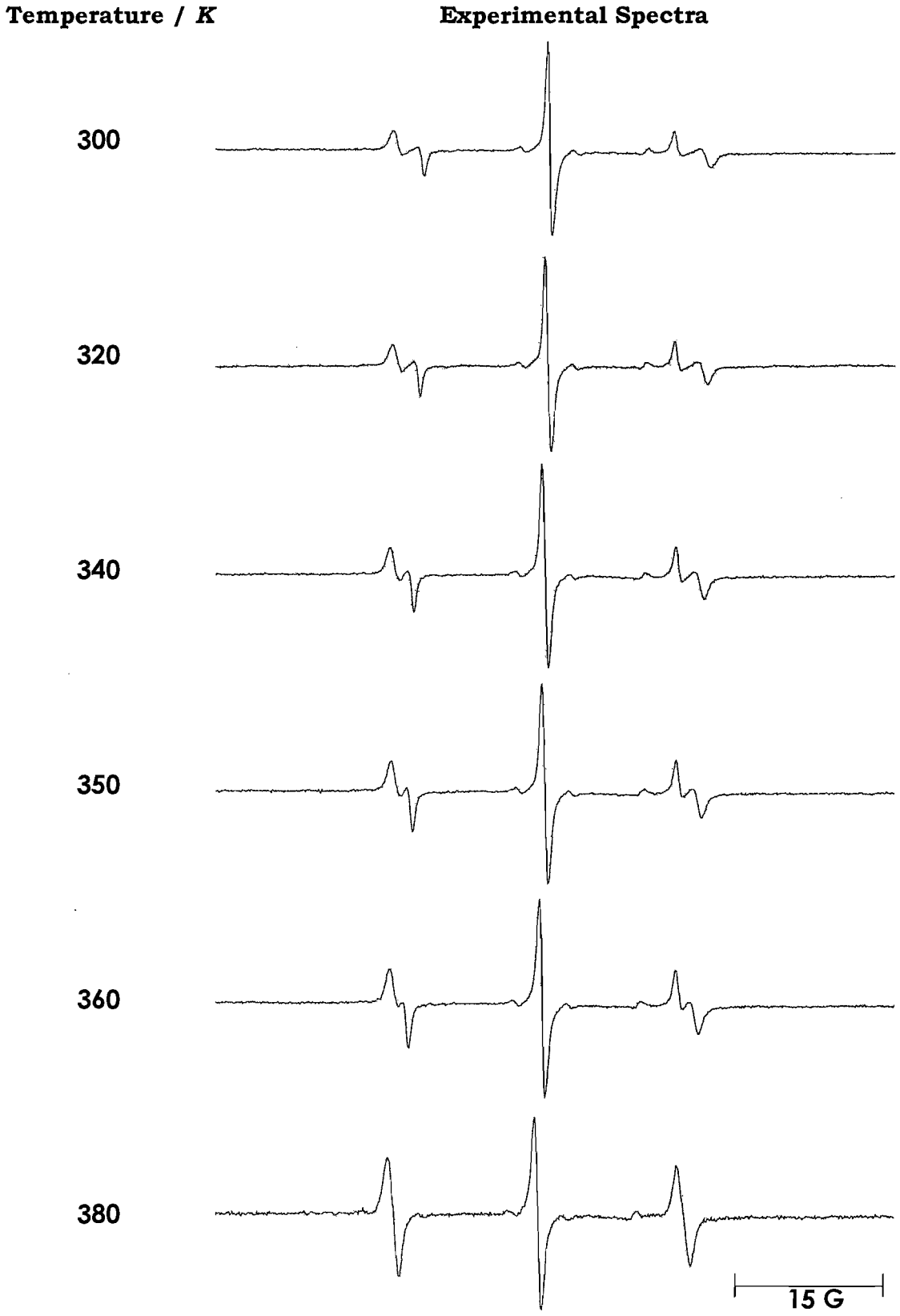

Figure 13: *(a) ESR spectra for Tempone in chiral nematic ZLI-4792 doped with 0.5wt% cholesteryl propionate.*

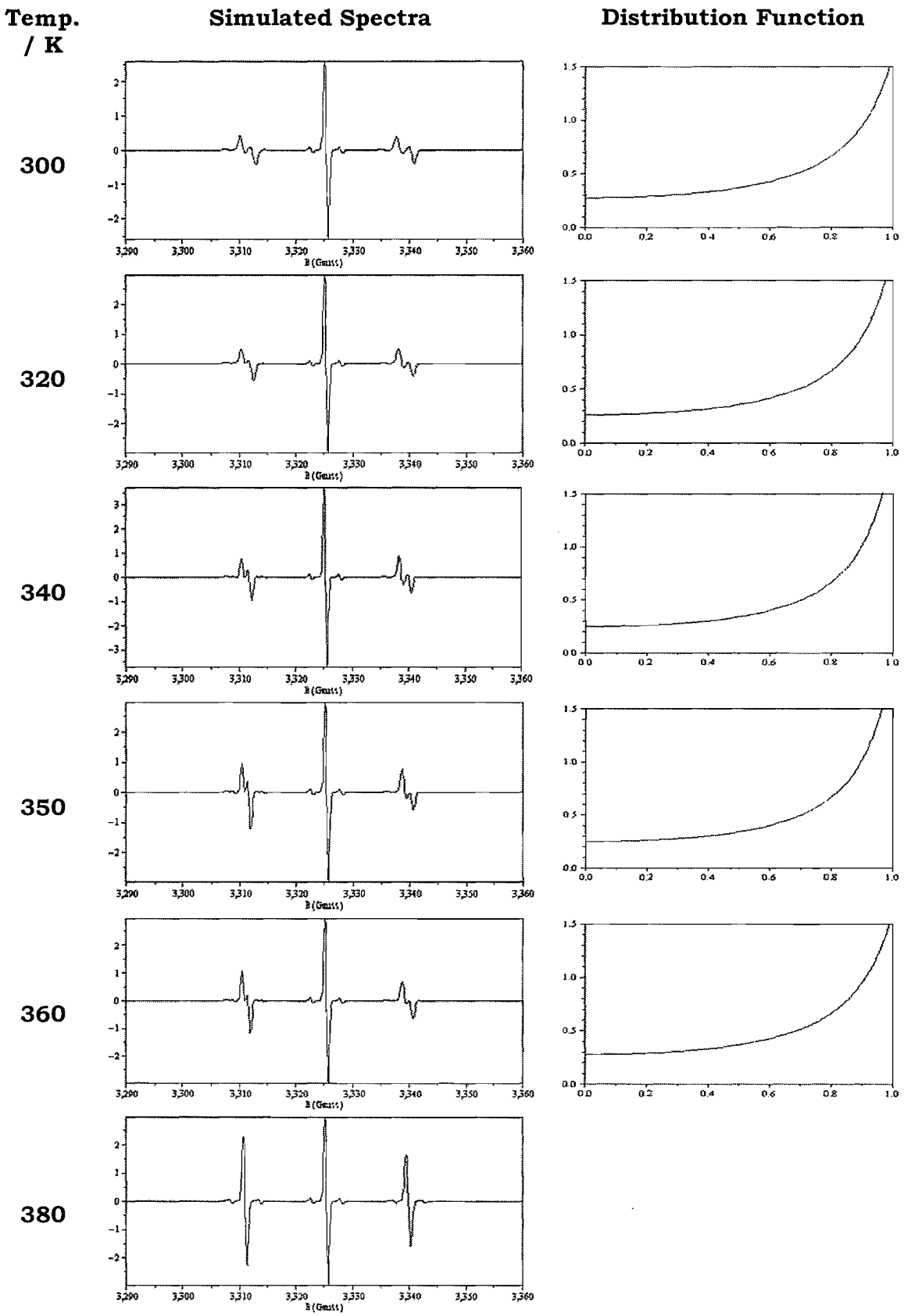

Figure 13: *(b) Simulated ESR spectra for Tempone in chiral nematic ZLI-4792 with 0.5wt% cholesteryl propionate together with the resultant director distribution function (x-axis represents $\cos\theta$, while y-axis represents $f(\theta)$).*

7.4.2 Concentration of Chiral Dopant in Chiral Nematic: 1.0wt%

We examined two samples containing 1.0wt% cholesteryl propionate in nematic ZLI-4792; they were named as A and B. The samples were prepared at different times but are very similar and have the same properties. Figures 14 (a) and 15 (a) show the ESR spectra measured for sample A and B, respectively. The ESR measurements for both sample A and B produce relatively similar results, which meant the reproducibility for this measurement is good.

At 300K, the perpendicular peaks seem much more intense than the parallel. It seems that the limiting 2D director distribution, as we have seen before for 0.5wt% sample, no longer exists. We might say the director distributions, consistent with the ESR spectra, are closer to 3D than 2D. Increase in temperature does not change the height ratio for the parallel and perpendicular peaks. The perpendicular peaks remain more intense than parallel peaks. However, the increase in temperature does decrease the molecular orientational order and we know this because the parallel and perpendicular peaks get closer to each other until the mixture reaches its isotropic phase. There is another interesting feature that we have found for the ESR spectrum at 360K. Both parallel and perpendicular peaks overlap significantly so that the spectrum now shows a broad single peak. These broad peaks sharpen when the isotropic phase forms at 380K. We have simulated all of the ESR spectra to compare them with their experimental counterparts. They are shown in Figures 14 (b) and 15 (b) for sample A and B, respectively. The parameters chosen for these simulations are listed in Table 3 for sample A and Table 4 for sample B. The director distribution parameter, a, only increases slightly over the 50K temperature range, therefore the director order parameters only change slightly indicating weak alignment by the magnetic field. The simulated spectra are in good agreement with the equivalent experimental spectra.

Table 3: *The hyperfine spacings, linewidths, and distribution parameter used to simulate the ESR spectra for Tempone in ZLI-4792 doped with 1.0wt% cholesteryl propionate (A) (for Figure 14).*

Temp. / K	$\tilde{A}_{\parallel}/G$	$\tilde{A}_{\perp}/G$	$T_2^{-1}(-1)/G$	$T_2^{-1}(0)/G$	$T_2^{-1}(1)/G$	a
300	12.10	15.30	0.40	0.33	0.40	1.7
320	12.50	15.35	0.40	0.33	0.40	1.7
340	12.70	15.23	0.40	0.33	0.35	1.5
350	13.60	14.58	0.40	0.33	0.38	1.4
360	14.38	14.40	0.75	0.42	0.58	10
380	14.42	14.42	0.40	0.40	0.40	-

Table 4: *The hyperfine spacings, linewidths and distribution parameter used to simulate ESR spectra for Tempone in ZLI-4792 doped with 1.0wt% cholesteryl propionate (B) (for Figure 15).*

Temp. / K	$\tilde{A}_{\parallel}/G$	$\tilde{A}_{\perp}/G$	$T_2^{-1}(-1)/G$	$T_2^{-1}(0)/G$	$T_2^{-1}(1)/G$	a
300	12.34	15.50	0.40	0.32	0.40	1.7
320	12.50	15.30	0.40	0.32	0.40	1.7
340	12.80	15.18	0.40	0.32	0.38	1.6
350	13.20	14.88	0.50	0.32	0.40	1.6
360	14.36	14.42	0.55	0.38	0.48	10
380	14.43	14.43	0.40	0.40	0.40	-

Figure 14: (a) ESR spectra for Tempone in chiral nematic ZLI-4792 with 1.0wt% cholesteryl propionate.

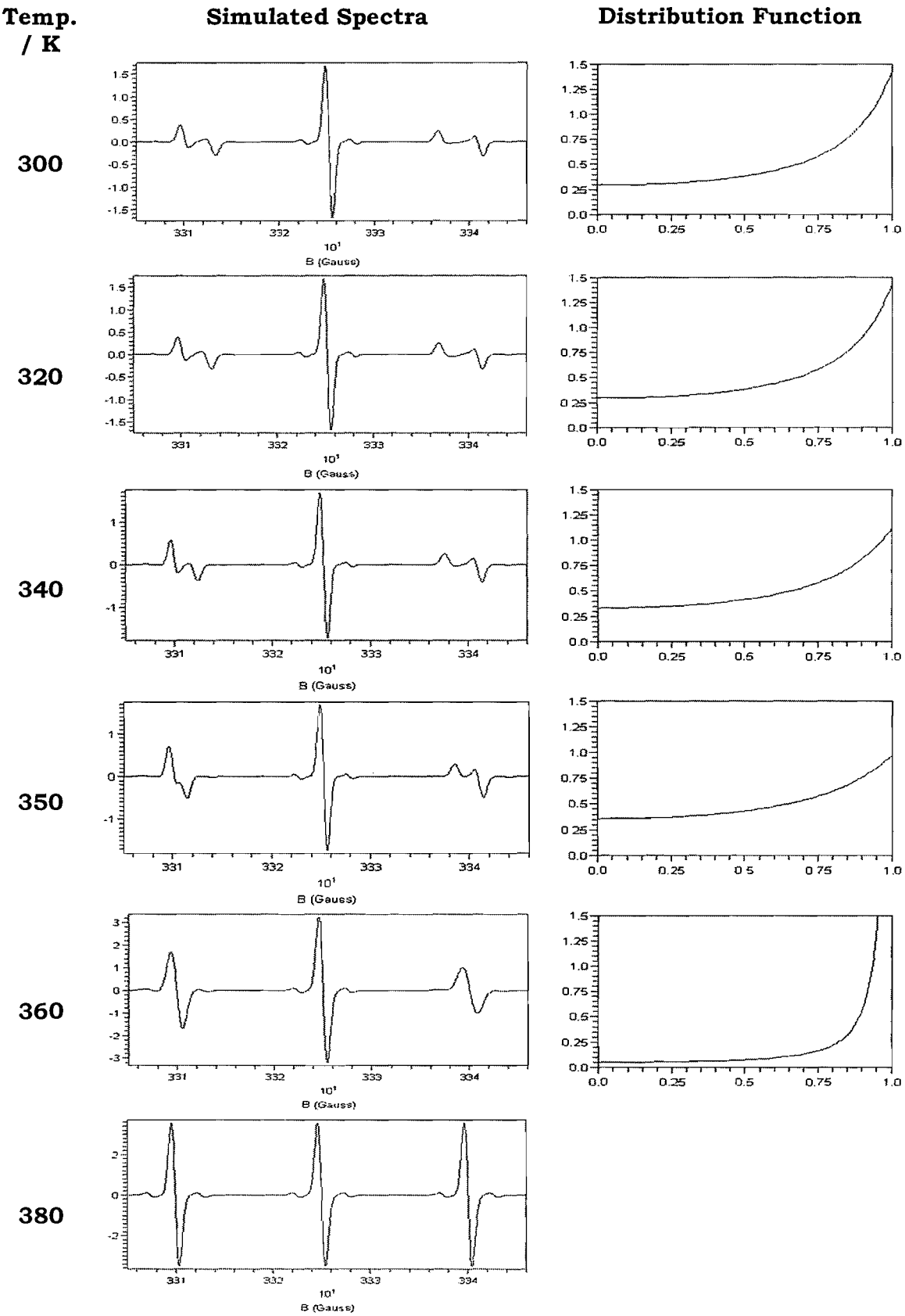

Figure 14: *(b) Simulated ESR spectra for Tempone in chiral nematic ZLI-4792 with 1.0wt% cholesteryl propionate, together with the resultant director distribution function (x-axis represents $\cos\theta$, while y-axis represents $f(\theta)$).*

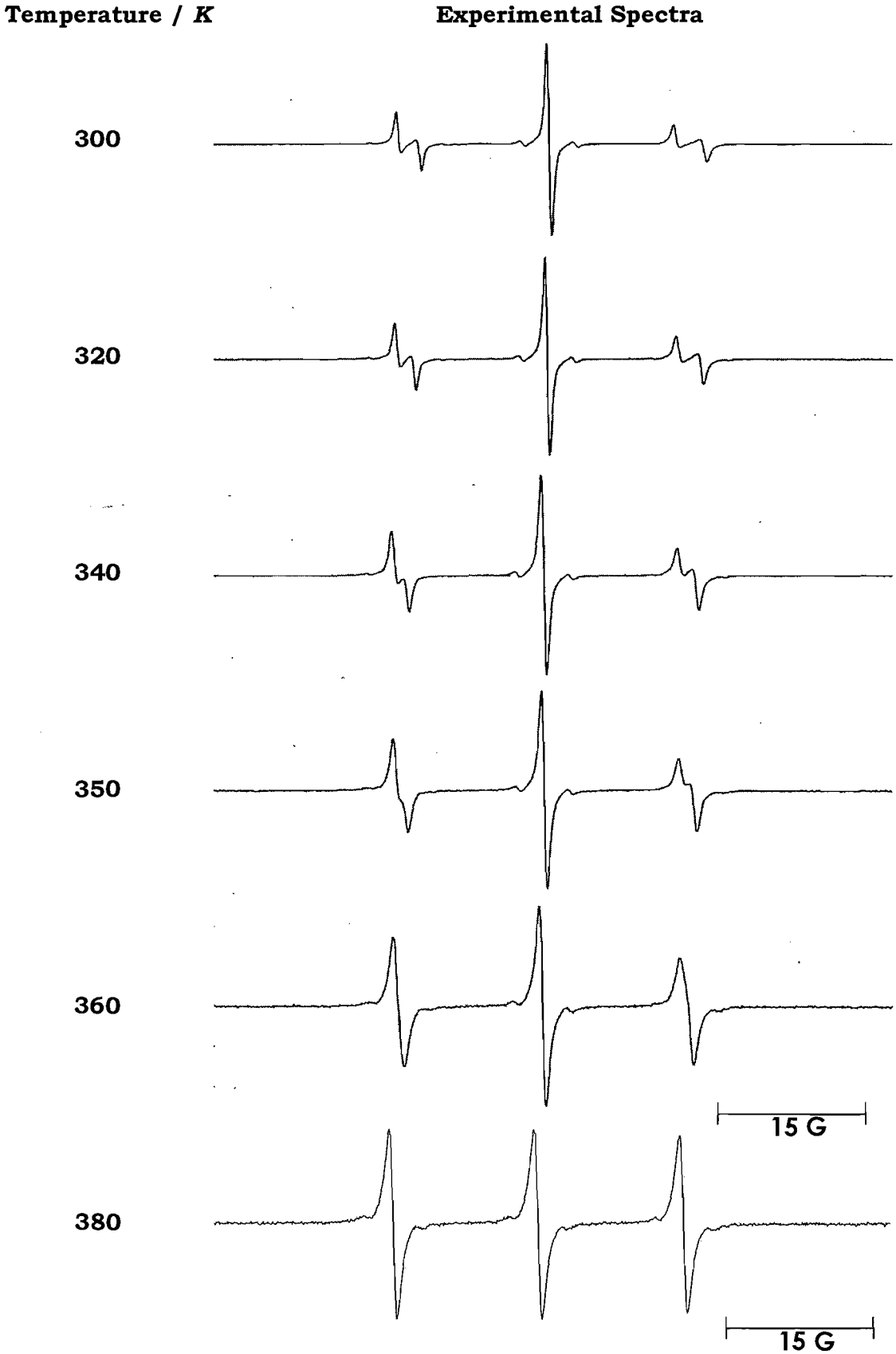

Figure 15: (a) ESR spectra for Tempone in chiral nematic ZLI-4792 with 1.0wt% cholesteryl propionate.

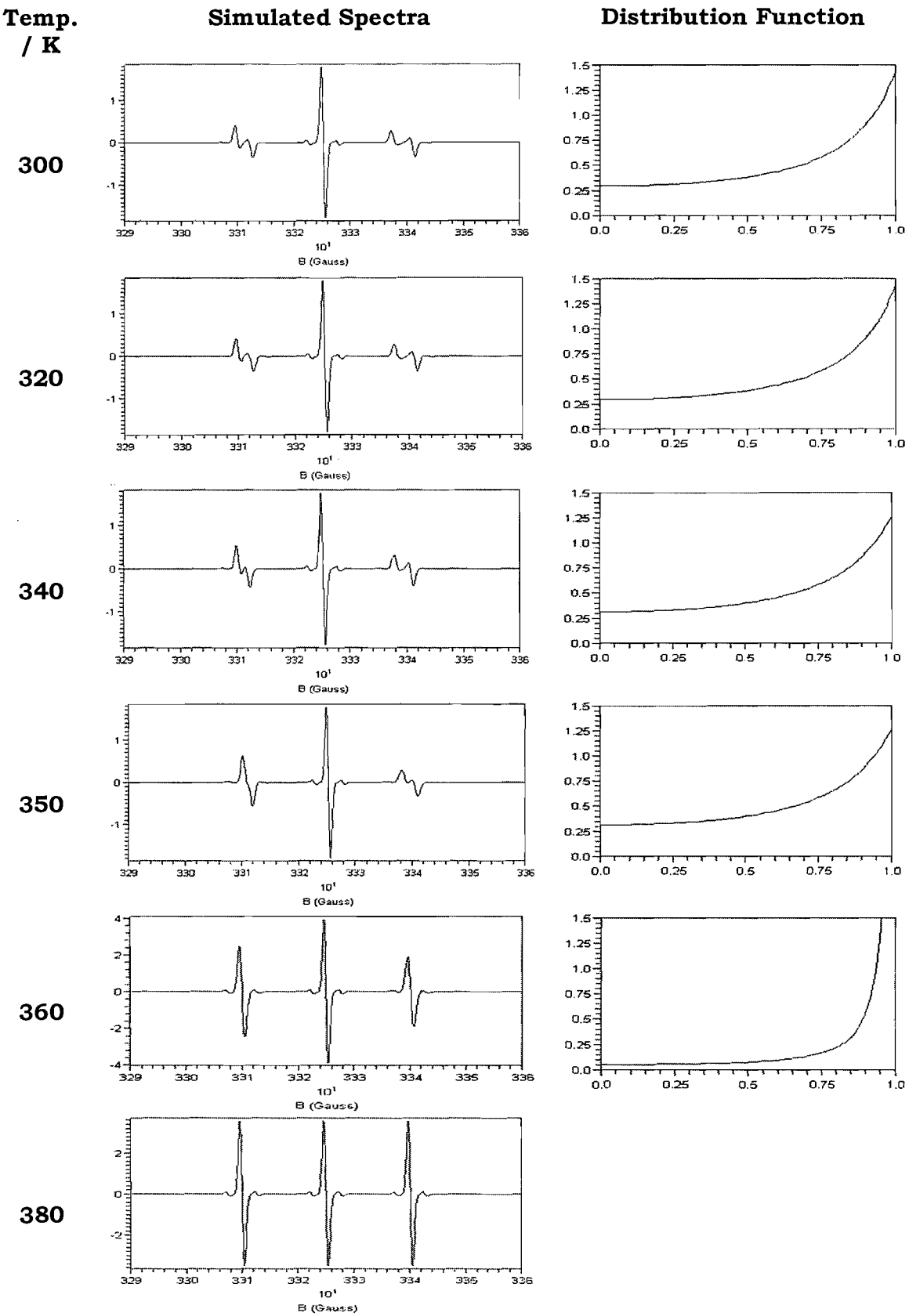

Figure 15: *(b) Simulated ESR spectra for Tempone in chiral nematic ZLI-4792 with 1.0wt% cholesteryl propionate, with the resultant director distribution function (x-axis represents $\cos\theta$, while y-axis represents $f(\theta)$).*

7.4.3 Concentration of Chiral Dopant in Chiral Nematic: 1.5wt%

Two identical samples were prepared for this study, C and D. Figures 16 (a) and 17 (a) show that the ESR spectra recorded for C and D, respectively. At 300K, the ESR results observed for sample C differ slightly from sample D, basically, the parallel peaks are more intense for sample D, compared to C. However, they share the important character of this study, where they both correspond to the ESR spectra for 3D director distribution rather than 2D. That is the intensities of the perpendicular peaks seem greater than those observed for 1.0wt% *cholesteryl propionate*. The spectra change with increasing temperature and, as usual, the isotropic phase is reached at 380K. The simulated ESR spectra for this concentration are shown in Figures 16 (b) and 17 (b) for sample C and D, respectively. The simulation parameters are given in Tables 5 and 6. The distribution parameter, *a*, only increases slightly over the 40K temperature range, and so the director order parameters only change slightly indicating the expected weak alignment by the magnetic field. The simulated spectra are in good agreement with the equivalent experimental spectra.

Table 5: *The hyperfine spacings, linewidths, and distribution parameter used to simulate the ESR spectra for Tempone in ZLI-4792 doped with 1.5wt% cholesteryl propionate (A) (for Figure 16).*

Temp. / K	$\tilde{A}_{\parallel}/G$	$\tilde{A}_{\perp}/G$	$T_2^{-1}(-1)/G$	$T_2^{-1}(0)/G$	$T_2^{-1}(1)/G$	*a*
300	12.35	15.45	0.40	0.33	0.40	1.3
320	12.55	15.30	0.40	0.33	0.40	1.4
340	12.70	15.25	0.40	0.33	0.38	1.5
350	13.10	14.98	0.40	0.33	0.38	1.3
360	13.80	14.70	0.40	0.33	0.38	1.2
380	14.42	14.42	0.40	0.40	0.40	

Table 6: *The hyperfine spacings, linewidths, and distribution parameter used to simulate ESR spectra for Tempone in ZLI-4792 doped with 1.5wt% cholesteryl propionate (B) (for Figure 17).*

Temp. / K	$\tilde{A}_{\parallel}/G$	$\tilde{A}_{\perp}/G$	$T_2^{-1}(-1)/G$	$T_2^{-1}(0)/G$	$T_2^{-1}(1)/G$	a
300	12.34	15.46	0.40	0.32	0.40	1.5
320	12.50	15.35	0.40	0.32	0.40	1.6
340	12.80	15.20	0.40	0.32	0.40	1.5
350	13.00	15.10	0.40	0.32	0.40	1.4
360	13.48	14.88	0.40	0.30	0.38	1.0
380	14.43	14.43	0.40	0.40	0.40	

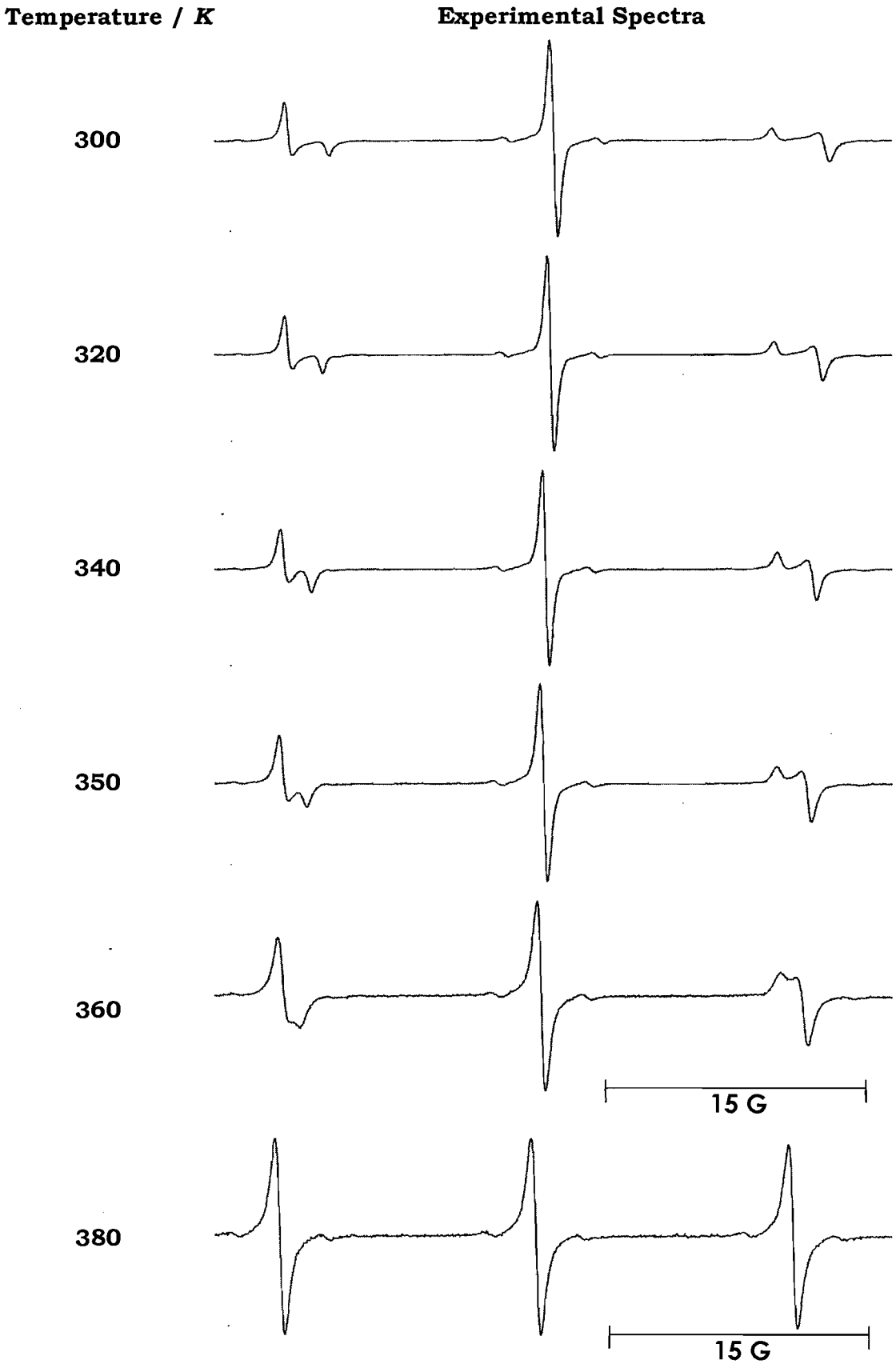

Figure 16: *(a) ESR spectra for Tempone in chiral nematic ZLI-4792 with 1.5wt% cholesteryl propionate.*

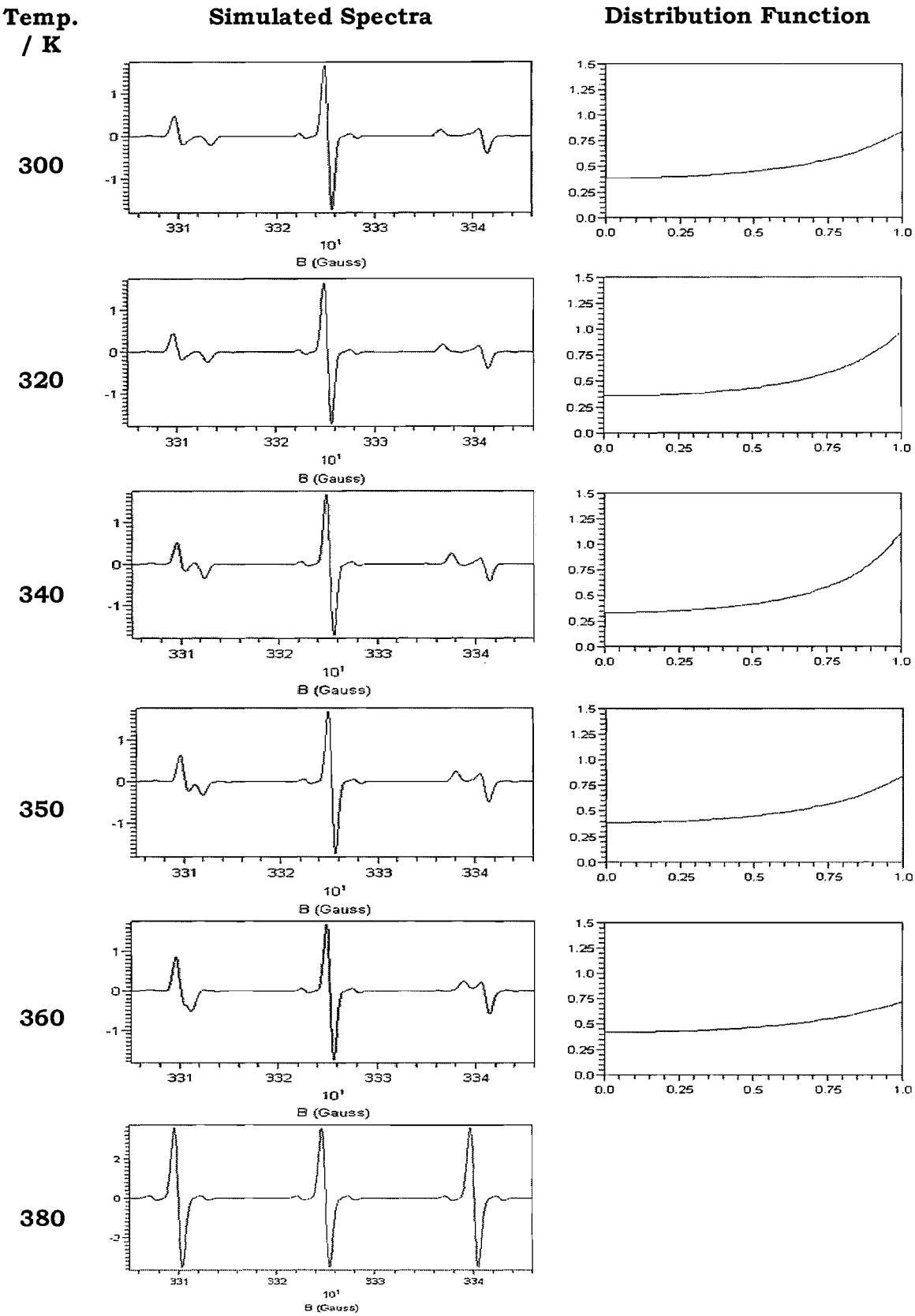

Figure 16: *(b) Simulated ESR spectra for Tempone in chiral nematic ZLI-4792 with 1.5wt% cholesteryl propionate, with the resultant director distribution function (x-axis represents $\cos\theta$, while y-axis represents $f(\theta)$).*

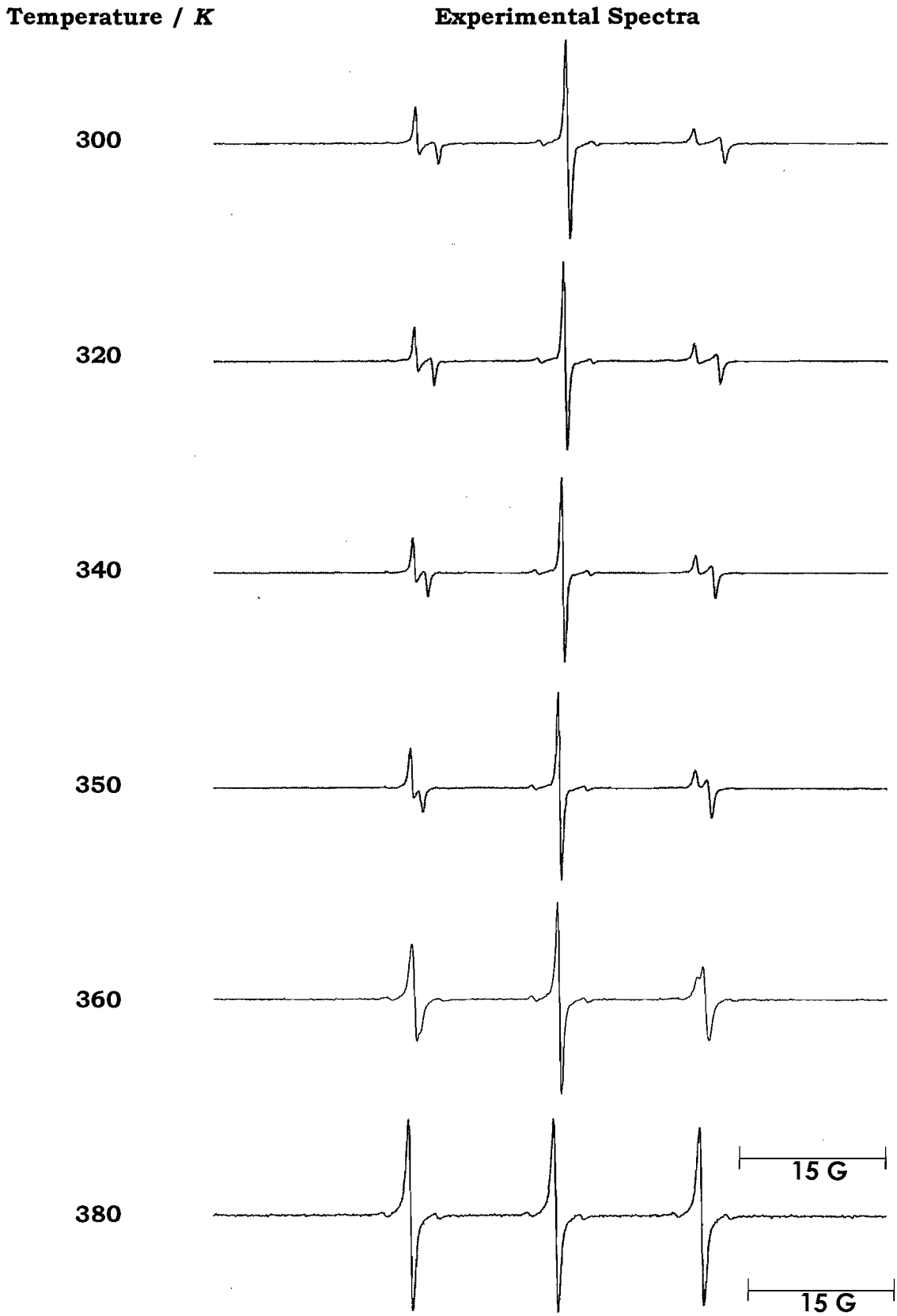

Figure 17: (a) ESR spectra for Tempone in chiral nematic ZLI-4792 with 1.5wt% cholesteryl propionate.

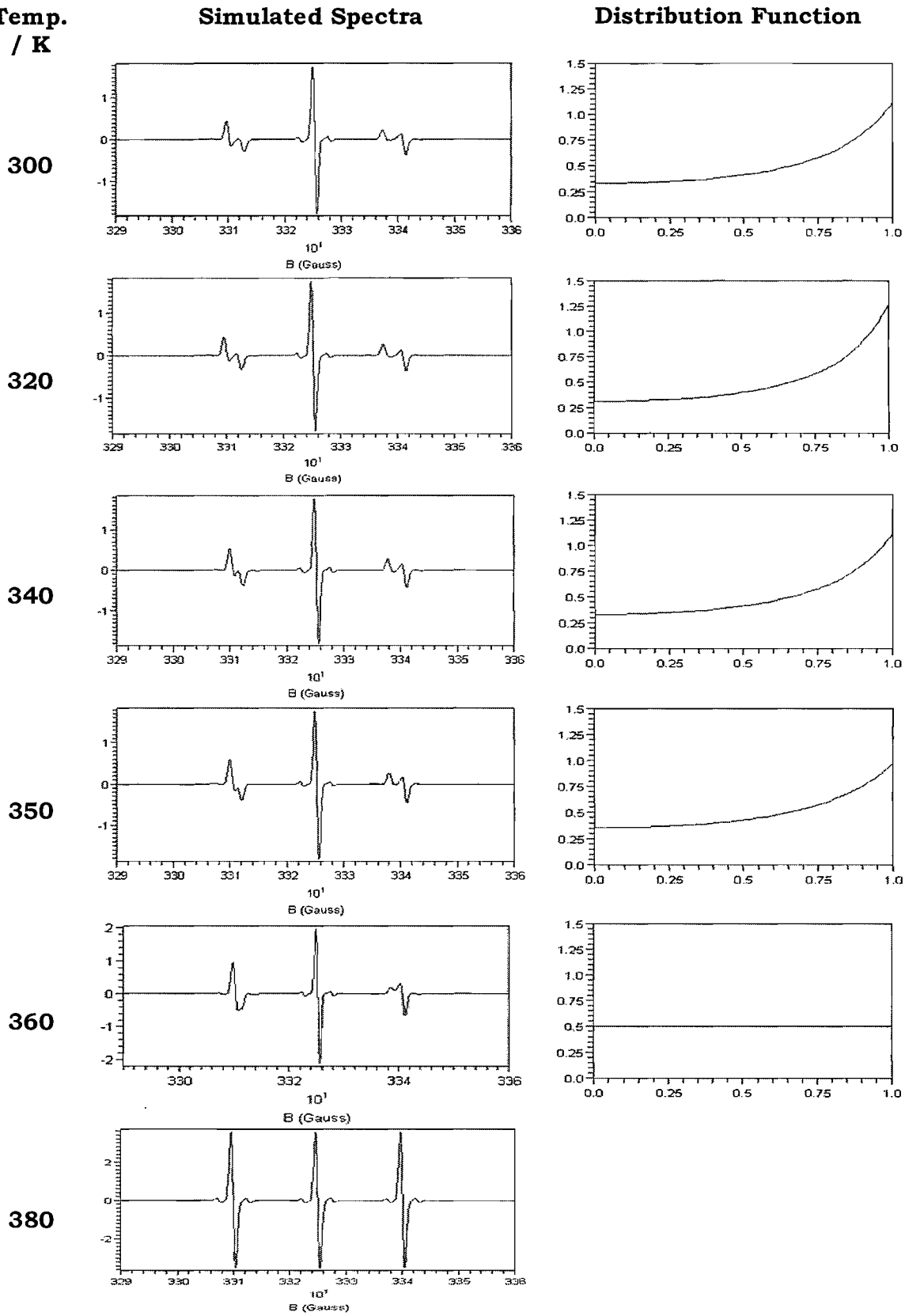

Figure 17: *(b) Simulated ESR spectra for Tempone in chiral nematic ZLI-4792 with 1.5wt% cholesteryl propionate, together with the resultant director distribution function (x-axis represents $\cos\theta$, while y-axis represents $f(\theta)$).*

7.4.4 Concentration of Chiral Dopant in Chiral Nematic: 2.0wt%

Figure 18 (a) shows the ESR spectra recorded for sample ZLI-4792 with 2.0wt% *cholesteryl propionate*. It is interesting to see the parallel peaks in the ESR spectra get weaker and weaker as the concentration of chiral dopant is increased. The relative intensity between the parallel and perpendicular peaks is important in our qualitative study since it reflects the director distribution for our chiral liquid crystals. The observation for 3D director distribution even for 1.0wt% of *cholesteryl propionate* is actually interesting since the previous study made by *Luckhurst* and *Smith* [16] could only observe the 3D distribution for a highly concentration of chiral dopant, ~10wt%; although they studied a different chiral dopant, namely *cholesteryl chloride*. Therefore, the difference of our respective findings might results from the difference in the properties of the two dopants, e.g. HTP value. The increase in temperature gives a similar result to the systems studied before. Again, the isotropic phase is reached at 380K. Figure 18 (b) shows the simulated spectra along with the distribution function for this system while Table 7 shows the parameters used in order to simulate the spectra. The distribution parameter, a, only increases slightly over the 40K temperature range, therefore the director order parameters only change slightly indicating poor director alignment by the magnetic field. The simulated spectra are in good agreement with the equivalent experimental spectra.

Table 7: *The hyperfine spacings, linewidths and distribution parameter used to simulate the ESR spectra for Tempone in ZLI-4792 doped with 2.0wt% cholesteryl propionate.*

Temp. / K	$\tilde{A}_{\parallel}/G$	$\tilde{A}_{\perp}/G$	$T_2^{-1}(-1)/G$	$T_2^{-1}(0)/G$	$T_2^{-1}(1)/G$	a
300	12.31	15.50	0.40	0.30	0.40	1.0
320	12.38	15.44	0.40	0.30	0.40	1.1
340	12.40	15.41	0.40	0.30	0.50	1.3
350	12.80	15.20	0.40	0.30	0.35	1.2
360	13.50	14.85	0.40	0.30	0.42	3.0
380	14.42	14.42	0.40	0.40	0.40	

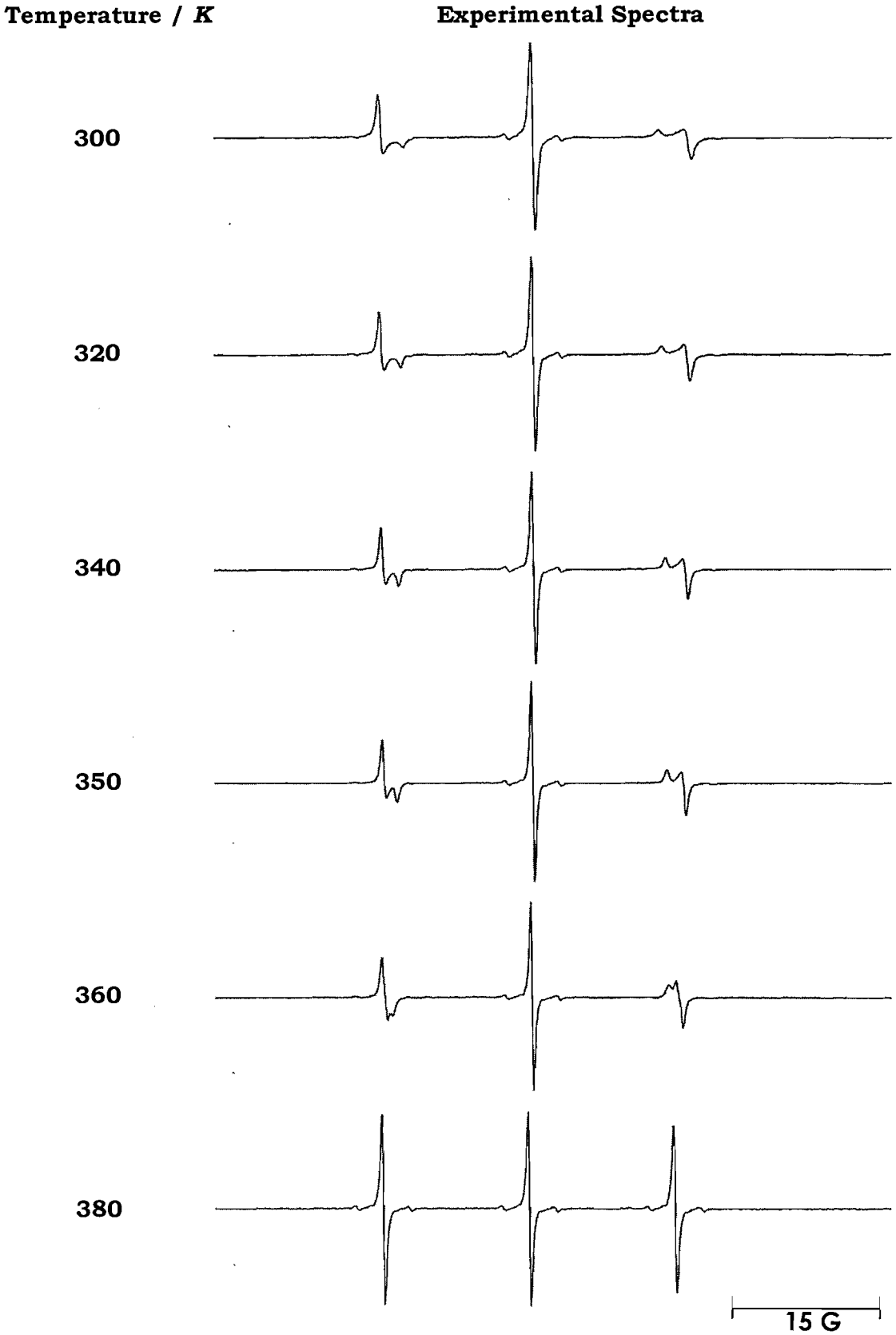

Figure 18: *(a) ESR spectra for Tempone in chiral nematic ZLI-4792 with 2.0wt% cholesteryl propionate.*

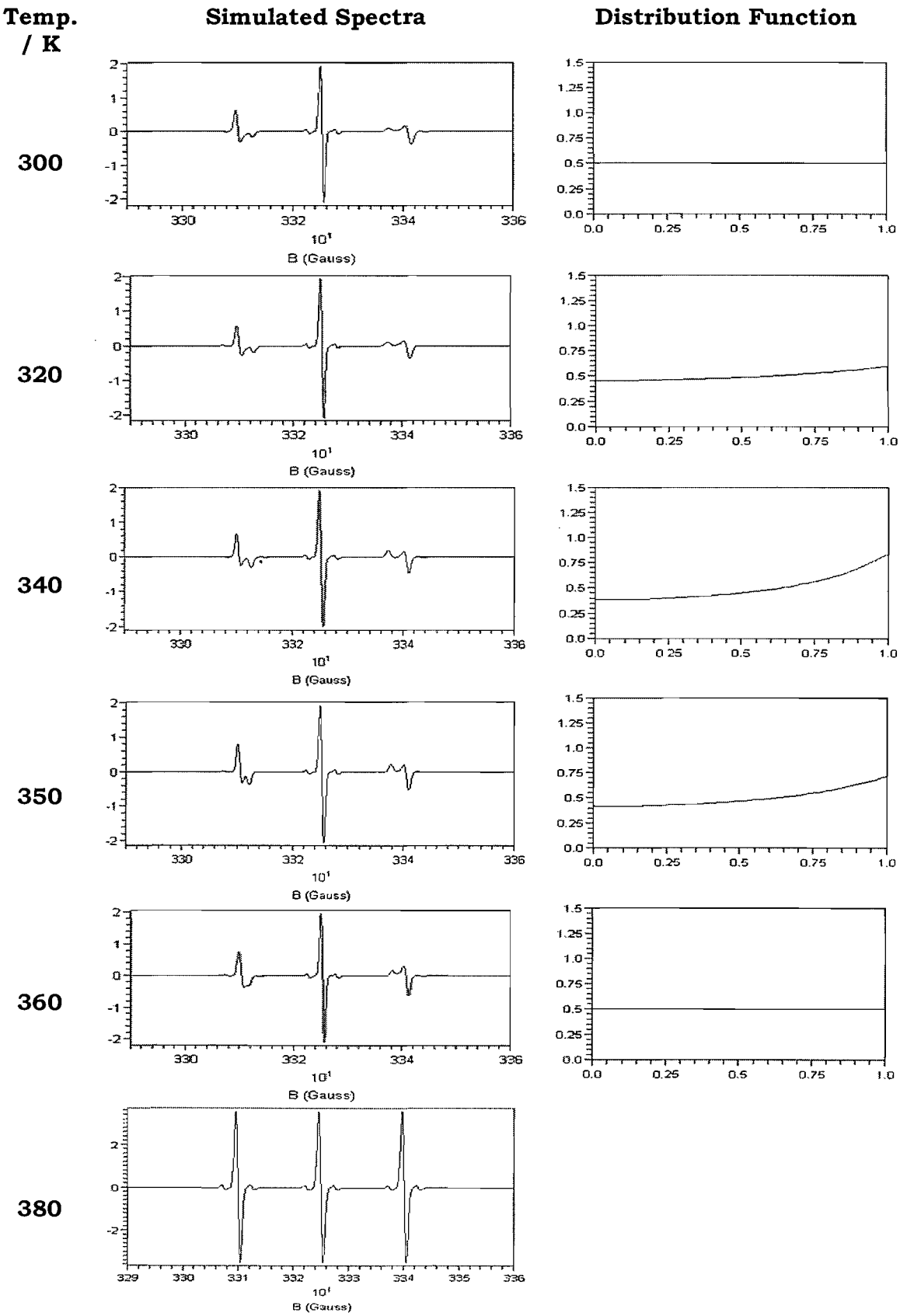

Figure 18: *(b) Simulated ESR spectra for Tempone in chiral nematic ZLI-4792 with 2.0wt% cholesteryl propionate, together with the resultant director distribution function (x-axis represents $\cos\theta$, while y-axis represents $f(\theta)$).*

7.4.5 Concentration of Chiral Dopant in Chiral Nematic: 5.0wt%

Figure 19 (a) shows the series of ESR spectra for 5.0wt% of *cholesteryl propionate* in ZLI-4792 measured from 300K to 380K. Since this sample is the most concentrated *cholesteryl propionate* in nematic ZLI-4792, we certainly expect the ESR spectra to correspond to a random 3D director distribution and so to follow the trend shown by other samples with lower concentrations of chiral dopant. The results obtained here confirm our expectation so we see the perpendicular peaks getting more intense and parallel peaks getting less intense. We have discussed the possible explanation for this kind of director distribution earlier in this Section. The simulation for these spectra along with the corresponding director distribution functions are shown in Figure 19 (b). Table 8 shows the parameters used in order to simulate the spectra. The distribution parameter, *a*, only increases slightly over the 40K temperature range, therefore the director order parameters only change slightly indicating weak alignment by the magnetic field. The simulated spectra are in good agreement with the equivalent experimentally obtained spectra. However, as with the lower concentrations the director distribution is found not to correspond to a perfectly 3D distribution.

Table 8: *The hyperfine spacings, linewidths, and distribution parameter used to simulate ESR spectra for Tempone in ZLI-4792 doped with 5.0wt% cholesteryl propionate.*

Temp. / K	$\tilde{A}_{\parallel}/G$	$\tilde{A}_{\perp}/G$	$T_2^{-1}(-1)/G$	$T_2^{-1}(0)/G$	$T_2^{-1}(1)/G$	*a*
300	12.34	15.45	0.40	0.30	0.28	1.20
320	12.48	15.39	0.30	0.30	0.28	1.35
340	12.60	15.33	0.28	0.30	0.25	1.50
350	13.00	15.10	0.30	0.30	0.30	1.40
360	13.60	14.52	0.40	0.30	0.30	1.00
380	14.42	14.42	0.40	0.40	0.40	

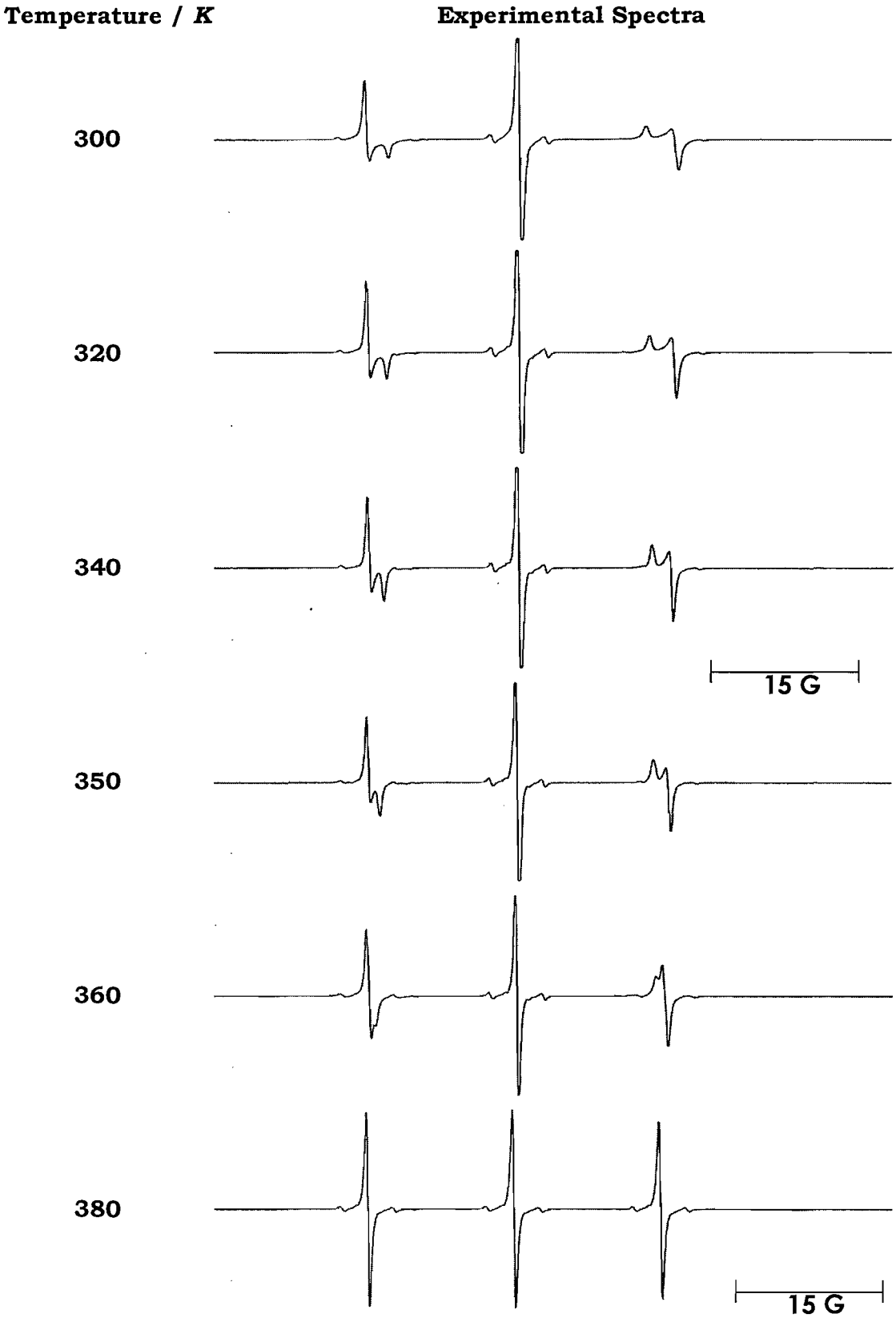

Figure 19: *(a) ESR spectra for Tempone in chiral nematic ZLI-4792 with 5.0wt% cholesteryl propionate.*

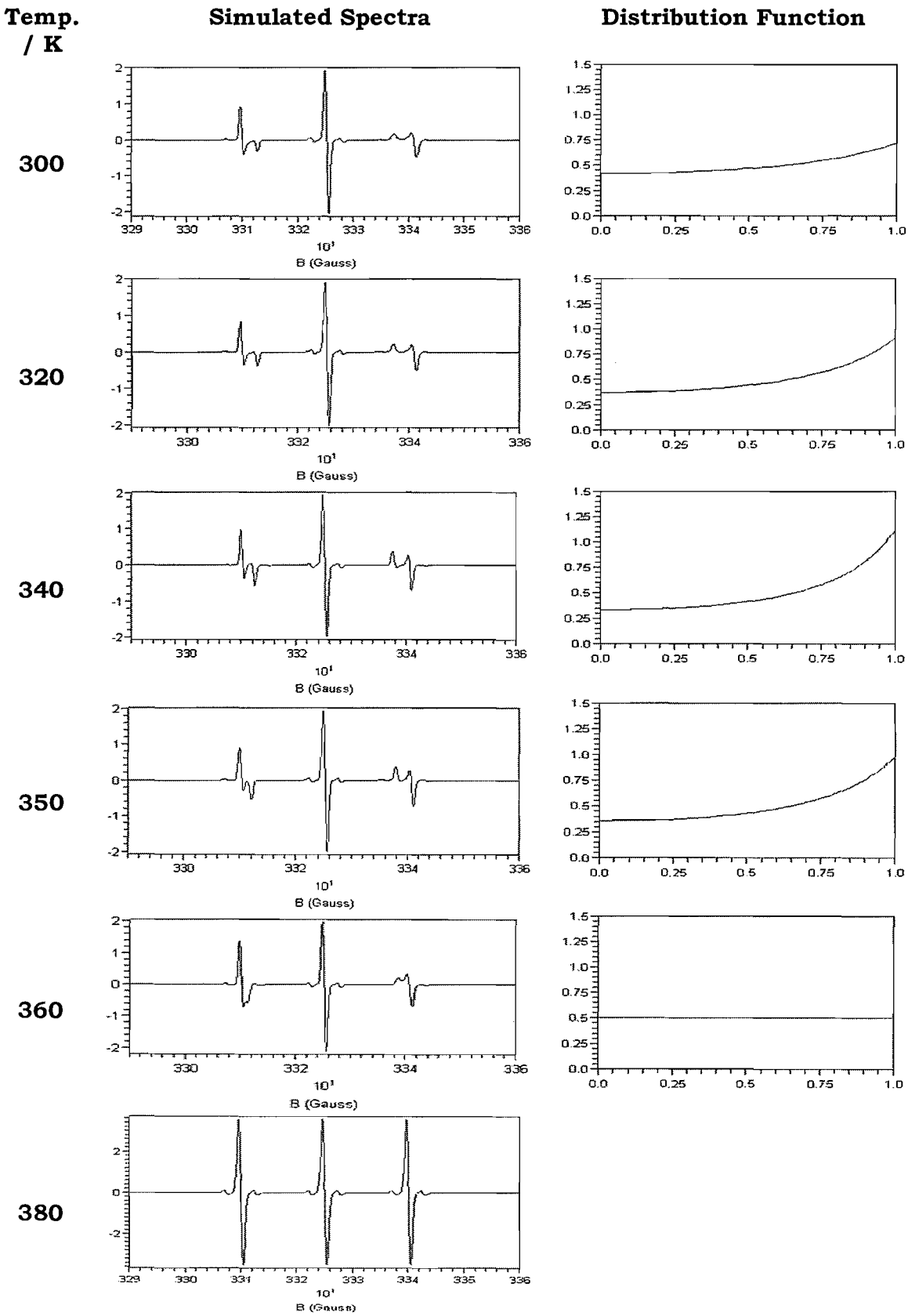

Figure 19: *(b) Simulated ESR spectra for Tempone in chiral nematic ZLI-4792 with 5.0wt% cholesteryl propionate, together with the resultant director distribution function (x-axis represents $\cos\theta$, while y-axis represents $f(\theta)$).*

7.5 Quantitative Calculations for the ESR Spectra

In the previous Section, we have considered at a qualitative level how the intensities of both parallel and perpendicular peaks vary with the chiral dopant concentration, as well as with temperature. The signal intensities of both parallel and perpendicular peaks are our main route to understand the structure of the chiral nematic system in the presence of the magnetic field. In order to study these results quantitatively we need to find a set of data for the spectra that we have measured. These data are acquired from the variation in the heights of the parallel and perpendicular peaks as a function of the chiral dopant concentration and the temperature. The heights of the lines can be measured directly from the ESR spectra, as shown in Figure 20.

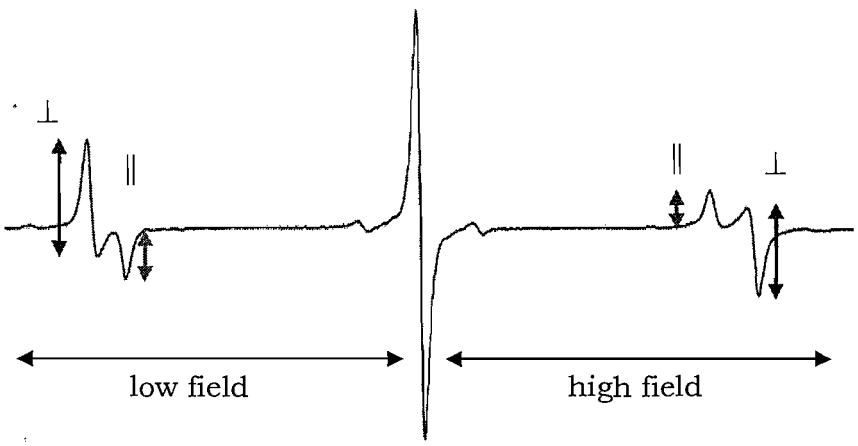

Figure 20: Measurement of peak heights for the parallel and perpendicular peaks.

The calculation involves the height ratio for both parallel and perpendicular peaks, for two types of results, $(\| / \perp)$ and $(\perp / \|)$. In order to simplify this measurement, we divide a single ESR spectrum into two parts; low field and high field. Then, we take the average values for both height ratios, $(\| / \perp)$ and $(\perp / \|)$ of the low and high field peaks. Since our experimental studies depend on two variables; temperature and chiral dopant concentration, so the results will be classified into the temperature and concentration dependence. Our calculation involves the spectra recorded at temperatures from 300K to 350K only, since it is quite hard to measure the height of the peaks when the chiral nematic is close to the nematic-isotropic transition, ~360K, because of the peaks overlap.

7.5.1 Temperature Dependence: $(\| / \perp)$ VS $(\perp / \|)$

The temperature dependence plots for the height ratios, $(\| / \perp)$ and $(\perp / \|)$ are shown in Figure 21; the blue plot represents $(\| / \perp)$, while the red plot represents $(\perp / \|)$. In general, for most samples studied, as the temperature is increased, the height of the parallel peaks increases slightly, and so too do those of the perpendicular peaks but the changes are not so obvious compared to parallel peaks. This indicates that the director order parameter for the chiral nematic phase changes with temperature. Therefore, the height ratios at each temperature, from 300K to 350K should be equal, or almost equal since both peaks are changing with temperature in similar ways.

The plots in Figure 21 show, just for the 0.5wt% chiral nematic system, the height ratio for both peaks is ~1 for $(\| / \perp)$, which means both parallel and perpendicular peaks have almost the same height; or parallel peaks are more intense than perpendicular peaks; corresponding to the 2D director distribution. As for other concentrations, the height ratio is less than one, which indicates that the parallel peaks are weaker than the perpendicular peaks. They are also dependent to the changes in temperature, especially for samples with higher chiral dopant concentrations, namely >2.0wt%. We do not see this behaviour for the 0.5wt% chiral nematic. As for concentrations 1.0wt% and 1.5wt% both of which were studied in duplicate; from the plots, we have found that they behave slightly differently to each which provides an indication of the overall error in the relative heights; this error seems to be significant.

0.5wt%

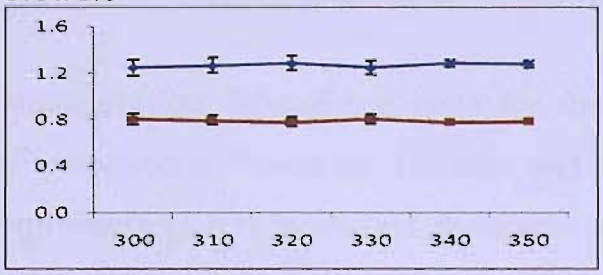

1.0wt% (A)

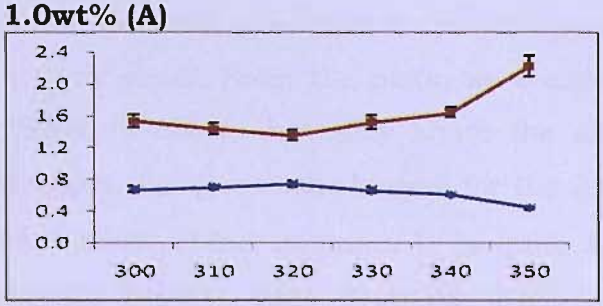

1.0wt% (B)

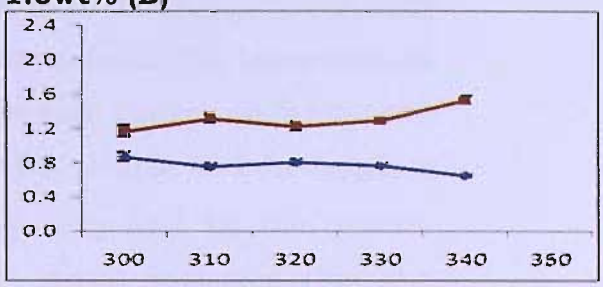

1.5wt% (C)

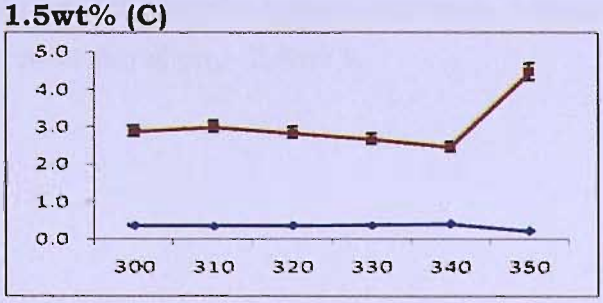

1.5wt% (D)

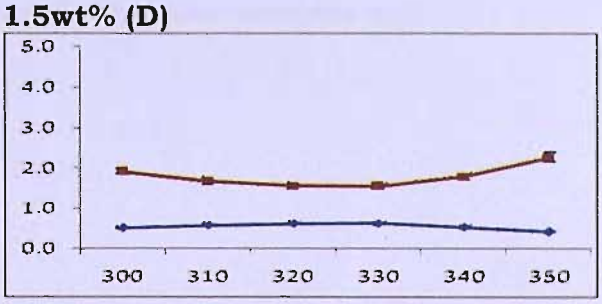

2.0wt%

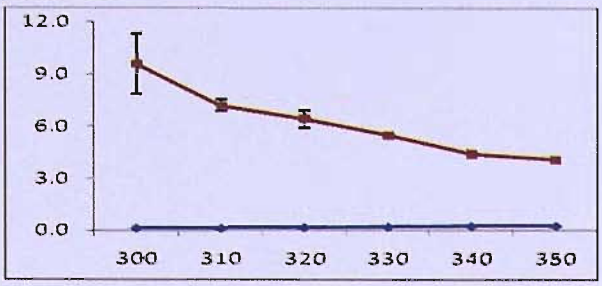

5.0wt%

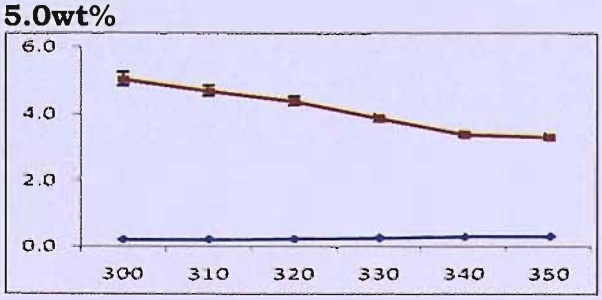

Figure 21: The height ratio for the temperature dependence of (|| / ⊥) (blue) and (⊥ / ||) (red). The y-axis represents the height ratio while the x-axis represents temperature, K.

7.5.2 Concentration Dependence: $(\| / \perp)$ VS $(\perp / \|)$

The concentration dependence plots for the height ratios of $(\| / \perp)$ and $(\perp / \|)$ are shown in Figure 22. The blue plot represents $(\| / \perp)$, while the red plot represents $(\perp / \|)$. In general, for most spectra recorded in this study, as the chiral dopant concentration increased so the perpendicular peaks also increase in intensities, but not for parallel peaks; here the change is essential zero or very small. From the plots, we could conclude for the temperatures from 300K to 350K, that they share the same plot pattern in which the height ratios, $(\perp / \|)$ are the biggest for the 2.0wt%, sample and the smallest for the 0.5wt% chiral nematic. It is quite surprising that for the 5.0wt% sample the height ratios decrease drastically, which indicates that the parallel peaks gain their intensity back, but not similar to those samples with lower concentration, <2.0wt%.

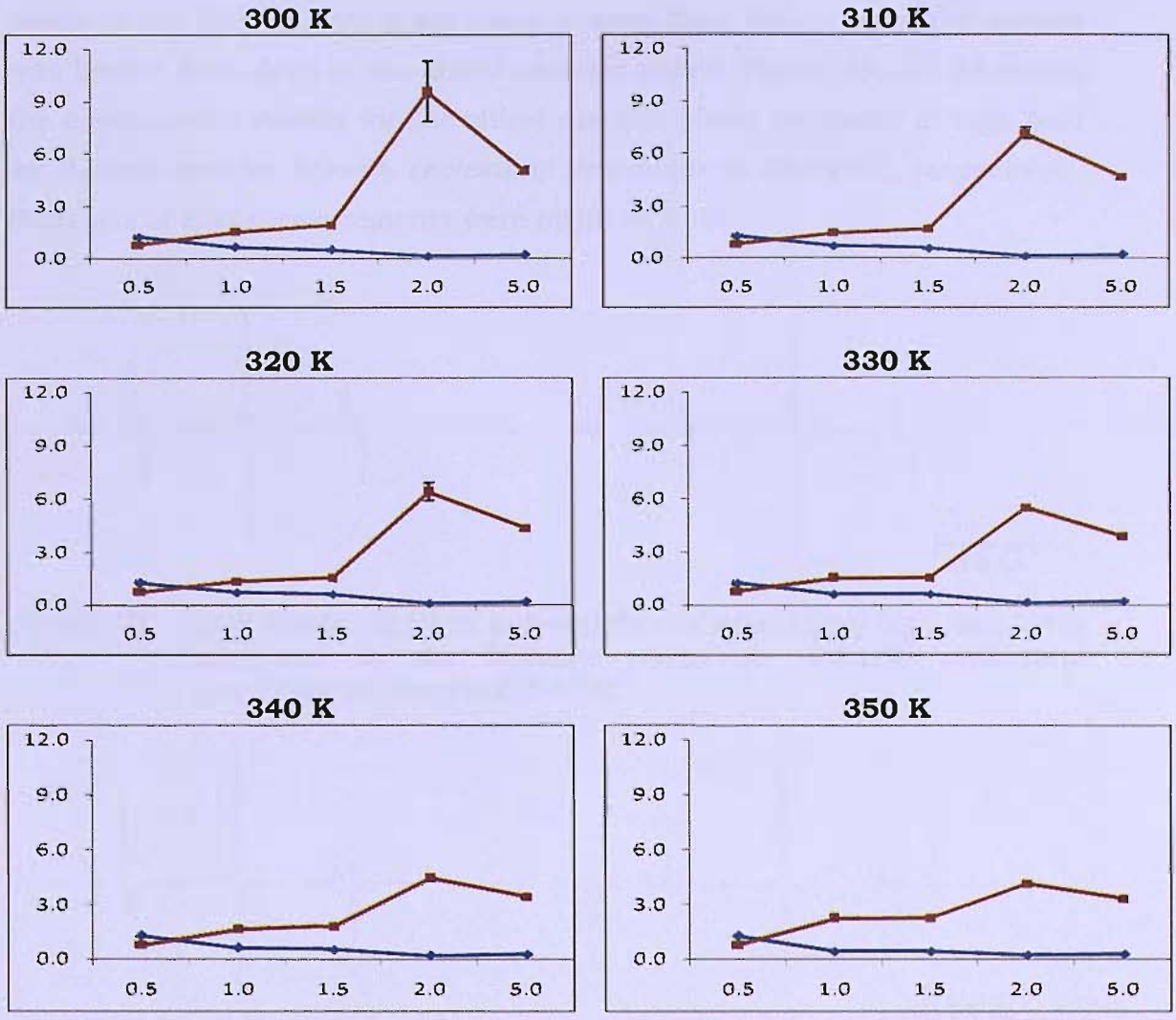

Figure 22: *(a) The concentration dependence of the height ratio for (|| / ⊥) (blue) and (⊥ / ||) (red). The y-axis represents the height ratio while the x-axis represents temperature, K.*

7.6 Isotropic to Chiral Nematic Cooling Experiment

This experiment was carried out to see if there were any changes in the field alignment for the director in the magnetic field, when the sample is heated to isotropic phase at 380K then cooled into the biphasic region before it returns to the chiral nematic phase. Between the phase transitions from isotropic to the biphasic, the field is increased to 6kG for 30min. The idea here was to allow the liquid crystal director to be aligned by the magnetic field. In other words, this method is designed to unwind the helical structure in the chiral nematic phase. If this change occurs, we expect to observe that the parallel

peaks in the ESR spectrum are more intense than before when the sample was heated from deep in the chiral nematic phase. Figure 23 and 24 shows the experimental results for the chiral nematic phase produced at high field for 0.5wt% and for 5.0wt% *cholesteryl propionate* in ZLI-4792, respectively. Both sets of ESR measurements were made at 340K.

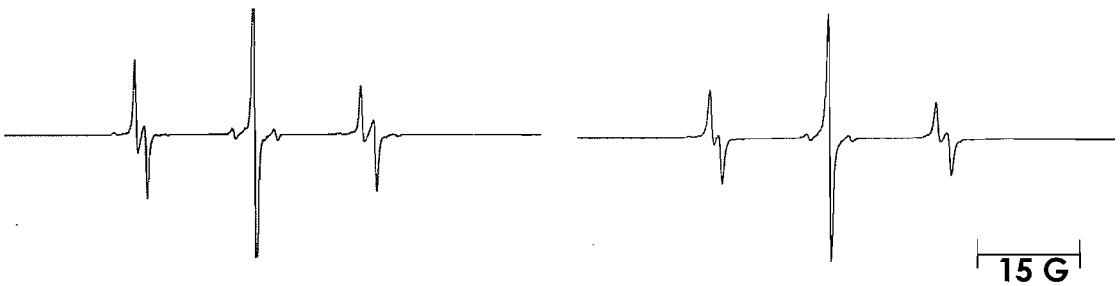

Figure 23: *ESR spectra at 340K before (left) and after (right) high field (6kG) alignment in the biphasic region for 0.5wt% cholesteryl propionate in nematic ZLI-4792.*

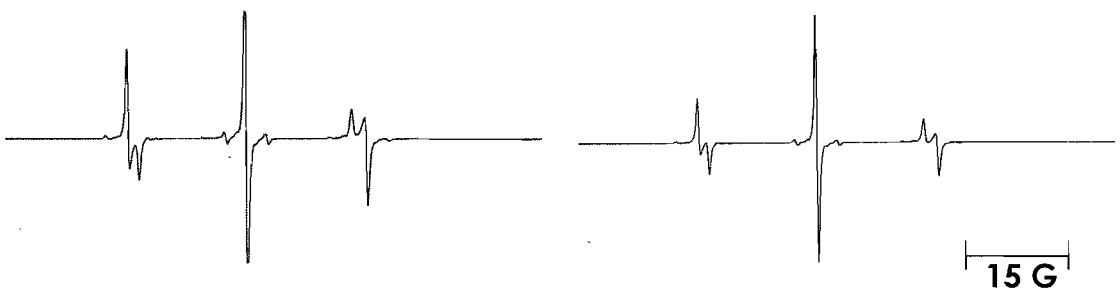

Figure 24: *ESR spectra at 340K before (left) and after (right) high field (6kG) alignment for 5.0wt% cholesteryl propionate in nematic ZLI-4792.*

In Figure 23, the ESR spectra show the difference in the peak intensities between the spectrum of before and after the field alignment. However, the relative heights of the parallel and perpendicular peaks seem equal for both spectra. Therefore, we do not see any sign of the field alignment here. In contrast, the ESR spectra in Figure 24 are in the agreement with our expectations for this experiment. The 6kG field has aligned the director alignment and so has increased the relative height for parallel peaks. However, it might have been expected that the results should be the other way round since the field tends to align easily the director for a sample with a low chiral dopant concentration compared to the high chiral dopant concentration.

7.7 Conclusion

The field-induced director alignment of chiral nematic phase has been characterized successfully by ESR spectroscopy. Most of the results obtained in this experiment are expected and in good agreement with both theory and past studies. An ESR spectrum showing a 2D director distribution, which is expected for the chiral nematic phase was only found for sample ZLI-4792 doped with 0.5wt% *cholesteryl propionate*. The samples with higher chiral dopant concentrations gives a director distribution which approaches 3D, which suggests the director distribution in the chiral nematic phase can go beyond the 2D distribution. The 3D director distribution could be observed for ESR spectra for samples with chiral dopant concentrations as low as 1.0wt%, as was recognised by the appearance of the perpendicular peaks are more intense than the parallel peaks. As the chiral dopant concentration increases, the intensity of the perpendicular peaks also increase. The approximate 3D director distribution indicates that the helixes might be dispersed and freely distributed in a smaller helical structure with multiple orientations and so no preferred directions. The increasing temperature changes the molecular orientational order in the chiral nematic phase. We have observed this behaviour in all of our measurements, where $\widetilde{A}_{\parallel}$ and $\widetilde{A}_{\perp}$ changes their positions and approach closer to each other as the temperature increases until the isotropic phase reached. The molecular order parameter for Tempone in the chiral nematic liquid crystal could be measured from the $\widetilde{A}_{\parallel}$ and $\widetilde{A}_{\perp}$ values. Finally we note that the creation of a near 3D director distribution could be used to determine the phase symmetry; in these experiments it is clear that the symmetry of the local director is uniaxial.

7.8 References

[1] P. J. Collings, M. Hird; *Introduction to Liquid Crystals: Chemistry and Physics*, Taylor and Francis, London (1997).

[2] D. Ionescu, G. R. Luckhurst, D. S. De Silva; *Liq. Cryst.*, **23**, 833 (1997).

[3] F. C. Frank; *Discussions Faraday Soc*, **25**, 19 (1958).

[4] P. Oswald, P. Pieranski; *Nematic and Cholesteric Liquid Crystals,* Taylor and Francis, London (2005).

[5] R. S. Pindak, C. C. Huang, J. T. Ho; *Solid State Comm.*, **14**, 821 (1974).

[6] J. M. Ruxer, G. Solladie, S. Candau; *Mol. Cryst. Liq. Cryst.*, **41**, 109 (1978).

[7] M. R. Wilson, D. J. Earl; *J. Mater. Chem.*, **11**, 2672 (2001).

[8] C. Stützer, W. Weissflog, H. Stegmeyer; *Liq. Cryst.*, **21**, 557 (1996).

[9] S. N. Yarmolenko, L. A. Kutulyas, V. V. Vashchenko, L. V. Chepeleva; *Liq. Cryst.*, **16**, 877 (1994).

[10] H.-G. Kuball, E. Dorr; *Physical Properties of Liquid Crystals,* Ed. by D. A. Dunmur, A. Fukuda, G. R. Luckhurst, Chapt. 7.2, An Inspec Publication, London (2001).

[11] A. Ferrarini, G. J. Moro, P. L. Nordio; *Liq. Cryst.,* **19**, 397 (1995).

[12] A. Ferrarini, G. R. Luckhurst, G. J. Moro, P. L. Nordio; *Mol. Phys,* **77**, 1 (1992).

[13] M. M. Green, S. Zanella, H. Gu, T. Sato, G. Gottarelli, S. K. Jha, G. P Spada, A. M. Schoevaars, B. Feringa, A. Teramoto; *J. Am. Chem. Soc.*, **120**, 9810 (1998).

[14] R. Meyer; *App. Phys. Lett.*, **12**, 281 (1968).

[15] R. Meyer; *App. Phys. Lett.*, **14**, 208 (1969).

[16] G. R. Luckhurst, H. J. Smith; *Mol. Cryst. Liq. Cryst.*, **20**, 319 (1973).

[17] G. Gottarelli, G. F. Pedulli, C. Zannoni; *Chem. Phys,* **64**, 143 (1982).

[18] P. G. de Gennes; *Solid State Comm.*, **6**, 163 (1968).

[19] E. Sackmann, S. Meiboom, L. C. Snyder; *J. Am. Chem. Soc.*, **89**, 5981 (1967).

[20] P. G. de Gennes; *Mol. Cryst. Liq. Cryst.*, **7**, 325 (1969).

[21] G. Durand, L. Leger, F. Rondelez, M. Veyssie; *Phys. Rev. Lett.*, **22**, 227 (1969).

[22] G. R. Luckhurst; *Thin Solid Films.* **506**, 36 (2006).

[23] A. Ferrarini, G. J. Moro, P. L. Nordio; *Mol. Phys,* **87**, 485 (1996).

[24] I. Dierking, F. Giebelmann, P. Zugenmaier, K. Mohr, H. Zaschke, W. Kuczynski; *Liq. Cryst.*, **18**, 443 (1995).

[25] J. J. Wysocki, J. E. Adams, D. J. Oleckna; *Liquid Crystals and Ordered Fluids.*, Plenum Press, New York (1970).